Mechanisms and kinetics of the galvannealing reactions on Ti IF steels

David Zapico Alvarez

To cite this version:

David Zapico Alvarez. Mechanisms and kinetics of the galvannealing reactions on Ti IF steels. Engineering Sciences [physics]. Ecole Centrale Paris, 2014. English. NNT : 2014ECAP0019 . tel-02917919

HAL Id: tel-02917919
https://theses.hal.science/tel-02917919v1

Submitted on 20 Aug 2020

ÉCOLE CENTRALE DES ARTS ET MANUFACTURES
ECOLE CENTRALE PARIS

THESIS

submitted by

David ZAPICO ÁLVAREZ

for the degree of

Docteur de l'École Centrale des Arts et Manufactures

Speciality: **Materials Science**

Host Laboratory: **Laboratoire de Génie des Procédés et Matériaux**

Partnership: **ArcelorMittal Global R&D**

Mechanisms and kinetics of the galvannealing reactions on Ti IF steels

Defended on the 12th February 2014 in front of the examining board:

Yves BIENVENU	**Ecole des Mines de Paris**	**Rapporteur**
Dominique MANGELINCK	**IM2NP - CNRS**	**Rapporteur**
Florence BERTRAND	**ArcelorMittal Global R&D**	
Dominique CHATAIN	**CINaM - CNRS**	
Marie-Laurence GIORGI	**Ecole Centrale Paris**	
Jean-Michel MATAIGNE	**ArcelorMittal Global R&D**	
Eduardo SAIZ GUTIERREZ	**Imperial College London**	

ACKNOWLEDGEMENTS

This thesis is the result of a research work carried out in the frame of a collaboration between the Laboratoire de Génie des Procédés et Matériaux of the Ecole Centrale Paris and the Surface and Coatings department of the Automotive Centre of ArcelorMittal Maizières Research and would not have been possible without the great help and support of many people.

First of all, I would like to express my most sincere gratitude to my thesis director, Marie-Laurence Giorgi, and my company supervisors, Jean-Michel Mataigne and Florence Bertrand, for their numerous advices and scientific contributions but also for their guidance and availability and for the warmth that they have always shown towards me.

I am also very grateful to Yves Bienvenu and Dominique Mangelinck for having evaluated this work as rapporteurs, as well as to Dominique Chatain and Eduardo Saiz Gutierrez for agreeing to participate in my thesis examining board.

My thanks are also addressed to Michel Babbit, head of the Automotive Centre of ArcelorMittal Maizières Research, Jacques Petitjean, Hervé Derule and Luc Diez, heads of the Surface and Coatings department of this centre, and Patrick Perré, head of the Laboratoire de Génie des Procédés et Matériaux of the Ecole Centrale Paris, for having welcomed me perfectly within their respective organizations.

I would also like to gratefully acknowledge Lydia Rachiele and Pascale Feltin for their daily work in the sample preparation and heat treatments, Céline Musik, Patrick Barges, Nathalie Ruscassier and Annick Willems for the valuable assistance in the sample preparation and the characterizations in the Scanning and Transmission Electron Microscopes, Ian Zuazo and Brahim Dkill for their support in crystallography, Sébastien Cremel and Valérie Philippe for the characterizations by Secondary Ion Mass Spectroscopy, Fanny Collignon and Franco del Frate for their support in the galvanizing experiments and Jean-Marc Mougeolle for the chemical analyses. They all have strongly contributed to this work.

I also wish to thank all those who helped me during my work and who patiently answered all my questions, in particular Christophe Klam, Jonas Staudte, Didier Dauchelle, Christian Allély, Aymeric Corbel and Tiago Machado Amorim.

Thanks also to all my colleagues from both the Laboratoire de Génie des Procédés et Matériaux of the Ecole Centrale Paris and the Surface and Coatings department of ArcelorMittal Maizières Research, for the cordial welcome they reserved for me and the good humour they make prevail at work. In addition to those I have already mentioned above, I think especially to ladies Delphine Thai, Marine Kieffer, Caroline Mengouchi, Céline Mallé, Michele Orsini, Isabelle Souedet, Florence Meyer, Déborah Herry, Marcele Salgueiro, Nadine Moussa and Sepideh Habibi and gentlemen Jean-Jacques Piezanowski, Joris Giroux, Serge Santini, Mustafa Sager, Julien Colombeau and Wei Ai.

Special mention deserves the Spanish-speaking group of ArcelorMittal Maizières Research. Thank you so much for all the funny moments spent during the wonderful lunches every Thursday in the canteen.

Finally, as it could not be otherwise, I would like to wholeheartedly thank family and friends for the support received. More especially, I want to emphasize my gratefulness to my mother, my brothers, Marcos and Borja, my uncle Maximiliano and my girlfriend, Patricia, for helping and encouraging me at any time and for their continuous signs of affection and confidence towards me.

TABLE OF CONTENTS

LIST OF FIGURES

LIST OF TABLES

NOMENCLATURE

a_{Fe} , a_{Al} , a_{Zn}	Activities of iron, aluminium and zinc in the iron-supersaturated liquid phase
$a_{Fe}^{comp,sat}$, $a_{Al}^{comp,sat}$, $a_{Zn}^{comp,sat}$	Activities of iron, aluminium and zinc in the iron-saturated liquid phase in equilibrium with the intermetallic compound
c_{Fe}^{int}	Iron concentration at the ferrite / liquid zinc interface (mol.m^{-3})
c_{Fe}^{int2}	Iron concentration at the interfacial alloy / liquid zinc interface (mol.m^{-3})
c_{Fe}^{met}	Iron concentration in the liquid zinc in metastable equilibrium with ferrite (mol.m^{-3})
c_{Fe}^{sat}	Iron concentration in the liquid zinc in equilibrium with the interfacial alloy (mol.m^{-3})
$c_{Zn}^{l_1/l_2}\left(x_k -\right)$, $c_{Zn}^{l_1/l_2}\left(x_k +\right)$	Zinc concentrations at the two sides of the l_1 / l_2 interface (mol.m^{-3})
$D_{Al}^{Zn(L)}$, $D_{Fe}^{Zn(L)}$	Diffusion coefficients of aluminium and iron in liquid zinc (m^2.s^{-1})
D_{Fe}^{comp}	Diffusion coefficient of iron in the interfacial compound (m^2.s^{-1})
$D_{Fe}^{\mathrm{Fe_2Al_5}}$, $D_{Zn}^{\mathrm{Fe_2Al_5}}$	Diffusion coefficients of iron and zinc in Fe_2Al_5 (m^2.s^{-1})
D_{M}^{steel} , D_{O}^{steel}	Diffusion coefficients of the alloying element M and oxygen in the steel (m^2.s^{-1})
$D_{Zn}^{i.l.}$	Diffusion coefficient of zinc in the inhibition layer (m^2.s^{-1})
D_{Zn}^{δ}, $D_{Zn}^{Fe_2Al_5Zn_x}$	Diffusion coefficients of zinc in δ and $Fe_2Al_5Zn_x$ (m^2.s^{-1})
D_0	Pre-exponential factor of the diffusion coefficient of zinc in the inhibition layer (m^2.s^{-1})
E	Potential difference between the working electrode and the SCE (mV)
E_a	Activation energy for the diffusion of zinc in the inhibition layer (J.mol^{-1})
$e_{coating}$	Coating thickness (µm)
$e_{Fe_2Al_5Zn_x}$, e_{δ}	Thicknesses of the $Fe_2Al_5Zn_x$ and δ layers (nm)
f_S	Surface area fraction covered by $Fe_2Al_5Zn_x$ (%)
G	Grain size number (ASTM International)
I	Rate of heterogeneous nucleation (m^{-2}.s^{-1})
J	Current density (µA.cm^{-2})
J_{Fe}^{diss}	Iron dissolution flux (mol.m^{-2}.s^{-1})
J_{Fe}^{cons}	Iron flux consumed by the growth of the interfacial alloy (mol.m^{-2}.s^{-1})
k_B	Boltzmann’s constant (J.K^{-1})

k_{diss}	Iron dissolution rate constant (m.s^{-1})
k_{growth}	Interfacial alloy growth rate constant (m.s^{-1})
k_{nucl}	Nucleation rate constant (Pa.m^{-2})
L_{im}	Immersion length (m)
L_{crit}	Critical length in the bath including the quantity of aluminium necessary to form a covering $Fe_2Al_5Zn_x$ layer with $e_{Fe_2Al_5Zn_x}$ and $w_{Al}^{Fe_2Al_5Zn_x}$ (µm)
m_{Al}	Aluminium uptake by the inhibition layer (g.m^{-2})
N_{AE}	Number of grains per square inch at 100 X magnification (ASTM International)
Q_c	Critical quantity on zinc diffused at the steel grain boundaries necessary for the inhibition layer breakdown (mol m^{-2})
$Q_{hold,\exp}$	Quantity on zinc diffused at the steel grain boundaries during an isothermal heat treatment for $t_{hold,\exp}$ at $T_{hold,\exp}$ in the Gleeble 3500 device (mol m^{-2})
Q_{Rhesca}	Quantity of zinc diffused at the steel grain boundaries during immersion and cooling in the Rhesca pilot simulator (mol m^{-2})
R	Universal gas constant (J mol^{-1} K^{-1})
R_a	Arithmetic mean of the absolute deviations of the roughness profile from the mean line (µm)
$S^{\mathrm{Zn(L)}/comp}$	Contact surface between liquid zinc and the intermetallic compound (m^2)
$S^{steel/comp}$	Contact surface between steel and the intermetallic compound (m^2)
T	Temperature (°C or K)
T_{bath}	Bath temperature (°C)
$T_{hold,\exp}$	Experimental holding temperature in the Gleeble 3500 device (°C or K)
t_c	Critical time necessary for the inhibition layer breakdown (s)
t_{im}	Immersion time (s)
t_{growth}	Time necessary for the growth of a covering inhibition layer (s)
$t_{hold,\exp}$	Experimental holding time in the Gleeble 3500 device necessary for the inhibition layer breakdown during an isothermal heat treatment at $T_{hold,\exp}$ (s)
$t_{outburst}$	Time required for outbursts formation during immersion in the bath (s)
v	Line speed (m. min^{-1})
W_a	Arithmetic mean of the absolute deviations of the waviness profile from the mean line (µm)

w_{Al}	Bath aluminium content (wt.%)
$w_{Al}^{Fe_2Al_5Zn_x}$, w_{Al}^{δ}	Aluminium weight fractions in $Fe_2Al_5Zn_x$ and δ
w_{Al}^{sat} , w_{Fe}^{sat}	Aluminium and iron weight fractions in the liquid phase in equilibrium with the intermetallic compound
w_{Fe}^{met}	Difference between the iron concentration in the liquid phase in metastable equilibrium with ferrite and the iron concentration at the ferrite / liquid zinc interface (wt.%)
w_C , w_N , w_S , w_P , w_{Si}	Weight fractions of carbon, nitrogen, sulphur, phosphorus and silicon in the steel
$w_{Ti_{total}}$	Weight fraction of total titanium in the steel
$w_{Ti_{excess}}$	Weight fraction of excess solute titanium in the steel
$w^{*}_{Ti_{excess}}$, $w^{**}_{Ti_{excess}}$, $x_{Ti_{excess}}$	Excess solute titanium in the steel (different estimations)
x_{Fe}^{comp} , x_{Al}^{comp} , x_{Zn}^{comp}	Iron, aluminium and zinc mole fractions in the intermetallic compound
x_i	Sum of the iron and zinc mole fractions in the intermetallic compound i
x_M^{steel} , x_O^{steel}	Mole fractions of the alloying element M and oxygen in the steel
β_{comp} ,	Degree of iron supersaturation in the liquid phase with respect to the equilibrium with the intermetallic compound
ΔG	Gibbs free energy of formation of the intermetallic compound in equilibrium with the liquid phase ($kJ.mol^{-1}$)
ΔG_{het}^{comp}	Gibbs free energy of formation of an embryo containing *n* molecules of the intermetallic compound from an-iron supersaturated liquid phase ($kJ.mol^{-1}$)
ΔG_{vol}^{comp}	Energy gain of creating a new volume by the formation of an embryo of the intermetallic compound ($kJ.mol^{-1}$)
ΔG_{surf}^{comp}	Energy cost due to the creation of new interfaces by the formation of an embryo of the intermetallic compound ($kJ.mol^{-1}$)
ΔH	Enthalpy of formation of the intermetallic compound in equilibrium with the liquid phase ($kJ.mol^{-1}$)
$\nabla c_{Zn}^{i.l.}$	Zinc concentration gradient in the inhibition layer ($mol\ m^{-4}$)
θ	Wetting angle (°)
ρ_{δ} , $\rho_{Fe_2Al_5Zn_x}$, ρ_{Zn}	Densities of δ, $Fe_2Al_5Zn_x$ and zinc ($kg.m^{-3}$)
$\sigma^{steel/comp}$	Interfacial tension between steel and the intermetallic compound ($J.m^{-2}$)
$\sigma^{Zn(L)/comp}$	Interfacial tension between liquid zinc and the intermetallic compound ($J.m^{-2}$)
$\sigma^{\mathrm{Zn(L)}/steel}$	Interfacial tension between liquid zinc and steel ($J.m^{-2}$)

$\phi_{Zn}^{i.l.}$	Zinc diffusion flux in the inhibition layer (mol m^{-2} s^{-1})
CDL	Characteristic Diffusion Length
CSP	Cross Section Polishing
DP	Dual Phase
EBSD	Electron Back-Scatter Diffraction
EDS	Energy Dispersive Spectroscopy
EG	ElectroGalvanizing
EPMA	Electron Probe Micro-Analysis
FIB	Focused Ion Beam
GI	GalvanIzed
GA	GalvAnnealed
HDG	Hot-Dip Galvanizing
HDGA	Hot-Dip GalvAnnealing
HMTA	HexaMethyleneTetrAmine
HXRD	Hot X-Ray Diffraction
ICP-MS	Inductively Coupled Plasma Mass Spectrometry
IF	Interstitial Free
IPF	Inverse Pole Figure
JCPDS	Joint Committee on Powder Diffraction Standards
OCP	Open-Circuit Potential
OES	Optical Emission Spectrometry
PVD	Physical Vapour Deposition
SCE	Standard Calomel Electrode
SEM	Scanning Electron Microscopy
SIMS	Secondary Ion Mass Spectrometry
TEM	Transmission Electron Microscopy
TRIP	TRansformed Induced Plasticity
XMA	X-ray Micro-Analysis
XRD	X-Ray Diffraction

INTRODUCTION

In order to protect it against corrosion, the steel is usually covered with a zinc layer. On the one hand, zinc gets preferentially dissolve and act as a sacrificial anode for iron in case of scratch up to the steel; on the other hand, the corrosion products formed act as a barrier against corrosive media.

In this field, the continuous hot-dip galvanizing process has a major impact. This process is worldwide spread and concentrates most of the production of zinc coatings. It consists in the immersion of the steel strip in a molten zinc bath containing small amounts of aluminium. As the steel strip enters the bath, two interfacial reactions occur: the dissolution of iron and the formation of a very thin aluminium-rich intermetallic layer on the steel substrate. This layer inhibits the alloying reactions between iron and zinc and, consequently, is commonly known as *inhibition layer*. After exiting the zinc bath, the steel strip is rapidly cooled down to room temperature. The final coating is therefore composed of this very thin interfacial layer and the solidified zinc overlay.

A process route alternative to the conventional hot-dip galvanizing process is to perform an annealing step after immersion in the molten zinc bath (hot-dip galvannealing process) in order to destabilize the inhibition layer (*inhibition layer breakdown*) and favour the alloying reactions between iron and zinc (*liquid zinc consumption* and *iron enrichment of the solid coating*). Coatings made by means of this process route are commonly known as galvannealed coatings and their final microstructure is therefore composed of different Fe-Zn phases.

The work presented here focuses on galvannealed coatings on Ti IF steels. The in-use properties of this kind of coatings are very sensitive to the Fe-Zn phase distribution within the coating microstructure. Nowadays, the hot-dip galvannealing process is relatively well mastered. However, increased needs to improve the coatings quality and reduce production costs demand an accurate knowledge of the complex reactions involved in the development of the coating along the thermal cycle in terms of mechanisms and kinetics. Separate physical modelling of these reactions is crucial to ensure these needs.

In the first chapter of this work, a literature review is presented. After a brief presentation of the issues and characteristics of the industrial process, focus is given to those studies on the thermodynamics of the Al-Fe-Zn ternary system and, more particularly, to the experimental measurements of the equilibrium liquidus lines in order to determine the phase diagram which describes the best the galvannealing reactions. These reactions are then reviewed in detail, with special interest in the effect of process parameters such as the galvanizing conditions, the Ti IF steel features or the thermal cycle on reaction mechanisms and kinetics.

The second chapter focuses on the formation of the inhibition layer. The galvanizing conditions are expected to play an important role on the nature of this layer. In order to evidence this effect, the nature of this inhibition layer has been characterized for two different galvanizing conditions on industrially galvanized Ti IF steel samples. The results obtained allow proposing a reaction mechanism accounting for the formation of this layer. The kinetics of this reaction is extremely fast (less than one second), so it has not been investigated in this study.

The third chapter focuses on the inhibition layer breakdown. This reaction represents a key step in the hot-dip galvannealing process as it is responsible for the onset of the alloying reactions between iron and zinc leading to the final microstructure of the coating. In the present work, this reaction has been studied on industrial full-hard steel samples, galvanized and subsequently annealed in laboratory pilots. A logical mechanism accounting for this reaction is proposed. The kinetics of this reaction has been accurately investigated and the effect of the bath aluminium content and the Ti IF steel chemical composition on it has been quantified.

The two last reactions, i.e., the liquid zinc consumption and the iron enrichment of the solid coating, have not been studied in the present work.

Finally, the conclusions extracted from the results obtained and the perspectives for future work are discussed.

CHAPTER I: GENERAL PRESENTATION OF THE PROBLEM

I.1. Industrial context

I.1.1. Zinc-based coatings [1-4]

The guarantees for corrosion resistance of steel sheets, currently required by customers, match with the expected life of the equipment (12 years for the automotive market and 10 to 30 years for the industry&construction market). In order to meet this specification, the steel is usually covered with a protective coating (Figure 1).

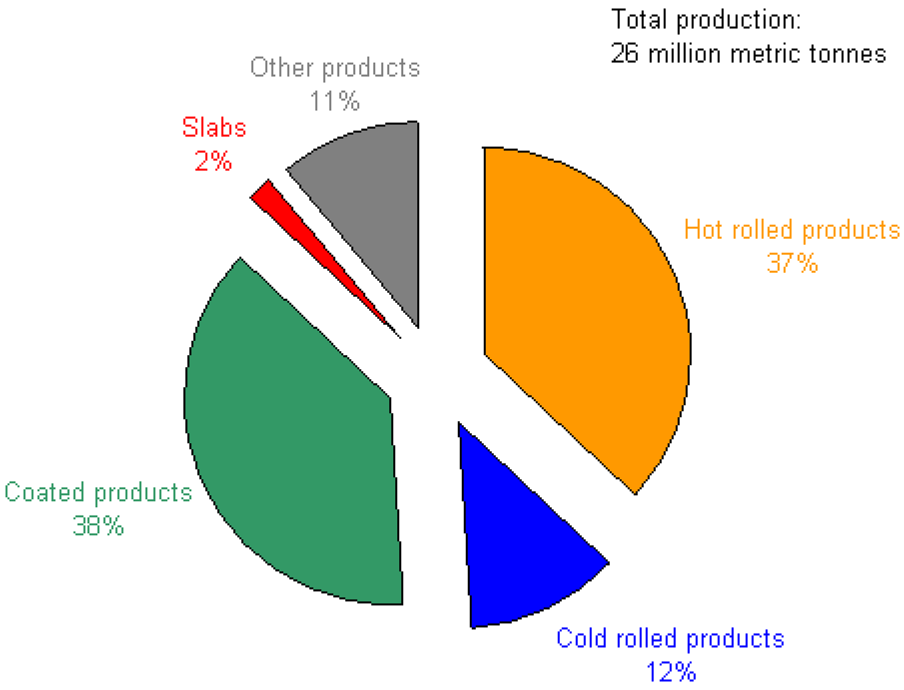

Figure 1: Distribution of Flat Carbon Europe ArcelorMittal's segment steel production by product type in 2012 [5].

In order to ensure its corrosion resistance, the steel is usually coated with a zinc-based coating. As a matter of fact, zinc offers an extremely efficient protection to the steel substrate. On the one hand, this element reacts preferentially and acts as a sacrificial anode with respect to iron when a scratch reaches the steel substrate. On the other hand, the corrosion products formed play the role of a physical barrier against the corrosive environment.

Nowadays, there are mainly three different technologies to produce zinc-based coatings:

- Hot-Dip Galvanizing (HDG);
- ElectroGalvanizing (EG);
- Physical Vapour Deposition (PVD)[1].

---

[1] The PVD technology is currently being introduced by some steelmakers in industry and the production of zinc-based coatings by means of this technology is still extremely low compared to the EG technology and, above all, the HDG technology. In the case of ArcelorMittal, the PVD technology is currently under development at pilot scale and in process of industrialization.

While the HDG process consists in the immersion of the steel strip into a liquid zinc bath containing small amounts of aluminium, the EG process is based in the electrodeposition of zinc on the steel surface by immersion of the steel strip in an aqueous solution containing zinc cations (Zn^{+2}).

In our work, the focus will be on the HDG process technology, the most widespread one in industry among the previous ones (Figure 2).

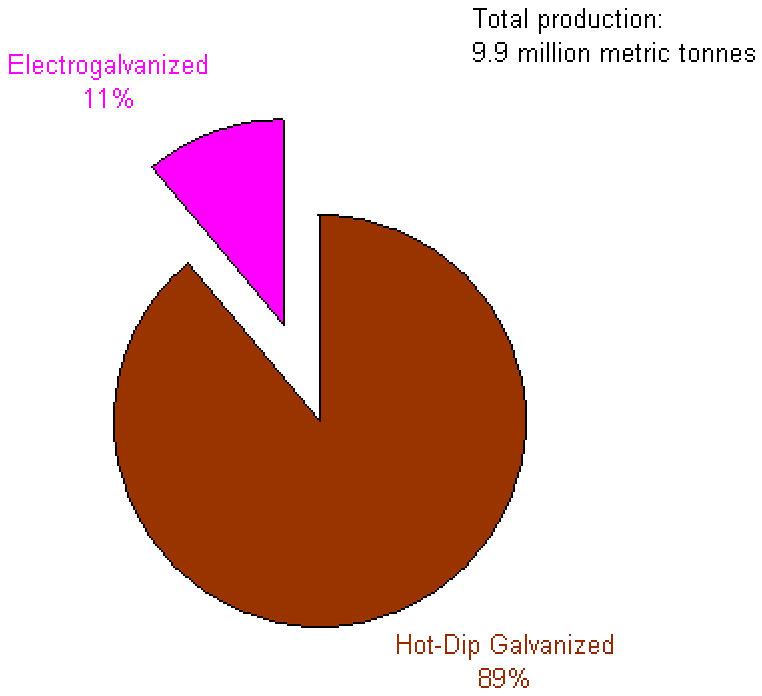

Figure 2: Distribution of Flat Carbon Europe ArcelorMittal's segment coated steel production by process technology in 2012 [5].

The Hot-Dip Galvanized steel volume production is mainly distributed between the automotive and industry&construction markets (Figure 3).

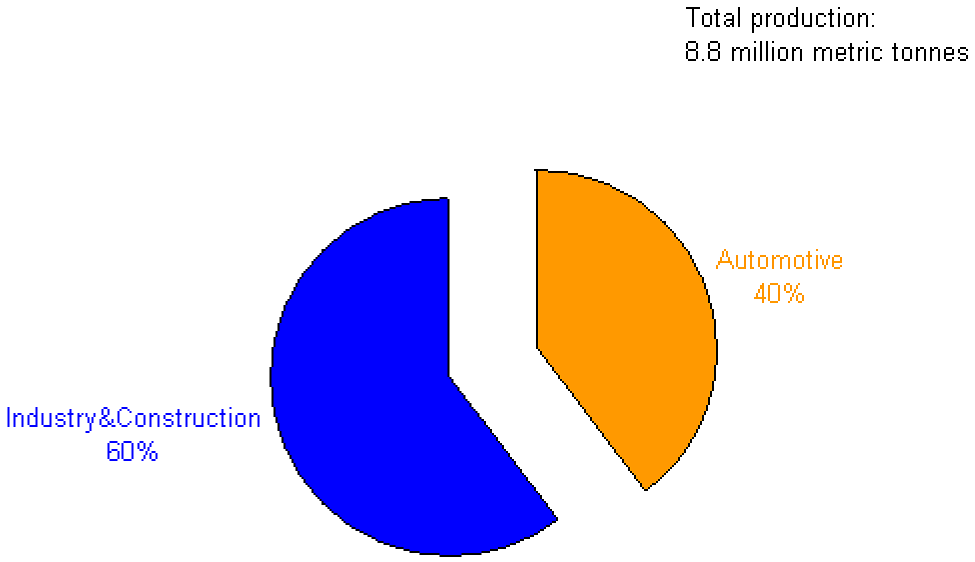

Figure 3: Distribution of Flat Carbon Europe ArcelorMittal's segment Hot-Dip Galvanized steel production by destination market in 2012 (source: ArcelorMittal's internal documents).

The galvanizing process conditions for a given steel coil highly depend on its future use. Any process data presented hereafter will be specific to galvanized steel products for the automotive market. These products are usually galvanized in zinc baths with low bath aluminium contents: generally either between 0.16 and 0.3 wt.% (section I.1.2) or between 0.1 and 0.135 wt.% (section I.1.3). More particularly, the present work focuses in those coatings galvanized in zinc baths with aluminium content within this latter range.

I.1.2. The Hot-Dip Galvanizing process [2-4]

The first HDG industrial lines date from the mid-19th century. In those days, the process was discontinuous and consisted in the immersion of the metallic parts in several baths corresponding to different stages of treatment: degreasing, pickling, fluxing and, finally, galvanizing by means of immersion in a molten zinc bath. This methodology is still in use today in the case of finished products such as telegraph poles, beams, guardrails ...

However, in the case of galvanized steel sheets, the continuous HDG lines allow increasing efficiency, reducing costs and improving the quality of the coatings. The first continuous HDG lines appeared in the 1930s in Europe and USA. Since then, the continuous HDG process has known a constant technical evolution and is currently spread worldwide. A schematic view of a typical continuous HDG line is depicted in Figure 4, where the following operations can be easily distinguished:

- At the line entry (right-hand side of Figure 4), the steel coils are positioned onto the pay-off reels and are transported along the HDG line continuously by means of a welder and an entry looper or accumulator.

- The steel strip is then submitted to a thermal (direct flame preheating), chemical (alkaline bath) or electrochemical degreasing in order to remove rolling oils. Fine particles are subsequently removed from the strip surface by means of a mechanical brushing (only in the case of chemical or electrochemical degreasing).

- A recrystallization annealing is then performed. The aim of this operation is to recrystallize the steel substrate microstructure, strongly hardened during cold rolling, and to obtain its microstructural requirements (grain size and distribution, phase distribution). Typical soaking temperatures and times for this annealing step are around 800 °C and 40 s. The annealing furnace is atmosphere-controlled (a mixture of N_2 and H_2) in order to prevent external oxidation and to ensure a good wettability of the steel surface by the liquid zinc. The last step of this recrystallization annealing, the equalizing step, is usually performed at a temperature slightly higher than that of the zinc bath.

- The next step is the immersion of the steel strip in an iron-saturated zinc bath, which contains small amounts of aluminium (from 0.16 to 0.3 wt.%, normally), at around 460 °C. The residence time in the zinc bath is obviously dependent on both the line speed and the immersed length and is usually around 2-3 s. A schematic view of a typical galvanizing bath is available in Figure 5. As can be seen, the steel strip enters the zinc bath through a kind of tunnel called *snout*. This tunnel is under controlled atmosphere (a mixture of N_2 and H_2) in order to avoid the steel surface oxidation. The strip is guided into the zinc bath by the so-called *sink* and *correcting rolls*[2]. As the strip enters the bath, interface reactions[3], which will be described in detail in section I.3.1, occur very rapidly. The temperature of the strip at

---

[2] In some galvanizing baths, the steel strip guiding operation is performed by a third roll placed between the *correcting roll* and bath exit, commonly known as *stabilizing roll*.

[3] A result of the reactions taking place in the bath is the formation of suspended particles, called dross particles. Two types of drosses can be mainly differentiated. The so-called *surface drosses*, less dense than the liquid zinc, are regularly skimmed from the bath surface by an operator. The so-called *bottom drosses*, denser than the liquid zinc, are removed from the bottom of the pot through different bath management operations. It is important to remove these particles efficiently or to try to avoid their formation because they can be the cause of coating defects leading to the final product downgrading. More information about the chemical nature of these drosses will be given in section I.2.2.

immersion is chosen to be that of the zinc bath in order to limit undesired heat exchanges and have a controlled and steady interface reaction temperature. As these reactions modify the bath composition, an ingot feeding system is used to maintain it at the set value. The bath temperature is also fixed at the aimed value by means of an induction heating system.

- At the bath exit, the steel strip is covered with a too important thickness of liquid zinc because of its viscous drag induced by the strip movement. The coating thickness is reduced to around 10 µm by means of a nitrogen or air wiping operation.

- After wiping, the steel strip is progressively cooled in the cooling tower and the liquid zinc is consequently solidified. The strip steel is then water quenched down to room temperature.

- The skin-pass operation, a low thickness reduction rolling operation, is subsequently performed in order to provide to the strip a suitable flatness as well as its final roughness and mechanical properties.

- Depending on its final use, the steel strip can then be submitted to a chromate treatment to prevent the surface corrosion of zinc (white rust) during its storage.

- Finally, the strip is inspected, cut and coiled.

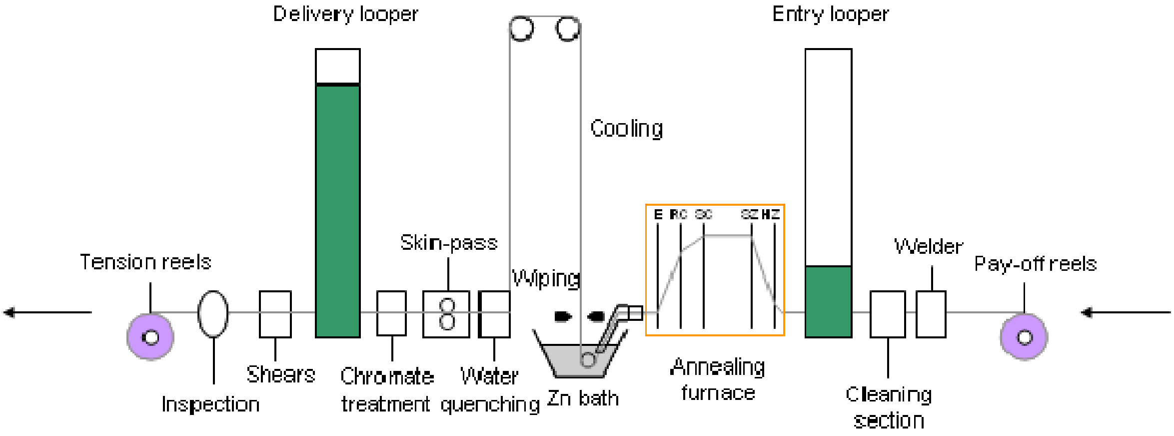

Figure 4: Schematic view of a continuous HDG line (direction of production from right to left) (source: ArcelorMittal Global R&D).

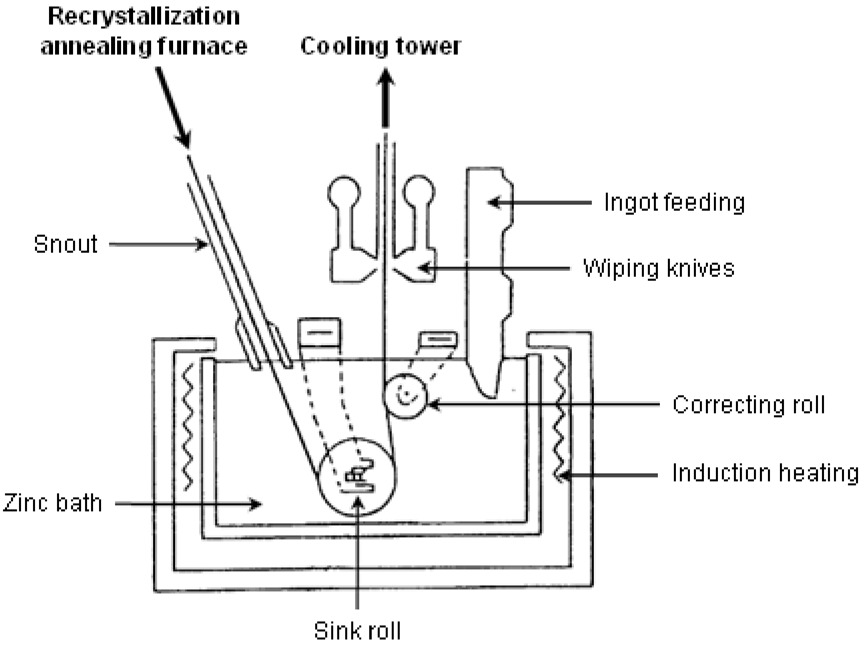

Figure 5: Schematic view of a galvanizing bath [3].

Although the strip speed in typical HDG lines can range between 40 and 180 m/min, a very usual speed line is around 120 m/min. Such galvanizing lines can process an average production of 500,000 metric tonnes/year.

The final microstructure of a conventional galvanized (GI) coating consists of a very thin intermetallic layer of $Fe_2Al_5Zn_x$ ($0 < x < 1$), a formula commonly used to indicate a ternary compound in the vicinity of the binary compound Fe_2Al_5 (around 150 nm), commonly known as *inhibition layer*, and the solidified zinc overlay (Figure 6).

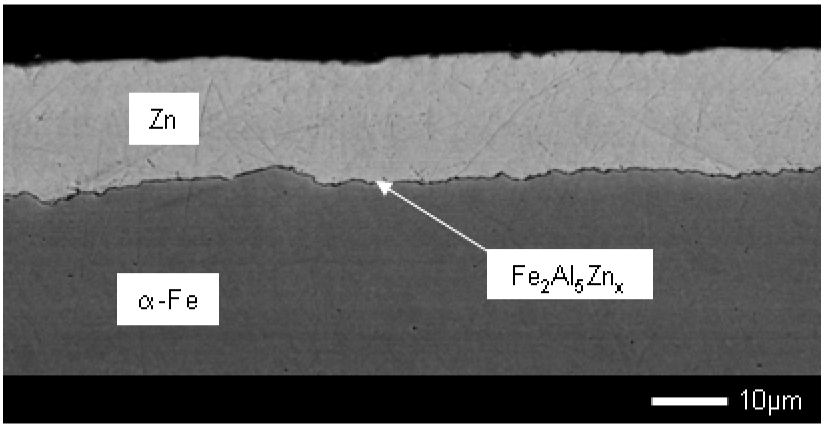

Figure 6: Cross section micrograph of a GI coating, whose microstructure is composed of a very thin layer of $Fe_2Al_5Zn_x$ and the solidified zinc overlay (source: ArcelorMittal Global R&D).

I.1.3. The Hot-Dip Galvannealing process [2-4]

An alternative to the conventional HDG process is the Hot-Dip GalvAnnealing (HDGA) process. As will be seen below, the main difference between these two processes is that the later includes an annealing step after immersion in the zinc bath in order to trigger the alloying reactions between iron and zinc. It will also be seen that the bath aluminium content is lowered compared to the HDG process in order to favour these alloying reactions. From now on, the present document will focus on this alternative process and its reactions.

The HDGA process consists in different stages. As in the HDG process, the steel strip is immersed, just after the recrystallization annealing, in an iron-saturated zinc bath at around 460℃. However, as said before, this bath contains a lower amount of aluminium (from 0.1 to 0.135 wt.%). An intermetallic layer is formed very rapidly on the steel surface during immersion. This layer is known as *inhibition layer*[4] as it inhibits, although temporarily, the alloying reactions between iron and zinc.

Figure 7 shows a schematic representation of the industrial HDGA tower, located at the exit of the galvanizing bath. A typical thermal cycle performed on such an industrial facility to produce galvannealed (GA) coatings can be observed in Figure 8. Once the strip leaves the zinc bath, a wiping step is performed in order to fix the coating thickness to its targeted value (about 10 µm). This step causes a little decrease in the strip temperature. After wiping, the steel strip is heated to about 500-530 ℃ in an induction furnace in order to trigger the Fe-Zn alloying reactions. The steel strip is then cooled to 300 ℃ in about 20 s in two steps: a slow cooling followed by a fast cooling. It is worth noting here that most of the HDGA lines also produce GI coatings. In that case, the induction furnace is off-line.

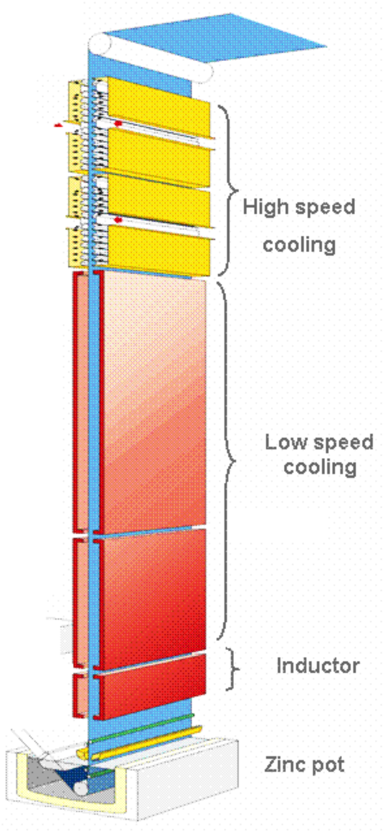

Figure 7: Schematic representation of an industrial HDGA tower (source: ArcelorMittal Global R&D).

---

[4] It will be seen in section I.3.1.1.1 that, according to thermodynamics, the nature of the inhibition layer which forms in HDGA baths is expected to be different from the one which nucleates in typical HDG baths for GI coatings production ($Fe_2Al_5Zn_x$).

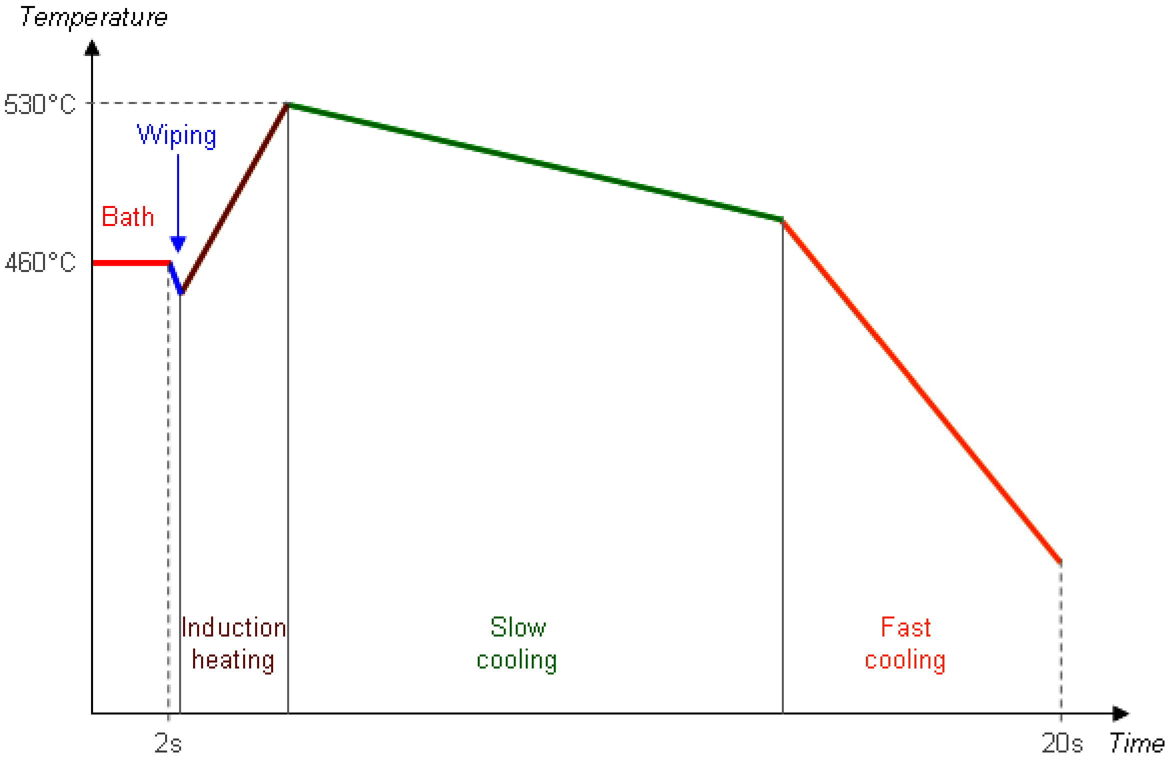

Figure 8: Typical thermal cycle performed in a HDGA tower (source: ArcelorMittal Global R&D).

The development of a GA coating along a typical industrial thermal cycle as the one depicted in Figure 8 occurs through different and complex phenomena ruled by the reactive interdiffusion of iron and zinc. These reactions, described in detail in section I.3, lead to a final coating microstructure characterized by a sequence of stratified Fe-Zn phase layers (section I.2.4). Figure 9 depicts a cross section micrograph of a GA coating where the different Fe-Zn phase layers can easily be distinguished. The quality of this kind of coating will depend on its Fe-Zn phase distribution so that an accurate control of this distribution is required to guarantee a good quality of the coating.

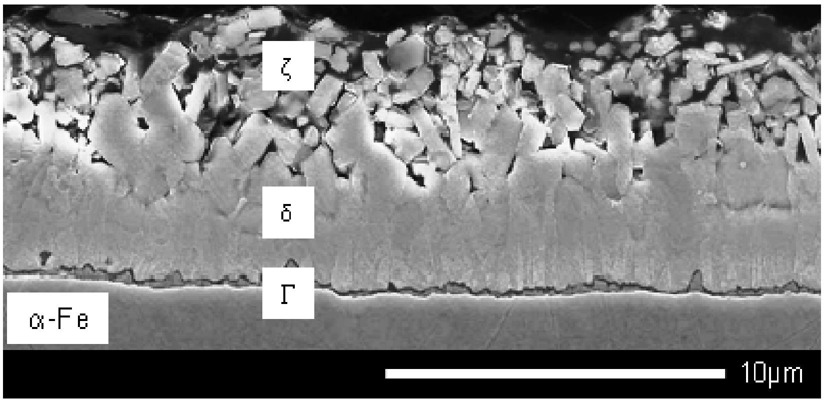

Figure 9: Cross section micrograph of a GA coating composed of a sequence of stratified Fe-Zn phase layers: Γ (gamma), δ (delta) and ζ (dzeta) (source: ArcelorMittal Global R&D).

Nowadays, the continuous HDGA process is relatively well controlled. However, the ongoing effort to increase the productivity of industrial lines and improve the quality of the coatings leads to question some issues of the current process. In this framework, a thorough knowledge of the nature of the intermediate phases and the reaction mechanisms through which the galvannealed coatings get formed becomes essential to optimise their industrial production.

In the following, a critical overview of the Al-Fe-Zn ternary phase diagrams that have been published in the literature will be presented. Interest will also be given to the Fe-Zn binary system.

I.2. Thermodynamic considerations: description of the Al-Fe-Zn ternary system

The aim of this section is to provide a very succinct introduction to the thermodynamics of the Al-Fe-Zn system in order to facilitate the comprehension of the different mechanisms described in the subsequent sections. The most accurate diagrams are chosen here both in the entire domain of composition (section I.2.1) and in the zinc-rich corner (section I.2.2).

I.2.1. Whole Al-Fe-Zn ternary phase diagram

Several research teams have contributed to the construction of the Al-Fe-Zn ternary phase diagram since the seventies [6-11]. Figure 10 illustrates the whole Al-Fe-Zn ternary phase diagram at 450 ℃ proposed by Tang [10]. Widely accepted among galvanizers, it seems to be the most accurate diagram proposed to date. Only binary Fe-Zn (ζ, δ, Γ) and Fe-Al phases ($FeAl_2Zn_x$, $Fe_2Al_5Zn_x$, $FeAl_3Zn_x$) are present in this diagram and no ternary phases exist. The characteristics of these binary phases will be described in section I.2.4. Among the characteristics of the ternary intermetallic compounds, it should be noted that the solubility of zinc in $Fe_2Al_5Zn_x$ (up to 20 wt.%) as well as the solubility of aluminium in δ (up to 3 wt.%) are very high.

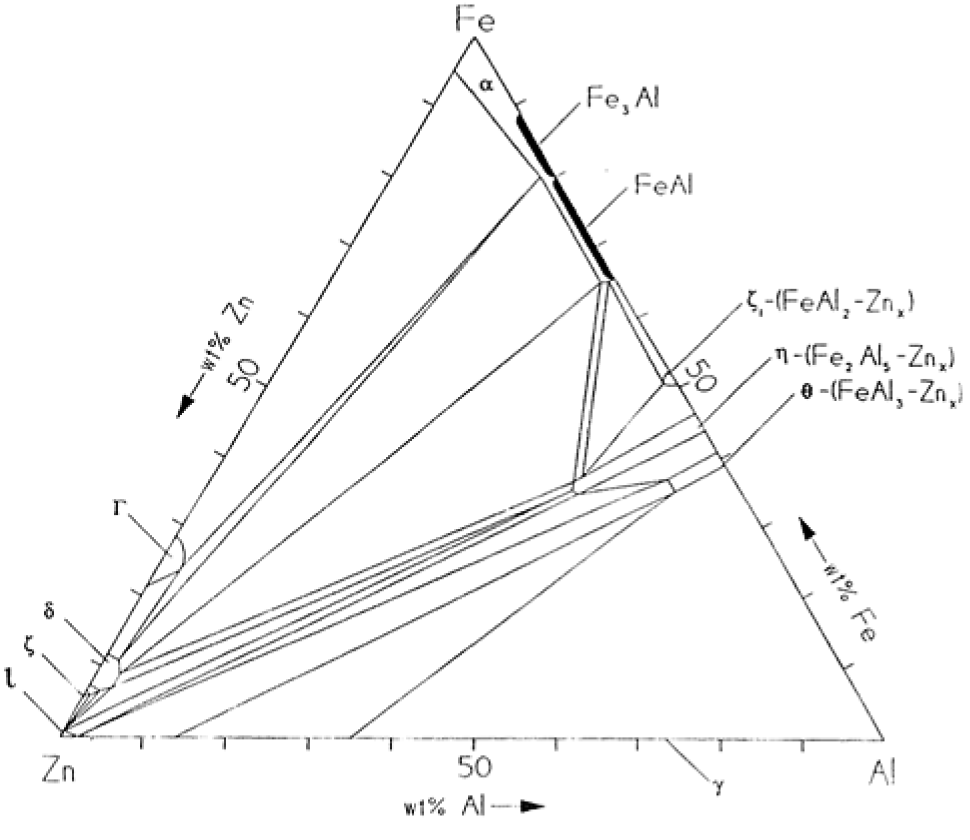

Figure 10: Al-Fe-Zn ternary phase diagram at 450 ℃ proposed by Tang [10].

It should be noted that research work is still needed for the construction of the Al-Fe-Zn diagram. For instance, a binary Fe-Zn phase, Γ_1, is not represented in the diagram proposed in Figure 10. The domain for this phase should be placed between the Γ and δ domains on the Fe-Zn edge of the diagram. Tang and Su [11] recently proposed a new version of the diagram with Γ_1 and a ternary phase referred to as T phase in the zinc-rich corner. This version was not chosen because it has not been validated yet. In particular, the domain of composition of the T phase is close to that of the δ phase, meaning that the T phase could be the δ phase.

I.2.2. The zinc-rich corner of the Al-Fe-Zn ternary phase diagram

For the needs of continuous HDG and HDGA processes, the zinc-rich corner of the Al-Fe-Zn phase diagram received further attention [6,8-14]. Figure 11 represents the diagram proposed by Tang [12] at 450 °C. Three different binary equilibriums involving the liquid phase can be distinguished in this diagram depending on the aluminium concentration: with $Fe_2Al_5Zn_x$, δ or ζ. In addition, a significant lowering of the iron solubility in molten zinc when aluminium is added at a very low concentration (0.2 wt.% Al) can be observed.

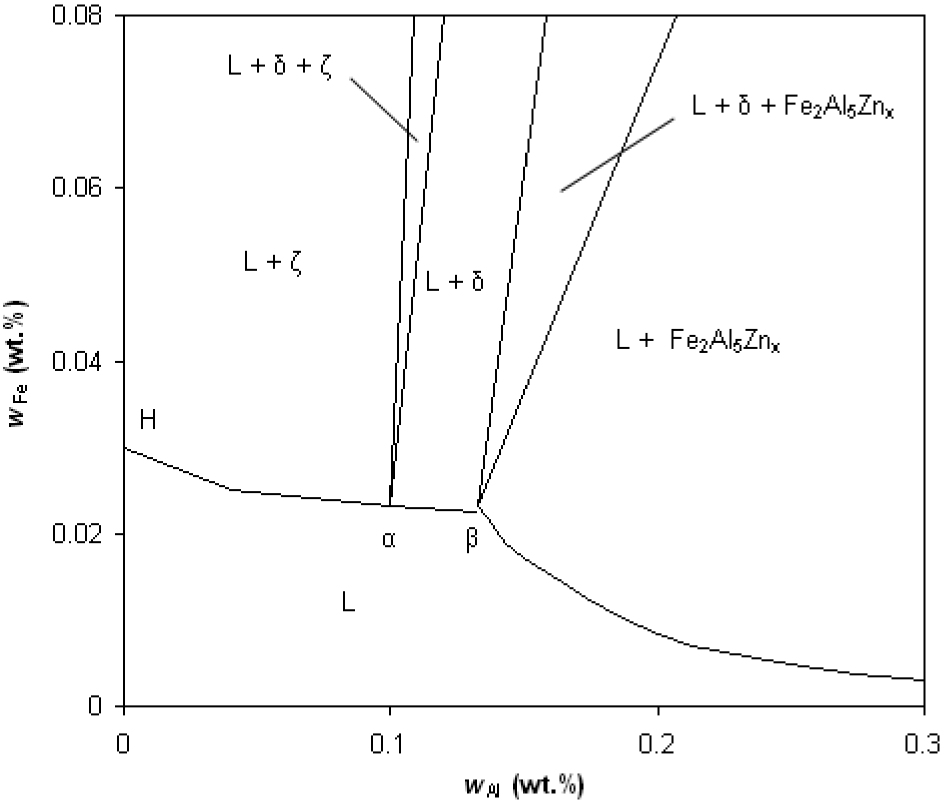

Figure 11: Zinc-rich corner of the Al-Fe-Zn phase diagram at 450 °C proposed by Tang [12].

The three most recent liquidus lines have been proposed by Tang [12], Dauzat *et al*. [13] and McDermid *et al.* [14]. They are all compared in Figure 12. As it can be seen, the liquidus line at 450 °C proposed by Dauzat *et al*. [13] is considerably different from the liquidus lines at the same temperature proposed by Tang [12] and McDermid *et al.* [14]. Dauzat *et al*. [13] do not consider the equilibrium with the ζ phase and suppose that the δ phase is the stable compound for very low aluminium contents in the liquid phase (see the position of the knee point β, in red, in Figure 12). In addition, the iron solubility in the liquid phase in equilibrium with $Fe_2Al_5Zn_x$ is considerably lower compared with the liquidus lines from Tang [12] and McDermid *et al.* [14]. As will be seen below, the liquidus lines proposed by these authors are quite in agreement with the experimental points available in the literature. For this reason, the diagram by Dauzat *et al*. [13] will be rejected.

The main differences between the diagrams proposed by Tang [12] and McDermid *et al.* [14] lie in the iron solubility in the liquid phase in equilibrium with $Fe_2Al_5Zn_x$ (higher in the case of the liquidus line proposed by Tang [12]), with δ (fairly constant with the aluminium concentration in the case of the liquidus line from Tang [12] contrarily to that proposed by McDermid *et al.* [14]) but also in the aluminium concentration of the knee point α (considerably lower in the case of the diagram proposed by McDermid *et al.* [14]). The two diagrams are quite in agreement with the aluminium concentration of the knee point β.

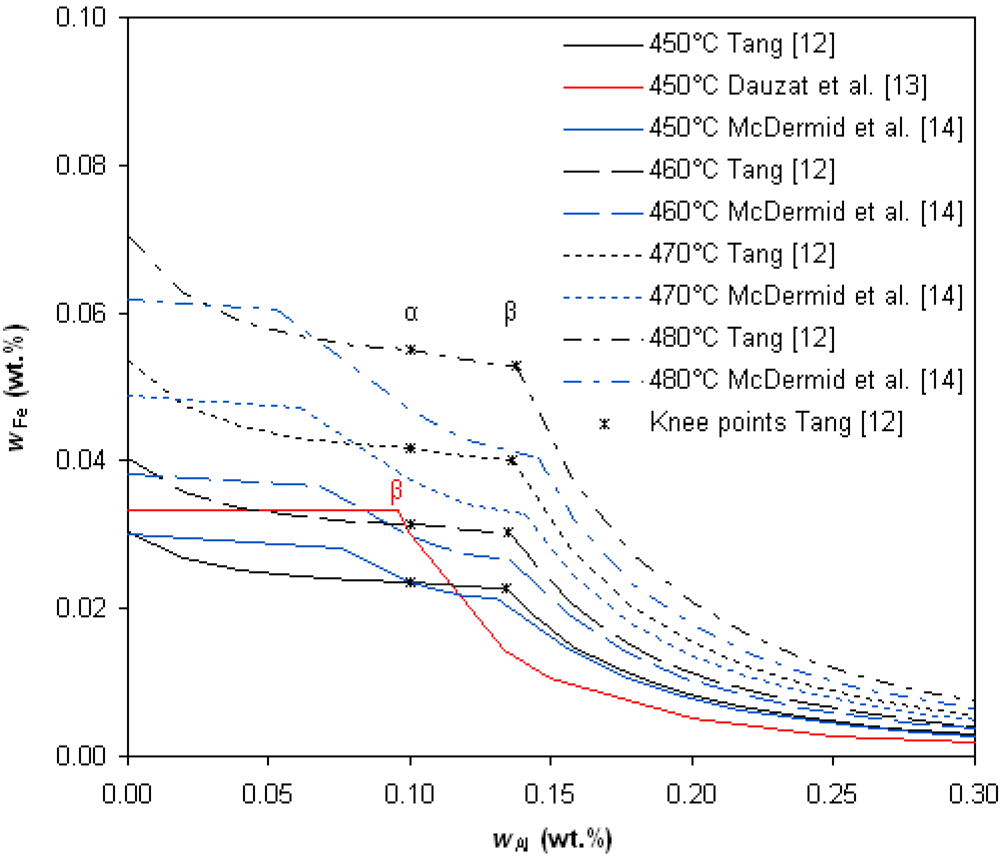

Figure 12: Comparison of the liquidus lines of the zinc-rich corner of the Al-Fe-Zn phase diagram proposed by Tang [12], Dauzat *et al.* [13] and McDermid *et al*. [14].

In order to choose the most accurate diagram in the zinc-rich corner, the liquidus corresponding to the equilibrium with $Fe_2Al_5Zn_x$, δ or ζ respectively is compared hereinafter with the experimental points available in the literature.

Equilibrium with $Fe_2Al_5Zn_x$

Many experiments [9,12-21] have been carried out in the region where the solid phase in equilibrium with the liquid zinc is $Fe_2Al_5Zn_x$ in order to determine the solubility of iron in liquid zinc in the temperature range of 450-485 °C. The experimental procedure is often the same. First, the liquid phase is separated from the suspended intermetallic compounds in a still bath: aluminium-rich drosses ($Fe_2Al_5Zn_x$) will float to the surface, its density being lower than that of zinc, whereas drosses based on the ternary extension of the binary Fe-Zn compound of δ phase contain only a small amount of aluminium in solid solution and will sink to the bottom. Samples of the liquid phase are then taken in the bath at mid-depth and sent for analysis. Less often, the samples taken in the bath are filtered to remove the suspended particles [14].

The obtained results are plotted in Figure 13 together with the liquidus lines from Tang [12] and McDermid *et al.* [14] concerning the equilibrium with $Fe_2Al_5Zn_x$. The experimental points [9,12-21] are globally located between the two extreme liquidus lines proposed by both authors [12, 14] (450-480 °C). The triple point β is better predicted by Tang [12] and McDermid *et al.* [14] than by Dauzat *et al.* [7] (Figure 12). The liquidus lines from Tang [12] seem to overestimate the solubility of iron in liquid zinc at 470 and 480 °C, compared to the liquidus lines from McDermid *et al.* [14].

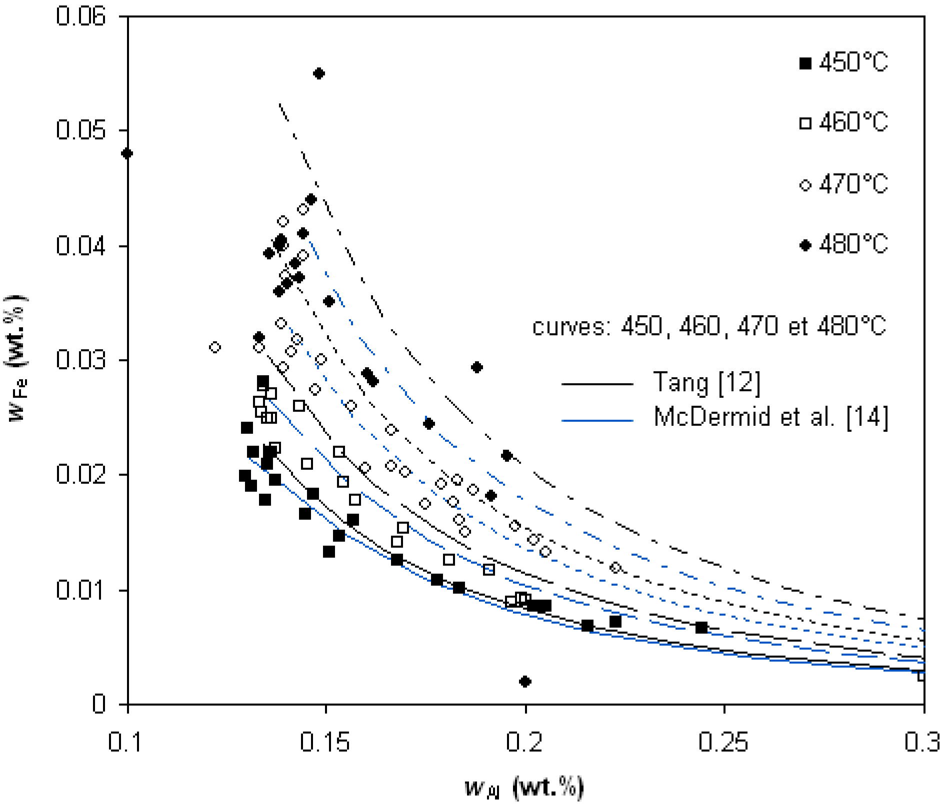

Figure 13: Liquidus lines proposed by Tang [12] and McDermid *et al*. [14] for the equilibrium with $Fe_2Al_5Zn_x$ compared with available experimental data for different temperatures [9,12-21].

Equilibrium with δ or ζ

Some experiments have also been carried out in the regions where the solid phase in equilibrium with the liquid zinc is δ [12,14,18] or ζ [12]. The experimental points obtained are plotted together with the liquidus lines from Tang [12] and McDermid *et al.* [14] concerning the equilibrium with δ in Figure 14 and with ζ in Figure 15. In both regions, the experimental points are well described by both liquidus lines. The triple point α seems to be better described by Tang [12] than by McDermid *et al*. [14].

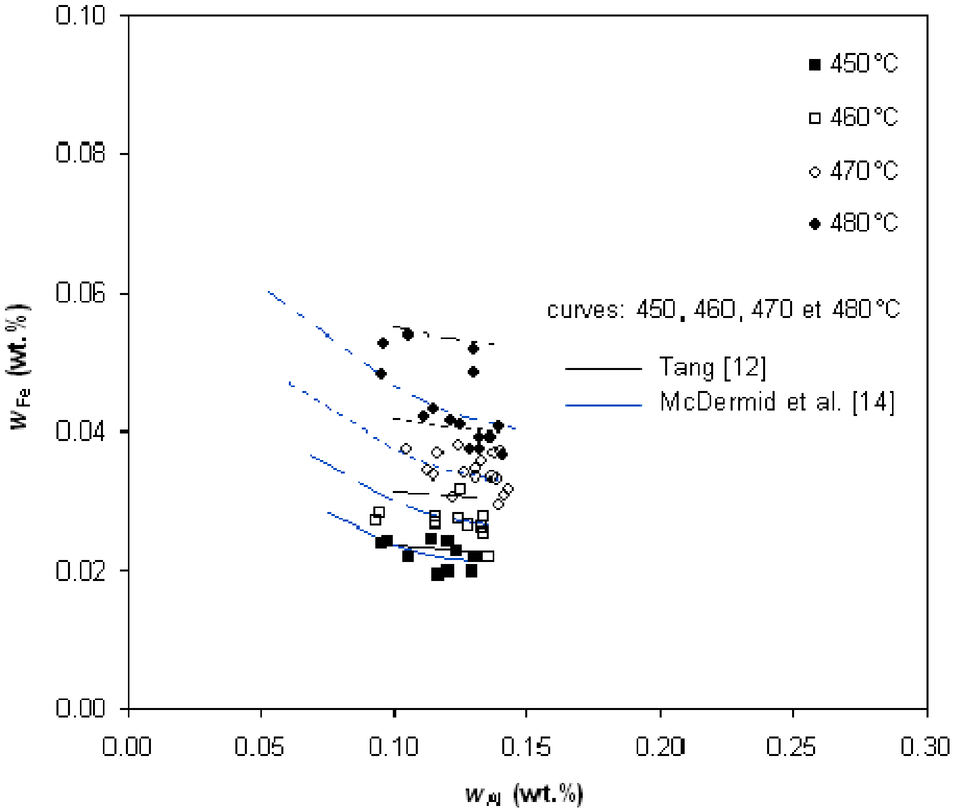

Figure 14: Liquidus lines proposed by Tang [12] and McDermid *et al*. [14] for the equilibrium with δ compared with available experimental data for different temperatures [12,14,18].

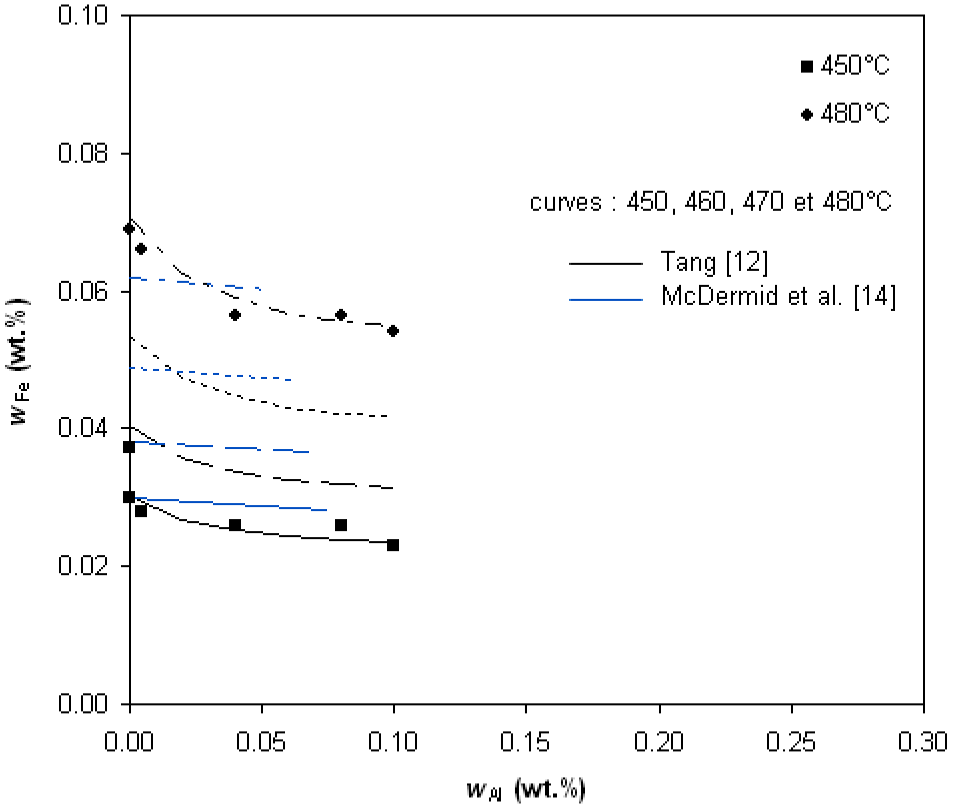

Figure 15: Liquidus lines proposed by Tang [12] and McDermid *et al*. [14] for the equilibrium with ζ compared with available experimental data for different temperatures [12].

The most accurate Al-Fe-Zn ternary phase diagram in the zinc-rich corner

As shown earlier, the two liquidus lines proposed by Tang [12] and by McDermid *et al.* [14] well describe the experimental points obtained for the equilibrium between the liquid phase and the three possible intermetallic compounds in the zinc-rich corner of the diagram ($Fe_2Al_5Zn_x$, δ or ζ) and for the triple point β (equilibrium between the liquid phase, $Fe_2Al_5Zn_x$ and δ). The liquidus corresponding to the equilibrium with $Fe_2Al_5Zn_x$ from Tang [12] seem to overestimate slightly the solubility of iron in liquid zinc at 470 and 480 °C, compared to the liquidus lines from McDermid *et al.* [14]. The triple point α (equilibrium between the liquid phase, δ and ζ) seems to be better described by Tang [12] than by McDermid *et al.* [14].

The experimental points pertaining to each temperature indicate some scatter, making the choice of one or the other of the two liquidus lines difficult. The liquidus from Tang [12] is, at the present time, the most greatly accepted liquidus among the galvanizing research community. This is the reason why the liquidus from Tang [12] will be chosen for the explanations given in the following sections of the present work. His equations describing the liquidus line in the $Fe_2Al_5Zn_x$, δ and ζ domains are detailed hereinafter. He proposed these equations from his own experimental data and thermodynamics models [12].

The link between the iron and aluminium solubilities in the liquid phase in equilibrium with $Fe_2Al_5Zn_x$ is given by the following equation:

$$\left(w_{Fe}^{sat}\right)^2\left(w_{Al}^{sat}\right)^5 = \exp\left(28.1-\frac{33066}{T}\right) \tag{I.1}$$

where w_{Fe}^{sat} (wt.%) and w_{Al}^{sat} (wt.%) are, respectively, the iron and aluminium weight fractions in the liquid phase in equilibrium with $Fe_2Al_5Zn_x$ and T (K) is the temperature.

According to Tang [12], the modelling of the liquidus line in the regions where ζ or δ are in equilibrium with the liquid phase was difficult because no information about the aluminium content in δ and ζ was available in the literature. Therefore, the relationship between the iron solubility in the liquid phase and the aluminium content in the solid compound is not obvious. The author developed a new approach in both cases. This approach is not detailed here and only the final equations describing the liquidus lines in both domains are presented below.

Concerning the equilibrium with ζ, the liquidus line can be described by the following equation:

$$w_{Fe}^{sat} = \exp\left(17.78-\frac{15388}{T}\right)\exp\left[\frac{14\left(4.1x_{Al}x_{\zeta}+x_{\zeta}\ln x_{\zeta}+x_{Al}\ln x_{Al}\right)}{x_{\zeta}}\right] \tag{I.2}$$

with

$$x_{\zeta} = 1-x_{Al} \tag{I.3}$$

and

$$x_{Al} = 0.164\,w_{Al}^{sat} \tag{I.4}$$

where w_{Fe}^{sat} (wt.%) is the iron weight fraction in the liquid phase in equilibrium with ζ, x_{Al} is the aluminium mole fraction in the ζ phase, x_{ζ} the sum of the iron and zinc mole fractions in the ζ phase and w_{Al}^{sat} (wt.%) the aluminium weight fraction in the liquid phase in equilibrium with ζ.

Concerning the equilibrium with δ, the liquidus line can be described by the following equation:

$$w_{Fe}^{sat} = 1.22 \exp\left(17.78 - \frac{15388}{T}\right) \exp\left[\frac{8\left(3x_{Al}x_{\delta} + x_{\delta} \ln x_{\delta} + x_{Al} \ln x_{Al}\right)}{x_{\delta}}\right] \quad (I.5)$$

with

$$x_{\delta} = 1 - x_{Al} \quad (I.6)$$

and

$$x_{Al} = 0.42\, w_{Al}^{sat} \quad (I.7)$$

where w_{Fe}^{sat} (wt.%) is the iron weight fraction in the liquid phase in equilibrium with δ, x_{Al} is the aluminium mole fraction in the δ phase, x_{δ} the sum of the iron and zinc mole fractions in the δ phase and w_{Al}^{sat} (wt.%) the aluminium weight fraction in the liquid phase in equilibrium with δ.

The Al-Fe-Zn phase diagram in the zinc-rich corner obtained with the equations (I.1) to (I.7) at 450 °C has been presented earlier (Figure 11). It will be systematically used to comment and analyze the galvanizing experiments carried out by the different authors. In particular, the composition of the knee point β will be a critical data for analysis in the subsequent sections. Its variation with temperature, according to Tang [12], is shown in Table 1 together with that of the knee point α. The aluminium content at the knee points α and β varies very little with temperature, which will facilitate the analysis.

Table 1: Composition of the knee points α and β at different temperatures (Tang [12]).

T (°C)	Knee point α		Knee point β	
	w_{Al}^{sat} (wt.%)	w_{Fe}^{sat} (wt.%)	w_{Al}^{sat} (wt.%)	w_{Fe}^{sat} (wt.%)
450	0.101	0.024	0.134	0.023
460	0.101	0.031	0.135	0.030
470	0.101	0.042	0.137	0.040
480	0.101	0.055	0.138	0.053

I.2.3. The most accurate Fe-Zn binary phase diagram

As it will be seen in section I.3.3, the thermal cycle performed during galvannealing (Figure 8) may have an important influence on the reaction mechanisms through which the liquid zinc gets consumed during Fe-Zn alloying. However, the evolution with temperature of the Al-Fe-Zn ternary phase diagram is not precisely known. The Fe-Zn binary phase diagram can then be a useful tool to understand those mechanisms.

Figure 16 represents the Fe-Zn binary phase diagram from Kubaschewski [22]. Currently, it is the most accepted Fe-Zn binary phase diagram among galvanizers.

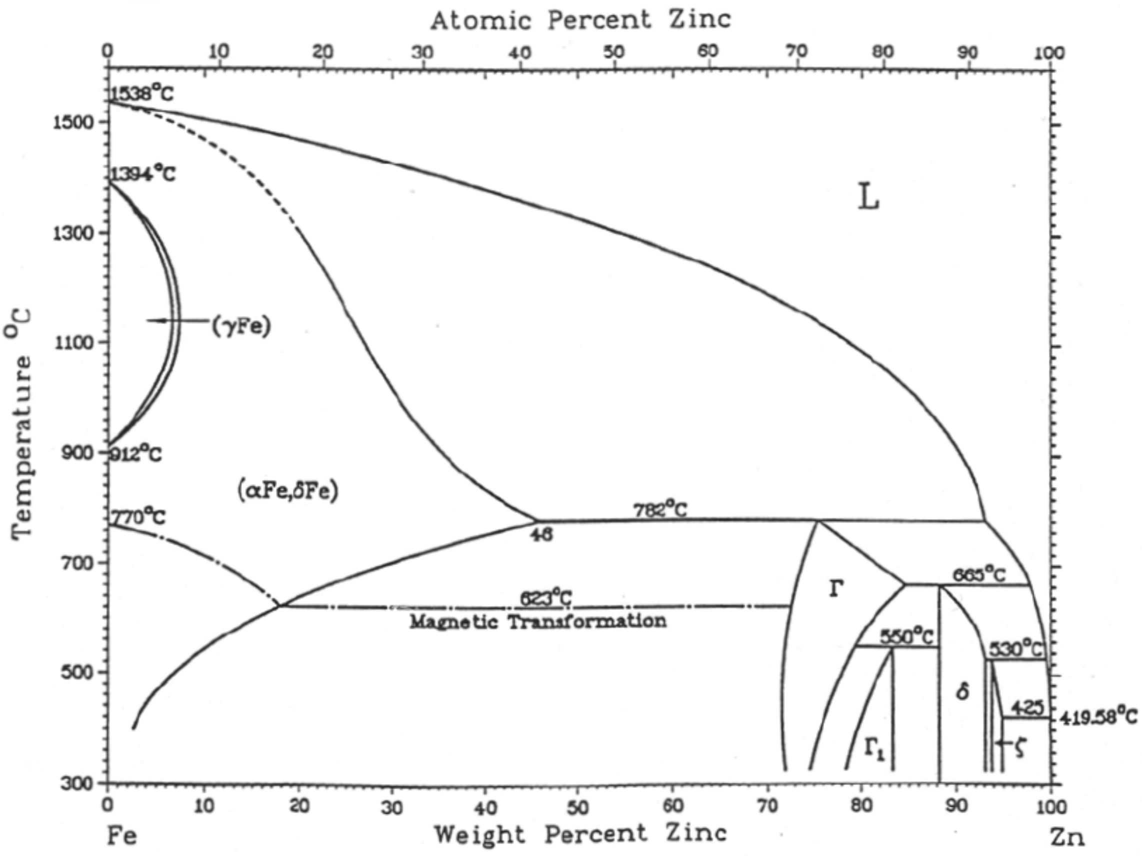

Figure 16: Fe-Zn binary phase diagram proposed by Kubaschewski [22].

As depicted in Figure 16, this Fe-Zn binary phase diagram includes a liquid phase, two solid solutions of zinc in iron (α and γ), a pure zinc solid solution and four non-stoichiometric Fe-Zn intermetallic compounds: Γ, Γ_1, δ and ζ. The characteristic points of this diagram are described in Table 2.

Table 2: Characteristic points of the Fe-Zn phase diagram proposed by Kubaschewski [22].

Characteristic Point		w_{Zn} (wt.%)	x_{Zn} (at.%)	T (°C)
Peritectic	L + α-Fe = Γ	75	71	782
Peritectoid	Γ + δ = Γ_1	83	81	550
Peritectic	Γ + L = δ	88	86	665
Peritectic	L + δ = ζ	94	93	530
Melting point	L = η-Zn	100	100	419.58
Melting point	L = α-Fe	0	0	1538

Special attention should be kept to the peritectic point at 530 °C because it is located in the domain of temperature of typical galvannealing treatments (Fig. 8). Thus, as it will be advanced in section I.3.3, the reactions involved in the liquid zinc consumption will be different below or above the peritectic reaction temperature.

If we now consider the Al-Fe-Zn ternary system, a precise knowledge of the evolution of the peritectic reaction temperature as a function of the liquid zinc aluminium content would be highly desirable to accurately control the reactions that are taking place during a given galvannealing cycle. However, it remains unclear at this time whether the aluminium content has actually an effect on the peritectic reaction temperature or not.

I.2.4. Characteristics of the Fe-Zn and Fe-Al binary phases

Finally, some of the main characteristics (chemical formula, crystal lattice, number of atoms per cell, iron content, enthalpy *ΔH* and Gibbs free energy *ΔG*) of the Fe-Zn phases, together with those of zinc and ferrite, are shown in Table 3. Similar characteristics for the Fe-Al phases are available in Table 4. The chemical formulas of most of the Fe-Zn and Fe-Al phases are given by an average composition. With the exception of the Fe-Zn ζ phase, the composition of each of these phases can vary substantially, as can be observed in the Al-Fe-Zn ternary phase diagram at 450 °C proposed by Tang [10] (Figure 10). This is also noticeable, in the case of the Fe-Zn phases, when taking a look to their extreme values of iron content presented in Table 3.

It should also be noted that the enthalpies and Gibbs free energies of formation (*ΔH* and *ΔG*, respectively) are close to each other. According to Guttmann [23], this contributes to the unstable behaviour of the Al-Fe-Zn system: minute perturbations can cause sudden and unpredictable changes in the phase precipitation sequence due to the small differences in *ΔG*.

Table 3: Characteristics of the Fe-Zn phases (Guttmann [23]).

Phase	Formula	Crystal lattice	atoms/cell	Fe content (450°C) (wt.%)	*ΔH* (450 °C) (kJ.mol^{-1})	*ΔG* (450 °C) (kJ.mol^{-1})
η-Zn		hexagonal	2	<0.03		
ζ	$FeZn_{13}$	monoclinic	28	5 - 6	-11.7	-2.8
δ	$FeZn_7$	hexagonal	551± 5	7 - 12	-11.5	-3.5
Γ_1	$FeZn_4$	FCC	408	17 - 19	-11.7	-4.1
Γ	Fe_3Zn_{10}	BCC	52	23 - 28	-10.9	-4.2
α-Fe		BCC	2	95		

Table 4: Characteristics of the Fe-Al phases (Guttmann [23]).

Phase	Formula	Crystal lattice	*ΔH* (450 °C) (kJ.mol^{-1})	*ΔG* (450 °C) (kJ.mol^{-1})
θ	$FeAl_3$	monoclinic	-35.1	-30
η	Fe_2Al_5	orthorhombic	-34.6	-32
ζ	$FeAl_2$	rhomboedric		-31
α	FeAl	BCC		-32

In the present work, we will get especially interested in the $Fe_2Al_5Zn_x$, δ and ζ phases, and more particularly in the $Fe_2Al_5Zn_x$ and δ phases. As has been stated previously, the high solubilities of zinc in $Fe_2Al_5Zn_x$ (up to 20 wt.%) and aluminium in δ (up to 3 wt.%) are to highlight (Figure 10). According to Guttmann [23], this latter phase has an iron content between 7 and 12 wt.% and the ζ phase, which contains almost no aluminium, between 5 and 6 wt.%.

By their side, Chen *et al*. [7] investigated the composition of different phases in the Al-Fe-Zn ternary system. The compositions reported by these authors for δ and $Fe_2Al_5Zn_x$ are presented in Table 5.

Table 5: Compositions and errors (90% confidence) of δ and $Fe_2Al_5Zn_x$ (Chen *et al*. [7]).

Element	δ		$Fe_2Al_5Zn_x$	
	wt.%	at.%	wt.%	at.%
Al	2.8 ± 0.3	6.4	43.1 ± 1.1	62.3
Fe	9.0 ± 0.6	10.0	36.0 ± 0.6	25.2
Zn	88.2 ± 0.7	83.6	20.9 ± 1.7	12.5

I.3. State of the art of the galvannealing reactions

The present section aims at providing a critical literature review on the complex phenomena involved in the HDGA process.

As shown below, a thin layer of intermetallic compounds is formed on the steel surface when it is immersed in the galvanizing or galvannealing baths. This layer is called the inhibition layer because it prevents temporarily the Fe-Zn alloying reactions. The mechanisms through which the Fe-Zn alloying reactions are inhibited by small aluminium additions in the zinc bath (section I.3.1) as well as the transient character of this inhibition (section 0) will be discussed, with particular emphasis on the nature of the inhibition layer and on the way it breaks down. Kinetic considerations will also be described.

In addition, and in spite of the fact that this work does not focus on them, the Fe-Zn alloying reaction mechanisms (liquid zinc consumption and iron enrichment of the solid coating) will be briefly reviewed in order to give the reader a complete description of the development of a galvannealed coating (section I.3.3).

I.3.1. The inhibition layer formation

The aim of this section is to detail the current state of knowledge about the inhibition layer formed on the steel surface in the earlier stages of immersion in the molten zinc bath during the continuous HDG and HDGA processes, trying to focus, as far as possible, on typical zinc bath aluminium contents for galvannealed coatings production (GA baths).

I.3.1.1. The nature of the inhibition layer

I.3.1.1.1. Intermetallic compounds in equilibrium with hot-dip galvanizing baths

At first, the intermetallic compounds in equilibrium with the liquid zinc bath are considered, based on the Al-Fe-Zn ternary phase diagram. The nature of these intermetallic compounds should depend on three operating parameters: the aluminium and iron contents and temperature in the galvanizing bath. However, with the present HDG and HDGA operations, the temperature and iron content in the bath are fairly stable (sections I.1.2 and I.1.3, iron-saturated baths at around 460 °C, typically). Therefore the intermetallic compound formed during galvanizing can be deduced from the bath aluminium content. Based on the zinc-rich corner of the Al-Fe-Zn ternary phase diagram at 450 °C from Tang [12] (Figure 11), three different domains of bath aluminium contents can be distinguished: the intermetallic compounds in thermodynamic equilibrium with the liquid phase are ζ ($FeZn_{13}$) from 0 to 0.10 wt.% Al, δ ($FeZn_7$) from 0.10 to 0.134 wt.% Al (GA baths) and $Fe_2Al_5Zn_x$ from 0.134 to 1.3 wt.% Al (GI baths).

In the following, the literature review will focus only on the composition of industrial GI and GA baths, i.e., with the aluminium content in the liquid zinc higher than 0.10 wt.%. The contributions of different researchers to the experimental determination of the nature of the inhibiting layer will be gathered for GI baths (section I.3.1.1.2), GA baths (section I.3.1.1.3) and baths with an aluminium content close the knee point β (section I.3.1.1.4, 0.134 wt.%, Figure 11). The experimental results will be compared to the intermetallic compounds that should be formed if the thermodynamic equilibrium was reached at the steel / liquid zinc interface.

I.3.1.1.2. Nature of the inhibition layer in GI baths

Most of the investigations on the nature of the inhibition layer focused on GI bath compositions, more precisely on bath aluminium contents around 0.20 wt.%. For such galvanizing baths, it is generally admitted that the main component of the inhibition layer is the $Fe_2Al_5Zn_x$ phase [23-43], in agreement with the phase diagram.

It should be pointed out, however, that a small group of researchers has suggested the presence of other compounds mixed with $Fe_2Al_5Zn_x$ within the inhibition layer formed in GI baths: $FeAl_3Zn_x$ [44-47], $FeAl_2Zn_x$ [46], δ [47,48] and even an Fe-Al-Zn ternary compound [49-51] (see Appendix A for more details).

I.3.1.1.3. Nature of the inhibition layer in GA baths

Concerning the nature of the inhibition layer which forms on the steel surface in the case of GA baths, far fewer studies are available and very controversial results have been reported by different researchers. These studies (analysis techniques used, aluminium content in the bath, nature of the inhibition layer) are summarized in Table 6.

Table 6: Summary of studies carried out on the nature of the inhibition layer in GA baths.

Authors [Ref.]	Analysis techniques	wt.% Al	Nature of the inhibition layer
Saito *et al*. [26]	XRD, XMA	0.10-0.2	$Fe_2Al_5Zn_x$
Vitkin *et al.* [52]	Electron Diffraction (TEM)	0.05	$Fe_2Al_5Zn_x$
Chen *et al.* [45]	EBSD	0.13	$Fe_2Al_5Zn_x$, transient $FeAl_3Zn_x$
Úředníček and Kirkaldy [46]	Low angle XRD	0.12	$Fe_2Al_5Zn_x$, transient $FeAl_3Zn_x$, $FeAl_2Zn_x$
Leprêtre [33]	EDS	0.13	δ

Metastable $Fe_2Al_5Zn_x$

Guttmann [23] has reported the presence of the $Fe_2Al_5Zn_x$ phase in a much wider range of composition than the one predicted by the equilibrium phase diagram, both at lower and higher aluminium contents in the zinc alloy bath. Indeed, a large group of researchers [26,31,45-47,52,53] affirmed that the inhibition layer formed in GA baths is composed of metastable $Fe_2Al_5Zn_x$.

Saito *et al*. [26] investigated the nature of the inhibition layer formed in zinc baths at 450 °C for 15 and 60 s dipping times and different aluminium contents (0.10, 0.14, 0.16, 0.18 and 0.20 wt.%). The authors reported that the inhibition layer is constituted of $Fe_2Al_5Zn_x$ in all cases, even for the bath with 0.10 wt.% Al. However, they only showed in their paper the X-Ray Diffraction (XRD) patterns and the results of X-ray Micro-Analysis (XMA) for the intermetallic compound nucleating in the bath containing 0.20 wt.% Al, which effectively seems to be $Fe_2Al_5Zn_x$.

In addition, the studies of electron diffraction in Transmission Electron Microscope (TEM) on galvanized samples performed by Vitkin *et al*. [52] have shown the presence of a zinc-containing $Fe_2Al_5Zn_x$ layer for very low aluminium contents in the galvanizing bath, even out of the GA domain (0.05 wt.% Al).

Other metastable Fe-Al compounds

Chen *et al*. [45], Sugiyama *et al*. [53] as well as Úředníček and Kirkaldy [46] have found other metastable Fe-Al compounds together with $Fe_2Al_5Zn_x$ in the case of GA baths. Chen *et al*. [45] observed a transient $FeAl_3Zn_x$ phase together with $Fe_2Al_5Zn_x$ in the case of a galvanizing bath with 0.13 wt.% Al and Úředníček and Kirkaldy [46] identified $Fe_2Al_5Zn_x$, $FeAl_3Zn_x$ and $FeAl_2Zn_x$ in the inhibition layer formed in a zinc bath with 0.12 wt.% Al. Sugiyama *et al*. [53] also presumed metastable $Fe_2Al_5Zn_x$ and/or $FeAl_3Zn_x$ as constituents of the inhibition layer formed in a zinc bath containing 0.10 wt.% Al. However, if the presence of metastable $FeAl_3Zn_x$ is already quite doubtful in the case of GI baths, its presence within the inhibition layer which forms in GA baths is even more unlikely.

Presence of δ phase

Yamaguchi and Hisamatsu [47] presumed that both δ and metastable $Fe_2Al_5Zn_x$ phases are present in the inhibition layer which forms in GA baths.

Other researchers [27,30,33] have pointed out that the inhibition layer is mainly composed of the δ phase, in thermodynamic equilibrium with liquid zinc and the steel substrate. During his PhD thesis, Leprêtre [33] thereby investigated the nature of the inhibition layer formed in galvanizing baths with 0.13, 0.135 and 0.18 wt.% Al at 460 °C. For the samples galvanized in the bath containing 0.13 wt.% Al, he observed, after selective removal of the zinc overlay, a continuous thin interfacial layer composed of hexagonal crystals. The author confirmed by Energy Dispersive Spectroscopy (EDS) analysis on extracted Rhodoïd replicas that these hexagonal crystals are composed of the δ phase. This contribution was then supported by Mataigne [30] and Leprêtre *et al*. [27].

I.3.1.1.4. Nature of the inhibition layer in zinc baths at the knee point β

The knee point β is considered here as the critical aluminium content for which δ and $Fe_2Al_5Zn_x$ are in thermodynamic equilibrium with an iron-saturated liquid zinc at a given temperature. Obviously, it can be supposed that all the authors [31,45-47], who do not find any substantial difference between the inhibition layer formed in GI and GA baths, consider that the inhibition layer which forms in a zinc bath with an aluminium content at the knee point β also remains unchanged. As a result, only specific research close to the knee point β (0.134 wt.% Al for 450 °C, Figure 11) will be presented below. If very few works have been carried out on the nature of the inhibition layer for GA baths, much less have been specifically published for galvanizing baths with an aluminium content close to the knee point β.

As said before, Leprêtre [33] investigated the nature of the inhibition layer which forms in a zinc bath containing 0.135 wt.% Al at 460 °C. By means of successive selective chemical dissolutions, the author found a two-phase inhibition layer composed of both δ and $Fe_2Al_5Zn_x$. The latter phase consists of small shapeless crystals and is found at the interface between the δ phase and the steel substrate. The author indicated that the transition from an inhibition by the $Fe_2Al_5Zn_x$ phase to an inhibition by the δ phase is made gradually through the variation of the proportion of both phases as a function of the aluminium content in the galvanizing bath.

By their side, Dionne *et al*. [54] reported similar results. Through Scanning Electron Microscopy (SEM) observations and Transmission Electron Microscopy (TEM) analysis on Focused Ion Beam (FIB) thin specimens, the authors confirmed the presence of δ crystals over a $Fe_2Al_5Zn_x$ layer in the case of galvanizing baths containing 0.133 or 0.135 wt.% Al at 470 °C.

It should be highlighted that Yamaguchi and Hisamatsu [47] had already presumed the same type of inhibition layer for such galvanizing baths. This is also supported by Leprêtre *et al*. [27].

I.3.1.1.5. Brief summary

It is widely accepted that $Fe_2Al_5Zn_x$ is the main constituent of the inhibition layer that forms in GI baths. In the case of GA baths, very controversial results have been found. It is not clear whether the inhibition layer in these baths is constituted of $Fe_2Al_5Zn_x$, δ or both. The inhibition layer formed in zinc baths at the knee point, studied by very few researchers only, would be composed of both $Fe_2Al_5Zn_x$ and δ.

I.3.1.2. Experimental data on the inhibition layer growth kinetics

The effect of the bath aluminium content and the immersion time on the inhibition layer growth kinetics is discussed here in the case of GA baths. This growth will be represented by the aluminium uptake by the inhibition layer. Very few kinetic data on the growth of the inhibition layer which forms in

GA baths is available in the literature [55]. Actually, most of the kinetic data published corresponds to the growth of the inhibition layer in GI baths (Appendix A).

Isobe [55] investigated the growth of the inhibition layer in the case of zinc baths at 470 °C and different aluminium contents, varying from 0.11 to 0.20 wt.% Al, i.e., in both GA and GI domains. He found that increasing the bath aluminium content resulted in a higher thickness of the interfacial layer, as can be observed in the left-hand side of Figure 17. Two different steps are distinguished in the formation of the inhibition layer. A high aluminium uptake rate takes place within the first second of immersion, which corresponds to a step of nucleation and lateral growth of the inhibition layer. Then, this rate decreases considerably, corresponding to the growth step of this layer.

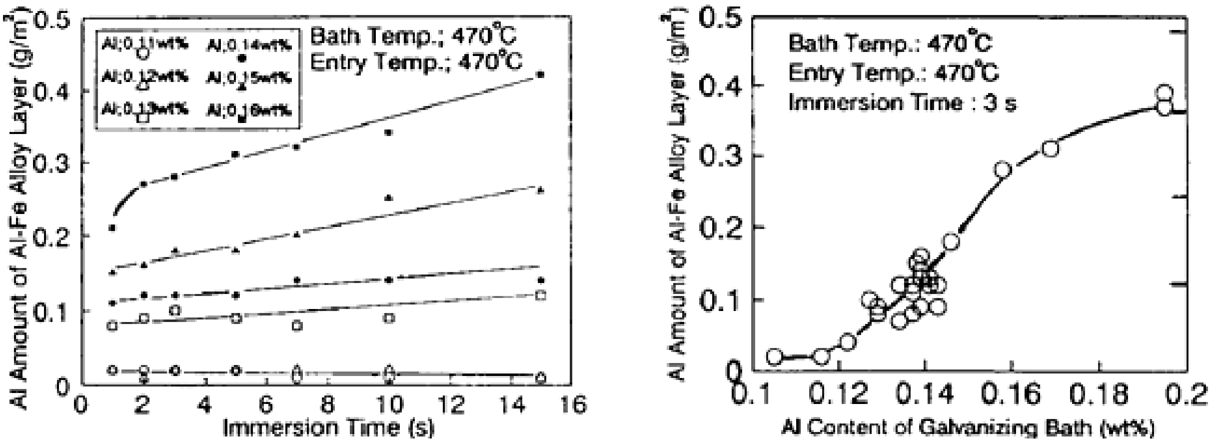

Figure 17: Effect of the bath aluminium content on the inhibition layer growth kinetics [55].

The experimental results presented in the right-hand side of Figure 17, corresponding to a fixed immersion time of 3 s, show once again that the growth of the inhibition layer is favoured by higher bath aluminium contents [55].

I.3.1.3. Mechanisms of formation of the inhibition layer

Regardless the type of the intermetallic compound which forms on the steel surface, most of the researchers agree with the mechanisms of formation of the inhibition layer. These reaction mechanisms can be divided into the following steps after the steel sheet enters the galvanizing bath [23]: the wetting of the substrate by liquid zinc, the dissolution of the former by the latter and the nucleation and growth of the inhibition layer.

I.3.1.3.1. Wetting of the substrate by liquid zinc

The reactions between steel and liquid zinc depend on the quality of the wetting, which is strongly influenced by the surface conditions of both the liquid and the solid at the moment of immersion [23,56].

In this framework, the external selective oxidation phenomenon during the recrystallization annealing prior to HDG must be highlighted. This annealing step is performed at about 800 °C under a N_2-H_2 protective atmosphere. At this temperature, the equilibrium between H_2, H_2O and O_2 is reached on the steel surface:

$$H_{2(v)} + \frac{1}{2} O_{2(v)} \Leftrightarrow H_2O_{(v)} \qquad \text{(I.8)}$$

Under the annealing conditions chosen, i.e., 5 to 20 vol.% H_2, about -40 to -30 °C dew point (partial water pressure of 20 to 50 Pa) and 800 °C, the native iron oxides are reduced and the steel surface is composed of metallic iron. At the same time, the segregation and selective oxidation of minor alloying elements such as aluminium, silicon, manganese or boron cannot be avoided [30].

According to Wagner's theory [57], two limiting cases of selective oxidation can be differentiated:

The internal selective oxidation is controlled by the inward diffusion of oxygen and occurs under the steel surface when:

$$D_M^{steel} \big/ D_O^{steel} << x_O^{steel} \big/ x_M^{steel} << 1 \tag{I.9}$$

where x_M^{steel} and x_O^{steel} are the alloying element M and oxygen mole fractions and D_M^{steel} and D_O^{steel} are the diffusion coefficients of the alloying element M and oxygen in the steel. In this case, M is immobile and there is no enrichment of the steel surface in this element.

The external selective oxidation is controlled by the outward diffusion of the alloying element:

$$x_O^{steel} \big/ x_M^{steel} << D_M^{steel} \big/ D_O^{steel} << 1 \tag{I.10}$$

In this case, oxide particles or films are formed at the steel surface.

The presence of external selective oxides on the steel surface can prevent the interface reactions between iron and liquid zinc because the wettability of these oxides by liquid zinc is very poor [58,59]. When this bad wetting occurs, numerous bare spots (i.e., holes in the zinc coating, Figure 18) are present in the coating.

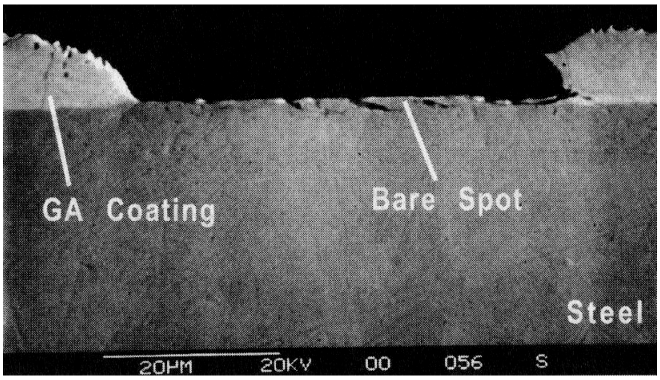

Figure 18: Cross section of a bare spot defect due to external selective oxidation [59].

Segregation and external selective oxidation depend on many factors such as the characteristics of the annealing cycle (temperature profile, gas composition, dew point) and the chemical nature of the elements involved (their diffusion coefficients in the steel and their affinity to oxygen). The transition from external to internal selective oxidation is achievable by choosing the appropriate dew point of the annealing atmosphere [60,61].

Depending on the steel grade, external selective oxidation can be more or less decisive for galvanizability. For example, Interstitial Free (IF) steels contain low concentrations of alloying elements so that the wettability is not limited by the presence of external selective oxides. On the contrary, Dual Phase (DP) or TRansformed Induced Plasticity (TRIP) steels are highly charged with alloying elements and external selective oxidation can become a real problem in industrial HDG processes. In the case of these steels grades, the annealing conditions should be carefully chosen and controlled (especially the dew point) in order to achieve the transition from external to internal selective oxidation and obtain a metallic surface at immersion which allows a good wettability. As most of the research works analysed in this literature review were performed on IF steels, all the reaction mechanisms exposed afterwards assume that the steel surface is in a metallic state at immersion, even if an annealed steel surface is never fully metallic.

I.3.1.3.2. Iron dissolution

General mechanisms

Several authors [23,27,30,32,45,47,54] have submitted that the triggering stage for the nucleation and growth of the inhibition layer is the dissolution of iron into the liquid zinc. Possible alternative reaction could be the diffusion of zinc into solid iron but it is kinetically negligible.

When the steel sheet is dipped into the galvanizing bath, the steel / liquid zinc interface is out of equilibrium. Leprêtre *et al*. [27] explained that, at this moment, the solubility of iron in the liquid zinc in metastable equilibrium with ferrite is higher than the solubility of iron in the liquid zinc in stable equilibrium (e.g. with $Fe_2Al_5Zn_x$ for a GI bath). Therefore, even if the zinc bath is saturated in iron (presence of dross particles), the iron dissolves from the steel surface into the liquid zinc during the first moments of immersion. This has also been reported by Yamaguchi and Hisamatsu [47].

Effect of the substrate surface microstructure

Giorgi [32] reported that the iron dissolution rate is higher at the substrate grain boundaries than in the middle of the grains. As a result, it can be thought that the substrate grain size plays an important role on the global flux of dissolved iron. If the grain size is fine, the grain boundary length per unit area is high and the iron dissolution rate is then expected to be large. On the contrary, a high grain size implies a low density of grain boundaries, giving rise to a lower iron dissolution rate.

Modelling of the dissolution step in the case of GI baths

Even if the kinetic laws accounting for the galvanizing reactions are validated only in the case of GI baths, it has been decided to present them because they are thought to be more general and applicable to GA baths.

In agreement with the general mechanism described earlier, Giorgi [32] proposed a model for the iron dissolution flux (mol.m^{-2}.s^{-1}) in GI baths:

$$J_{Fe}^{diss} = k_{diss}\left(c_{Fe}^{met} - c_{Fe}^{\text{int}}\right) \tag{I.11}$$

where c_{Fe}^{int} (mol.m^{-3}) is the iron concentration at the ferrite / liquid zinc interface, c_{Fe}^{met} (mol.m^{-3}) the iron concentration in the liquid zinc in metastable equilibrium with ferrite and k_{diss} (m.s^{-1}) the iron dissolution rate constant.

This first order reaction law is generally admitted [62,63].

I.3.1.3.3. Nucleation and growth of the inhibition layer

The dissolution process leads to an increase of the iron concentration in the liquid zinc in the vicinity of the steel strip. When this local supersaturation becomes sufficient, small nuclei of an intermetallic compound are formed on the steel surface. The nature of this intermetallic compound is well known in the case of GI baths ($Fe_2Al_5Zn_x$) and is subject to controversy in the case of GA baths (section I.3.1.1).

At this stage, the formation of the inhibition layer occurs in two steps [23,31,32,55]:

- A first step, corresponding to the nucleation and lateral growth of the crystals of the intermetallic compound until the formation of a continuous layer. This step is controlled by atom exchanges along an interface and is characterized by its high reaction rate, assumed to be proportional to the reaction time (linear kinetics).
- A second step, corresponding to the thickening of the inhibition layer. This step is controlled by the solid state diffusion of iron within the inhibition layer itself and is characterized by

slower kinetics, assumed to be proportional to the square root of the reaction time (parabolic kinetics). This second step is therefore much less dependent on the hydrodynamic conditions.

As said before, the basic mechanisms of formation of the inhibition layer developed above can be generalized regardless the nature of the nucleating intermetallic layer. As advanced in section I.3.1.1, the nature of the phases nucleating on the steel surface is supposed to change as a function of bath aluminium content. The models proposed in the literature were mainly validated in the case of GI baths [32,45,62-66]. Indeed, among these authors, only Liu and Tang [62] have also validated their model for GA baths (see Appendix A for more details). The specific mechanisms proposed by different researchers for GA baths and zinc baths with an aluminium content at the knee point β will be presented below.

I.3.1.3.3.1. Mechanisms of formation of the inhibition layer in GA baths

As stated earlier in this chapter (section I.3.1.1.3), very few studies have been published on the inhibition layer formed in GA baths. In addition, many of these studies provide conflicting results and a reaction mechanism is not always proposed.

δ phase formation

A group of researchers [27,30,33] support the nucleation and growth of an aluminium-saturated δ phase, in thermodynamic equilibrium with both the substrate and the liquid zinc.

When the strip is immersed in the bath, the steel / liquid zinc interface is out of equilibrium. Mataigne [30] reported that, at this moment, the system will tend to reach the thermodynamic equilibrium: the iron dissolution starts and the increase in the iron concentration at the interface leads to the nucleation and growth of the solid phase in equilibrium with liquid zinc, the δ phase. In addition, the particular structure of the Al-Fe-Zn ternary phase diagram allows the system to reach the local equilibrium along the interface with the steel. The schematic representation of the ternary diagram in Figure 19 shows that the aluminium content of a δ phase in equilibrium with liquid zinc (given by points between A and B) is higher than the minimum aluminium content necessary to ensure its equilibrium with iron (point C). As a result, the system does not require the nucleation of any other intermetallic compound. The thermodynamic equilibrium reached along the newly created interfaces is the reason why an inhibition of the Fe-Zn reactions is possible.

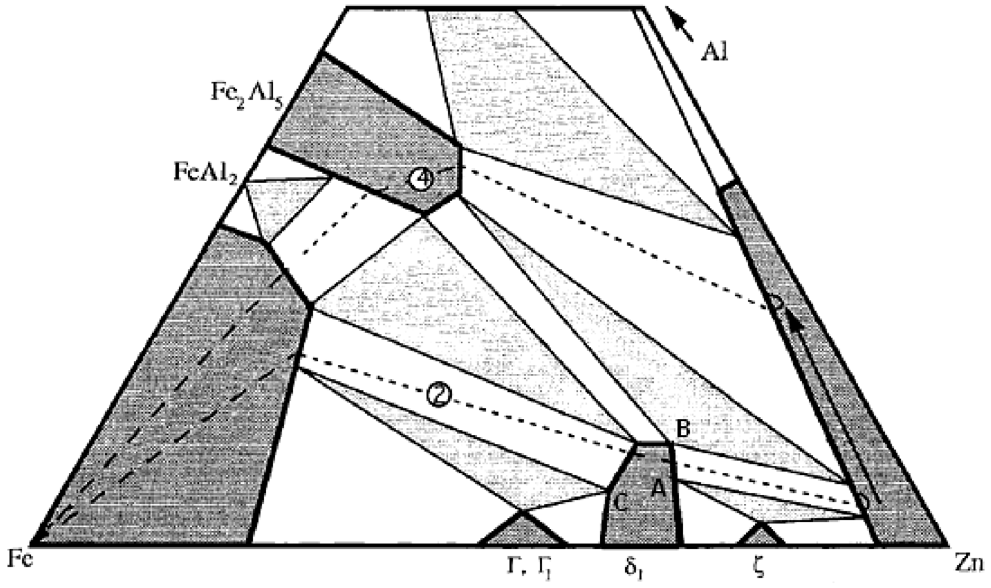

Figure 19: Schematic representation of the isothermal Al-Fe-Zn phase diagram at 450 °C illustrating the diffusion path corresponding to the Fe-Zn inhibition in GA baths (path 2) (Leprêtre [33]).

Leprêtre *et al.* [27,33] used the concept of diffusion path in the Al-Fe-Zn ternary phase diagram in order to explain the inhibition by δ in GA baths. As the obtained microstructure is characterized by a δ layer with planar interfaces where thermodynamic equilibria are satisfied, this inhibition can be represented by a real diffusion path [5] (path 2 in Figure 19).

$Fe_2Al_5Zn_x$ phase formation

Other authors [23,26,31,45-47,52,53] affirmed that metastable $Fe_2Al_5Zn_x$ is present in the inhibition layer formed in GA baths. Some of them [23,26,31,52] reported that the $Fe_2Al_5Zn_x$ phase is the only component of the inhibition layer.

Guttmann [23] also reported that $Fe_2Al_5Zn_x$ forms epitaxially on the steel surface [23,33,43-45]. This could be the most reasonable explanation to the possible metastability of $Fe_2Al_5Zn_x$ in GA baths.

Formation of both δ and $Fe_2Al_5Zn_x$

Finally, Yamaguchi and Hisamatsu [47] proposed that the $Fe_2Al_5Zn_x$ phase nucleates first on the steel surface followed by the nucleation of the δ phase at the solid / liquid interface due to a local decrease of the aluminium concentration at this location. This mechanism is also the same that they suggested for GI baths with less than 0.15 wt.% Al.

I.3.1.3.3.2. Mechanisms of formation of the inhibition layer in zinc baths at the knee point β

As stated in section I.3.1.1.4, very few researchers [27,33,47,54] have been interested specifically in the inhibition layer formed in zinc baths with an aluminium content corresponding to the knee point β (Figure 11). In this case, the interface layer was found to be composed of a lower layer of $Fe_2Al_5Zn_x$ and an upper layer of δ.

Leprêtre [33] assumed that the intermetallic compounds formed can be predicted by the phase diagram. Figure 20 shows the evolution of the iron and aluminium concentrations in the liquid phase close to the steel surface due to the galvanizing reactions (black and blue paths), in the zinc-rich corner of the Al-Fe-Zn diagram. The bath considered is composed of a liquid phase, represented by point A, in equilibrium with $Fe_2Al_5Zn_x$. The dissolution of the steel surface in the zinc bath leads to an increase in the iron content, resulting in a rapid displacement of the bath composition at the interface towards point B (black path [33]). This point can be located in the δ / $Fe_2Al_5Zn_x$ / liquid zinc triphasic domain or in the δ / liquid zinc biphasic domain, if point A is sufficiently close to the knee point β. Along the black path, the iron dissolution will then result in the nucleation of both $Fe_2Al_5Zn_x$ (at first) and δ (when it becomes stable). In agreement with this proposed mechanism, aluminium is also consumed by the nucleation and growth of the interface compounds and the black path should not remain vertical. The composition of the bath at the interface should rather be given by the blue path AC. The respective proportions of these two phases are directly dependent on the position of point A and on the amount of dissolved iron. The closer the bath aluminium content to the knee point β is, the higher the proportion of δ phase will be [6].

---

[5] Leprêtre *et al.* [27,33] used the concept of diffusion paths in the Al-Fe-Zn ternary phase diagram proposed by Úředníček and Kirkaldy [46] as a powerful tool to detail the mechanisms of formation of the inhibition layer. A diffusion path is the locus, in the ternary phase diagram, of the points representing the average compositions within planes perpendicular to the direction of diffusion. A diffusion path that only crosses single phase domains or crosses two-phase domains along the tie lines is called a real diffusion path. Such diffusion paths represent stratified structures with planar interfaces. Any diffusion path that is not real is called a virtual diffusion path [27,33]. Clark [67] described complex microstructures by means of diffusion paths. His work may facilitate the understanding of the concept of diffusion path (Appendix D).

[6] The same explanations are valid when the bath aluminium content is less than the one at the knee point β. The inhibition layer is predicted to be composed of δ phase, as Leprêtre [33] found experimently in the case of a zinc bath containing 0.13 wt.% Al.

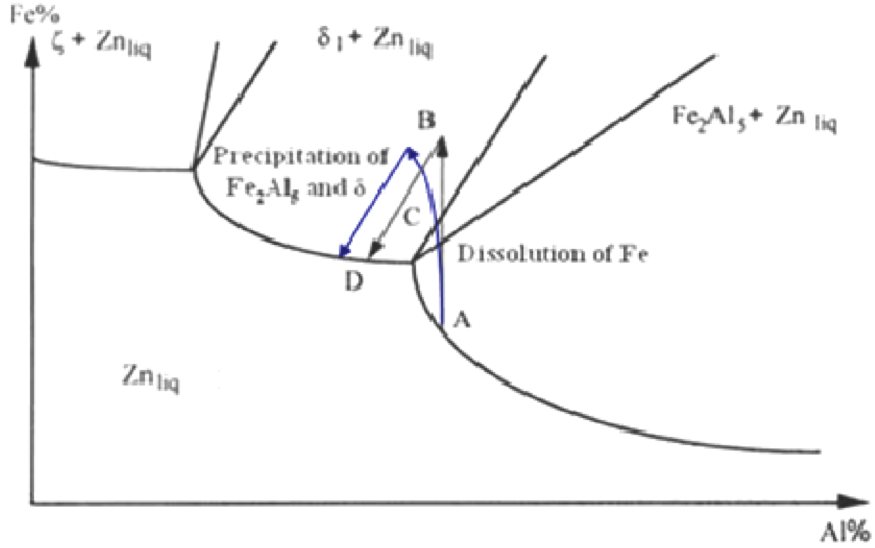

Figure 20: Schematic representations of the mechanism of formation of the inhibition layer in the case of a zinc bath with an aluminium content close to the knee point β (black path, proposed by Leprêtre [33], and blue path, proposed by the present author).

According to Leprêtre [33], it is better to consider that the formation of the biphasic inhibition layer occurs through this mechanism in zinc baths in equilibrium with $Fe_2Al_5Zn_x$, rather than as a result of the nucleation of metastable $Fe_2Al_5Zn_x$ in a zinc bath that would be in equilibrium with δ phase, because the formation of $Fe_2Al_5Zn_x$ would have to overcome two obstacles: first, it would not be the stable compound and, secondly, its formation would be kinetically limited by the diffusion of aluminium in the liquid.

The mechanism proposed by Dionne *et al*. [54] is almost the same, except that it is not based on thermodynamics (i.e., formation of the stable intermetallic compound) but on kinetics considerations only, in agreement with Yamaguchi and Hisamatsu [47]. These authors indicated that, when the strip enters the zinc bath, the iron dissolution process induces an enrichment in iron of the liquid phase in the vicinity of the steel surface, leading to the nucleation of a first layer of $Fe_2Al_5Zn_x$. At this moment, the liquid zinc near the strip does not contain enough aluminium to allow the subsequent growth of $Fe_2Al_5Zn_x$. However, the iron content there is probably still high. Consequently, δ crystals precipitate on top of the $Fe_2Al_5Zn_x$ layer.

I.3.1.3.3.3. Metastable ζ phase formation

Several researchers [28,30,33,68,69] observed the nucleation of epitaxial ζ rod crystals in coexistence with the inhibition layer in the case of GA baths. Leprêtre [33] and Mataigne [30] reported that, as the stability difference between δ and ζ in GA baths is very small (*ΔG*, Table 3), metastable ζ crystals can precipitate on the steel surface simultaneously to the nucleation of the δ phase (Figure 21), provided that their nucleation energy is lowered. This condition can be fulfilled at the surface of appropriately oriented steel grains due to possible epitaxial relationships between ζ phase and steel. Leprêtre [33] and Mataigne [30] disagree in the everlasting behaviour of this metastable compound. While the former [33] indicated that these crystals should disappear if the galvanizing time is long enough, as they are out of equilibrium, the latter [30] reported that they persist within the coating.

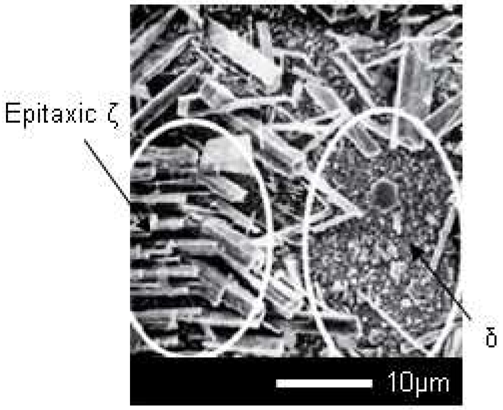

Figure 21: Inhibition layer relative to GA baths, made of stable δ and metastable epitaxial ζ crystals (Mataigne [30]).

Some crystallographic orientations of the steel are not favourable for the development of epitaxial relationships with ζ. The corresponding grains will be covered by the δ phase only. The effect of the steel grains orientation on the nucleation of epitaxial ζ has been studied by Nakamori [68] and is illustrated in Figure 22, where a perfect correspondence between colonies of ζ crystals with the same orientation and the underlying base steel grains (2 and 5) can be observed. In addition, it can also be appreciated that some steel grains (3 and 4) do not present an appropriate orientation for epitaxial growth of ζ crystals. Adachi *et al*. [69] reported that the epitaxial nucleation and growth of ζ occurs preferentially on some ferrite surface planes, such as (113), (313), (111).

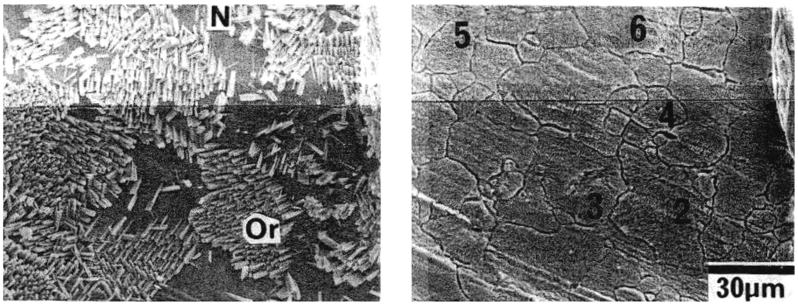

Figure 22: Correspondence between the distribution of epitaxial ζ crystals and the microstructure of the base steel (Nakamori [68]).

It is also important to highlight that other metastable ζ crystals different from the epitaxial ones described before have been observed by different researchers [27,28,33,54]. These ζ crystals, known as “evanescent”, were first identified by Leprêtre [33]. While epitaxial ζ crystals form in zinc baths with low aluminium content and develop as colonies of crystals with a preferred orientation relationship with the underlying substrate, the so-called “evanescent” ζ crystals are randomly oriented on the top of the inhibition layer. These evanescent ζ crystals form from iron-supersaturated liquid zinc during the solidification process, independently of the bath aluminium content. As stated in section I.3.1.3.3, the formation of the inhibition layer is firstly limited by the diffusion of aluminium in the liquid zinc. If the solidification of the coating occurs before all the dissolved iron in supersaturation has precipitated, the excess iron will not entirely solidify as a solute element, but will lead to the formation of metastable ζ crystals. As the duration of galvanizing increases, the amount of excess iron is consumed by the growth of the inhibition layer and, consequently, the amount of the evanescent ζ crystals decreases [27,33]. This is the reason why these metastable ζ crystals have been named by Leprêtre [33] as “evanescent”. It should be noted that “evanescent” ζ crystals do not form during typical galvannealing production, as cooling below the melting point of zinc usually takes place after full consumption of the liquid zinc.

I.3.1.4. Recapitulation

The final structure and phase composition of the inhibition layer proposed by the different researchers presented above is summarized below, for the bath compositions used for galvannealing.

Final structure and phase composition of the inhibition layer in GA baths

Controversial results have been published concerning the final structure and phase composition of the inhibition layer formed in GA baths.

An important group of researchers [23,26,31,45,46,52] reported that the final composition of this inhibiting layer totally corresponds to metastable $Fe_2Al_5Zn_x$.

By their side, Yamaguchi and Hisamatsu [47] proposed that the inhibition layer is composed of a two-layer structure with $Fe_2Al_5Zn_x$ (lower layer) and δ (upper layer).

On the other hand, another group of authors [27,30,33] submitted that the inhibition layer in GA baths is fully composed of δ, which is the intermetallic compound in equilibrium with the liquid phase.

Some authors [28,30,33,68,69] reported as well the nucleation of metastable epitaxial ζ crystals simultaneously to the one of the inhibition layer, especially in the case of GA baths with low aluminium contents.

Final structure and composition of the inhibition layer in zinc baths at the knee point β

Only Leprêtre [33] and Dionne *et al*. [54] have specifically studied the inhibition layer which forms in zinc baths at the knee point β. Both authors proposed a two-layered inhibition layer composed of $Fe_2Al_5Zn_x$ (lower layer) and δ (upper layer) as presumed by other authors [27,47].

I.3.2. The inhibition layer breakdown

As advanced above, the inhibiting behaviour of the interfacial layer which forms in the earlier stages of immersion in the zinc bath is always transient, even if the thermodynamic equilibria along all the interfaces are satisfied. In this way, Hisamatsu [25] showed that even a predeposited 5 µm-thick layer of Fe_2Al_5 in equilibrium with an iron-saturated zinc bath containing 0.16 wt.% Al at 450 ℃ is eventually destroyed into the bath for long immersion times (around 30 min).

In this section, the proposed mechanisms through which the inhibition layer is expected to be destabilized as well as the numerous reported factors which may influence the kinetics of the inhibition layer breakdown will be reviewed.

The inhibition layer breakdown will be presented in the case of GA baths only, as the industrial objective of the HDGA process is to obtain an alloyed coating with the targeted Fe-Zn phase distribution and the first step of the alloying reactions is the inhibition layer breakdown [7].

I.3.2.1. Proposed mechanisms for the inhibition layer breakdown

Different mechanisms have been proposed to explain the inhibition layer breakdown. While a very small group of researchers [28,49] reported that the Fe-Zn reactions are likely activated by the dissolution of the inhibition layer in the liquid zinc (section I.3.2.1.1), it is generally admitted in the

---

[7] In the case of zinc baths with lower aluminium contents, as no inhibition is expected to exist, the growth of Fe-Zn compounds is not well controlled. On the other hand, the inhibiting effect of the interfacial layer which forms in GI baths is too strong. Consequently, energy requirements to achieve the inhibition layer breakdown and subsequent controlled growth of Fe-Zn phases will be higher in GI baths than in GA baths.

literature that an outburst reaction is the responsible for the rupture of the inhibition layer in the case of Ti IF steels [23-27,29-31,33,46-48,54,70] (section I.3.2.1.2). In the following paragraphs, a critical review of the different mechanisms will be given.

I.3.2.1.1. Dissolution of the inhibition layer

As said before, a minority of the analysed authors [28,49] suggested that the inhibition layer is dissolved in the molten zinc. As already seen in section I.1.3, GA coatings are produced by reheating the strip at the exit of the zinc bath, just after wiping. Increasing the temperature during reheating enhances the iron solubility (Figure 13, Figure 14 and Figure 15) and the inhibition layer is expected to be dissolved in the liquid zinc.

McDevitt and Meshii [28] studied the inhibition layer breakdown by means of a laboratory simulator by dipping Ti-Nb IF and P-added Ti IF steel samples in a zinc bath containing 0.14 wt.% Al before galvannealing. The galvannealing treatment was interrupted at different times. They reported no evidence of outbursts or mechanical crackings within the inhibition layer and did not rule out the fact that the inhibition layer may have broken due to a dissolution process.

By their side, Nitto *et al*. [49] reported that the small-sized crystals of the inhibition layer (Fe_2Al_4Zn, according to them) are dissolved with long immersion times and, as a result, the growth of Fe-Zn compounds starts from such parts.

However, as indicated by Guttmann *et al*. [23], the destruction of a 5 µm-thick Fe_2Al_5 layer during a long immersion time in a GI bath (0.16 wt.% Al at 450 °C) [25] cannot be explained by its dissolution, as Fe_2Al_5 is in thermodynamic equilibrium with liquid zinc (Figure 11). Therefore, another mechanism should be expected to occur in competition with the dissolution of the inhibition layer (section I.3.2.1.2).

I.3.2.1.2. Outburst formation

At the exit of the galvanizing bath, the increase in temperature during reheating enhances the iron and zinc interdiffusion through the inhibition layer, leading to the formation of outbursts. These outbursts, generated by the formation of Fe-Zn compounds which nucleate as a result of changes in the local concentrations caused by a diffusional process, penetrate the inhibition layer and break it down. This is the most accepted mechanism in the literature. Several experiments confirm that this last mechanism is, in most cases, the one responsible for the inhibition layer breakdown in the case of Ti IF steels (section I.3.2.1.2.1).

Some subtleties such as the diffusing element which causes the outburst formation, the nature of the nucleating Fe-Zn compounds or the exact locations of these outbursts remain quite controversial.

As stated above, the iron and zinc interdiffusion through the inhibition layer is accelerated when temperature is increased. Some researchers [46-48] thus submitted that the diffusion of iron towards the liquid zinc, leading to the growth of the inhibition layer and consequent aluminium depletion at the solid / liquid interface, is responsible for the outburst formation (section I.3.2.1.2.2). On the contrary, an important group of researchers [23-27,29-31,33,54,70] reported that the triggering phenomenon in the mechanism of outburst formation is the diffusion of zinc towards the steel substrate (section I.3.2.1.2.3).

I.3.2.1.2.1. Experimental evidence of outburst formation

Nishimoto *et al*. [48] were the first researchers to reveal that outburst structures are formed at the steel grain boundaries for long immersion times in GA baths.

Hisamatsu [25] confirmed later that the steel grain boundaries are preferential locations for outburst formation. Figure 23 shows the cross section of an outburst located at the steel / zinc interface. The outburst root is located in a steel grain boundary. It can also be appreciated how zinc is present along the steel grain boundary (zinc is given by the white colour, Figure 23-4).

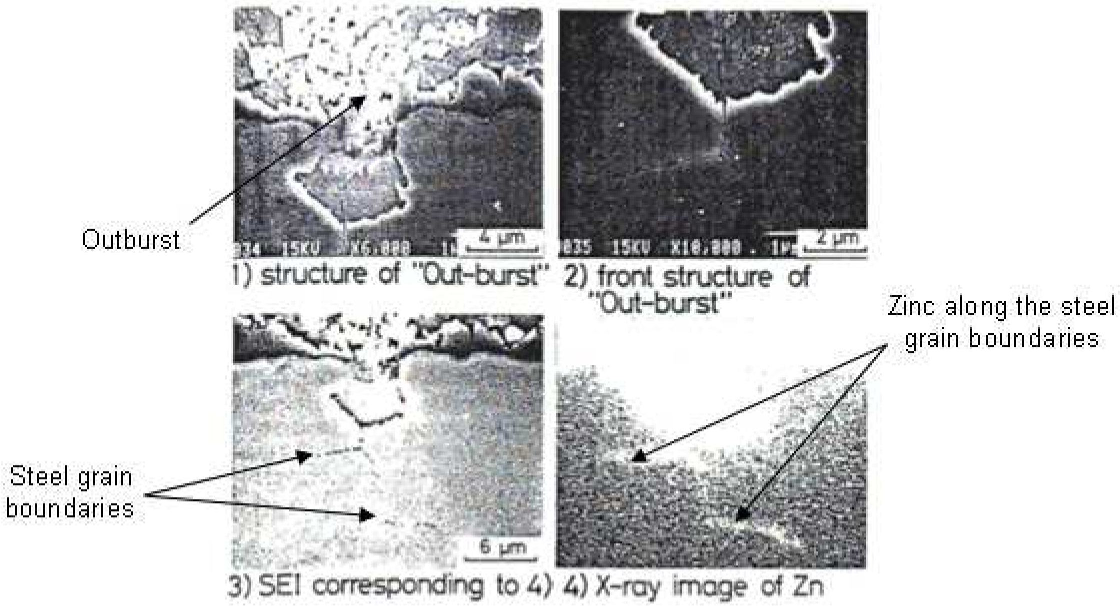

Figure 23: Detailed cross section of an outburst area and its zinc distribution (Hisamatsu [25]).

Later, other authors [27,33] gave new experimental evidence of the well known preferential formation of outbursts at the emergence of the steel grain boundaries (Figure 24). After selective dissolution of the Fe-Zn compounds and the zinc overlay, a triple grain boundary of steel is clearly visible in Figure 24. This triple grain boundary is surrounded by a $Fe_2Al_5Zn_x$ layer. This observation indicates that the nucleation of outbursts takes place at the emergence of the triple grain boundaries of steel.

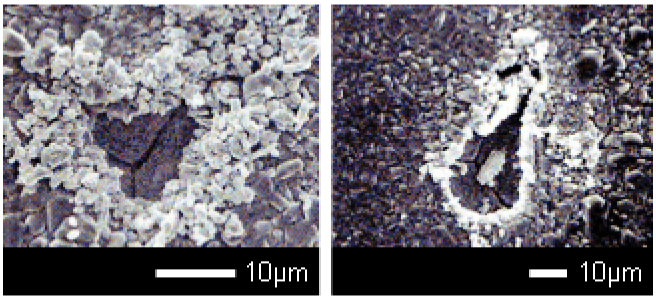

Figure 24: Location of the outbursts at the emergence of triple grain boundaries of steel in the case of an inhibition by $Fe_2Al_5Zn_x$ only (Leprêtre *et al.* [27]).

I.3.2.1.2.2. Outburst formation via an aluminium depletion at the solid / liquid interface

Description of the aluminium depletion mechanism

Úředníček and Kirkaldy [46] explained the evolution of the coating microstructure in the early stages of the process in the basis of a decrease in the aluminium concentration at the solid / liquid interface. Once the inhibition layer is completely transformed into $Fe_2Al_5Zn_x$, further growth of this layer via solid state diffusion of iron towards the liquid requires an aluminium supply from the bath. As a result, subsequent decrease in aluminium in the liquid leads to the nucleation of the δ phase which rapidly penetrates the $Fe_2Al_5Zn_x$ layer (outburst formation).

Yamaguchi and Hisamatsu [47] also submitted, in total agreement with the previous authors, that the outburst formation is related to a decrease in the aluminium concentration in the liquid near the solid / liquid interface.

Nishimoto *et al*. [48] pointed out that outbursts form preferentially at the steel grain boundaries. They suggested that the decrease in the aluminium concentration occurs initially at these sites. The higher reactivity of the steel grain boundaries causes a faster aluminium depletion in these locations, leading to the nucleation of the δ phase which penetrates the inhibition layer. Figure 25 shows a schematic illustration of the mechanisms proposed by these authors concerning the development of Fe-Zn compounds within the coating. The two first stages (a and b) illustrate how the inhibition layer initially breaks up at the steel grain boundaries. The two last stages (c and d), concerning further development of the coating, are described in Appendix C (section C.1.1.2).

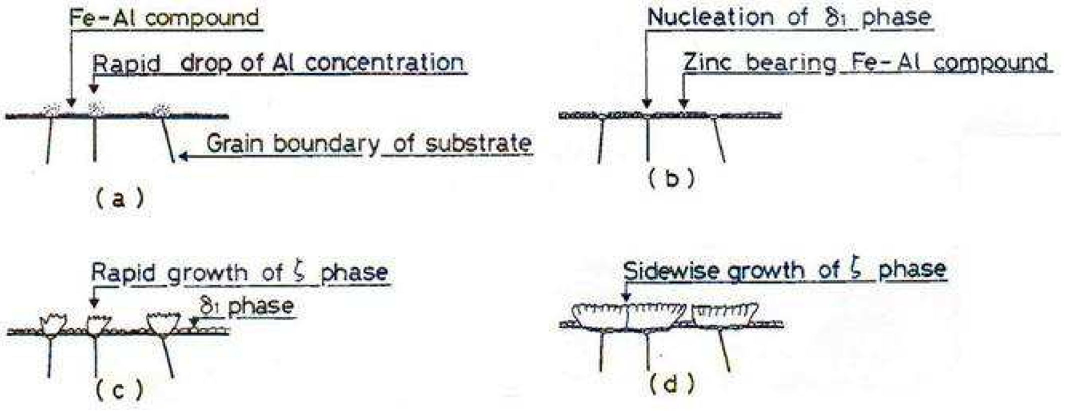

Figure 25: Schematic illustration of the mechanisms of formation of Fe-Zn compounds suggested by Nishimoto *et al*. [48].

Relevance of the aluminium depletion mechanism

The outbursts were observed by Nishimoto *et al*. [48] in a zinc bath containing 0.16 wt.% Al at 470 °C (GI bath).

Guttmann *et al.* [31] tried to evaluate the relevance of the aluminium depletion mechanism by means of a galvanizing model developed for GI baths by Linarès [64]. In the case of a bath containing 0.155 wt.% Al, the model calculations showed that the growth of the inhibition layer depletes the aluminium concentration at the interface of 0.015 wt.%, thus insufficient to allow the nucleation of the δ phase. This calculation rules out the mechanism of outburst formation via an aluminium depletion at the solid / liquid interface in the bath.

After wiping, the amount of aluminium in the liquid becomes limited. A higher aluminium depletion at the solid / liquid interface is therefore expected to occur, depending on both the continued growth of the $Fe_2Al_5Zn_x$ layer and the thickness of the liquid film (about the same composition as the bulk of the bath when the strip leaves the zinc pot). Rough calculations, using two different values of the diffusion coefficient of iron in Fe_2Al_5 $D_{Fe}^{Fe_2Al_5}$ at 460 °C found in the literature (9×10^{-16} [71] and 5×10^{-17} [72] $m^2.s^{-1}$), show that the aluminium depletion in the liquid zinc coating should not be neglected (after wiping, the time necessary for a 10 µm-thick liquid zinc film containing 0.155 wt.% Al at 460 °C to reach the aluminium content of the knee point β was found to be 49 and 885 s respectively) [8]. It should be also considered, as seen in section I.3.1.1.3, that metastable $Fe_2Al_5Zn_x$

---

[8] The calculation is performed considering the thickness of the inhibition layer after typical immersion times (around 0.15 µm for 3 s, according to Figure 17 [55] in section I.3.1.2 and Figure 114 [32] in section A.2.1 of Appendix A). A steady iron concentration gradient through the inhibition layer has been assumed. The iron concentrations in $Fe_2Al_5Zn_x$ at the steel / $Fe_2Al_5Zn_x$ and $Fe_2Al_5Zn_x$ / liquid zinc interfaces have been supposed to be those at thermodynamic equilibrium (Figure 10 [10]). These concentrations differ in 1 wt.% Fe only. The densities of $Fe_2Al_5Zn_x$ and liquid zinc at 460 °C have been supposed equal to 4570 kg m^{-3} [32] and 6525 kg m^{-3} respectively [73].

likely exists at lower aluminium contents and that an aluminium depletion in the liquid reaching the knee point β would remain insufficient to allow the nucleation of the δ phase.

As a conclusion, it is quite doubtful that this aluminium depletion mechanism can lead to the inhibition layer breakdown. One can better imagine the nucleation of a layer of δ crystals at the solid / liquid interface and its growth towards the liquid rather than the penetration of the just nucleated δ crystals through the underlying $Fe_2Al_5Zn_x$ layer until reaching the steel substrate. Although it is a little premature to absolutely reject the possibility of an inhibition layer breakdown through a dissolution process or through outburst formation via an aluminium depletion in the liquid zinc, it can be confirmed that other mechanism is expected to occur at least in competition with the two previous ones.

I.3.2.1.2.3. Outburst formation via the diffusion of zinc through the inhibition layer

Description of the zinc diffusion mechanism

Hisamatsu [25] was the first researcher to propose that the inhibition layer breaks up through an outburst formation reaction. At first, zinc diffuses within the inhibition layer and then into the steel grain boundaries. As a result of the accumulation of zinc atoms at these locations, a Fe-Zn compound nucleates. By the volume expansion of this Fe-Zn compound, the steel grain boundaries are opened, which induces cracks in the inhibition layer. Liquid zinc then infiltrates through these cracks, leading to a rapid Fe-Zn alloying reaction and the formation of Fe-Zn intermetallic compound outbursts. A schematic illustration of this mechanism, suggested by the author in the framework of his work concerning the breakdown of a 5 µm-thick Fe_2Al_5 layer during long immersion times in a zinc bath containing 0.16 wt.% Al at 450 ℃, is shown in Figure 26.

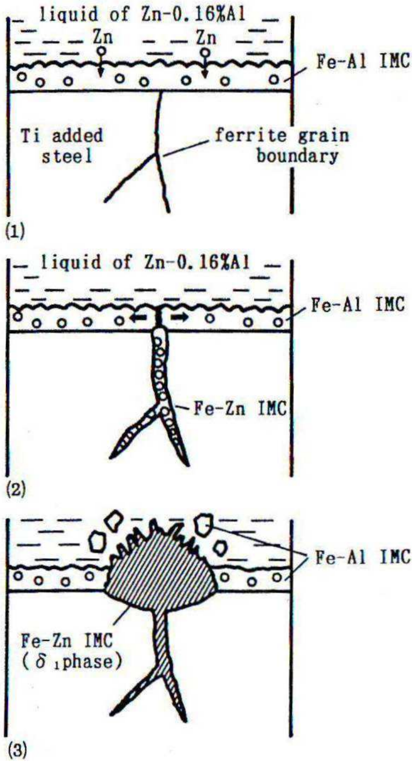

Figure 26: Schematic representation of the mechanism of inhibition breakdown through outburst formation proposed by Hisamatsu [25].

With a totally different mechanism, Hisamatsu [25] confirms what had been already advanced by Nishimoto *et al*. [48]: steel grain boundaries are preferential locations for outburst formation. As shown in Figure 23-4, zinc is present along the steel grain boundary, indicating that its diffusion to these sites is the responsible of the outburst formation.

Since then, numerous researchers [23,24,26,27,29-31,33,70] have supported the mechanism proposed by Hisamatsu [25]. The current discussions concern the mechanisms of zinc diffusion to the steel grain boundaries. Mataigne [30] submitted that the temperature during the galvannealing process is not high enough to activate the diffusion of zinc atoms within the steel grains, so once they have crossed the inhibition layer, they rapidly diffuse towards the emerging lines of the steel grain boundaries, where they are accumulated. This author does not report any preferred circuit for zinc diffusion within the inhibition layer. Guttmann [23] suggested, however, that preferential short circuits exist for zinc diffusion through the inhibition layer as a result of the epitaxial relationships between this layer and the steel [23,33,43-45]. As the orientation of the crystals constituting the inhibition layer depend on the crystallography of each of the underlying steel grains, adjacent colonies of these crystals with different orientations meet each other at the emergence of steel grain boundaries, forming high angle random boundaries which represent short circuits for zinc diffusion through the inhibition layer.

Since zinc diffusion is more rapid in the inhibition layer and in the steel grain boundaries than in the steel matrix, the zinc isoconcentration profiles in the vicinity of emergent grain boundaries can be represented as shown in Figure 27. The nucleation of Fe-Zn compounds can occur when the critical zinc supersaturation is achieved over the critical volume (sphere of radius R_c), which will obviously be reached earlier at these locations.

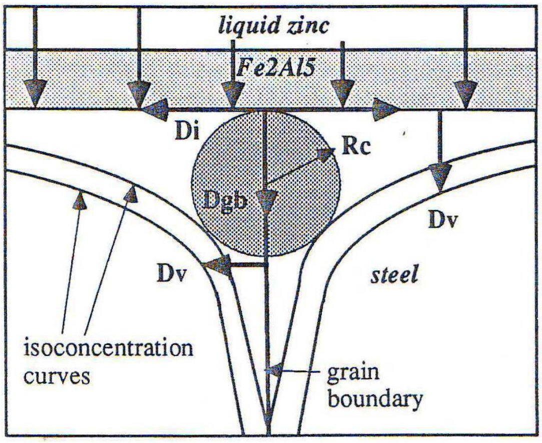

Figure 27: Schematic representation of grain boundary diffusion of zinc in steel, where D_i, D_v and D_{gb} are the diffusion coefficients of zinc at the interface, in the volume and at the grain boundary, respectively, and R_c is the critical radius of the embryo (Guttmann *et al*. [31]).

When the zinc concentration at the steel grain boundaries reaches the critical value, a Fe-Zn compound nucleates. Leprêtre *et al.* [27,33] suppose that the intermetallic compound formed is the stable one and can be predicted by the phase diagram. The nature of this nucleating Fe-Zn compound depends on the nature of the steel / inhibition layer interface, which will in turn depend on the aluminium content of the zinc bath. Separate analysis of the mechanism of outburst formation proposed by these authors will be presented hereinafter for GA baths (and in Appendix B in the case of GI baths).

Nature of the outbursts in the case of GA baths

As seen in section I.3.1.3.3, Leprêtre *et al.* [27,33] used the concept of diffusion paths in the Al-Fe-Zn ternary phase diagram to explain the mechanism of formation of the inhibition layer. They have also used this tool to explain their experimental results concerning the outburst formation.

According to the phase diagram (Figure 11), the inhibition layer in GA baths is composed of the δ phase and the different interfaces (steel / δ / liquid zinc) can be described by diffusion path 2 in Figure 28. The diffusion of zinc through the δ inhibition layer leads to a local enrichment in zinc of the steel / δ interface, at the steel grain boundaries. The representation of this enrichment consists in a displacement towards higher zinc contents (see arrow from point A) of the tie-line corresponding to the equilibrium satisfied at this interface. The zinc concentration at the steel grain boundaries increases progressively and, after a while, it finally reaches the critical content corresponding to the three-phase equilibrium domain involving the Γ phase. The diffusion path is no longer real but virtual (path V2 in Figure 28) and represents the local nucleation of the Γ phase at the steel / δ interface.

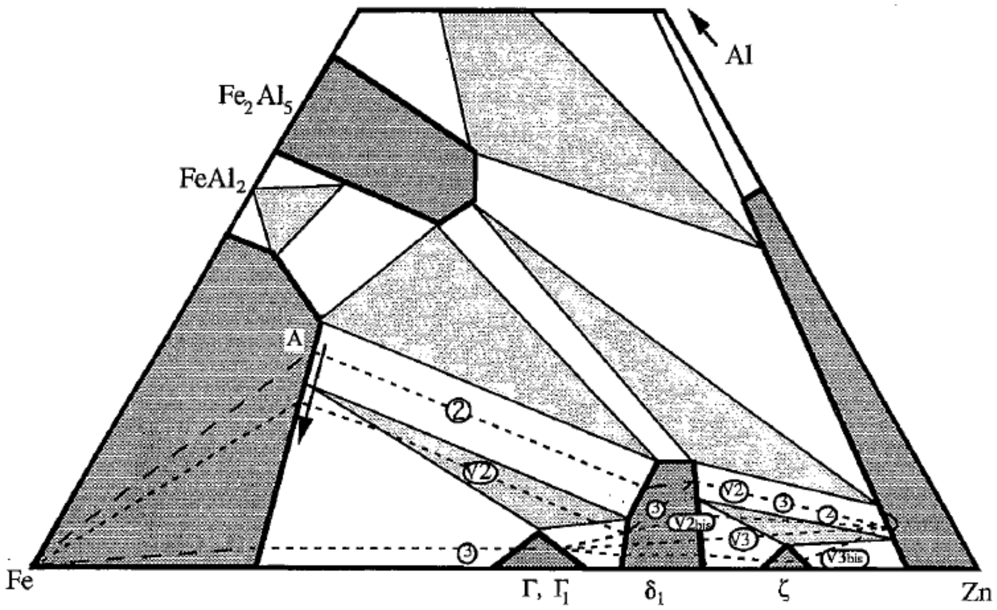

Figure 28: Schematic representation of the isothermal Al-Fe-Zn phase diagram at 450 °C illustrating diffusion paths representing the evolution of the microstructure of coatings in GA baths (Leprêtre [33]).

The volume expansion associated with the nucleation of the Γ phase leads to the detachment of the δ layer and, as a result, the Γ nucleus gets in direct contact with the liquid zinc. As the Γ phase and the liquid zinc are not in equilibrium, an intermediate intermetallic compound is formed. As described by paths V2 and V2bis, the only phase which can nucleate at the Γ / liquid zinc interface is δ. This mechanism has been also reported by Mataigne [30].

Nature of the outbursts in the case of zinc baths at the knee point β

By their side, Dionne *et al*. [54] studied the inhibition layer breakdown on industrial Ti IF, Ti-Nb IF and P-added Ti IF steel samples galvanized in zinc baths containing 0.133 and 0.135 wt.% Al, i.e., with a composition in the vicinity of the knee point β. By means of a laboratory simulator, the authors conducted interrupted galvannealing treatments, designed to induce the partial breakdown of the inhibition layer. Based on their observations, they proposed the following sequence of phase formation to describe the inhibition layer breakdown at the beginning of the galvannealing reaction:

- The first step is the zinc enrichment of the inhibition layer, initially composed of a $Fe_2Al_5Zn_x$ layer with δ crystals on its top, as seen in section I.3.1.1.4. After interrupted galvannealing treatments, numerous discontinuities were observed by the authors in the $Fe_2Al_5Zn_x$ layer on samples selectively etched to dissolve the Fe-Zn compounds (such as δ), suggesting that the breakdown of the inhibition layer is not uniform at a fine scale. This is consistent with a partially reacted inhibition layer, containing zinc-enriched boundaries and/or zinc-rich phases.

- The second step in the breakdown of the inhibition layer is the transformation of the zinc-enriched $Fe_2Al_5Zn_x$ phase. δ crystals nucleate at discontinuities in the $Fe_2Al_5Zn_x$ layer. The authors indicated that it is not clear whether they form directly from the $Fe_2Al_5Zn_x$ crystals by a phase transformation or whether a ternary phase acts as a transition phase. The δ outburst formation is therefore attributed to a phase transformation induced by the supersaturation of the inhibition layer in zinc and not to the zinc enrichment at the steel grain boundaries as reported by all the previous researchers [23-27,29-31,33,70].

After nucleation, the δ crystals grow very quickly. The subsequent thinning of the $Fe_2Al_5Zn_x$ layer and transformation into a layer of δ crystals did not occur uniformly on the steel surface. The breakdown of the inhibition layer was significantly faster in the regions surrounding the emerging steel grain boundaries than in the interior of the grains. Dionne *et al*. [54] also reported a zinc enrichment of the steel grain boundaries. However, it is not clear whether the diffusion of zinc to these locations occurs concurrently with the breakdown of the inhibition layer or once the δ outbursts are formed. The fact that Dionne *et al*. [54] have indicated that the breakdown of the inhibition layer takes place first in the vicinity of the steel grain boundaries would be consistent with Guttmann's assumption [23] that preferential short-circuits for zinc diffusion within the $Fe_2Al_5Zn_x$ layer exist over the steel grain boundaries due to epitaxial relationships between this layer and the steel.

I.3.2.1.3. Brief summary

Concerning the mechanisms proposed in the literature accounting for the inhibition layer breakdown, it can be drawn that:

- The dissolution of the inhibition layer seems very unlikely and it is rather the outburst formation which is responsible for the inhibition layer breakdown in the case of Ti IF steels.

- Experimental results show that outbursts form preferentially at the steel grain boundaries.

- The nature of these outbursts is thought to depend on the zinc bath composition. In the case of GA baths, the intermetallic compound which nucleates first at the steel grain boundaries is expected to be Γ. However, it is important to highlight that no strong experimental evidence of the nature of the outbursts has been found in the literature. It means that the different contributions are, by the moment, nothing else than assumptions.

- Two different mechanisms accounting for the outburst formation have been proposed: the aluminium depletion at the solid / liquid interface and the diffusion of zinc through the inhibition layer towards the steel grain boundaries. Experimental evidence has only been found for the latter.

I.3.2.2. Kinetics of the inhibition layer breakdown

It is well known that the kinetics of the inhibition layer breakdown can be affected by several factors. In the following sections, a literature review of these factors will be presented, focusing on the mechanisms through which each of them anticipates or delays the inhibition layer breakdown. To explain the different effects, it will be supposed that the inhibition layer breakdown is caused by the outburst formation due to the diffusion of zinc through this layer.

I.3.2.2.1. Effect of the bath conditions

The effect of the aluminium content and temperature of the zinc bath on the kinetics of the inhibition layer breakdown will be discussed below.

I.3.2.2.1.1. Effect of the bath aluminium content

It is generally admitted that the higher the zinc bath aluminium content is, the slower the inhibition layer breakdown kinetics is [33]. Experimental evidence of this effect is given, for example, by Leprêtre [33], who studied the inhibition layer breakdown in the case of Ti IF steels galvanized in zinc baths containing 0.13 and 0.18 wt.% Al. While outbursts began to appear after 10 s of immersion in the bath containing 0.13 wt.% Al (they were numerous after 30 s of immersion), it lasted around 20 min of immersion before the outburst formation in the case of the bath containing 0.18 wt.% Al.

For these experiments, the main reason of the difference observed in the inhibiting period is the nature of the inhibition layer, δ in Zn - 0.13 wt.% Al and $Fe_2Al_5Zn_x$ in Zn - 0.18 wt.% Al. The phase composition of the inhibition layer will play an important role on the diffusion of both zinc and iron through the layer itself. To our knowledge, the diffusion coefficient of zinc in δ has not been measured yet, but it can be reasonably supposed that zinc diffuses faster in this phase than in $Fe_2Al_5Zn_x$ (the diffusion coefficient of zinc in Fe_2Al_5 $D_{Zn}^{\mathrm{Fe_2Al_5}}$ at 460 °C is 5 x 10^{-15} $m^2.s^{-1}$ [74]). As the zinc content is much higher in the δ phase than in the $Fe_2Al_5Zn_x$ phase, zinc atoms would more easily diffuse through the δ structure by a vacancy substitution mechanism. This leads to an earlier inhibition layer breakdown.

Moreover, as stated in section I.3.1.2, increasing the aluminium content in the zinc bath generally favours the growth of the inhibition layer (Figure 17). As a result, zinc atoms will need to diffuse through a larger distance to reach the substrate grain boundaries and, consequently, the inhibition layer breakdown will be delayed.

One could therefore summarize that the bath aluminium content may strongly modify the kinetics of the inhibition layer breakdown as it plays an important role in the phase composition, thickness and structure of this layer.

I.3.2.2.1.2. Effect of the bath temperature

On the one hand, an increase in the bath temperature favours the growth of the inhibition layer by increasing the diffusion rate of iron towards liquid zinc [75], but on the other hand, it also enhances the diffusion rate of zinc towards the steel substrate. In spite of these two contradictory effects, it is generally accepted that an increase in the bath temperature leads to a faster kinetics of the inhibition layer breakdown.

Although long immersion time experiments are commonly performed to study these effects [24-26,33,46,70], it should be reminded that the breakdown of the inhibition layer in typical industrial lines generally occurs during reheating after wiping, thus out of the zinc bath. Results of laboratory experiments, where an annealing step is performed after the zinc bath as in industrial lines, are also discussed in this section [28,48,54,76,77]. Nonetheless, the reported effects are expected to be unchanged. Kinetic data obtained through both types of experiments will be shown below (Table 7 and Table 8).

I.3.2.2.2. Effect of the steel

The kinetics of the inhibition layer breakdown can also be significantly affected by the grain size and the chemical composition of the steel substrate.

I.3.2.2.2.1. Effect of the steel grain size

Based on the mechanism he proposed for the inhibition layer breakdown (section I.3.2.1.2.3), Hisamatsu [25] suggested that a steel with finer grain size is more reactive, since more grain boundaries are available for the reaction with zinc. Consequently, the outbursts efficiency to peel the inhibition layer off is higher because they will form closer to each other than in the case of a coarser grain size substrate. Since then, different researchers [24,70,76] have been interested in the effect of the substrate grain size on the kinetics of the inhibition layer breakdown. The parameters measured are the incubation time for outburst formation [24] and the amount of iron in the coating [76].

Incubation time

Jordan and Marder [24] performed two different annealing treatments on the same steel substrate in order to develop two different grain sizes (namely 15 and 85 µm). These samples were then galvanized in a zinc bath containing 0.20 wt.% Al, allowing the authors to study the effect of the substrate grain size on Fe-Zn reactivity. The outburst formation was significantly delayed in the case of the substrate with larger grain size. Figure 29 gives the incubation time for outburst formation as a function of substrate grain size during galvanizing. As can be seen, whereas the outburst formation was observed in the 15 µm grain size steel after 10 s of immersion time, it required 1200 s to nucleate just a few outbursts in the 85 µm grain size steel. These results reinforce the theory that the inhibition layer breakdown through outburst formation takes place first at the steel grain boundaries. The remaining point in Figure 29 corresponds to a 10000 µm grain size steel substrate used by the authors in a parallel study. It should be noted that this last substrate differs in chemical composition from the other (0.015 to 0.032 wt.% C compared to 0.005 wt.% C) and, as it will be shown later, any direct comparison of the two substrates should take this difference in chemistry into account.

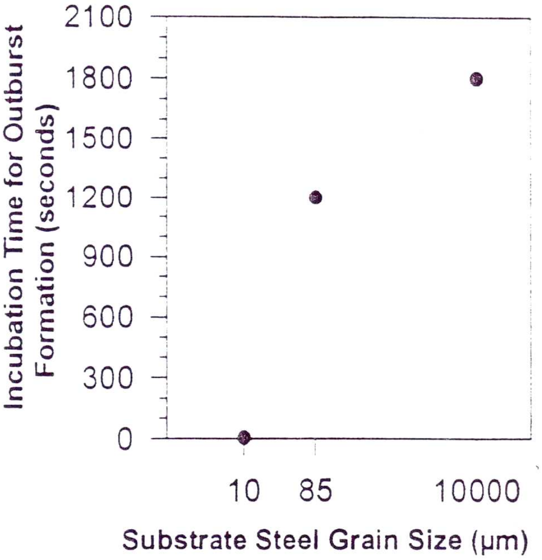

Figure 29: Incubation time for outburst formation as a function of the steel grain size during galvanizing in a zinc bath containing 0.20 wt.% Al (Jordan and Marder [24]).

As seen before, Guttmann [23] thought that short-circuits for zinc diffusion, present in the inhibition layer, are aligned with the steel grain boundaries (section I.3.2.1.2.3). In agreement with this theory, Jordan and Marder [24] explained that many diffusion paths for zinc were available in the $Fe_2Al_5Zn_x$ inhibition layer formed on the 15 µm grain size steel, resulting in much more localized zinc attack and outburst formation on this substrate, compared to the 85 and 10000 µm grain size steels. However, this assumption can perfectly explain the higher efficiency to completely peel the inhibition layer off when the steel grain size is finer but does not explain why the incubation time for outburst appearance was different. There is no reason to think that the zinc supersaturation at the steel grain boundaries necessary for outburst formation is achieved at different incubation times depending on the substrate grain size since direct short diffusion paths from the liquid bulk to the steel grain boundaries exist and the amount of zinc in the liquid is unlimited.

Mataigne [30] suggested that zinc diffusion through the inhibition layer is uniform and is followed by zinc diffusion along the steel / inhibition layer interface towards the steel grain boundaries (section I.3.2.1.2.3). If this assumption is considered now, the availability in zinc at the steel grain boundaries is expected to depend on zinc diffusion distances and rates. With a finer grain size substrate, the grain boundary length per unit area is higher and, consequently, the zinc atoms are distributed among a larger number of outburst nucleation sites. On the other hand, the average distance covered by the zinc atoms to reach a nucleation site is reduced. The incubation time to achieve the critical zinc supersaturation for outburst formation would therefore depend on the relative weight of these two opposite effects.

Another explanation could be that the effect of the substrate grain size on the kinetics of the inhibition layer breakdown for commercial galvanized steels is closely related to its chemical composition. As it will be seen in section I.3.2.2.2.2, segregation of some chemical elements at the steel grain boundaries can reduce their reactivity with respect to the inhibition layer breakdown by limiting the diffusion of zinc to these sites. It could be thought that, as a finer grain size provides a higher grain boundary length per unit area, the concentration of the segregating elements in these nucleation sites would be less important so that the critical zinc supersaturation could be reached earlier. This assumption can totally explain the results obtained by Jordan and Marder [24] that incubation time for outburst formation is reduced with finer grain sizes (segregation of different elements, especially carbon, cannot be neglected in the steel used by these authors, Table 7).

Amount of iron in the coating

Toki *et al*. [76] investigated in a global manner the effect of the substrate grain size on the kinetics of the Fe-Zn alloying reactions. To study this effect, the authors performed different annealing treatments in order to obtain different grain sizes on two steels with different carbon and titanium contents (0.004 wt.% C and 0.057 wt.% Ti in steel #1 compared to 0.037 wt.% C and no titanium in steel #2). The samples obtained were then galvanized in a zinc bath containing 0.12 wt.% Al for 10 s of immersion time. Figure 30 shows the amount of iron in the coating (which is related to the kinetics of the Fe-Zn alloying reactions), as a function of the *grain size number* G, which is defined by the ASTM International as follows:

$$N_{AE} = 2^{G-1} \tag{I.12}$$

where N_{AE} is the number of grains per square inch at 100 X magnification.

As can be observed in Figure 30, in the case of steel #2, the amount of iron in the coating was approximately constant. In the case of steel #1, the amount of iron is decreased, reaching the amount of iron of steel #2, when the grain size number is decreased, i.e., when the substrate grain size is increased. As will be seen in section I.3.2.2.2.2, titanium in the steel decreases the segregation of carbon at the steel grain boundaries. It could reasonably be assumed that the segregation of carbon at these locations in the case of steel #2 is so important that no effect of the steel grain size is observed. However, in the case of steel #1, segregation at grain boundaries is much less important and the effect of the substrate grain size on the kinetics of the Fe-Zn alloying reactions is evident.

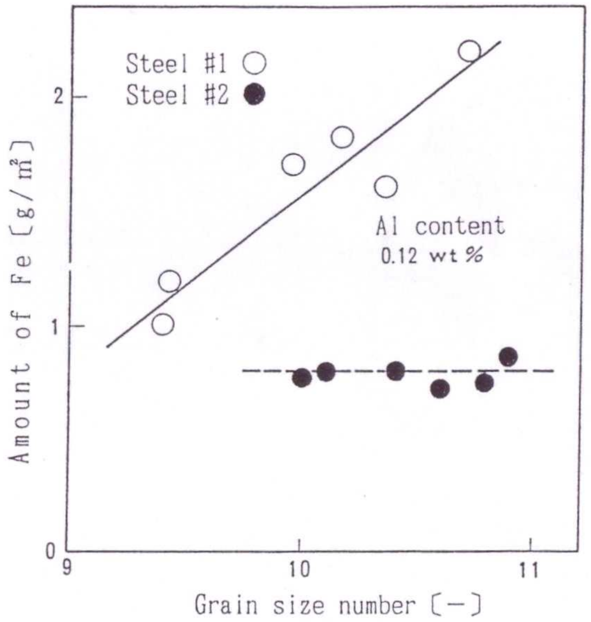

Figure 30: Effect of the steel grain size on the amount of iron in the coating (Toki *et al*. [76]).

It can be summarized that the effect of the substrate grain size on the kinetics of Fe-Zn reactions, and more particularly on the incubation time for outburst appearance, is closely linked to the segregation of alloying elements to the steel grain boundaries. Although the samples from Jordan and Marder [24] were not very concentrated in segregating elements, studies on pure iron samples with different grain sizes should be analysed in order to completely decorrelate both effects and achieve a better understanding of the intrinsic effect of the steel grain size on the kinetics of outburst formation.

I.3.2.2.2.2. Effect of the steel chemical composition

As stated here above, experimental evidence indicates that the chemical composition of the steel substrate also plays an important role on the kinetics of the inhibition layer breakdown. The mechanisms through which some chemical elements such as carbon, nitrogen, sulphur or phosphorous delay the inhibition layer breakdown and others such as titanium or niobium accelerate it will be discussed in the next paragraphs.

Effect of carbon and nitrogen

Various researchers have submitted that carbon [48,76] and nitrogen [25] in the steel slow the kinetics of the inhibition layer breakdown. Toki *et al*. [76] have provided experimental evidence of the inhibiting effect of carbon (steel #2, Figure 30). This inhibiting effect is attributed to the segregation of solute carbon at the steel grain boundaries during recrystallization annealing, which delays the outburst formation.

As stated above (section I.3.2.1.2.2), Nishimoto *et al*. [48] have proposed that the Fe-Zn outburst formation is due to an aluminium depletion at the solid / liquid interface as a result of the nucleation and growth of the inhibition layer. They postulated that the clean steel grain boundaries are more active than the substrate grain interior. Therefore, the aluminium content in the liquid would decrease more rapidly in the vicinity of the steel grain boundaries than on the substrate grain interior. Segregation of carbon at the steel grain boundaries reduces the higher decrease of aluminium content in the liquid at the emergence of grain boundaries, which delays the inhibition layer breakdown at these places. A schematic illustration of this mechanism is depicted in Figure 31.

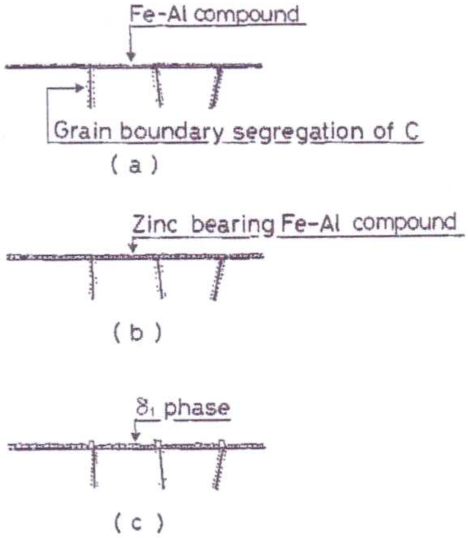

Figure 31: Schematic illustration showing a decrease in the outburst formation due to the segregation of carbon at ferrite grain boundaries (Nishimoto *et al*. [48]).

It has been already commented that the above mechanism from Nishimoto *et al*. [48] to explain the inhibition layer breakdown is less pertinent than the mechanism of outburst formation via the diffusion of zinc towards the steel grain boundaries (section I.3.2.1.2.3). As reported by other authors [25,76], the segregation of solute carbon or nitrogen at the steel grain boundaries more likely delays the inhibition layer breakdown by hindering the diffusion of zinc to these locations.

Effect of phosphorous

Several researchers [23,25,30,31,33,48,54,76] have reported that the higher the amount of phosphorous in the steel substrate is, the slower the kinetics of the inhibition layer breakdown is. Experimental evidence of the effect of phosphorous is shown in Figure 32, which illustrates the different Fe-Zn alloying degree in steel samples with different phosphorous contents subjected to the same process (recrystallization annealing at 800 °C, galvanizing in a zinc bath containing 0.12 wt.% Al at 460 °C for 10 s and galvannealing at 500 °C for a given period of time not specified by the authors). Indeed, in the top left-hand side micrograph of Figure 32, corresponding to the steel with the lowest phosphorous content (0.01 wt.%), the galvannealing reactions are well advanced and almost all the liquid zinc has been consumed. The coating is mainly composed of Fe-Zn phases. However, in the top right-hand micrograph of Figure 32, corresponding to the steel with the highest phosphorous content (0.069 wt.%), the galvannealing reactions are not advanced at all and, consequently, most of the zinc is still available. These micrographs clearly show that the galvannealing kinetics is reduced as the phosphorous content in the steel is increased. The just reported effect is associated with a delay in the inhibition layer breakdown.

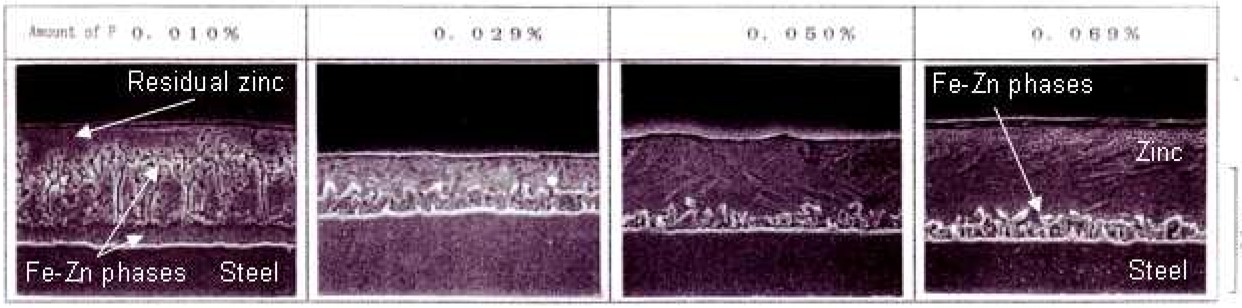

Figure 32: Cross section micrographs illustrating the effect of the phosphorous content in the steel (in wt.%) on the galvannealing kinetics (Toki *et al*. [76]).

Several mechanisms have been proposed to explain the effect of phosphorous.

Nishimoto *et al*. [48] reported the tendency of phosphorous to segregate at the steel grain boundaries, similarly to carbon, inhibiting the formation of outburst structures by lowering the reactivity at these locations.

Toki *et al*. [76] attributed to phosphorous a different inhibiting effect. Phosphorous precipitates as FeTiP during recrystallization annealing and consequently consumes titanium. As will be detailed later, solute titanium in steel decreases the segregation of carbon at the substrate grain boundaries by the formation of TiC precipitates. Phosphorous would therefore have an indirect influence on the kinetics of the inhibition layer breakdown by favouring the segregation of carbon at the steel grain boundaries. In addition, the authors observed that the precipitates of FeTiP can form at both grain interior and grain boundaries, which is also expected to hamper the diffusion of zinc towards the steel grain boundaries.

Guttmann [23] has proposed another mechanism to explain the inhibiting effect of phosphorous. He submitted that it is very likely that phosphorous is insoluble in the inhibition layer and, consequently, it will be rejected to the liquid zinc as a result of steel dissolution (section I.3.1.3.2), leading to its segregation at the grain boundaries of the inhibition layer when it is formed. This presence of phosphorus atoms inhibits the intergranular diffusion of zinc through this layer. This would explain the delaying effect of phosphorous on the inhibition layer breakdown.

Finally, Leprêtre [33] reported two possible delaying mechanisms depending on the amount of phosphorous in the steel: 1) with intermediate phosphorous contents (below 40×10^{-3} wt.%), the segregation of phosphorous at the steel grain boundaries delays the inhibition layer breakdown by hindering the diffusion of zinc to these locations, and 2) with higher phosphorous contents (above 40×10^{-3} wt.%), the thermodynamic equilibrium along the steel / δ interface can be kept, even after zinc enrichment induced by diffusion, and the Γ phase cannot nucleate anymore. In order to verify the effect of high phosphorous content, Fe-P alloys with different phosphorous contents were galvanized in pure zinc baths. In this case, the development of the coating occurs through successive nucleation of the stable Fe-Zn compounds in a decreasing zinc content order and not through outburst formation. Leprêtre observed that for contents lower than 40×10^{-3} wt.% P, the Γ phase was formed at the steel / δ interface, while for contents higher than 40×10^{-3} wt.% P, the Γ phase did not nucleate as if thermodynamic equilibrium was established along the steel / δ interface. Galvannealing on such steel grades proceeds by the growth of the δ layer, without any inhibition breakdown. Kinetics becomes very slow and governed by the diffusion of iron through the δ phase. The above mechanisms are totally consistent with the experimental results provided by Toki *et al*. [76] (Figure 32).

Effect of titanium and niobium

It is well known that titanium in the steel accelerates the kinetics of the inhibition layer breakdown [23,25,31,48,76,78]. This effect is illustrated by the micrographs provided by Hisamatsu [25] for Al-killed [9], Ti-added and P-added steels, galvanized in a zinc bath containing 0.16 wt.% Al at 450 ℃ for 15 s. As can be observed in Figure 33, while in the Al-killed and P-added steels the inhibition layer remains intact, in the Ti-added steel the outburst formation is already noticeable (see arrows).

Figure 33: Cross section micrographs showing the effects of the steel chemical composition on the kinetics of the inhibition layer breakdown during galvanizing in a zinc bath containing 0.16 wt.% Al at 450 ℃ for 15 s (Hisamatsu [25]).

The mechanism generally proposed to account for the influence of titanium is the following [23,25,31,48,76]: solute titanium in the steel can precipitate with different chemical elements (carbon, nitrogen, sulphur, phosphorous) capable to segregate at the steel grain boundaries during recrystallization annealing. It could therefore be assumed that the higher the titanium content in the steel is, the cleaner the steel grain boundaries are and the faster the inhibition layer breakdown will occur. In addition to this indirect effect of titanium, Abe and Kanbara [78] reported an intrinsic effect of solute titanium, which would accelerate the kinetics of the inhibition layer breakdown.

The pertinent parameter for the reactivity of a given steel is therefore the excess solute titanium, $w^{**}_{Ti_{excess}}$ (wt.%), rather than the total titanium content in the steel $w_{Ti_{total}}$ (wt.%). Toki *et al*. [76] proposed the following equation for the calculation of this parameter:

$$w^{**}_{Ti_{excess}} = w_{Ti_{total}} - \frac{48}{12} w_C - \frac{48}{14} w_N - \frac{48}{32} w_S - \frac{48}{31} w_P \tag{I.13}$$

where w_C, w_N, w_S and w_P are the weight fraction of carbon, nitrogen, sulphur and phosphorus present in the steel. The excess solute titanium, $w^{**}_{Ti_{excess}}$, corresponds to the remaining solute titanium when all the amounts of carbon, nitrogen, sulphur and phosphorous in the steel were stabilized as TiC, TiN, TiS and FeTiP respectively. This parameter is not a precise estimation of the titanium content in solution in the steel (e.g., it could be negative for a given steel composition) but it is taken by the authors as a measure of the cleanliness of the steel grain boundaries and, therefore, of the reactivity of the steel with respect to the inhibition layer breakdown. The calculation of the excess solute titanium will be discussed in detail in chapter III.

Similar effect as titanium is also attributed to niobium. However, Ti IF steels are more reactive than Nb-Ti IF steels. Guttmann *et al.* [31] reported that it is likely that the affinity of phosphorous for niobium is much smaller than for titanium. While precipitates of FeTiP are usually observed, no niobium phosphides are observed in the case of Nb-Ti IF steels. In addition, titanium can make carbon precipitate more easily than niobium: TiC precipitates are more stable (lower activation energy) than NbC precipitates.

---

[9] The term *killed* indicates that the steel has been sufficiently deoxidized by a deoxidizing agent to quiet the molten metal when poured into the ingot mold. In the case of an Al-killed steel, aluminium is used as deoxidizing agent.

I.3.2.2.3. Experimental data in the literature

Once the main factors influencing the kinetics of the inhibition layer breakdown have been presented, it is important to highlight that very few studies [24,26,28,33,54,70] providing specific data of the kinetics of the inhibition layer breakdown have been found.

The experimental conditions performed in each of these studies (steel substrate chemical composition and grain size, galvanizing and galvannealing conditions) are shown below. Two main families of laboratory experiments were performed to study the kinetics of the inhibition layer breakdown: 1) long immersion times in galvanizing baths [24,26,33,70] (Table 7), and 2) galvannealing treatments after galvanizing as in the industrial process [28,54] (Table 8).

Concerning the long immersion time experiments [24,26,33,70] (Table 7), the experimental conditions vary considerably from one study to another and many effects are involved. Some key data are missing to interpret the results (the bath temperature in the case of Jordan and Marder [24,70] and the steel grain size and its nitrogen content in the case of Saito *et al*. [26]). In addition, the times $t_{outburst}$ required for the inhibition layer breakdown appear to be inconsistent with each other in many cases. Thus, for example, the difference between the time provided by Leprêtre [33] in the case of the zinc bath containing 0.18 wt.% Al (1200 s) and the one given by Jordan and Marder [24,70] in the case of the 15 µm grain size steel (10 s) cannot be explained. Indeed, under the assumption that the bath temperature in the case of the experiments carried out by Jordan and Marder [24,70] is typical of galvanizing operations, the main difference between these two experiments is the excess solute titanium $w^{**}_{Ti_{excess}}$, that would favour the inhibition layer breakdown in the experiments performed by Leprêtre [33] (higher value).

Table 7: Experimental data obtained for long immersion time experiments ($t_{outburst}$ corresponds to the time required to form the first outbursts on the steel samples in the zinc bath).

Authors [Ref.]		Leprêtre [33]		Jordan and Marder [24,70]		Saito *et al*. [26]	
Steel	Name	Ti IF		Low C		Ti-added	
	P (10^{-3} wt.%)	10		2		13	
	Ti (10^{-3} wt.%)	53		8		82	
	Nb (10^{-3} wt.%)			<5			
	Al (10^{-3} wt.%)	36		38		21	
	B (10^{-3} wt.%)			<0.3			
	Ni (10^{-3} wt.%)	22					
	Cu (10^{-3} wt.%)	6					
	Mn (10^{-3} wt.%)	125		258		130	
	Si (10^{-3} wt.%)	8		3		14	
	S (10^{-3} wt.%)	6		4		10	
	N (10^{-3} wt.%)	4		1.2		*unknown*	
	C (10^{-3} wt.%)	2		5		2	
	Cr (10^{-3} wt.%)	18					
	$w^{**}_{Ti_{excess}}$ **(10^{-3} wt.%) [76]**	**6.8**	**6.8**	**-25.2**	**-25.2**	***unknown***	***unknown***
	grain size (µm)	**20**	**20**	**15**	**85**	***unknown***	***unknown***
Galvanizing	w_{Al} **(wt.%)**	**0.18**	**0.13**	**0.20**	**0.20**	**0.16**	**0.18**
	T_{bath} **(℃)**	**460**	**460**	***unknown***	***unknown***	**450**	**450**
	$t_{outburst}$ **(s)**	**1200**	**10**	**10**	**1200**	**15**	**60**

Kinetic data for the experiments with an annealing step performed after immersion in the zinc bath and wiping [28,54] are presented in Table 8. As can be seen, there is no way to compare the experimental results provided by Dionne *et al*. [54] and McDevitt and Meshii [28] (see comments in Table 8), as too many key data are not specified in their publications (steel grain size, immersion time and eventually bath temperature in the case of Dionne *et al*. [54] and steel grain size and its nitrogen and sulphur contents in the case of McDevitt and Meshii [28]).

Table 8: Experimental data obtained for experiments with an annealing step performed after immersion in the liquid metal and wiping (outburst formation occurs out of the zinc bath).

Authors [Ref.]		Dionne *et al*. [54]			McDevitt and Meshii [28]	
Steel	Name	Steel A	Steel B	Steel C	Ti-Nb IF	P-Added Ti IF
	P (10^{-3} wt.%)	12	9	59	15	46
	Ti (10^{-3} wt.%)	68	35	36	20	62
	Nb (10^{-3} wt.%)	0	32	39	15	
	Al (10^{-3} wt.%)	37	48	37		
	B (10^{-3} wt.%)		<0.2	0.7		
	Ni (10^{-3} wt.%)	26	11	14		
	Cu (10^{-3} wt.%)	27	14	19		
	Mn (10^{-3} wt.%)	203	180	220	170	340
	Si (10^{-3} wt.%)	4	6	8		
	S (10^{-3} wt.%)	6	6	9	*unknown*	*unknown*
	N (10^{-3} wt.%)	2.6	2.9	4.2	*unknown*	*unknown*
	C (10^{-3} wt.%)	3	3.3	3.2	3	3
	Cr (10^{-3} wt.%)	27	20	20		
	$w_{Ti_{excess}}^{**}$ (10^{-3} wt.%) [76]	**19.5**	**-11.1**	**-96.1**	***unknown***	***unknown***
	grain size (µm)	***unknown***	***unknown***	***unknown***	***unknown***	***unknown***
Galvanizing	**w_{Al} (wt.%)**	**0.135**	**0.133**	**0.133**	**0.14**	**0.14**
	T_{bath} (℃)	**470**	***unknown***	***unknown***	**460**	**460**
	***t* (s)**	**Industrially galvanized samples**			**3**	**3**
Galvannealing	***T* (℃)**	**475-480**	**475-480**	**475-480**	**500**	**500**
	***t* (s)**	**1.6**	**2.3**	**2**	***unknown***	***unknown***
Comments		Outbursts are already present		No important attack of the inhibition layer is observed	Inhibition breakdown during heating to 500℃	Slower kinetics but not substantially different from the Ti-Nb IF steel

I.3.2.3. Recapitulation

It can be summarized from this section that:

- The inhibition layer breakdown in the case of Ti IF steels very likely occurs through outburst formation at the steel grain boundaries, due to the diffusion of zinc through the layer itself towards these locations and subsequent nucleation of a Fe-Zn phase.

- Kinetics of this reaction is obviously affected by temperature but also by different parameters such as the bath aluminium content, the steel grain size and its chemical composition. Carbon, nitrogen, sulphur and phosphorous in the steel delay the inhibition layer breakdown and titanium and niobium accelerate it. Although numerous qualitative results, proving the effect of these parameters, exist in the literature, very few kinetic data have been published. In addition, these data are often inconsistent with each other.

I.3.3. The Fe-Zn alloying reactions

As the present work does not focus on the Fe-Zn alloying reactions taking place after the inhibition layer breakdown, only a succinct summary of the main features of these reactions is presented here, with the purpose that the reader can understand the complete development of a galvannealed coating. For those readers especially interested in these reactions, a detailed critical literature review is available in Appendix C.

I.3.3.1. Proposed mechanisms for the Fe-Zn alloying reactions

The Fe-Zn alloying reactions occur in two steps: 1) The outbursts first develop and grow by consuming the liquid zinc; 2) the iron enrichment of the solid coating then occurs. As already shown in Figure 9, the final microstructure of the coating consists in a layered structure composed of different Fe-Zn phase layers.

I.3.3.1.1. Consumption of the liquid phase. Growth of Fe-Zn phases

When the inhibition layer is broken up by the outburst formation, new Fe-Zn phases nucleate very rapidly on the top of the outbursts, which grow both laterally, towards the adjoining outbursts, and in thickness, by consuming the liquid phase.

Although the precise reaction mechanisms accounting for the consumption of the liquid zinc are not accurately known yet, some few authors have provided assumptions about these mechanisms which are consistent with the experimental results found in the literature.

As advanced in section I.3.2.1.2.3, a group of authors [27,30,33] has reported that the inhibition layer is broken off by the growth of the Γ phase in the case of GA baths. This phase can reach thermodynamic equilibrium with the steel but not with the liquid zinc. In order to keep the liquid phase at equilibrium, the system requires at least the nucleation of the δ phase on the top of the outbursts (paths V2, V2bis, 3, V3 and V3bis in Figure 28).

Mataigne [30] reported that when the Γ phase gets in contact with the liquid zinc after the inhibition layer breakdown, it gets dissolved and a very intense flux of iron is then established. This sudden increase in the iron concentration is consumed by the formation of Fe-Zn compounds in the liquid zinc side. At this stage, two different regimes for outburst development can be differentiated depending on the galvannealing temperature and on the peritectic reaction temperature involving the ζ phase (Figure 16):

- If the galvannealing temperature is higher than the peritectic reaction temperature, the coating evolves under a solid state *diffusion regime*. The increase in the iron concentration at the Γ phase / liquid zinc interface due to the dissolution of the Γ phase leads to the nucleation of the δ phase. At this moment, thermodynamic equilibrium is reached along all the interfaces. This implies that further development of the coating is controlled by solid state interdiffusion of iron and zinc.

- If the galvannealing temperature is lower than the peritectic reaction temperature, the coating development evolves under a *dissolution regime*. As in the previous case, the increase in the iron concentration at the Γ phase / liquid zinc interface due to the dissolution of the Γ phase should lead to the nucleation of the δ phase. However, unlike the previous case, the δ phase cannot reach thermodynamic equilibrium along its interface with liquid zinc. Leprêtre [33] indicated that, at this moment, the δ phase gets dissolved in the liquid, leading to the simultaneous nucleation of a δ phase with different composition and the ζ phase.

The mechanisms of liquid zinc consumption presented here above can be more easily understood with the help of diffusion paths in the ternary Al-Fe-Zn phase diagram [30,33]. This analysis is available in Appendix C.

I.3.3.1.2. Iron enrichment of the coating. Fe-Zn phase distribution

When the liquid zinc has been fully consumed, the coating is already composed of a sequence of stratified Fe-Zn phase layers. The different interfaces then evolve by reactive solid state diffusion of iron from the steel matrix towards the coating. The Γ phase will grow to the detriment of the δ phase and the δ phase will grow to the detriment of the ζ phase, if this latter phase has nucleated within the liquid phase during the outburst development (dissolution regime when the galvannealing temperature is less than the peritectic reaction temperature). Once the ζ phase has completely disappeared, if it existed, with further iron enrichment of the coating, the Γ phase rapidly grows at the expense of the δ phase.

It should be noted that the counter-diffusion of zinc is neglected in the just proposed reaction mechanisms. However, this assumption may be reasonably accepted as the zinc diffusion flux in ferrite is expected to be very low at typical galvannealing temperatures (too low).

I.3.3.2. The Fe-Zn alloying reaction kinetics. Proposed models

Two different types of kinetic models have been identified in the literature: models describing the evolution of the iron content in the coating [79,80] and models describing the evolution of the Fe-Zn phase distribution within the coating [81,82]. Most of the few models found in the literature have been developed in a global manner, without differentiating each of the phenomena involved in the galvannealing process. It would be preferable to model the kinetics of each of these phenomena separately, in order to obtain characteristic parameters with a strict physical sense which can be perfectly extrapolated to other galvannealing conditions.

I.3.4. Conclusions

Key information on the just described galvannealing reactions is summarized here below:

The inhibition layer formation

Very controversial results have been found concerning the inhibition layer formed in GA baths. It remains not clear whether this inhibition layer is constituted of metastable $Fe_2Al_5Zn_x$, stable δ or both (two-layer structure with δ on top of $Fe_2Al_5Zn_x$). In addition, some authors have reported as well the nucleation of metastable epitaxial ζ crystals simultaneously to the one of the inhibition layer, especially in the case of GA baths with low aluminium contents. However, it remains doubtful whether these structures exert an inhibitory action or not.

Concerning the nature of the inhibition layer formed in zinc baths with an aluminium content corresponding to the knee point β, very few studies have been found in literature. Nevertheless, they agree with the fact that the inhibition layer can be described as a two-layer structure composed of $Fe_2Al_5Zn_x$ (lower layer) and δ (upper layer).

Regardless the nature of the intermetallic(s) compound(s) formed on the steel surface, most of the researchers agree with the mechanisms of formation of the inhibition layer. Those reaction mechanisms can be divided into the following steps after the steel sheet enters the galvanizing bath: wetting of the substrate by liquid zinc, iron supersaturation at the interface induced by the dissolution of the former by the latter, nucleation and lateral growth of the crystals of the intermetallic compound until forming a covering layer and thickening of this layer.

Two different kinetic regimes can be differentiated during the inhibition layer formation. The nucleation and lateral growth is characterized by its high reaction rate, assumed to be proportional to the reaction time (linear kinetics). The thickening of the inhibition layer is characterized by slower kinetics, assumed to be proportional to the square root of the reaction time (parabolic kinetics) as controlled by the solid state diffusion of iron within the inhibition layer itself.

In a global manner, it has also been observed that the inhibition layer growth is favoured by higher bath temperatures, longer immersion times and higher bath aluminium contents.

The inhibition layer breakdown

The inhibition layer breakdown very likely occurs through outburst formation at the steel grain boundaries due to the diffusion of zinc through the layer itself towards these locations and subsequent nucleation of a Fe-Zn phase.

The kinetics of the inhibition layer breakdown is affected by the bath conditions but also by some steel features. It is generally admitted that low bath aluminium contents and high temperatures accelerate the inhibition layer breakdown. Experimental results have shown that the time necessary for the inhibition layer breakdown increases with increased steel grain sizes. The steel chemical composition also plays an important role on the inhibition breakdown kinetics: it is well known that elements such as carbon, nitrogen, sulphur and phosphorous in the steel delay the inhibition layer breakdown and others as titanium and niobium accelerate it.

Although numerous qualitative results proving the effect of these parameters exist in the literature, very few kinetic data have been published. In addition, these data are often inconsistent with each other.

The Fe-Zn alloying reactions

The Fe-Zn alloying reactions occur in two steps: the liquid zinc consumption and the subsequent iron enrichment of the solid coating. During the liquid zinc consumption, the outbursts develop laterally, until joining each others, and in thickness. In the case of GA baths, the liquid zinc can be consumed through two different regimes depending on whether the galvannealing temperature is lower or higher than the peritectic reaction temperature involving the δ and ζ phases. When the galvannealing temperature is lower than this temperature, the liquid zinc consumption occurs under a dissolution regime characterized by the nucleation of both δ and ζ phases on the top of the outbursts. When the galvannealing temperature is higher than this temperature, the liquid zinc is consumed under a diffusion regime characterized by the growth of the δ phase without nucleation of the ζ phase. Once the liquid zinc has been consumed, the coating is composed of a sequence of Fe-Zn phase layers whose common interfaces evolve by solid state diffusion of iron within the coating.

The precise reaction mechanisms accounting for the Fe-Zn alloying reactions, especially concerning the consumption of the liquid phase, still remain quite unknown. Further investigation for a better understanding of the involved phenomena is highly required. In addition, no studies on the kinetics of each of the single Fe-Zn alloying reactions are available in literature.

I.4. Objectives of the present work

The main objective of this work is to better understand the formation of industrial galvannealed coatings, in order to ensure or improve their quality. The first key steps of the galvannealed reactions are the nucleation and growth of the inhibition layer in the galvanizing bath and the inhibition layer breakdown in the annealing treatment performed at the exit of the bath.

It has been seen before that the bath operating parameters influence the nature of the inhibition layer and consequently the kinetics accounting for its rupture. The remarkable influence of the steel substrate on the inhibition layer breakdown kinetics has also been reported. However, the experimental results presented in the literature are still subject to debate. As a result, a precise knowledge on the kinetics of these reactions is still needed to manage accurately the development of the coating during galvannealing and to obtain the targeted Fe-Zn phase distribution. The present work therefore focuses on the two first reactions involved in the development of a galvannealed coating: the inhibition layer formation and its rupture.

First of all, the nature of the inhibition layer formed on Ti IF steel surfaces in GA baths with different aluminium contents will be investigated in detail in terms of phase composition and structure (chapter II). A reaction mechanism accounting for the final microstructure of this inhibition layer will be proposed. Discussions about this mechanism will be tackled with the Al-Fe-Zn ternary phase diagram at 450℃ and assumptions to justify any deviation from thermodynamic equilibrium will be proposed.

The effect of the steel substrate and the bath aluminium content on the inhibition layer breakdown kinetics will then be quantified in the case of Ti IF steels (chapter III). Modelling of this reaction, taking into account these two effects, will be proposed as well.

CHAPTER II: THE INHIBITION LAYER FORMED IN GA BATHS

From an industrial point of view, a precise knowledge of the structure and composition of the inhibition layer is crucial to ensure or improve the quality of GA coatings for at least two reasons.

First of all, it has been seen in section 0 that, as the kinetics of the inhibition rupture is controlled by diffusion mechanisms in the inhibition layer, its nature is expected to play a direct and important role on the alloying degree and the homogeneity of the final coating: a discontinuous or heterogeneous inhibition layer, either in thickness or in composition within the planes parallel to the steel surface, may conduct to a heterogeneous final coating.

Secondly, the production of high-quality GA coatings demands an accurate bath management in order to keep the bath composition at the targeted values. As the galvanizing bath is saturated in iron, the main parameter to be controlled is the bath aluminium content, highly sensitive to the aluminium uptake by the inhibition layer (i.e., the aluminium flux consumed by the growth of the inhibition layer). Therefore, a fine knowledge of the nature of this layer would facilitate the management of industrial galvanizing baths.

The facts presented above highlight the need for investigating in detail the nature of the inhibition layer formed in GA baths, especially since this topic still remains today a subject of controversy as shown in section I.3.1.1.3. The aim of this work is therefore to provide new experimental results in order to gain a better understanding on the nature of the inhibition interface layer.

II.1. Experimental procedure

II.1.1. Materials

Two commercial Ti IF steel samples, A and B, galvanized in industrial baths with different aluminium contents (0.112 and 0.128 wt.% Al), have been selected for the present study. Industrial samples were chosen to identify possible differences in the nature of the inhibition layer formed in GA baths for different real industrial conditions.

The average chemical composition of steels A and B is presented in Table 9. The analysis was performed by means of Combustion and Infrared Detection for nitrogen (HORIBA EMGA-620W) and Spark-Optical Emission Spectrometry (Spark-OES, SPECTROLAB M10) for the other elements in ArcelorMittal laboratories. As can be observed, the compositions of both steels are very similar. The thicknesses of steels A and B are equal to 0.80 and 0.74 mm respectively.

Table 9: Average chemical composition (x 10^{-3} wt.%) of the commercial Ti IF steels studied.

Steel	C	Mn	P	S	N	Si	Cu	Ni	Cr	Sn	As	Nb	Mo	B	Ti	Al
A	1.6	103	11	6	3.4	9	13	17	14	<2	<2	<2	<2	<0.3	53	39
B	2.0	110.0	9.1	9.0	2.1	4.0	17.0	14.3	18.2	5.7	-	0.1	1.8	0.0	67.3	49.1

Full-hard specimens of both steels were sampled in order to evaluate and compare their surface state prior to galvanizing through surface profiling by means of a revamped profilometer from Taylor-Hobson. The surface three-dimensional (3D) cartographies depicted in Figure 34 indicate that the surface of steel A presents smaller patterns than the one of steel B. The roughness and waviness parameters R_a and W_a [10] given in Table 10 were calculated for both steels from five two-dimensional profiles (17 mm in length, spaced of 500 µm from each other). Unlike steel B, steel A has been submitted to a surface rectification step during cold rolling which has reduced its surface roughness and waviness. The influence of this difference in the surface roughness on the nature of the inhibition layer will be discussed in section II.3.1.3.

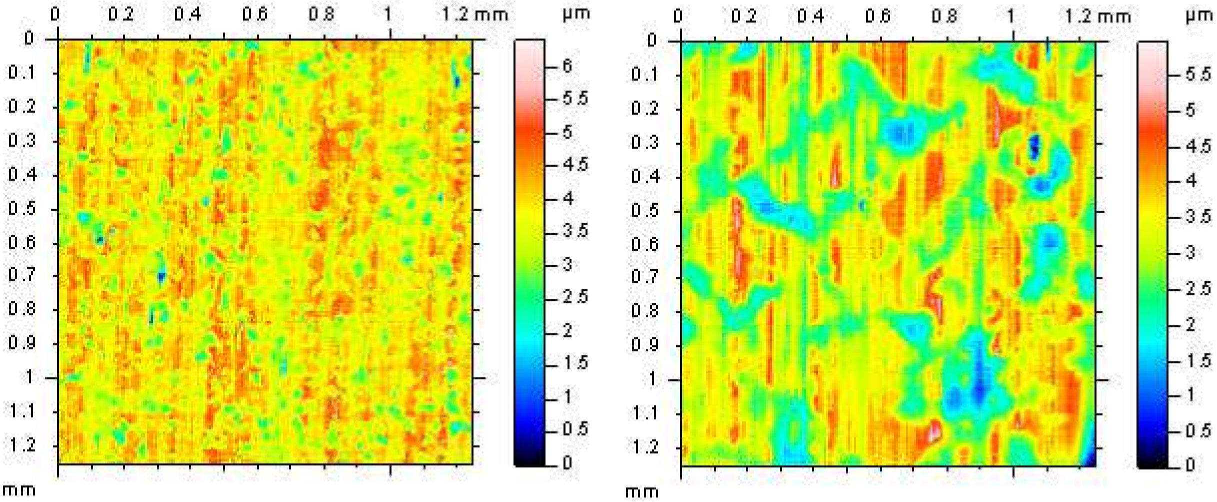

Figure 34: 3D cartographies of the surface of steels A (left) and B (right).

Table 10: Roughness and waviness parameters obtained from five 2D profiles of steels A and B (17 mm in length, spaced of 500 µm from each other).

Steel	R_a (µm) [a]	W_a (µm) [b]
A	0.38 ± 0.01	0.13 ± 0.02
B	0.54 ± 0.06	0.31 ± 0.05

[a] arithmetic mean deviation of the roughness profile obtained with a Gaussian filter of 2.5 mm;
[b] arithmetic mean deviation of the waviness profile obtained with a Gaussian filter of 0.8 mm.

The process data used to galvanize both steels are depicted in Table 11. The influence of the differences in the galvanizing conditions chosen, namely the bath aluminium content, the immersion time t_{im} and the bath temperature, will be discussed later in section II.3.1.2. In both cases, the galvannealing furnace was off-line in order to prevent Fe-Zn alloying reactions, so that the studied microstructures are supposed to be a representative result of the phenomena taking place in the GA bath.

Table 11: Process data used to galvanize both steels.

Steel	v (m/min) [a]	w_{Al} (wt.%) [b]	T_{bath} (°C) [c]	L_{im} (m) [d]	t_{im} (s) [e]	$e_{coating}$ (µm) [f]
A	120	0.112 ± 0.004	450 ± 2	2.7	1.4	5
B	130	0.128 ± 0.002	460 ± 2	4.0	1.9	9

[a] line speed; [b] bath aluminium content; [c] bath temperature; [d] immersion length; [e] $t_{im} = L_{im} / v$; [f] coating thickness.

---

[10] Parameter R_a is defined as the arithmetic mean of the absolute deviations of the roughness profile from the mean line. Parameter W_a is defined as the arithmetic mean of the absolute deviations of the waviness profile from the mean line.

II.1.2. Experimental techniques

II.1.2.1. Sample preparation techniques

Samples were first cleaned with ethanol to remove residual oil from former manipulations. They were then prepared through different techniques depending on the type of characterization they were going to be submitted to, namely surface (section II.1.2.1.1) or cross section characterization (section II.1.2.1.2).

II.1.2.1.1. Sample preparation techniques for surface characterization

II.1.2.1.1.1. Electrochemical dissolutions

Specimens for surface characterization were cut into 32 mm diameter discs and submitted to a controlled electrochemical dissolution protocol in order to remove zinc and Fe-Zn phases selectively. The electrochemical cell used for these dissolutions is schematized in Figure 35. It is composed of three electrodes: a standard calomel electrode (SCE) used as reference electrode, a platinum counter electrode used as cathode and the sample to be dissolved (working electrode) used as anode. All the electrodes were linked to a VMP3 multi-channel potentiostat from BioLogic Science Instruments. The electrolyte used is an aqueous pH 4 solution composed of 200 g/L NaCl (Fisher Chemical), 40 g/L $ZnSO_4•7H_2O$, 27 g/L CH_3COONa and 11 mL/L CH_3COOH (VWR BDH Prolabo).

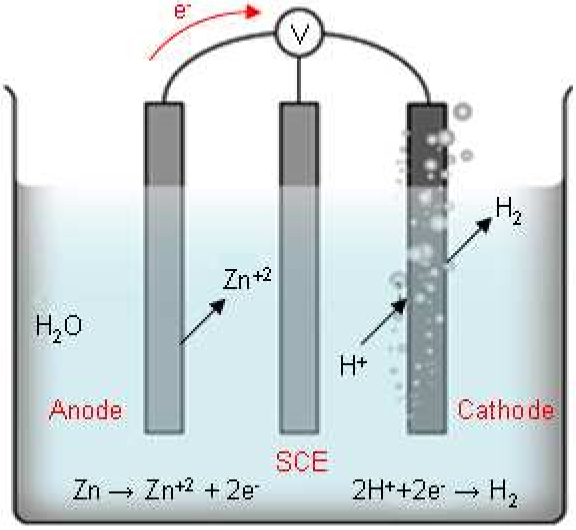

Figure 35: Schematic view of the experimental assembly used for electrochemical dissolutions.

The oxidation-reduction reactions involved during the dissolution process are the following[11]:

Oxidation reaction (anode): $Zn \rightarrow Zn^{+2} + 2e^-$

Reduction reaction (cathode): $2H^+ + 2e^- \rightarrow H_2$

The composition of the electrolyte was chosen to keep the pH and the Zn^{+2} concentration constant during dissolution, as both parameters may influence the dissolution potential of the sample surface with respect to SCE [83-86]. The couple CH_3COONa / CH_3COOH is used as a pH 4 buffer

---

[11] In addition to these reactions, the reduction of oxygen would also occur at very low current densities (20-30 μA/cm^2). However, for the much higher current densities recorded during dissolution, this reaction can be neglected.

[83-85]. The $ZnSO_4 \cdot 7H_2O$ compound allows the Zn^{+2} concentration of the electrolyte to be kept at a very high value almost constant during the dissolution process [85,86].

When a potential difference between the working electrode and the SCE (*E*) is imposed, all the phases present at the sample surface whose dissolution potential with respect to the SCE is lower will be dissolved. The electrochemical potentials to be imposed in order to achieve the selective removal of the different phases were determined with accurate electrochemical studies. They were found to be: -950 mV/SCE for zinc removal only, -800 mV/SCE for zinc and ζ rod crystals removal and -680 mV/SCE for zinc and all Fe-Zn phases removal. The last potential would keep $Fe_2Al_5Zn_x$ at the sample surface if present. These electrochemical studies are described in detail in section II.1.2.2 but also in section II.2 as they represent a means of characterization of the inhibition layer.

The current density *J* is measured as a function of time during dissolution at the chosen imposed potential. Controled dissolution is over when the current density falls to zero. At this moment, the sample is taken out of the electrolyte in order to avoid any further dissolution, which would occur naturally from this time on. A typical current density against time curve recorded during dissolution at -950 mV/SCE is depicted in Figure 36.

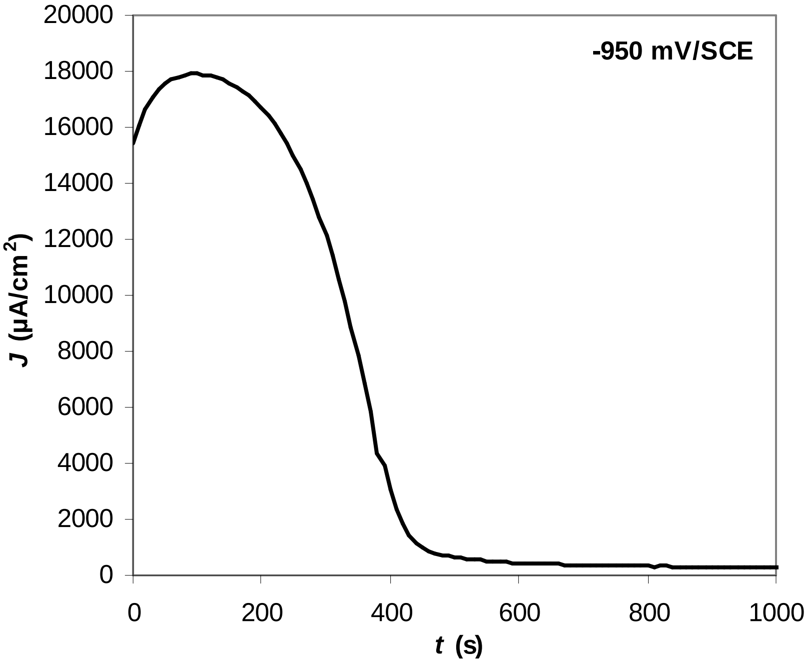

Figure 36: Current density against time during electrochemical dissolution at imposed potential of -950 mV/SCE for zinc removal only.

II.1.2.1.1.2. Thin films extraction technique

An extraction technique was then applied to the samples submitted to the electrochemical dissolution at -680 mV/SCE in order to obtain thin $Fe_2Al_5Zn_x$ films for analysis in the Transmission Electron Microscope (TEM). The dissolved surface of the samples was rinsed and cleaned with ethanol, submitted to the deposition of a 40 to 50 nm-thick carbon film by an Edwards E306A thermal evaporator coating device and dipped into a 10 vol.% aqueous solution of 65 wt.% HNO_3 (Merck). Prior to dipping, the carbon film was carefully scarified in order to make the HNO_3 solution penetrate between the steel surface and the intermetallic layer. The steel in contact with the acid solution was dissolved, causing the separation from the steel matrix of the intermetallic layer embedded into the carbon film. Floating carbon films were then rapidly collected at the surface of the solution, rinsed with ethanol and transferred onto copper grids for TEM observations. TEM bright field images of such carbon films containing the extracted intermetallic layer are available in Figure 37.

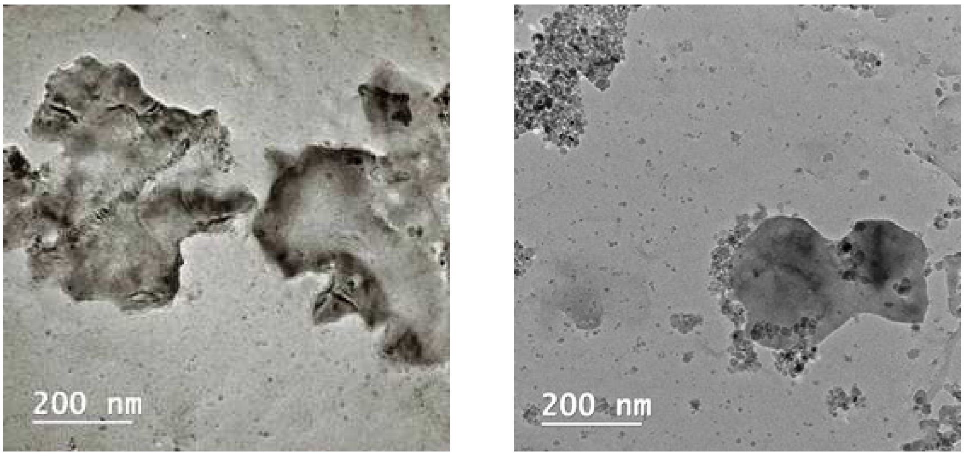

Figure 37: TEM bright field images of the carbon films containing the intermetallic compounds extracted from steels A (left) and B (right) after electrochemical dissolution at -680 mV/SCE.

II.1.2.1.2. Sample preparation techniques for cross section characterization

II.1.2.1.2.1. Cross Section Polishing (CSP) sample preparation

Cross section specimens for Scanning Electron Microscope (SEM) analysis were prepared by argon ion beam Cross Section Polishing (CSP) in a JEOL SM-09010 device. Prior to this operation, a mechanical polishing step was performed on one side of the galvanized steel samples in order to reduce the sample thickness to around 400 µm. Ion beam polishing from the steel matrix towards the coating was then accomplished at an accelerating voltage of 6 kV and an ion beam current around 150 µA during a processing time of 3 h. The result of this operation is shown in Figure 38.

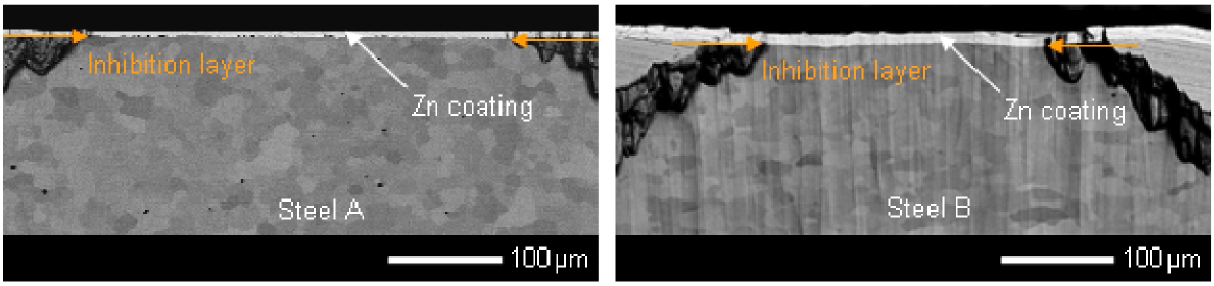

Figure 38: Low magnification SEM micrographs of the polished area of the CSP samples prepared from steels A (left) and B (right).

II.1.2.1.2.2. Mechanically polished sample preparation

In parallel, cross section samples for Electron BackScattered Diffraction (EBSD) analysis were prepared by means of an automatic polisher (Struers RotoPol-22 with RotoForce-4 head) with diamond slurries of decreasing diamond abrasive size at each polishing step until reaching 0.25 µm and subsequently submitted to a final polishing on the same device for 30 s using a colloidal silica suspension (OP-U suspension from Struers, 0.04 µm granularity). The force applied in each polishing step was of 30 N.

II.1.2.1.2.3. FIB thin foils preparation

Cross section thin foils for TEM analysis were prepared by Focused Ion Beam (FIB) technology, using a SMI 3050TB device from SII Nanotechnology Inc. In order to obtain high-quality foils, samples were previously submitted to an electrochemical dissolution at -950 mV/SCE in order to remove the zinc overlay. In addition, a very thin gold layer was deposited on the sample surface for conductivity reasons before it was entered in the FIB device. Once in the FIB device, a local platinum deposition was first conducted on the sample surface in order to protect the foil against the ion beam. The main and coarsest milling operation was conducted with a gallium ion beam. The foil was then extracted from the bulk material by means of a needle and then carbon-welded on the top of one of the four teeth of a comb-shaped copper grid. An argon ion beam was subsequently used for the final thinning as well as a cleaning source to remove possible gallium ion implantations within the foil. A schematic explanation of how the FIB device works and the foils are prepared is available in Appendix E. The final dimensions of the foils, depicted in Figure 39, are around 14 µm x 7 µm x 50 nm.

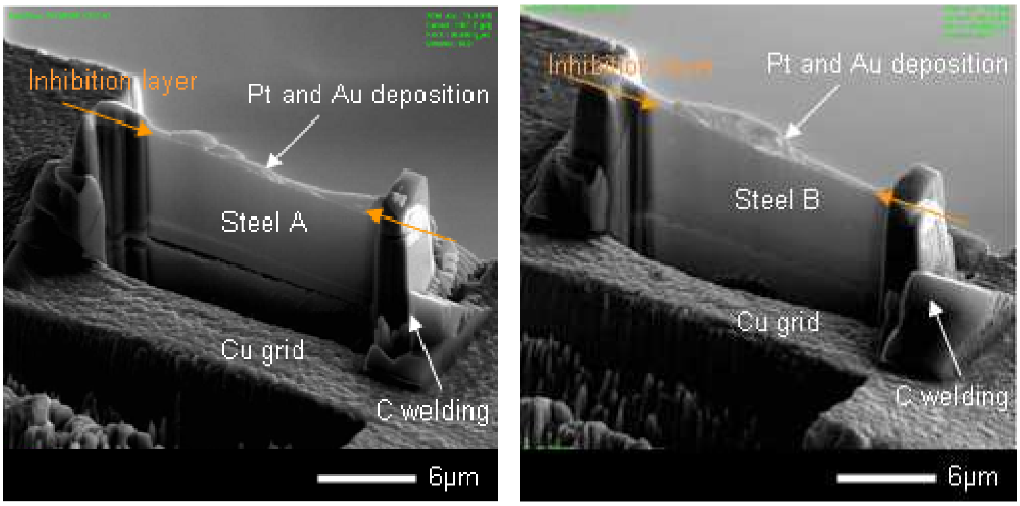

Figure 39: Low magnification SEM micrographs of the FIB foils prepared from steels A (left) and B (right).

II.1.2.2. Sample characterization techniques

At first, the general structure of the inhibition layer was characterized through a controlled selective electrochemical dissolution protocol coupled with Energy Dispersive Spectroscopy (EDS, Thermo Scientific) surface analysis in a SEM (LEO DSM 982) (section II.2.1). The electrochemical protocol was performed by means of the experimental assembly and the electrolyte described in section II.1.2.1.1.1. It consisted in two consecutive dissolution steps. First of all, most of the zinc coating was removed by applying a dissolution potential of -950 mV/SCE until the density current was reduced to 1000 µA/cm^2. The open-circuit potential (OCP) of the sample surface was then followed-up during the dissolution of the residual zinc, the inhibition layer and the steel surface. In order to limit possible external interferences, the electrochemical cell was systematically located into a Faraday cage. An example of the electrochemical curves obtained by means of this protocol is available in Figure 40. From the so-obtained potential against time electrochemical curves, the characteristic dissolution potentials of the phases constituting the inhibition layer were identified and samples at different dissolution stages were prepared by applying these key potentials and analysed by EDS surface analysis.

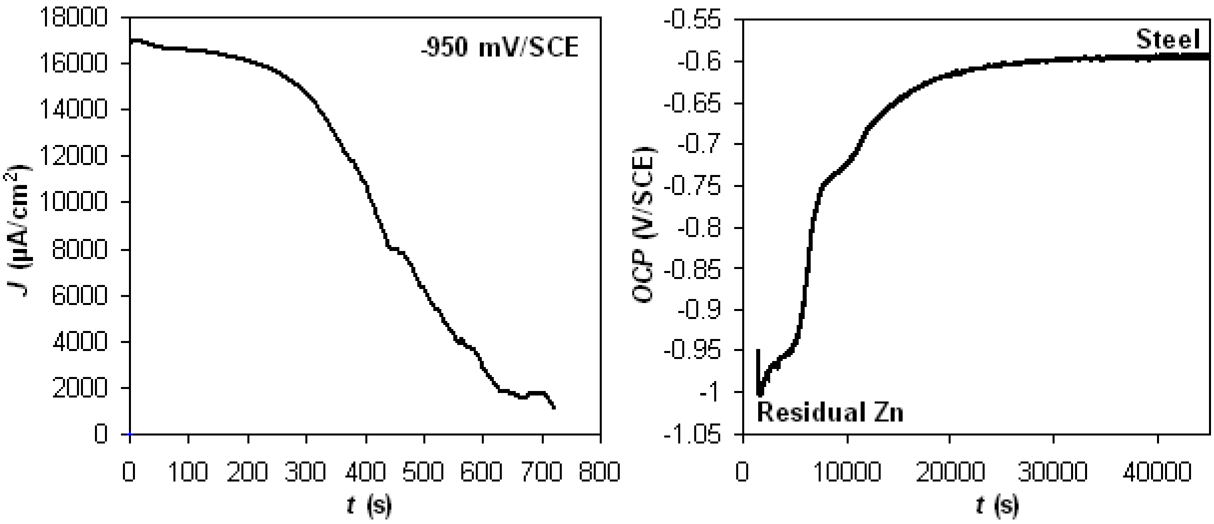

Figure 40: Current density against time curve obtained at imposed potential of -950 mV/SCE up to 1000 µA/cm^2 for removal of most of the zinc coating (left), followed by OCP against time curve until reaching bare steel surface (right).

In parallel, the CSP cross section samples were analysed by EDS (Bruker AXS XFlash 4010 SDD) in a SEM (JEOL JSM-7001F) with the same purpose of characterizing the general structure of the inhibition layer (section II.2.1).

In order to determine the nature of the phases present in the inhibition layer, the FIB thin foils and extracted films were analysed by EDS (Bruker AXS XFlash 5030T SDD) and Electron Diffraction in a TEM (JEOL JEM-2100F) at an accelerating voltage of 200 kV (sections II.2.2.1 and II.2.2.2). Possible epitaxial relationships with ferrite have also been investigated (section II.2.3.1).

The aluminium, iron and zinc concentration distribution within the different phase layers of the inhibition layer was then investigated through Secondary Ion Mass Spectrometry (Dynamic SIMS, CAMECA IMS 7f) (section II.2.3.2). The operating conditions were: cesium ion source (source voltage of +10 kV, sample voltage of +5 kV), primary current of 2.5 nA, analysis chamber pressure of $6x10^{-10}$ mbar, sputtered area of 500 x 500 µm^2, analysed field of 250 µm in diameter (only a smaller area located within the sputtered area is analysed in order to avoid edge effects), field diaphragm of 1800, contrast diaphragm of 150 and mass resolution of 400 (widely opened input, output and energy slots).

Interest was also given to the geometrical features of the inhibition layer (section II.2.3.3). Thus, the crystals size and surface homogeneity of the different layers were characterized through high resolution SEM micrographs obtained during surface analysis of the electrochemically dissolved samples. Their thicknesses were determined by means of high resolution SEM and TEM micrographs obtained during the analysis of the CSP and FIB cross section samples respectively. In addition, the surface coverage, in the case of discontinuous layers, was determined from the SEM micrographs of the CSP samples.

The aluminium uptake by the inhibition layer was then calculated from the estimated values of thickness and surface coverage and the experimentally determined aluminium contents for each phase layer (section II.2.3.4).

Finally, EBSD analysis was performed in SEM (JEOL JSM-7001F) on the mechanically polished and CSP cross section samples in order to obtain the steel surface grains orientation (section II.3.1.3). The first type of samples was specifically prepared for such analysis because the length of the interface between the steel and the inhibition layer was considerably longer in these samples than in the CSP samples. The EBSD camera was a Nordlvs model (Oxford Instruments). The acquisition software was HKL Fast acquisition 1.3 (Oxford Instruments) and the analysis software was Project Manager 5.10 (HKL Technology). The acquisition conditions were: voltage of 20 kV, working distance of 15 mm, tilted angle of 70 °and step of 0.2 µm.

II.2. Experimental results

II.2.1. General structure

The Open-Circuit Potential (OCP) against time electrochemical curves obtained on steel samples A and B are presented in the left-hand side of Figure 41. As can be seen, both curves start at around -1000 mV/SCE, the corrosion potential of zinc. Once the residual zinc has been removed, dissolution of the different phases constituting the inhibition layer occurs progressively. When the dissolution of the inhibition layer is over, the OCP of the sample surface stabilizes around -600 mV/SCE, the corrosion potential of the steel substrate.

The electrochemical curve obtained on sample B (blue curve) suggests that the inhibition layer is composed of two different phase layers as two different dissolution stages (arrows 1 and 2) can be easily differentiated between the residual zinc and the steel matrix. In the case of sample A (red curve), only the dissolution stage corresponding to the phase layer in direct contact with zinc can be identified (arrow 1').

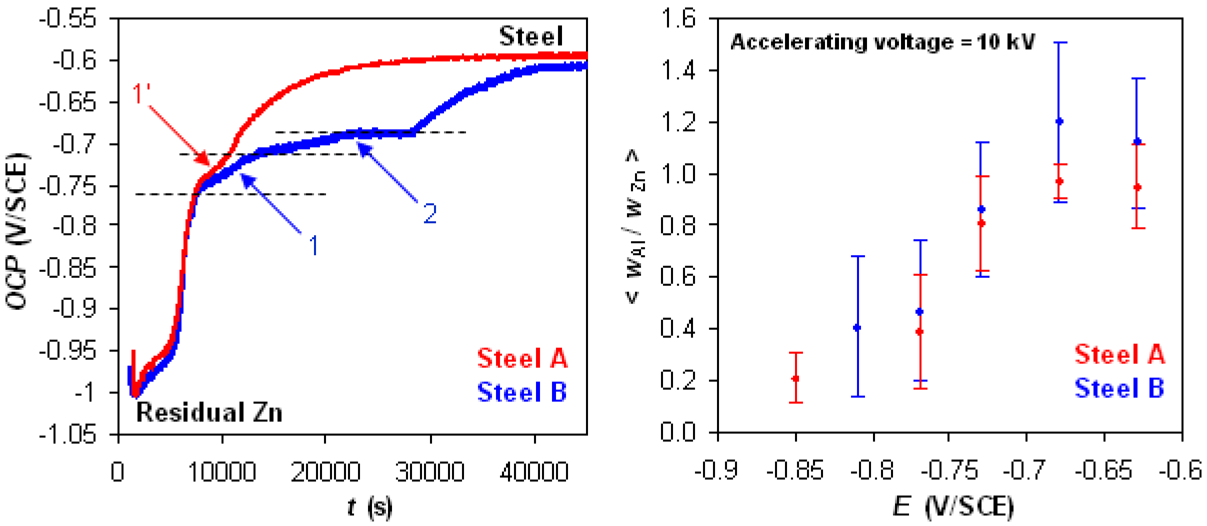

Figure 41: OCP against time electrochemical curves (left) and average Al/Zn mass ratio against imposed potential (right) for steels A and B (X-ray energies of lines K_α for aluminium and L_α for zinc used for EDS quantification).

EDS surface analysis in SEM after surface electrochemical dissolution at different imposed key potentials, identified from the just commented electrochemical curves, is shown in the right-hand side of Figure 41. As can be observed, two different Al/Zn mass ratio populations[12] can be easily distinguished in both cases depending on the imposed potential. It can be deduced from these results that the inhibition layer of both steels is composed of two different phases, the one in direct contact with the steel having a higher Al/Zn mass ratio than the one on its top.

The previous results can be confirmed through SEM analysis performed on the CSP samples obtained from steels A (Figure 42) and B (Figure 43): the inhibition layer is in both cases composed of a very thin aluminium-rich phase layer[13] and a thicker zinc-rich phase layer on top of it. It is also

---

[12] As the interaction volume in SEM (accelerating voltage of 10 kV) is high enough to include into analysis the iron contribution from the steel matrix, the Al/Zn mass ratio only is considered to characterize the different phases of the inhibition layer. Steels A and B do not contain zinc and their aluminium content (Table 9) is negligible compared to the one of the phases constituting the inhibition layer (Table 5).

[13] One could conclude from the EDS mapping analysis in the right-hand side of Figure 43 that, in the case of steel B, the aluminium-rich layer is actually as thick as the zinc-rich layer on its top. However, a drift problem occurred during EDS analysis and the thicknesses obtained by this analysis are overestimated. The real thicknesses of both layers can be appreciated in the corresponding micrograph in the left-hand side of Figure 43: the aluminium-rich layer is much thinner than the zinc-rich layer.

important to highlight that the aluminium-rich layer is discontinuous in the case of steel A and nearly continuous in the case of steel B. This observation, evidenced along the whole length of the CSP samples (usable length of around 430 and 220 µm for samples A and B respectively), could explain the differences observed in the shape of the electrochemical curves. In the case of sample B, the dissolution stage of the aluminium-rich layer is very likely easily differentiable because of the continuity of this layer. During its dissolution, the potential of the sample surface remains almost stable at the corrosion potential of this phase as the electrolyte is in contact with a monophased surface. On the contrary, in the case of sample A, the discontinuity of the aluminium-rich layer makes the electrolyte to be at any time in contact with two different phases (the aluminium-rich and zinc-rich phases at the beginning, and the aluminium-rich phase and the steel substrate later). As their dissolution rates are different, the surface of each phase in contact with the electrolyte is constantly being modified and the potential of the sample surface is evolving continuously up to the moment that the whole inhibition layer has been removed and the electrolyte is only in contact with the steel matrix. This is probably the reason why the dissolution stage of the aluminium-rich layer cannot be distinguished in the electrochemical curve of steel A.

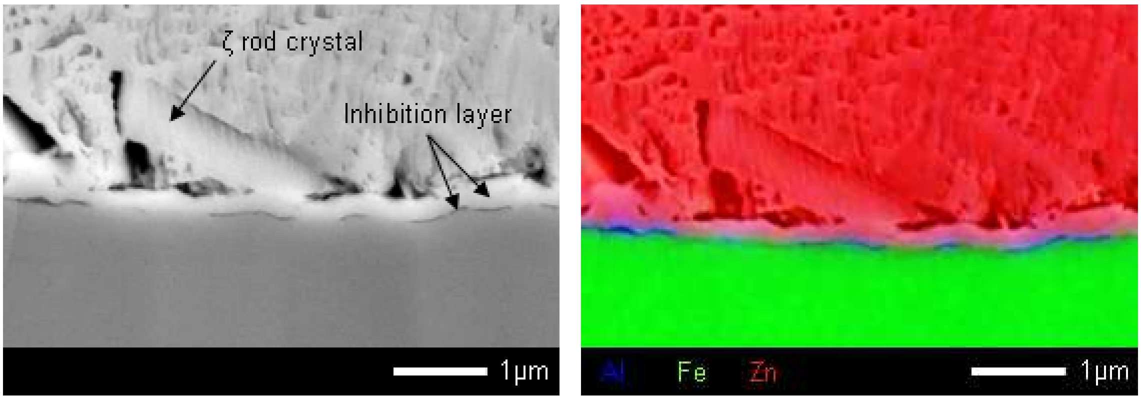

Figure 42: Cross section SEM micrograph (left) and EDS element mapping (right) of the inhibition layer performed on the CSP sample prepared from steel A.

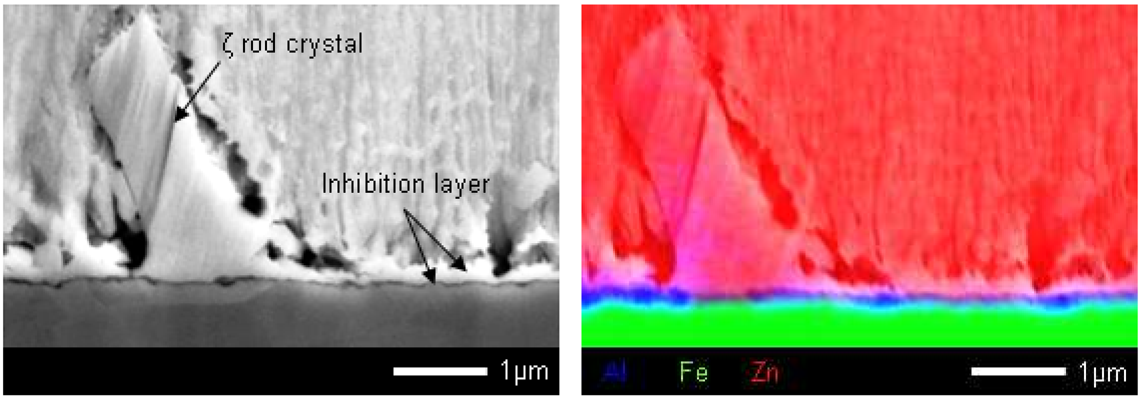

Figure 43: Cross section SEM micrograph (left) and EDS element mapping (right) of the inhibition layer performed on the CSP sample prepared from steel B.

In addition, other crystals have been seldom found in both CSP samples. These crystals have not been investigated in detail here but they are supposed to be ζ crystals, based on their rod shape. As already commented in section I.3.1.3.3.3, several authors in the literature have reported the presence of such crystals together with the inhibition layer [27,28,30,33,54,68,69]. A few further considerations concerning these ζ crystals will be given in section II.3.1.1.

The two-layer structure was also confirmed by EDS analysis of the FIB thin foils performed in the TEM. As shown in Figure 44 and Figure 45, the inhibition layer is composed in both cases of an aluminium-rich phase layer with a zinc-rich phase layer on its top. It should be reminded that the gold and platinum layers come from the FIB sample preparation (section II.1.2.1.2.3). Once again, the discontinuity of the aluminium-rich layer can be appreciated in the case of steel A (Figure 44).

Finally, it is important to note that both FIB foils have been locally damaged by the ion beam milling operation during their preparation. “Blurred zones” can be distinguished in the EDS mapping images, where the foils are mechanically damaged. At these places, the steel surface may have been slightly polluted with the aluminium-rich layer and this latter with the zinc-rich layer.

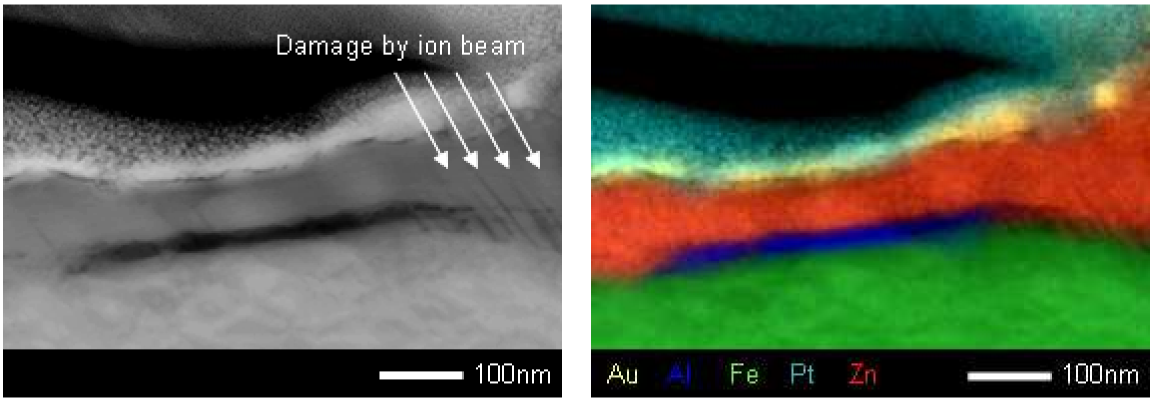

Figure 44: Cross section TEM bright field image (left) and EDS element mapping (right) of the inhibition layer performed on the FIB foil prepared from steel A.

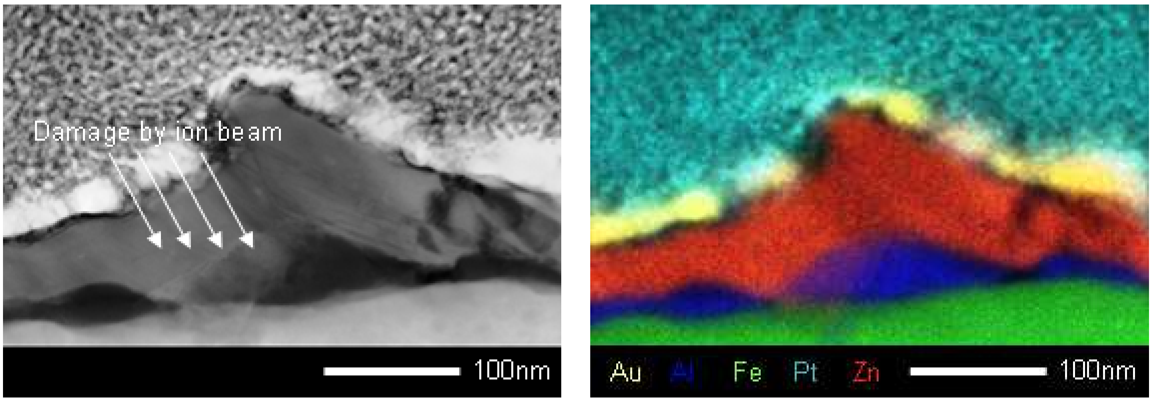

Figure 45: Cross section TEM bright field image (left) and EDS element mapping (right) of the inhibition layer performed on the FIB foil prepared from steel B.

II.2.2. Phase identification

II.2.2.1. Elemental analysis

The elemental composition of the two layers constituting the inhibition layer was investigated by EDS analysis performed on the FIB thin foils in the TEM. The experimental results obtained for steels A and B (Table 12) can be compared with the composition of the δ and $Fe_2Al_5Zn_x$ phases in thermodynamic equilibrium with the liquid phase published in the literature by Chen *et al*. [7] (Table 5).

Table 12: EDS analysis of the two layers constituting the inhibition layer performed in the TEM on the FIB foils prepared from steels A and B.

Elements	Steel A		Steel B	
	Top layer	Bottom layer	Top layer	Bottom layer
Al (wt.%)	2.7 ± 0.1	24.1 ± 0.8	2.7 ± 0.1	38.5 ± 1.2
Fe (wt.%)	12.0 ± 0.4	44.3 ± 1.4	11.1 ± 0.4	36.9 ± 1.2
Zn (wt.%)	85.3 ± 2.6	31.6 ± 1.0	86.2 ± 2.6	24.6 ± 0.8

As can be observed, very similar results have been obtained for both steels. The composition of the top layer is consistent with the composition found by Chen *et al*. [7] for the δ phase. The composition of the bottom layer given by EDS is very close to the stoichiometric one for the $Fe_2Al_5Zn_x$ phase given by Chen *et al*. [7] but with slightly higher iron and zinc contents. It has been reported before that both FIB foils had been locally damaged by the ion beam milling operation during their preparation. It is therefore very likely that some pollution of the aluminium-rich phase layer with the zinc-rich phase overlay may have occurred at this time.

In order to validate the chemical composition of the aluminium-rich phase, EDS analysis was performed in the TEM on the films extracted from the sample surface after electrochemical dissolution at -680 mV/SCE. At this potential, zinc and Fe-Zn phases are removed and the aluminium-rich layer is kept at the sample surface. The so-obtained results for steels A and B are summarized in Table 13.

Table 13: EDS analysis of the aluminium-rich layer of the inhibition layer performed in the TEM on the films extracted from steels A and B after surface electrochemical dissolution at -680 mV/SCE.

Elements	Steel A	Steel B
Al (wt.%)	44.3 ± 1.4	49.3 ± 1.5
Fe (wt.%)	36.4 ± 1.2	36.7 ± 1.1
Zn (wt.%)	19.3 ± 0.7	14.0 ± 0.5

The chemical composition of the aluminium-rich phase given by the EDS analysis performed on the extracted films is consistent, especially in the case of steel A, with the chemical composition of the $Fe_2Al_5Zn_x$ phase given by Chen *et al*. [7]. It should be recalled that, according to the Al-Fe-Zn ternary phase diagram at 450 °C from Tang [10] (Figure 10), the $Fe_2Al_5Zn_x$ phase can dissolve up to around 20 wt.% Zn. The composition of this phase given by Chen *et al*. [7] is actually the one at its zinc solubility limit. Although the composition of the aluminium-rich phase given by EDS analysis in the case of steel B slightly differs from the one reported by Chen *et al*. [7] for a zinc-saturated $Fe_2Al_5Zn_x$ phase, it falls within the composition domain for this phase in the Al-Fe-Zn ternary phase diagram.

It can be summarized that the compositions of the zinc-rich and aluminium-rich phase layers constituting the inhibition layer given by the EDS analysis performed in the TEM on the FIB thin foils and extracted films correspond to the stoichiometric ones for the δ and $Fe_2Al_5Zn_x$ phases respectively. The assumption that the aluminium-rich phase layer is polluted with the δ phase on its top in the case of the FIB foils can be confirmed as well.

II.2.2.2. Chemical nature

The chemical nature of the two layers constituting the inhibition layer was determined by Electron Diffraction performed on the FIB foils for the zinc-rich layer and on the extracted films for the aluminium-rich layer in the TEM. The diffraction patterns obtained are presented in Figure 46 and Figure 47.

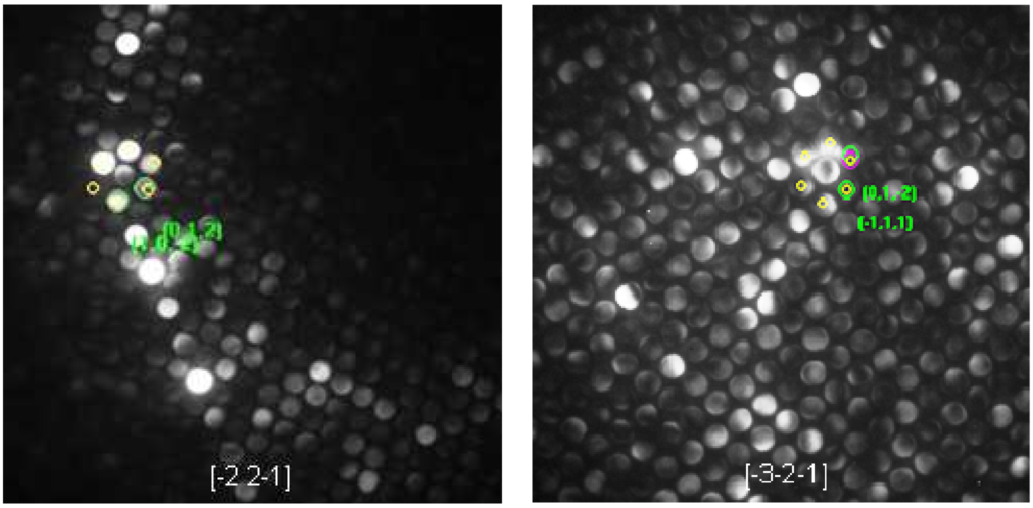

Figure 46: Electron diffraction patterns of the zinc-rich phase of the inhibition layer performed in the TEM on the FIB foils prepared from steels A (left) and B (right).

In Figure 46, the electron diffraction patterns obtained experimentally on both steels for the zinc-rich layer are compared with the electron diffraction patterns calculated from the Joint Committee on Powder Diffraction Standards (JCPDS) file #045-1186 for the δ phase (hexagonal lattice, space group P, lattice parameters *a* = *b* = 1.2799 nm, *c* = 5.759 nm) by means of the *Diffraction-Workshop* software (version 2.1) [14]. The measured distances and angles of the zinc-rich layer are characteristic of the δ phase (in the [-2 2 -1] and [-3 -2 -1] incidence electron planes for the examples chosen).

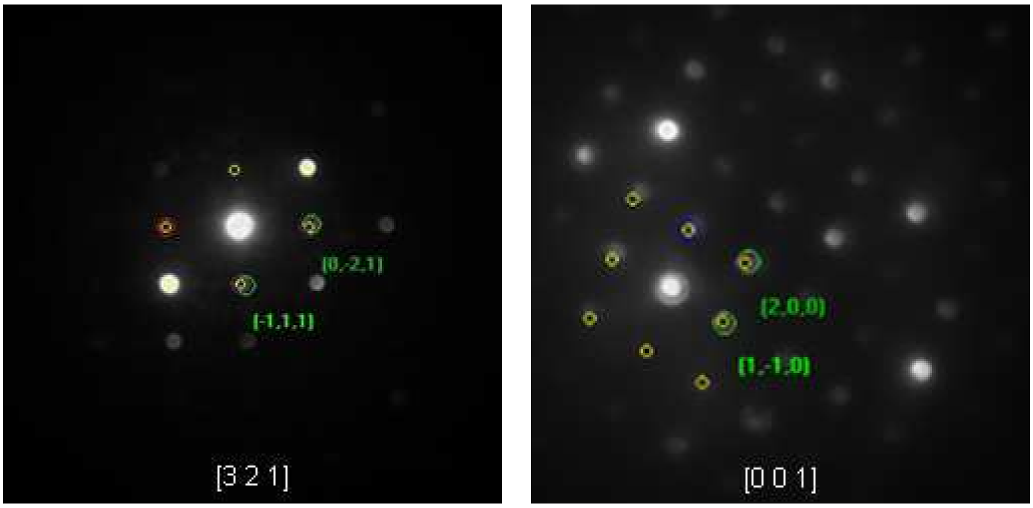

Figure 47: Electron diffraction patterns of the aluminium-rich phase of the inhibition layer performed in the TEM on the films extracted from steels A (left) and B (right) after surface electrochemical dissolution at -680 mV/SCE.

In Figure 47, the electron diffraction patterns obtained experimentally on both steels for the aluminium-rich layer are compared with the electron diffraction patterns calculated from the JCPDS file #049-1381 for the $Fe_2Al_5Zn_{0.4}$ phase (base-centered orthorhombic lattice, space group Cmcm, lattice parameters *a* = 0.7656 nm, *b* = 0.6407 nm, *c* = 0.4241 nm) after slight adjustment of the lattice parameters (*a* = 0.767 nm, *b* = 0.641 nm, *c* = 0.424 nm). The measured distances and angles of the

---

[14] The *Diffraction-Workshop* software (version 2.1) is a software for the analysis of diffraction patterns developed by Prof. Épicier from the INSA Lyon. From a database with different phases defined by their lattice system, angles and parameters, this software proposes the phase and zone axis which matches the best with the experimental diffraction pattern and provides the theoretical diffraction pattern. For the present study, the database was composed of all the Fe-Zn and Fe-Al compounds.

aluminium-rich layer are characteristic of the $Fe_2Al_5Zn_x$ phase (in the [3 2 1] and [0 0 1] incidence electron planes for the examples chosen).

It can therefore be confirmed that the inhibition layer formed on steels A and B is actually composed of a very thin layer of the $Fe_2Al_5Zn_x$ phase on the steel substrate and a thicker layer of the δ phase on top of it. The main difference observed in the structure of both inhibition layers is the clear discontinuity of the thin layer of $Fe_2Al_5Zn_x$ in the case of steel A.

II.2.3. Other features

Other important features of the inhibition layer formed in GA baths, such as possible epitaxial relationships, element concentration distribution as well as geometrical features (thickness, surface area fraction covered by $Fe_2Al_5Zn_x$ or crystal size and homogeneity of its two constituting phases) have been investigated. Finally, interest was also given to the aluminium uptake by the inhibition layer.

II.2.3.1. Epitaxial relationships

Brief literature review

Some researchers [23,33,43-45] have observed epitaxial relationships between steel and $Fe_2Al_5Zn_x$ in the field of hot-dip galvanizing.

Guttmann [23] reported that $Fe_2Al_5Zn_x$ can grow in epitaxial relationship on certain ferrite grain orientations: $(3\,\bar{1}\,1)_{Fe_2Al_5}$ // $(1\,1\,0)_{Fe_\alpha}$ and possibly $(2\,2\,1)_{Fe_2Al_5}$ // $(1\,1\,0)_{Fe_\alpha}$. When the epitaxial growth is possible for a given ferrite grain orientation, the $Fe_2Al_5Zn_x$ phase should form in colonies of crystals with identical orientation separated by very low angle boundaries. Conversely, at the emergence of steel grain boundaries, adjacent colonies of $Fe_2Al_5Zn_x$ crystals with different orientations should meet each other and form random boundaries, characterized by higher angles. A schematic representation of the epitaxial $Fe_2Al_5Zn_x$ inhibition layer suggested by Guttmann [23] is shown in Figure 48.

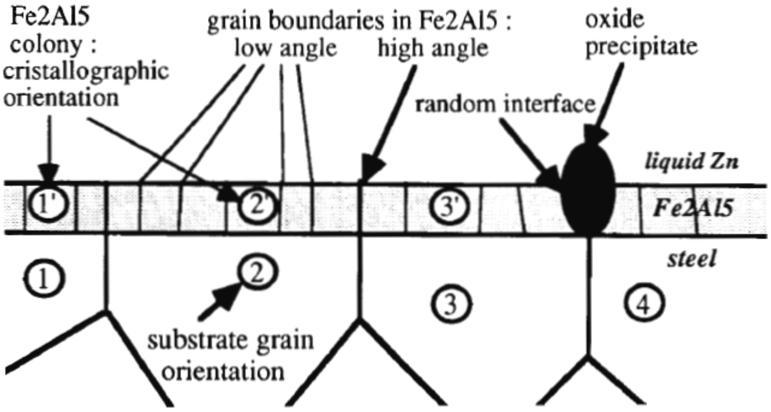

Figure 48: Proposed grain boundary structure of the $Fe_2Al_5Zn_x$ inhibition layer due to epitaxial nucleation on the steel (Guttmann [23]).

Several other orientation relationships between $Fe_2Al_5Zn_x$ and ferrite can be found in the literature:

- $(1\,\bar{3}\,0)_{Fe_2Al_5}$ // $(1\,0\,1)_{Fe_\alpha}$, $[0\,0\,1]_{Fe_2Al_5}$ // $[\bar{1}\,0\,1]_{Fe_\alpha}$ [33];
- $(0\,0\,1)_{Fe_2Al_5}$ // $(0\,1\,1)_{Fe_\alpha}$, $[\bar{1}\,\bar{3}\,0]_{Fe_2Al_5}$ // $[\bar{1}\,0\,0]_{Fe_\alpha}$ [44];
- $[1\,1\,0]_{Fe_2Al_5}$ // $[1\,1\,1]_{Fe_\alpha}$, $(0\,0\,1)_{Fe_2Al_5}$ // $(0\,\bar{1}\,1)_{Fe_\alpha}$ and $(1\,\bar{1}\,0)_{Fe_2Al_5}$ // $(2\,\bar{1}\,\bar{1})_{Fe_\alpha}$ [43].

The few orientation relationships between ferrite and $Fe_2Al_5Zn_x$ found in the literature are different from one reference to another. The main goal here is to contribute new experimental data on these orientation relationships.

Present study

In the framework of the present study, electron diffraction in TEM was performed in the vicinity of the steel / inhibition layer interface of the FIB foil prepared from steel A in order to evidence possible epitaxial relationships between ferrite and $Fe_2Al_5Zn_x$. The experimental electron diffraction pattern obtained in this zone is available in Figure 49.

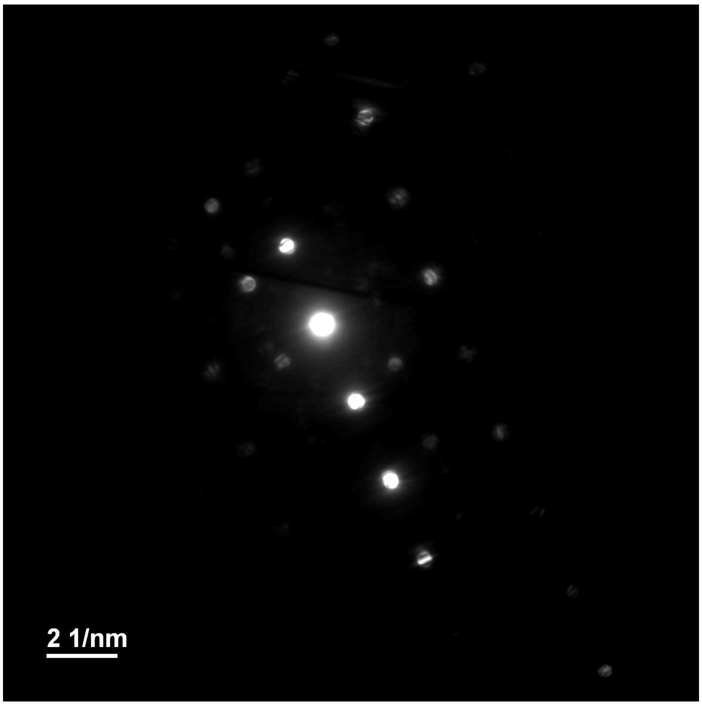

Figure 49: Electron diffraction pattern of the steel / $Fe_2Al_5Zn_x$ interface performed in the TEM on the FIB foil prepared from steel A.

Some simulations were then carried out by means of CaRIne Crystallography 3.1 software in order to reproduce as much as possible the electron diffraction pattern obtained experimentally. It should be noted that the positions of zinc atoms in substitution of iron or aluminium atoms within the unit cell of the $Fe_2Al_5Zn_x$ phase still remain unknown and no model with the precise position of each atom within this unit cell is therefore available in the literature. As a result, the Fe_2Al_5 unit cell models from Burkhardt *et al*. [87] and Chen *et al*. [88] were used by default for the simulations. Data needed to simulate the Fe_2Al_5 unit cell (base-centered orthorhombic lattice, space group Cmcm) are available from Table 14 to Table 16. Table 14 contains the lattice parameters of Fe_2Al_5 according to the two previous models. As it can be seen, these values are very close to the ones used in section II.2.2.2 to simulate $Fe_2Al_5Zn_x$ satisfactorily, which would mean that the lattice parameters of Fe_2Al_5 are not strongly influenced by the substitution of iron or aluminium atoms by zinc atoms. The atomic positions in the Fe_2Al_5 unit cell, according to the model proposed by Burkhardt *et al*. [87] (resp. Chen *et al*. [88]), are available in Table 15 (resp. Table 16). In order to simulate the ferrite unit cell (body-centered cubic lattice), lattice parameters of $a = b = c$ =0.2866 nm have been considered (JCPDS file #006-0696).

Table 14: Lattice parameters of Fe_2Al_5 according to the models of Burkhardt *et al*. [87] and Chen *et al*. [88].

Lattice parameters (nm)	Burkhardt *et al*. [87]	Chen *et al*. [88]
a	0.7656	0.7653
b	0.6415	0.6411
c	0.4218	0.4229

Table 15: Atomic positions in the Fe_2Al_5 unit cell according to the model of Burkhardt *et al*. [87].

Type of site	Multiplicity	Wyckoff letter	Occupation factor	Coordinates		
				x	y	z
Fe	4	c	1	0	0.8277	0.25
Al_1	8	g	1	0.1880	0.1467	0.25
Al_2	4	b	0.32	0	0.5	0
Al_3	8	f	0.24	0.5	0.034	0.830

Table 16: Atomic positions in the Fe_2Al_5 unit cell according to the model of Chen *et al*. [88].

Type of site	Multiplicity	Wyckoff letter	Occupation factor	Coordinates		
				x	y	z
Fe	4	c	1	0	0.332	0.25
Al_1	8	g	1	0.18	0.65	0.25
Al_2	4	a	0.7	0	0.5	0

The results of the simulation work are shown in Figure 50 and Figure 51 together with the experimental diffraction pattern. The calculated diffraction patterns of ferrite and Fe_2Al_5 are in blue and red colour respectively. Figure 50 (resp. Figure 51) presents the simulation of the electron diffraction pattern for the Fe_2Al_5 unit cell using the model from Burkhardt *et al*. [87] (resp. Chen *et al*. [88]). In both cases, the following epitaxial relationship between ferrite and $Fe_2Al_5Zn_x$ is very likely the one which matches the best with the experimental electron diffraction pattern:

$$(2\,2\,1)_{Fe_2Al_5} \;//\; (1\,1\,0)_{Fe_\alpha},\; [3\,1\,4]_{Fe_2Al_5} \;//\; [\bar{1}\,0\,1]_{Fe_\alpha}$$

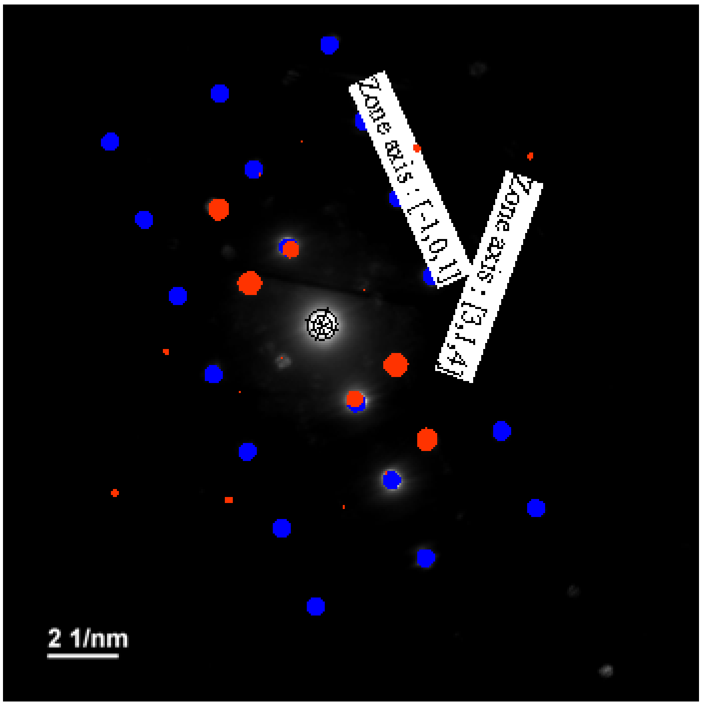

Figure 50: Electron diffraction patterns of ferrite (in blue) and Fe_2Al_5 (in red) corresponding to the epitaxial relationship $(2\,2\,1)_{Fe_2Al_5} // (1\,1\,0)_{Fe_\alpha}$, $[3\,1\,4]_{Fe_2Al_5} // [\bar{1}\,0\,1]_{Fe_\alpha}$ simulated with CaRIne Crystallography 3.1 software (Fe_2Al_5 unit cell described by the model from Burkhardt *et al*. [87]); superposition with the electron diffraction pattern obtained experimentally (grey diffraction spots).

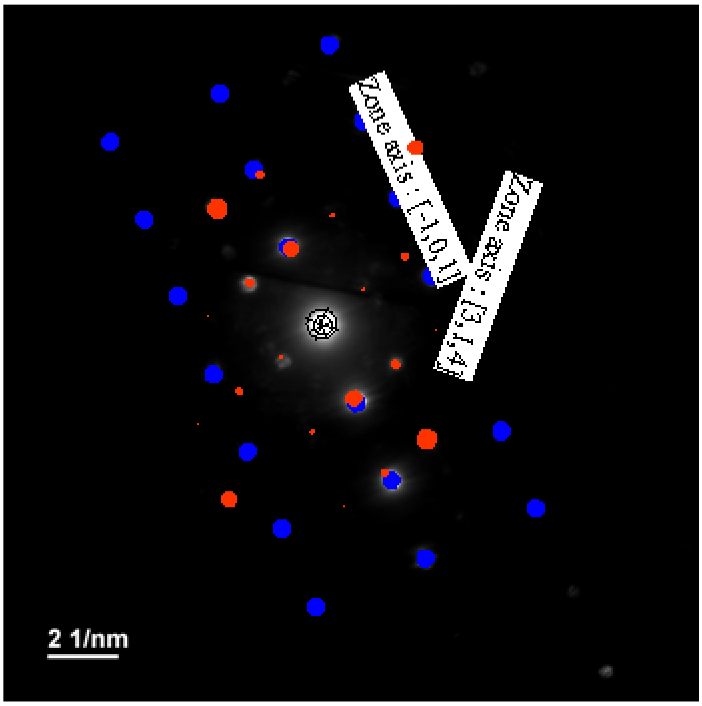

Figure 51: Electron diffraction patterns of ferrite (in blue) and Fe_2Al_5 (in red) corresponding to the epitaxial relationship $(2\,2\,1)_{Fe_2Al_5}$ // $(1\,1\,0)_{Fe_\alpha}$, $[3\,1\,4]_{Fe_2Al_5}$ // $[\bar{1}\,0\,1]_{Fe_\alpha}$ simulated with CaRIne Crystallography 3.1 software (Fe_2Al_5 unit cell described by the model from Chen *et al*. [88]); superposition with the electron diffraction pattern obtained experimentally (grey diffraction spots).

As can be appreciated in Figure 50 and Figure 51, the simulated electron diffraction patterns are quite in line with the experimental one. The position of the experimental spots matches very well with the position of the calculated ones. However, in the case of the $Fe_2Al_5Zn_x$ phase, the intensities of the experimental diffraction spots ($Fe_2Al_5Zn_x$) are different from the simulated ones (Fe_2Al_5). Indeed, the intensities of the spots depend on the nature of the atoms present within the unit cell and, as told before, the unit cell of Fe_2Al_5 was used for simulations instead of that of $Fe_2Al_5Zn_x$. It would be interesting to know precisely how iron and / or aluminium atoms are substituted by zinc atoms in the unit cell of $Fe_2Al_5Zn_x$ in order to check whether or not the intensities of the spots given by simulations when using the correct unit cell are in line with the experimental ones.

In any case, it can be confirmed that a precise epitaxial relationship between ferrite and $Fe_2Al_5Zn_x$ has been found in this study. Although this epitaxial relationship has never been reported before in the literature, the same relationship between planes had already been suggested by Guttmann [23].

II.2.3.2. Element concentration distribution

SIMS work was conducted on samples of steels A and B after removal of most of the zinc overlay in order to study the aluminium, iron and zinc concentration distribution within the two phase layers of the inhibiting structure. The element concentration profiles given by SIMS for two trials performed on steels A and B are presented in Figure 52.

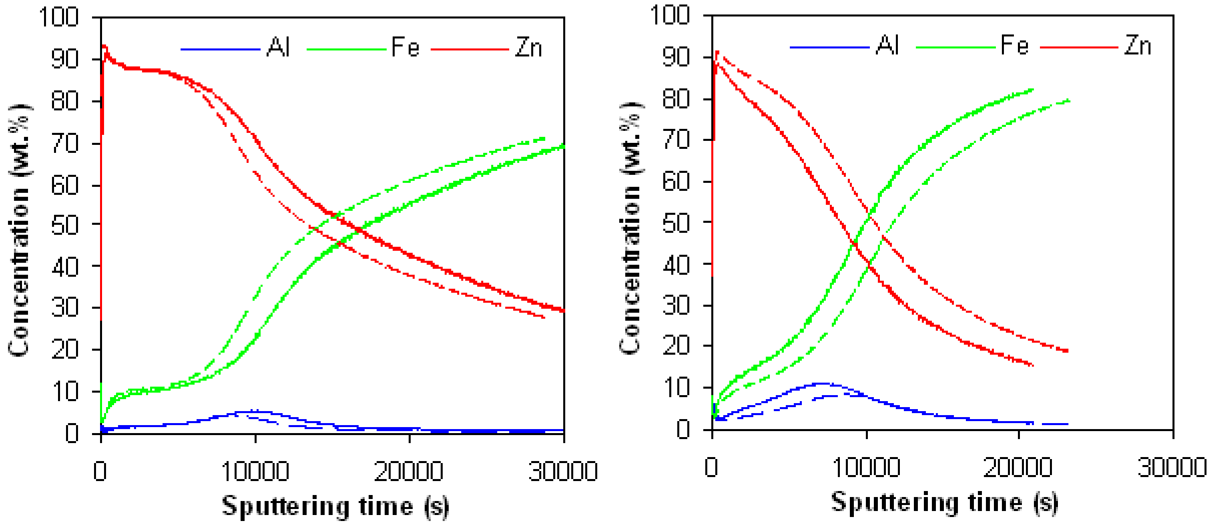

Figure 52: SIMS concentration profiles within the inhibition layer of steels A (left) and B (right).

In both cases, the SIMS profiles are reproducible and the two phases of the inhibition layer can be easily differentiated: the zinc-rich layer at the sample surface (sputtering time range of 0 - 10000 s) and the Al-rich layer (sputtering time range of 8000 - 12000 s). The measured concentrations for the top layer are those corresponding to the δ phase (Table 5). However, the obtained concentrations for the bottom layer are very different from those corresponding to the $Fe_2Al_5Zn_x$ phase (Table 5). In particular, the aluminium content is significantly lower than the stoichiometric one, especially in the case of steel A. In order to explain this observation, it can be assumed that the $Fe_2Al_5Zn_x$ phase layer is so thin that, due to little surface irregularities, sputtering can occur in the three phases, namely $Fe_2Al_5Zn_x$, δ and steel, at the same time. The discontinuity of the $Fe_2Al_5Zn_x$ phase (Figure 42) leads to an aluminium content of this phase measured in the case of steel A substantially lower compared to steel B.

In order to try to obtain the real concentrations within the $Fe_2Al_5Zn_x$ phase, additional SIMS profiles have been performed on both steels after removal of zinc and Fe-Zn phases. The results obtained for two trials on steels A and B are available in Figure 53.

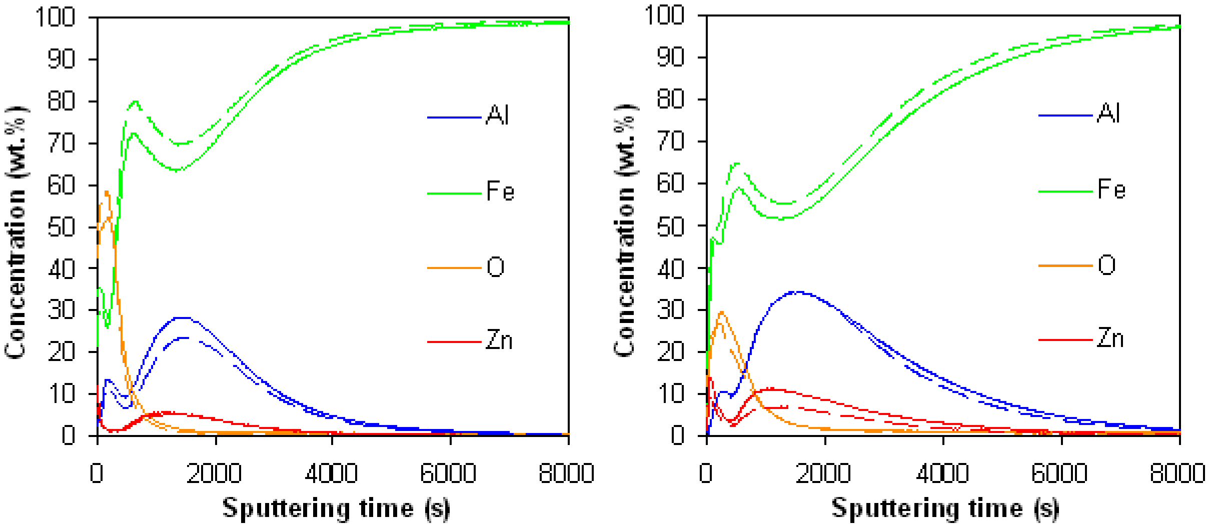

Figure 53: SIMS concentration profiles within the $Fe_2Al_5Zn_x$ layer of steels A (left) and B (right).

In this case, sputtering was expected to occur directly on the thin layer of $Fe_2Al_5Zn_x$ kept on the steel surface. From the sample surface (sputtering time of 0 s), a thin oxygen-rich layer is first identified, indicating that the sample surface has been oxidized or hydroxidized. The layer of $Fe_2Al_5Zn_x$

identified previously can then be distinguished. Although its aluminium content is, as expected, considerably higher than the one on the SIMS profiles of Figure 52, it still remains low, especially in the case of steel A. This observation is supposed to be due to the discontinuity of the $Fe_2Al_5Zn_x$ layer, and will be discussed in detail later in section II.2.3.3.2.

The SIMS profiles could be used to determine the thickness of the different intermetallic compounds constituting the inhibition layer. However, this analysis is not possible for at least two reasons. The two interfaces (δ / $Fe_2Al_5Zn_x$ and $Fe_2Al_5Zn_x$ / steel) are almost as extended as the phases themselves. For instance, an increase in the aluminium concentration corresponding to the sputtering of $Fe_2Al_5Zn_x$ is detected at the same time as a high concentration of zinc corresponding to the sputtering of δ (Figure 52). In addition, the sputtering rates are significantly different from one phase to another.

Although the previous element concentration profiles can provide valuable general information (the two phases constituting the inhibition layer can be easily identified), it is important to highlight that the SIMS technique presents important limitations for the current study and that any quantitative data extracted by means of this technique must be taken with caution.

II.2.3.3. Geometrical features

II.2.3.3.1. Thickness

In order to obtain reliable data, the average thicknesses of the two phases constituting the inhibition layer were estimated from measurements performed on the CSP samples and FIB foils. δ thickness measurements on SEM micrographs taken on the whole length of the CSP samples were carried out every 3-4 µm approximately (105 measurements for steel A and 66 for steel B). As will be seen in section II.2.3.3.2, these micrographs were also used to determine the steel surface area fraction covered by $Fe_2Al_5Zn_x$. In parallel, $Fe_2Al_5Zn_x$ thickness measurements were performed on TEM micrographs throughout the length of the FIB thin foils (9 measurements for steel A and 15 for steel B). Examples of these micrographs are available in Figure 54 for steel A and Figure 55 for steel B. The results of the thickness measurements are shown in Table 17.

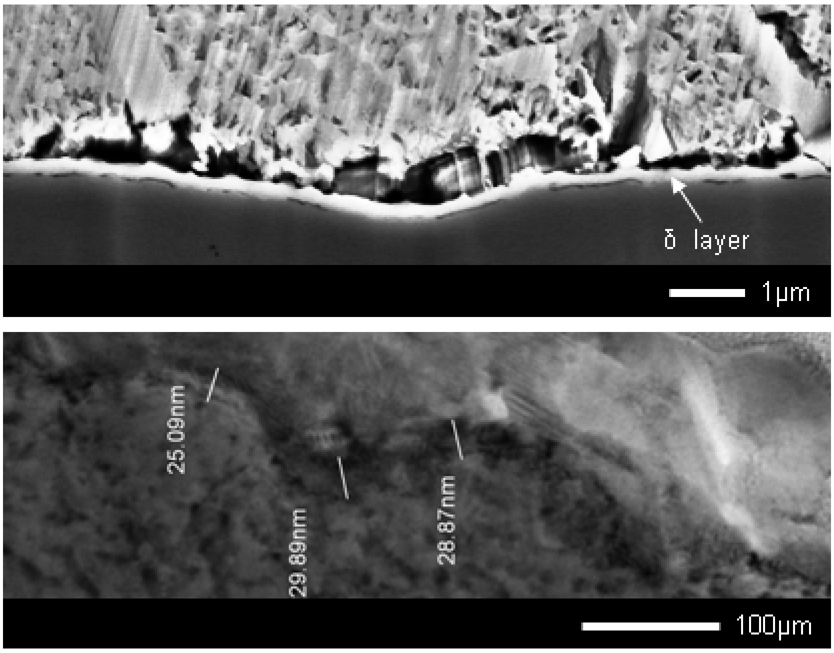

Figure 54: Examples of cross section SEM micrograph performed on the CSP sample obtained from steel A used to determine its δ phase average thickness and $Fe_2Al_5Zn_x$ surface coverage (top) and cross section TEM bright field image performed on the FIB foil prepared from the same steel used to determine its $Fe_2Al_5Zn_x$ average thickness (bottom).

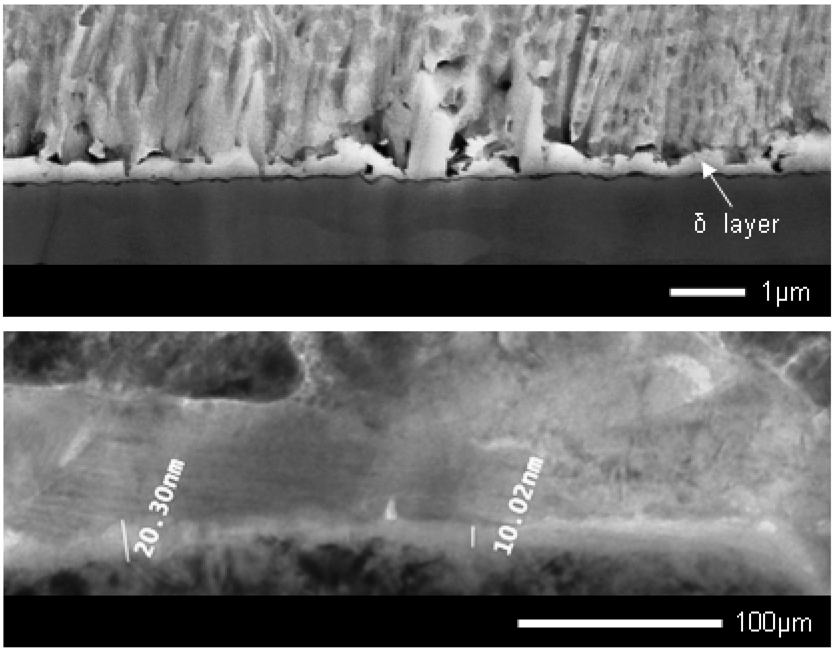

Figure 55: Examples of cross section SEM micrograph performed on the CSP sample obtained from steel B used to determine its δ phase average thickness and $Fe_2Al_5Zn_x$ surface coverage (top) and cross section TEM bright field images performed on the FIB foil prepared from the same steel used to determine its $Fe_2Al_5Zn_x$ average thickness (bottom).

Table 17: Estimation of the δ and $Fe_2Al_5Zn_x$ average thicknesses from measurements performed on the CSP and FIB micrographs.

Steel	δ (nm) [a]	$Fe_2Al_5Zn_x$ (nm) [b]
A	197 ± 61	24.1 ± 3.8
B	248 ± 77	23.2 ± 11.0

[a] estimated from the SEM observations of the CSP samples;
[b] estimated from the TEM observations of the FIB samples.

As can be seen in Table 17, the thicknesses obtained are fairly the same in both steels: the $Fe_2Al_5Zn_x$ layer has been found to be around 20 nm-thick and the δ layer around 200 nm-thick.

However, thickness measurements are subjected to some uncertainty. As far as the δ layer is concerned, measurements were relatively reliable. Indeed, δ thickness measurements were performed on the same type of SEM micrographs as depicted in the top of Figure 54 and Figure 55 at a magnification such that 20 mm in the image corresponded to the real distance of 1 μm. The error associated with the measurement itself may be estimated at around 0.5 mm, which corresponds to 25 nm in reality. If this approximate value is now compared to the standard deviations calculated from measurements (61 and 77 nm for steels A and B respectively) and the average thicknesses obtained are taken into account (197 and 248 nm for steels A and B respectively), one can conclude that the thickness of the δ layer varies substantially along the CSP samples. On the contrary, the thickness measurements performed on the $Fe_2Al_5Zn_x$ layer may be open to more criticism. The number of measurements and the length through which they were taken are much smaller than in the case of the δ layer. Measurements were performed on TEM bright field images, as the ones shown in the bottom of Figure 54 and Figure 55, but at different magnifications. As for the δ layer, the error in the thickness measurement can be estimated at around 0.5 mm, which corresponds, for the range of magnifications used, to about 2-3 nm in reality. Again, if this range of values is compared to the standard deviations calculated from measurements (3.8 and 11.0 nm for steels A and B respectively) and the average thicknesses obtained are taken into account (24.1 and 23.2 nm for steels A and B respectively), one can conclude that the thickness of the $Fe_2Al_5Zn_x$ layer changes along the FIB thin foils. This appreciation, particularly tangible in the case of steel B, can be clearly evidenced in Figure 45, where the thickness of the $Fe_2Al_5Zn_x$ layer formed on this steel reaches about 55 nm.

II.2.3.3.2. Surface coverage

The SEM observation of the CSP samples (Figure 42 and Figure 43) and the SIMS depth profiles (Figure 52) are consistent with each other in the fact that they both indicate that the δ phase layer is a completely covering layer. The SEM observations of the CSP samples also indicated that the $Fe_2Al_5Zn_x$ layer is clearly discontinuous in the case of steel A but fairly continuous in the case of steel B.

In order to obtain reliable data, the steel surface area fraction covered by $Fe_2Al_5Zn_x$ was estimated from the ratio between the total length of dark segments, corresponding to $Fe_2Al_5Zn_x$, and the total length of interface (this ratio is called segment density) precisely measured on the CSP samples by means of the same type of micrographs as depicted in the top of Figure 54 and Figure 55 for steels A and B respectively. Although the interface was generally flat, some interfacial curvatures were occasionally present (Figure 54 top). As a result, the real length of interface was rigorously considered in both cases. The estimation of surface coverage by $Fe_2Al_5Zn_x$ is justified by the work of geologists: Delesse [89] demonstrated in 1847 that the area density A_A of randomly-oriented particles measured in a random cross section of a sample is equivalent to their volume density V_V in the whole sample; Rosiwal [90] demonstrated in 1898 that the segment density L_L (i.e., the length of the intersection of a line with the particles over the total length of the line) is equivalent to the volume density, thus confirming and simplifying the principle put forward by Delesse [89]. These two principles, depicted in Figure 56, justify the methodology chosen here to determine the surface coverage by $Fe_2Al_5Zn_x$. More particularly, the principle applied is the one formulated by Rosiwal [90], with the assumption that the thickness of the $Fe_2Al_5Zn_x$ layer remains constant. It might also be seen that the number of $Fe_2Al_5Zn_x$–free segments and their average measured lengths compared to the total length of the interface is highly sufficient to consider that the so-obtained results of surface coverage by $Fe_2Al_5Zn_x$ are representative of both steel samples (Table 18).

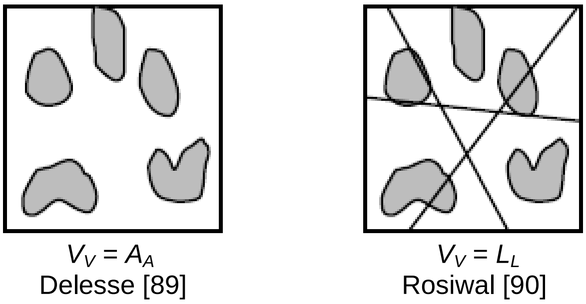

Figure 56: Schematic representation of the principles from Delesse [89] and Rosiwal [90] (V_V, A_A and L_L are the volume, area and segment densities respectively).

Table 18: Estimation of the surface coverage by $Fe_2Al_5Zn_x$ from measurements performed on the CSP micrographs.

Steel	Number of $Fe_2Al_5Zn_x$-free segments	Average length of the $Fe_2Al_5Zn_x$-free segments (µm)	Surface coverage by $Fe_2Al_5Zn_x$ f_S (%)	Total length (µm)
A	244	0.84 ± 0.70	52.1	428
B	33	0.82 ± 0.69	87.6	218

II.2.3.3.3. Crystal size and homogeneity

The crystal size and homogeneity of the two phase layers constituting the inhibition layer was evaluated from surface SEM micrographs after selective electrochemical dissolution either of zinc and ζ rod crystals at -800 mV/SCE, in the case of the δ phase layer characterization, or of zinc and Fe-Zn phases at -680 mV/SCE, in the case of the $Fe_2Al_5Zn_x$ phase layer characterization.

The general surface appearance of the δ phase layer can be appreciated in Figure 57 for steels A (left) and B (right). As can be seen, the crystals are well defined in both cases. As far as concerned the homogeneity of this layer, two zones with different morphologies have been identified in both cases: "compact zones" with small crystals and "porous zones" with slightly coarser crystals. These two morphologies can easily be distinguished in the surface SEM micrograph of steel B, especially with the zoomed area presented in Figure 58. The compact morphology only is present in the surface SEM micrograph of steel A. No difference in the Al/Zn mass ratio given by EDS surface analysis in SEM has been found between these two zones. It is very likely that the "porous zones" can be the result of a deeper attack during the electrochemical dissolution (it seems that some intergranular corrosion has occurred in the left-hand side of Figure 58). But, in any case, a substantial difference in the crystal size between the two zones can be appreciated. Considering the thickness of the δ layer (Table 17) and the present micrographs, it can be deduced that the δ layer is composed of pancake-shaped crystals. The characteristic dimension of these crystals varies between 200 and 500 nm in the compact zones and between 300 nm and 1 μm in the porous zones (Figure 58).

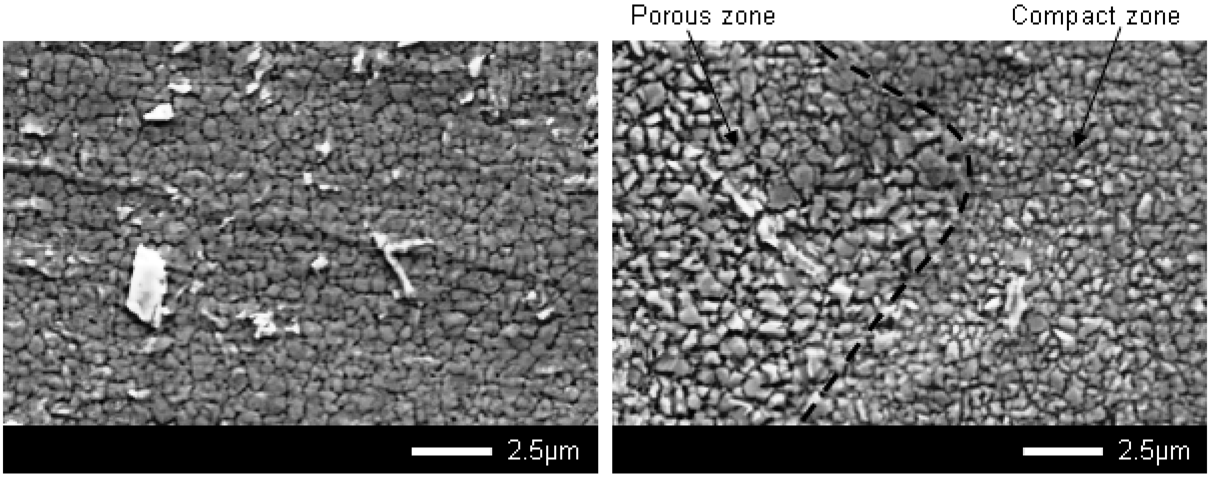

Figure 57: Surface SEM micrographs of the inhibition layer of steels A (left) and B (right) after electrochemical dissolution at -800 mV/SCE.

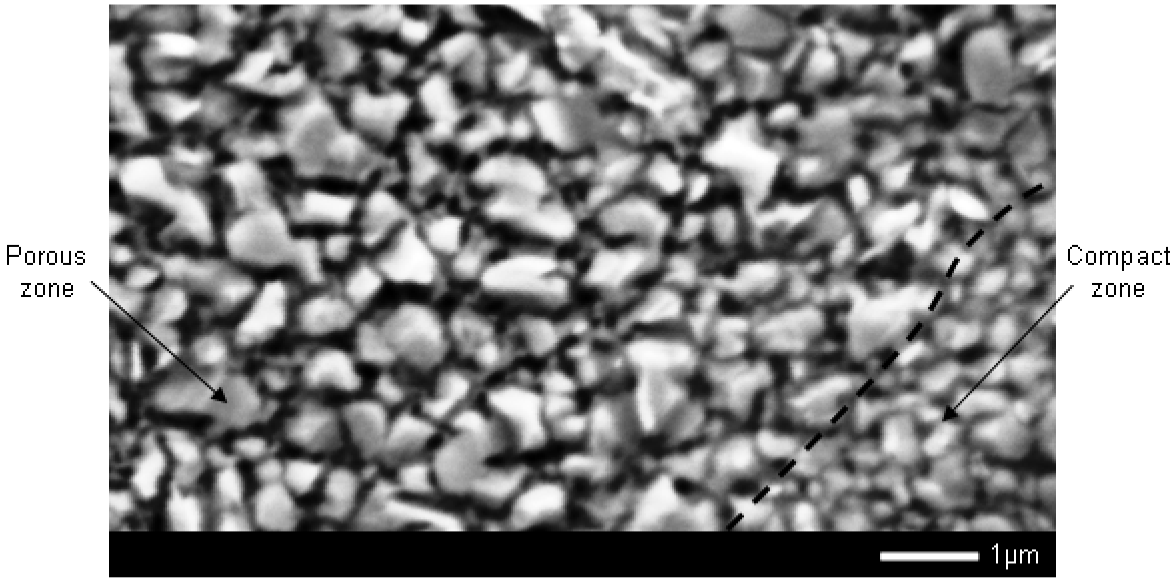

Figure 58: Zoomed area of the surface SEM micrograph of the inhibition layer of steel B after electrochemical dissolution at -800 mV/SCE (Figure 57 right).

The overall surface appearance of $Fe_2Al_5Zn_x$ is shown in Figure 59 for steels A (left) and B (right). $Fe_2Al_5Zn_x$ is corroded by the electrochemical dissolution at -680 mV/SCE, as shown by the pitting corrosion in Figure 59 (see arrows). Even if $Fe_2Al_5Zn_x$ was found to be discontinuous in the case of steel A, the steel surface is not visible after the electrochemical dissolution. It could be due to the oxidation of $Fe_2Al_5Zn_x$, enlightened before by the SIMS analysis in the same conditions (Figure 53). Several experiments performed to improve the quality of the $Fe_2Al_5Zn_x$ layer were undertaken (electrochemical dissolution at -630 mV/SCE, immersion into fuming HNO_3, Appendix F). The surfaces obtained were similar as the ones presented in Figure 59 and the mean crystal size cannot be measured from these experiments, probably due to the oxidation of $Fe_2Al_5Zn_x$.

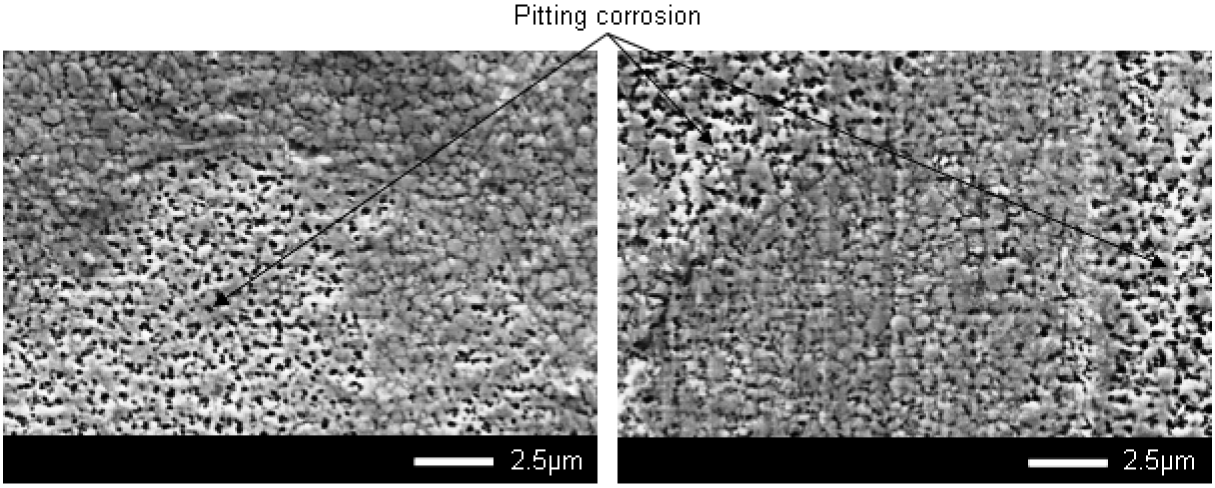

Figure 59: Surface SEM micrographs of the inhibition layer of steels A (left) and B (right) after electrochemical dissolution at -680 mV/SCE.

II.2.3.4. Aluminium uptake by the inhibition layer

As stated at the beginning of this chapter, a fine knowledge of the nature of the inhibition layer allows estimating the aluminium uptake by this layer (i.e., the aluminium flux consumed by the growth of the inhibition layer) accurately and, consequently, to control easierly the bath aluminium content. In order to calculate this quantity, the chemical composition (Table 12 and Table 13), thickness (Table 17) and surface coverage (Table 18) obtained experimentally for the two phase layers constituting this inhibition layer have been used. The densities of the two phases at room temperature must also be considered (ρ_δ = 7250 kg m^{-3} for δ [3] and $\rho_{Fe_2Al_5Zn_x}$ = 4570 kg m^{-3} for $Fe_2Al_5Zn_x$ [32]).

$$m_{Al} = w_{Al}^{Fe_2Al_5Zn_x} \cdot \rho_{Fe_2Al_5Zn_x} \cdot f_S \cdot e_{Fe_2Al_5Zn_x} + w_{Al}^{\delta} \cdot \rho_\delta \cdot \left[(1 - f_S) \cdot e_{Fe_2Al_5Zn_x} + e_\delta \right] \qquad \text{(II.1)}$$

where m_{Al} is the aluminium uptake by the inhibition layer (Table 19), f_S the surface area fraction covered by $Fe_2Al_5Zn_x$ (Table 18), $e_{Fe_2Al_5Zn_x}$ and e_δ the thicknesses of the $Fe_2Al_5Zn_x$ and δ layers (Table 17), $w_{Al}^{Fe_2Al_5Zn_x}$ and w_{Al}^{δ} the aluminium weigth fraction in $Fe_2Al_5Zn_x$ (Table 13) and in δ (Table 12).

The so-obtained results of aluminium uptake by the inhibition layer are available, for steels A and B, in Table 19.

Table 19: Estimation of the aluminium uptake by the inhibition layer from the chemical composition, thickness and surface coverage obtained experimentally for its two constituting phase layers.

Steel	**Aluminium uptake by the inhibition layer (g/m^2)**
A	0.066 ± 0.02
B	0.095 ± 0.04

As can be seen from Table 19, the inhibition layer formed on steel B consumes 40% more solute aluminium mass than the one on steel A.

The values of aluminium uptake by the inhibition layer obtained in the present study can be compared with those obtained by Isobe [55] (Figure 17 right). According to this author, the aluminium uptake by the inhibition layer after 3 s of immersion (1.4 and 1.9 s for steels A and B respectively) in a galvanizing bath at 470 ℃ (450 and 460 ℃ for steels A and B respectively) is about 0.02 g m^{-2}, for a bath aluminium content of 0.112 wt.% (steel A), and about 0.09 g m^{-2}, for a bath aluminium content of 0.128 wt.% (steel B). In spite of the different galvanizing conditions, the aluminium uptake by the inhibition layer in the case of steel B is totally in line with the results from Isobe [55]. However, the aluminium uptake by the inhibition layer of steel A is considerably higher (3 times) than the one reported by the previous researcher. This difference is difficult to evaluate because of the just reported different galvanizing conditions. In any case, the results obtained here for both steels are of the same order of magnitude than those published by Isobe [55].

II.3. Discussions

In the following sections, a discussion is held concerning the mechanism of formation of the inhibition layer in GA baths, its dependence on the steel surface state and the bath conditions (section II.3.1) and its final structure and phase composition (section II.3.2).

II.3.1. Mechanisms of formation of the inhibition layer

II.3.1.1. General mechanisms

It has been seen in section I.3.1.3 that a general agreement exists in the literature concerning the mechanisms accounting for the formation of the inhibition layer: wetting of the steel surface by the liquid zinc, iron dissolution from the steel surface, iron supersaturation at the steel / liquid zinc interface and nucleation and growth of the inhibition layer.

It has been demonstrated in this study that the inhibition layer formed in typical GA baths is actually composed of two different phase layers: a $Fe_2Al_5Zn_x$ layer, in epitaxial relationships with the underlying ferrite grains, and a δ layer on top of it. This microstructure is in agreement with the one proposed by Yamaguchi and Hisamatsu [47] for this kind of baths (section I.3.1.3.3.1). These authors suggested that the $Fe_2Al_5Zn_x$ layer nucleates first on the steel surface, followed by the subsequent nucleation of the δ layer at the $Fe_2Al_5Zn_x$ / liquid zinc interface. The present study provides some interesting elements allowing supporting this assumption. Figure 60 shows a high resolution cross section micrograph of steel A, for which the $Fe_2Al_5Zn_x$ layer was found to be discontinuous. As can be observed, several "holes" appear along the steel / coating interface in those zones where $Fe_2Al_5Zn_x$ has not nucleated. The mechanism proposed is therefore the following: $Fe_2Al_5Zn_x$ would first nucleate and grow at some places only on steel A. The iron dissolution would therefore be stopped in those zones where $Fe_2Al_5Zn_x$ is present while it would proceed in the adjoining areas, giving rise to the observed "holes", which would then be occupied by the subsequent nucleation of the δ phase.

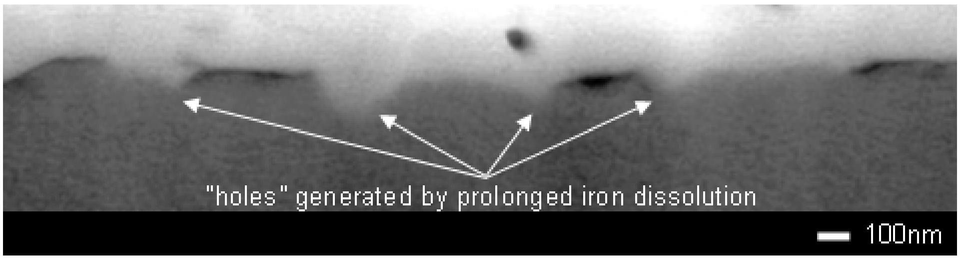

Figure 60: High resolution cross section micrograph illustrating that the iron dissolution from the steel surface lasts a longer time in those zones where $Fe_2Al_5Zn_x$ is not present (presence of "holes") (steel A).

Yamaguchi and Hisamatsu [47] assumed that the nucleation of the δ phase layer at the $Fe_2Al_5Zn_x$ / liquid interface is due to a depletion of the aluminium concentration at this location. This mechanism is evaluated here by the calculation of the orders of magnitude of two characteristic lengths (Table 20): the Characteristic Diffusion Length (*CDL*) of aluminium in the galvanizing bath for typical times necessary for the growth of a covering layer of $Fe_2Al_5Zn_x$ (around t_{growth} = 0.2 s according to Giorgi [32]) and the critical length (L_{crit}) in the bath including the quantity of aluminium necessary to make such a covering layer with the measured thickness and composition for each steel:

$$CDL = \sqrt{D_{Al}^{Zn(L)} \cdot t_{growth}} \tag{II.2}$$

$$L_{crit} = \frac{w_{Al}^{Fe_2Al_5Zn_x} \cdot \rho_{Fe_2Al_5Zn_x} \cdot e_{Fe_2Al_5Zn_x}}{\rho_{Zn} \cdot w_{Al}} \tag{II.3}$$

The diffusion coefficient of aluminium in liquid zinc $D_{Al}^{Zn(L)}$ has been chosen to be equal to 5 x 10^{-9} $m^2.s^{-1}$ [91] and the density of liquid zinc ρ_{Zn} to 6525 kg m^{-3} [73], both of them evaluated at 450 ℃ in spite of the slight difference in the bat h temperature between both samples.

The Characteristic Length of Diffusion *CDL* is higher than the critical length L_{crit}. It means that the growth of the $Fe_2Al_5Zn_x$ layer is not limited by the availability in aluminium in the galvanizing bath. Neither the discontinuity of $Fe_2Al_5Zn_x$ in the case of steel A nor the nucleation of δ on top of $Fe_2Al_5Zn_x$ in the case of both steels should be explained by means of such depletion.

Table 20: Comparison between the Characteristic Diffusion Length (*CDL*) and the critical length (L_{crit}) necessary for the growth of a complete layer of $Fe_2Al_5Zn_x$.

Steel	T_{bath} (℃) [a]	$D_{Al}^{Zn(L)}$ (m^2/s) [91] [b]	t_{growth} (s) [c]	*CDL* (µm) [d]	w_{Al} (wt.%) [e]	L_{crit} (µm) [f]
A	450	5x10^{-9}	0.2	31.6	0.112	6.7
B	460	5x10^{-9}	0.2	31.6	0.128	6.3

[a] bath temperature; [b] diffusion coefficient of aluminium in liquid zinc; [c] time of growth of a complete layer of $Fe_2Al_5Zn_x$; [d] characteristic diffusion length; [e] bath aluminium content; [f] critical length for the nucleation and growth of the complete layer of $Fe_2Al_5Zn_x$.

It is therefore thought that the nucleation of the δ phase after $Fe_2Al_5Zn_x$ is due to the attempt of the system to reach thermodynamic equilibrium along all interfaces. Metastable $Fe_2Al_5Zn_x$ would nucleate prior to the nucleation of stable δ due to epitaxial relationships with ferrite, which lower the surface energy for the nucleation of $Fe_2Al_5Zn_x$ compared to δ. The $Fe_2Al_5Zn_x$ / liquid zinc interface is then out of equilibrium and the system requires the nucleation of the δ phase to reach thermodynamic equilibrium along its interfaces. These mechanisms can easily be understood by means of the schematic path on the Al-Fe-Zn ternary phase diagram at 460 ℃ of Figure 61. To be rigourous, the representation of a diffusion path, real or virtual, in the ternary phase diagram only makes sense when describing a microstructure whose all interfaces are at thermodynamic equilibrium. In spite of the previous consideration, it has been decided to do so here in order to illustrate that $Fe_2Al_5Zn_x$ cannot be in thermodynamic equilibrium with a liquid zinc with an aluminium content typical of GA production (that is the reason why this part of the path has be represented by a dotted line) and this leads to the subsequent nucleation of δ (the diffusion path obtained will be presented later in Figure 73). Once the δ phase has nucleated on top of $Fe_2Al_5Zn_x$, the inhibition layer would grow. The δ / liquid zinc interface is expected to evolve by the consumption of the iron supersaturation first and then by diffusion of iron from the steel matrix towards the liquid zinc together with the $Fe_2Al_5Zn_x$ / δ interface.

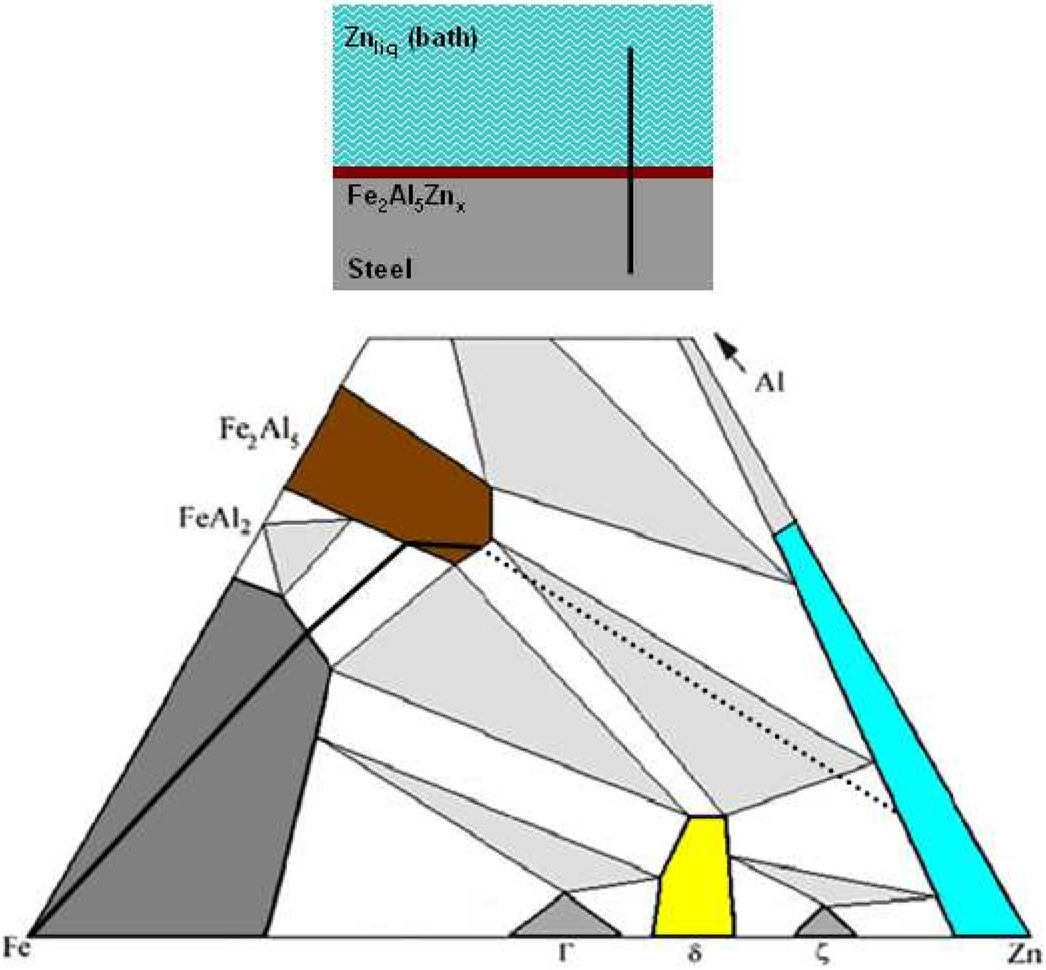

Figure 61: Schematic path on the Al-Fe-Zn ternary phase diagram at 450 - 460 ℃ showing a non-equilibrium situation along the $Fe_2Al_5Zn_x$ / liquid zinc interface in the case of GA baths (bottom) and temporary corresponding microstructure (top).

It is important to mention that metastable ζ rod crystals have also been observed within the inhibition layer of both steels A and B. As detailed in section I.3.1.3.3.3, the formation of these crystals may have two origins: they can be formed as colonies of the same orientation during immersion in the zinc bath due to epitaxial relationships with the underlying ferrite grains; or they are formed as randomly orientated crystals called by Leprêtre [33] as evanescents during the rapid solidification of the coating at the exit of the bath after wiping from an iron supersaturated liquid zinc. The quantity of crystals with the first origin is expected to increase when the bath aluminium content is lowered as their metastability is reduced. On the contrary, the quantity of evanescent crystals should not depend on the bath aluminium content but should depend on the immersion time.

Two ζ crystals can be distinguished in the cross section SEM micrographs of Figure 42 (steel A) and Figure 43 (steel B). It is difficult to conclude from these micrographs what the origin of these crystals is.

In order to characterize both the type and quantity of the ζ crystals present in the case of steels A and B, SEM surface characterization of samples electrochemically dissolved at -950 mV/SCE has been carried out. Only zinc is removed at this dissolution potential. Micrographs representative of the so-obtained microstructures are shown in Figure 62. While several colonies of epitaxial ζ crystals combined with some evanescent ζ crystals were observed in the case of steel A, very few epitaxial ζ crystals and mainly evanescent ζ crystals (in similar quantity compared to steel A) were present on steel B. It should also be noted how the epitaxial ζ rod crystals seem to nucleate and grow locally from the steel surface, as their bottoms are hidden by the δ layer, and how the evanescent ζ crystals nucleate after the formation of the δ layer, as they are clearly fully visible on top of this layer.

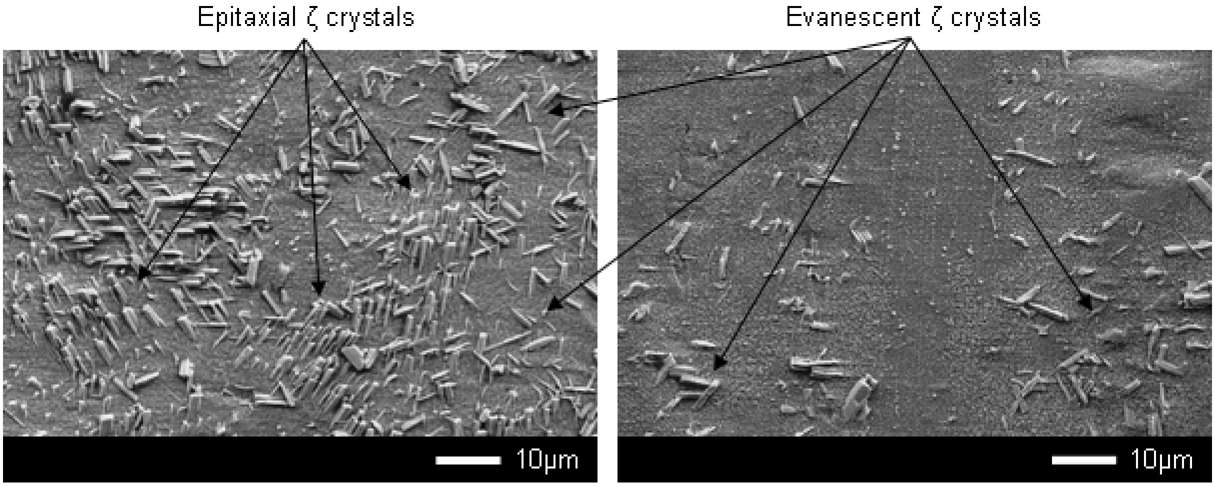

Figure 62: Surface SEM micrographs of the inhibition layer of steels A (left) and B (right) after electrochemical dissolution at -950 mV/SCE.

In addition, it can be deduced from this study that the epitaxial ζ rod crystals do not only nucleate directly on the ferrite grains, but also on the $Fe_2Al_5Zn_x$ layer. For instance, from the cross section SEM micrograph in the right-hand side of Figure 63 corresponding to steel B, the very few epitaxial ζ crystals observed nucleate on top of the $Fe_2Al_5Zn_x$ layer, the border between the ζ rod crystals and the $Fe_2Al_5Zn_x$ and δ layers being well defined. This local microstructure may also be appreciated in the case of the ζ crystal of Figure 43 (especially in the left-hand side of this crystal) and could represent an additional element to support the epitaxial nature of this particular crystal. Similar behaviour has been found in the case of steel A, as can be seen in the left-hand side micrograph of Figure 63. The ion beam polishing during the preparation of the CSP sample from this steel seems to have broken some of the epitaxial ζ rod crystals away from their nucleation surfaces, revealing that their nucleation occurs either on the $Fe_2Al_5Zn_x$ layer or on the underlying steel grains. However, this assumption needs to be confirmed by further characterizations. The $Fe_2Al_5Zn_x$ layer, formed in epitaxy with ferrite, could therefore act as a medium of crystallographic orientation transfer between ferrite and ζ crystals.

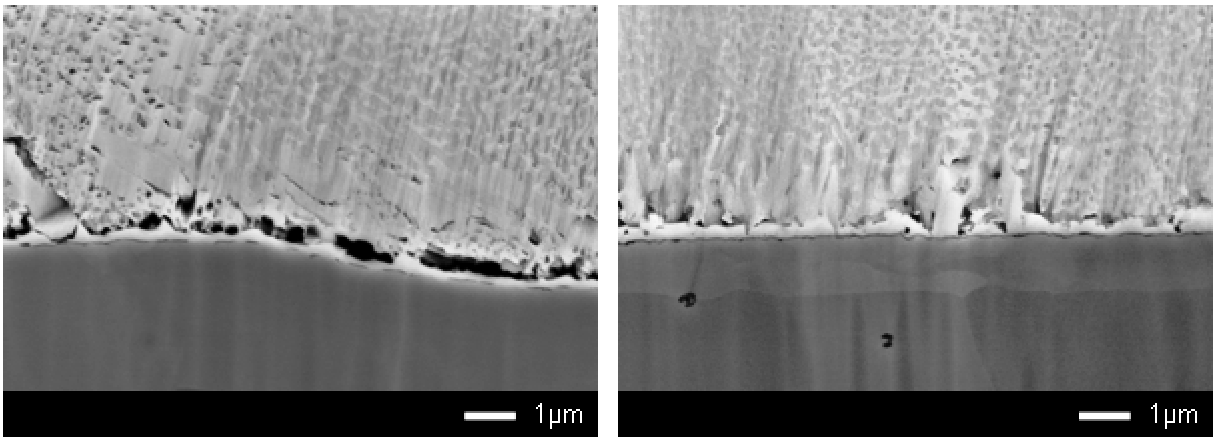

Figure 63: Cross section SEM micrographs of the inhibition layer performed on the CSP samples obtained from steels A (left) and B (right) showing the nucleation of epitaxial ζ rod crystals on the $Fe_2Al_5Zn_x$ layer.

The randomly-oriented ζ rod crystals formed during solidification of the sample will obviously nucleate on top of the δ layer or within the liquid zinc. As advanced in section I.3.1.3.3.3, these crystals are expected to be an artefact of the experimental procedure applied to study the inhibition layer so they will not be considered any longer in further discussions.

As can be seen, the mechanisms of formation of the inhibition layer formed in typical GA baths are more complex than expected, as ruled by the competition between the nucleation of epitaxial metastable $Fe_2Al_5Zn_x$ and ζ and stable δ on the steel surface. This competition will be obviously influenced by the steel surface state and the galvanizing conditions.

II.3.1.2. Effect of the galvanizing conditions

The effect of the galvanizing bath temperature (II.3.1.2.1), its aluminium content (II.3.1.2.2) and the immersion time (II.3.1.2.3) on the nature of the inhibition layer is discussed below on the basis of the results obtained in the present study.

II.3.1.2.1. Effect of the bath temperature

The galvanizing bath temperature was of 450 °C for steel A and 460 °C for steel B (Table 11). Figure 64 shows the zinc-rich corner of the Al-Fe-Zn ternary phase diagram at these two temperatures, according to the modelling work performed by Tang [12] concerning the liquidus line in the ζ, δ and $Fe_2Al_5Zn_x$ domains (section I.2.2). The composition of the two galvanizing baths used for steels A and B are also added in Figure 64.

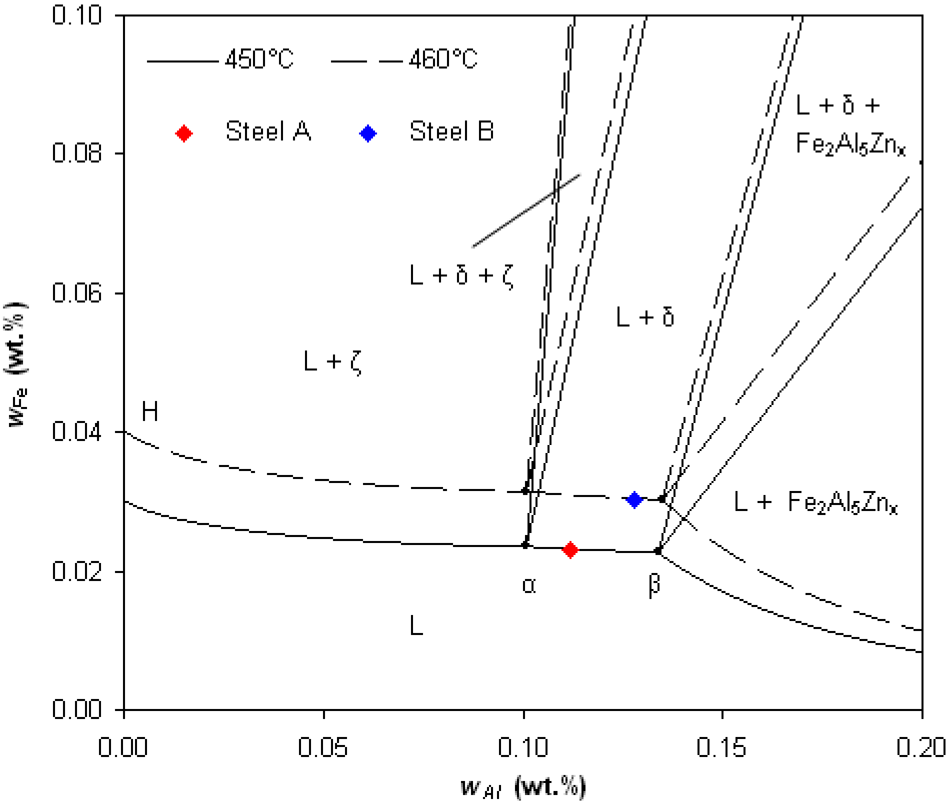

Figure 64: Zinc-rich corner of the Al-Fe-Zn ternary phase diagram at 450 and 460 °C (Tang [12]) with the galvanizing bath composition in the case of steels A (red point) and B (blue point).

As can be observed, the aluminium content of the knee points α (equilibrium between the ζ, δ and liquid phases) and β (equilibrium between the δ, $Fe_2Al_5Zn_x$ and liquid phases) is very slightly influenced by temperature (Table 1), so that the metastabilities of the ζ and $Fe_2Al_5Zn_x$ phases, for a given bath aluminium content between α and β, should not be affected by this difference in temperature.

However, the effect of temperature on the iron solubility in the liquid phase cannot be neglected. As expected, the bath at 460 ℃ is able to dissolve more iron than the one at 450 ℃. For instance, the iron dissolution flux is given by equation (I.11), reminded here:

$$J_{Fe}^{diss} = k_{diss}\left(c_{Fe}^{met} - c_{Fe}^{int}\right) \tag{II.4}$$

It depends on the driving force for dissolution given by the difference between the iron concentration in the liquid phase in metastable equilibrium with ferrite and the iron concentration at the interface, equal to the iron concentration in the liquid phase in thermodynamic equilibrium with the stable compound (in this case the δ phase) at the beginning of dissolution. The variation of this difference between 450 and 460 ℃ is of the order of magnitude of 5% only (w_{Fe}^{met} = 2.85 wt.% at 450 ℃ and 2.99 wt.% at 460 ℃ [32]).

Three main galvanizing reactions are influenced by temperature: 1) the iron dissolution flux J_{Fe}^{diss} (mol.m^{-2}.s^{-1}), 2) the rate of heterogeneous nucleation I (m^{-2}.s^{-1}) and 3) the flux of iron consumed by the growth of the interfacial alloy J_{Fe}^{cons} (mol.m^{-2}.s^{-1}) [32,91]. All these reactions are function of reaction rate constants (iron dissolution rate constant k_{diss} , nucleation rate constant k_{nucl} , rate constant for the growth of the interfacial alloy k_{growth}) and physical parameters such as the diffusion coefficients of iron and aluminium in liquid zinc, $D_{Fe}^{Zn(L)}$ and $D_{Al}^{Zn(L)}$, the diffusion coefficient of iron in the interfacial compound D_{Fe}^{comp} and the interfacial tension between this compound and liquid zinc $\sigma^{Zn(L)/comp}$.

The variation of the reaction rate constants and the physical parameters with temperature is not known. A parametric study for a model describing the galvanizing reactions in the case of GI baths was carried out by Giorgi [32], showing the influence of a variation of 10% of each parameter one by one on the thickness of the interfacial layer formed after 3 s (Table 21). It should be noted that the influence of constant k_{nucl} (Pa.m^{-2}) has not been specifically considered in this parametric study because the variation of the nucleation rate has already been fully taken into account by the variation the interfacial tension between the interfacial compound and liquid zinc. The small difference of 10 °C in temperature between the two conditions tested here (450 and 460 ℃) should entail a slight variation in the different physical parameters and reaction rate constants. If this variation is assumed to be less than 10%, the variation of the thickness of the interfacial alloy is very low except in the case of a variation of the interfacial tension between the interfacial compound and liquid zinc. Even then, the variation of the thickness of the interfacial alloy of 23% is less than the dispersion found in the measured thicknesses of the interfacial alloy (Table 17).

Table 21: Parametric study for a model describing the galvanizing reactions in the case of GI baths [32]. Influence of a variation of 10% of each physical parameter and reaction rate constant on the thickness of the interfacial alloy obtained ($Fe_2Al_5Zn_x$ in this case).

Physical parameters and reaction rate constants	Variation of the thickness of the interfacial alloy (%)
$D_{Fe}^{Zn(L)}$ (m^2.s^{-1})	-2
$D_{Al}^{Zn(L)}$ (m^2.s^{-1})	-0.1
D_{Fe}^{comp} (m^2.s^{-1})	+1
$\sigma^{Zn(L)/comp}$ (J.m^{-2})	+23
k_{diss} (m.s^{-1})	+2
k_{growth} (m.s^{-1})	+0.2

Finally, to sum up, a slight variation in the galvanizing bath temperature is not expected to change the chemical nature of the inhibition layer. It could have only a slight influence on its kinetics of formation and final thickness for a difference of 10 ℃ in the bath temperature.

II.3.1.2.2. Effect of the bath aluminium content

As stated in Table 11, steels A and B were galvanized in iron-saturated zinc baths with different aluminium contents. While steel A was galvanized in a zinc bath containing 0.112 wt.% Al, steel B was galvanized in a zinc bath containing 0.128 wt.% Al. The compositions of these galvanizing baths are represented in Figure 64 by the red point, in the case of steel A, and the blue one, in the case of steel B.

As shown previously (section II.3.1.2.1), the influence of the bath temperature in the range of 450 – 460 ℃ on the nature of the intermetallic compounds found in the phase diagram at a given aluminium content is negligeable. On the contrary, the bath aluminium content has a major influence on these intermetallic compounds found in equilibrium with the liquid phase and therefore probably in the inhibition layer. In particular, the Gibbs free energy of formation of metastable compounds such as the ζ and $Fe_2Al_5Zn_x$ phases from the supersaturated bath could strongly vary as a function of the bath aluminium content.

To go into further explanations based on Giorgi [32], because of the dissolution, the concentration of iron at the interface between steel and liquid zinc increases and exceeds the saturation limit with respect to an intermetallic compound denoted *comp* in the following (*comp* can be δ or $Fe_2Al_5Zn_x$). The degree of supersaturation, designated β_{comp}, is the driving force for heterogeneous nucleation of *comp* on the surface of the sheet, and is given by:

$$\beta_{comp} = \left(\frac{a_{Fe}}{a_{Fe}^{comp,sat}}\right)^{x_{Fe}^{comp}} \left(\frac{a_{Al}}{a_{Al}^{comp,sat}}\right)^{x_{Al}^{comp}} \left(\frac{a_{Zn}}{a_{Zn}^{comp,sat}}\right)^{x_{Zn}^{comp}} \tag{II.5}$$

where a_{Fe}, a_{Al}, a_{Zn} are the activities of iron, aluminium and zinc in the supersaturated bath, $a_{Fe}^{comp,sat}$, $a_{Al}^{comp,sat}$, $a_{Zn}^{comp,sat}$ the activities of iron, aluminium and zinc in the saturated bath in equilibrium with the intermetallic compound under consideration (stable equilibrium with δ and metastable equilibrium with $Fe_2Al_5Zn_x$), x_{Fe}^{comp}, x_{Al}^{comp}, x_{Zn}^{comp} the mole fractions of iron, aluminium and zinc in *comp* (Table 5, [7]).

The intermetallic compound is formed by heterogeneous nucleation on the steel surface. The nuclei are supposed to be hemispherical (Figure 65).

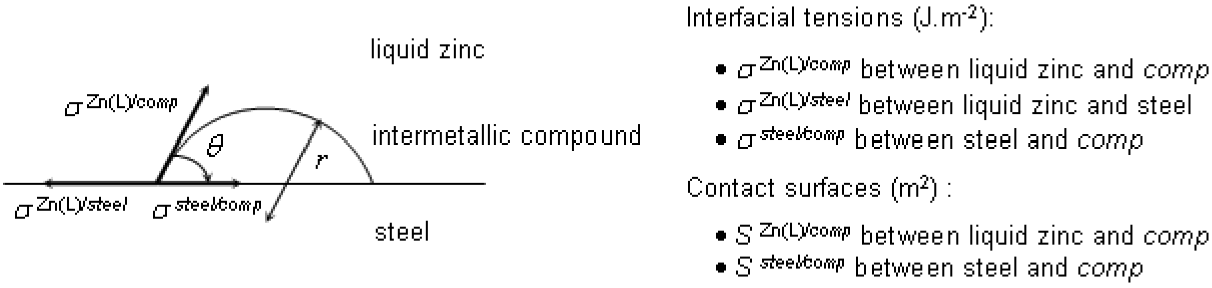

Figure 65: Interfacial tensions involved in the heterogeneous nucleation on the steel surface of an intermetallic compound denoted *comp*.

The Gibbs free energy ΔG_{het}^{comp} of formation of an embryo containing *n* molecules of the intermetallic compound *comp* from a supersaturated bath is given by:

$$\Delta G_{het}^{comp} = \Delta G_{vol}^{comp} + \Delta G_{surf}^{comp} = -n\, k_B\, T \ln \beta_{comp} + S^{\mathrm{Zn(L)}/comp}\, \sigma^{\mathrm{Zn(L)}/comp} + S^{steel/comp} \left(\sigma^{steel/comp} - \sigma^{\mathrm{Zn(L)}/steel} \right) \tag{II.6}$$

where $\sigma^{steel/comp} - \sigma^{\mathrm{Zn(L)}/steel} = -\sigma^{\mathrm{Zn(L)}/comp} \cos\theta$, θ is the wetting angle, *T* the temperature, k_B the Boltzmann's constant (1.38.10^{-23} J.K^{-1}). ΔG_{het}^{comp} is balanced by the energy gain of creating a new volume ΔG_{vol}^{comp} function of the degree of supersaturation β_{comp} and the energy cost due to the creation of new interfaces ΔG_{surf}^{comp} function of the interfacial tensions of the system.

In the case of steels A and B studied here, the first intermetallic compound to be formed will be the one with the lowest Gibbs free energy of formation ΔG_{het}^{comp}. As δ is the intermetallic compound in equilibrium with the liquid phase in both cases, $\beta_{\delta} > \beta_{Fe2Al5ZnX}$ and therefore $\Delta G_{vol}^{\delta} < \Delta G_{vol}^{Fe2Al5Znx}$. If $Fe_2Al_5Zn_x$ is formed, it can only be explained by the differences in the terms ΔG_{surf}^{comp}.

For high bath aluminium contents in the GA domain, when the bath composition is close to the knee point β, $Fe_2Al_5Zn_x$ could form easily out of equilibrium due to preferential epitaxial relationships between this compound and the ferrite or better wetting than δ which decreases $\Delta G_{surf}^{Fe2Al5Znx}$ compared to ΔG_{surf}^{δ}. In this case, ΔG_{het}^{δ} could become higher than $\Delta G_{het}^{Fe2Al5Znx}$. On the other hand, the metastability of ζ remains high when the bath composition is far away from the knee point α, i.e., $\Delta G_{vol}^{\delta} << \Delta G_{vol}^{\xi}$, and cannot be overcame by the preferential epitaxial relationships between this phase and the ferrite. This is the reason why, in the case of steel B, only metastable $Fe_2Al_5Zn_x$ nucleates on the steel surface and almost no presence of epitaxial ζ is detected.

If the bath aluminium content is now progressively lowered, the metastability of $Fe_2Al_5Zn_x$ becomes higher and higher, i.e. $\Delta G_{vol}^{Fe2Al5Znx}$ increases, and that of ζ lower and lower, i.e., ΔG_{vol}^{ξ} decreases. This is the reason why, in the case of steel A, the nucleation of $Fe_2Al_5Zn_x$ is more difficult and $Fe_2Al_5Zn_x$ grows discontinuously on the steel surface either with stable δ or epitaxial ζ crystals, which are now easily observed.

II.3.1.2.3. Effect of the immersion time

The immersion time will obviously have an important effect on the inhibition layer growth. A longer immersion time gives rise to a thicker inhibition layer. The mean thickness of the inhibition layer obtained on steel B is greater than the one obtained on steel A (Table 17). The immersion time could be one of the parameters explaining this difference.

II.3.1.3. Effect of the steel surface state

It is well known that the steel surface state can play an important role on the formation of the inhibition layer.

For instance, the presence of external selective oxides may hamper the wettability of the steel substrate by the liquid zinc leading to bare spots in the coating. Nevertheless, the steels investigated here are Ti IF steel grades, so they are not in principle subjected to this problem as they are very poor in those alloying elements with high affinity for oxygen such as manganese, silicon or aluminium which may give rise to the commented oxides [56] (section I.3.1.3.1).

One of the differences between the two steels investigated is the roughness and the waviness of the surface (Table 10). The influence of these differences on the formation of the inhibition layer (e.g., characteristic dimensions of the interfacial alloy) cannot be precisely deduced from our experiments. However, the structure of the inhibition layer seems to be very similar on both steels (section

II.2.3.3.3). As shown previously, the nature of the inhibition layer is probably not linked to the steel roughness and waviness.

Finally, as detailed earlier in this chapter, the crystallographic orientation of the steel surface grains has a major influence on the nature of the inhibition layer. Epitaxial metastable $Fe_2Al_5Zn_x$ and ζ crystals may nucleate, instead of stable δ, on the steel surface, depending on the grains orientation. The cold rolled and annealed ferritic steels as the ones investigated here are textured steels, i.e., they have grains with a precise and well-defined preferential cristallographic orientation [92]. As indicated in section II.1.2.2, EBSD characterizations were performed on the mechanically polished and CSP cross section samples in order to check the surface grains orientation of the two steels studied. All the Inverse Pole Figure (IPF) maps shown below correspond to crystal orientations according to the scheme depicted in Figure 66a. Red, green, and blue colours are assigned to grains whose <001>, <101> or <111> axes, respectively, are parallel to the projection direction of the IPF, in this case the normal direction (designated hereinafter ND, and the rolling direction RD). The legend for the understanding of misorientation angle distribution maps is available in Figure 66b.

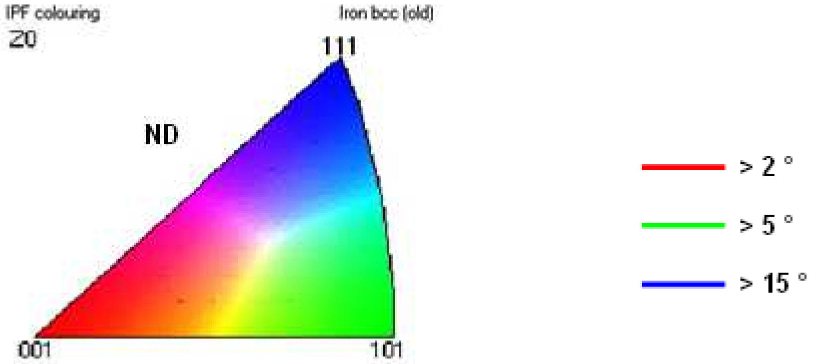

(a) (b)

Figure 66: Key orientation color legends for the understanding of IPF maps (a) and misorientation angle distribution maps (b).

The IPF maps and the misorientation angle distribution obtained in the case of the mechanically polished cross section samples (length of the interface between the steel and the inhibition layer around 1.2 mm) are presented in Figure 67, for steel A, and Figure 68, for steel B.

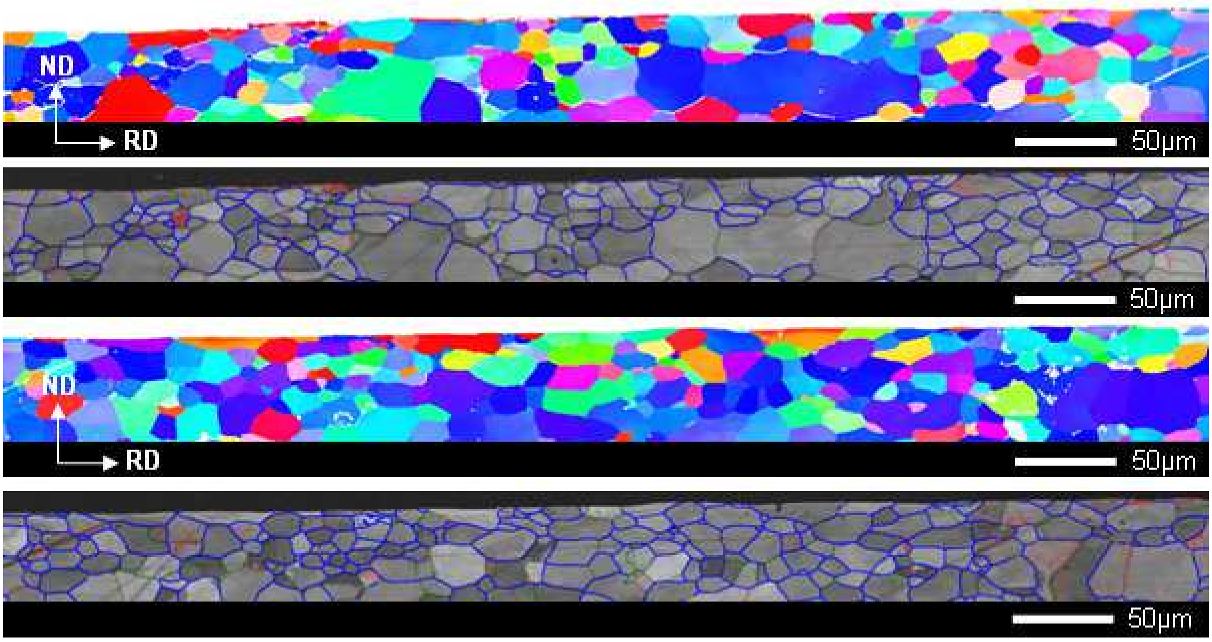

Figure 67: IPF and misorientation angle distribution maps corresponding to the mechanically polished cross section sample prepared from steel A.

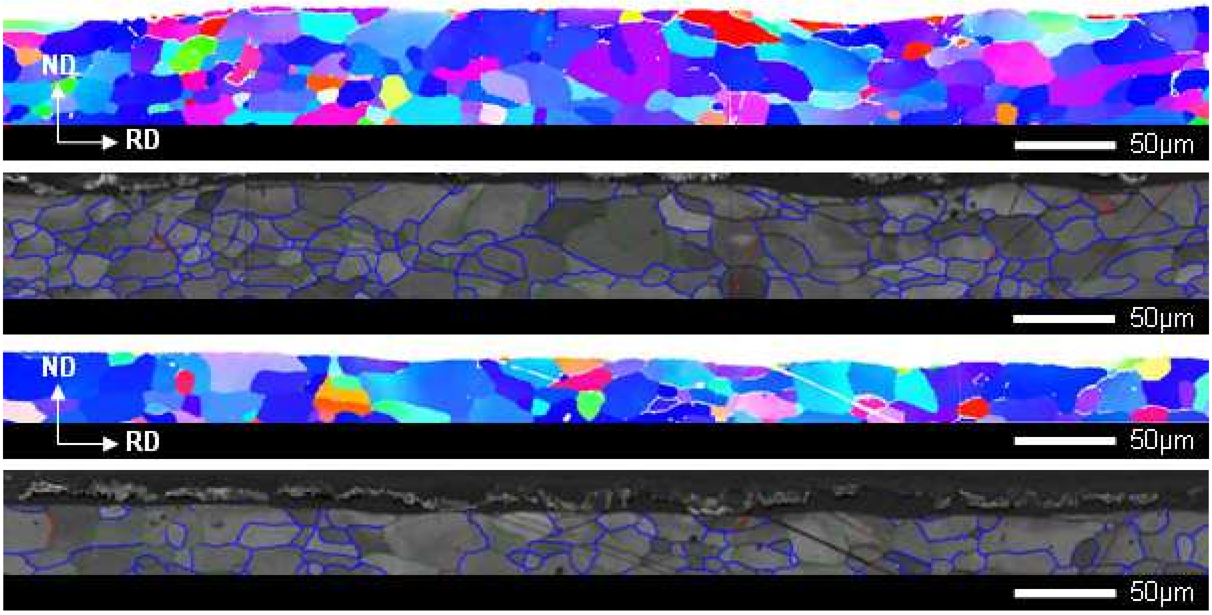

Figure 68: IPF and misorientation angle distribution maps corresponding to the mechanically polished cross section sample prepared from steel B.

As can be observed, grains are recrystallized in both steels and, as expected, these latter appear to be textured steels (their grains have a preferred crystallographic orientation, with their <111> axe parallel to the normal direction) and no substantial difference can be reported between the crystallographic orientations of the surface grains of both steels. However, in spite of the just reported similar surface state, the $Fe_2Al_5Zn_x$ layer has been found to be clearly discontinuous in the case of the mechanically polished cross section sample prepared from steel A and fairly continuous in the case of the one prepared from steel B (Figure 69), confirming the results obtained on the CSP samples (section II.2.1).

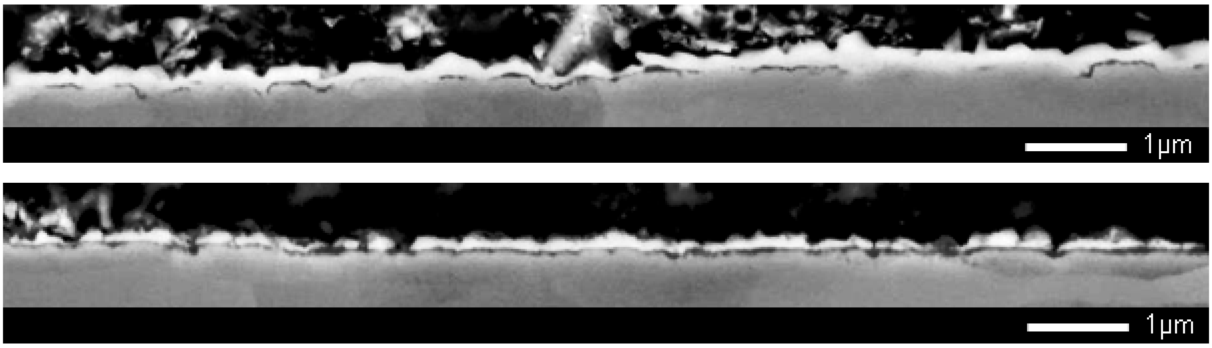

Figure 69: Cross section SEM micrographs of the inhibition layer performed on the mechanically polished samples prepared from steels A (top) and B (bottom).

Similar EBSD characterizations were performed on the CSP samples of both steels. Results are shown in Figure 70, for steel A, and Figure 71, for steel B.

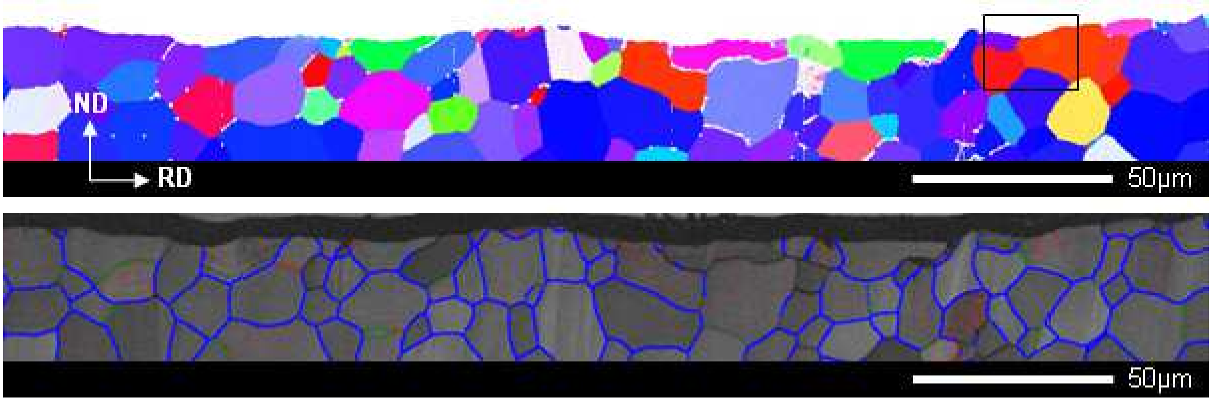

Figure 70: IPF and misorientation angle distribution maps corresponding to the CSP sample prepared from steel A.

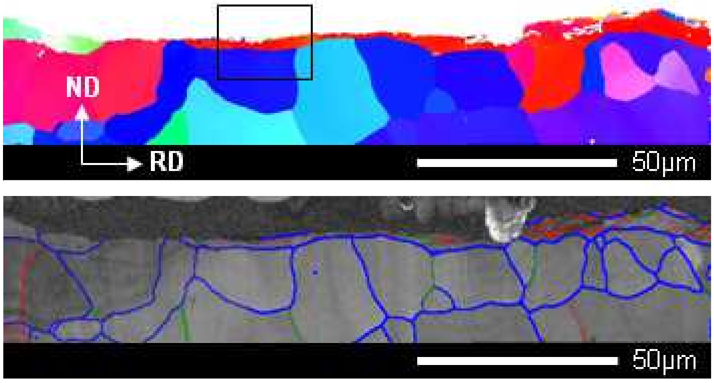

Figure 71: IPF and misorientation angle distribution maps corresponding to the CSP sample prepared from steel B.

Once again, the grains are globally recrystallized in both steels (with the exception of the right-hand side of the CSP sample from steel B). The inhibition layer was observed in those areas delimited by the black rectangles on the IPF maps of Figure 70, for steel A, and Figure 71, for steel B, corresponding to steel grains with the same crystallographic orientation, with their <001> axe parallel to the normal direction. As can be observed in Figure 72, the $Fe_2Al_5Zn_x$ layer on these grains is discontinuous on steel A and continuous on steel B.

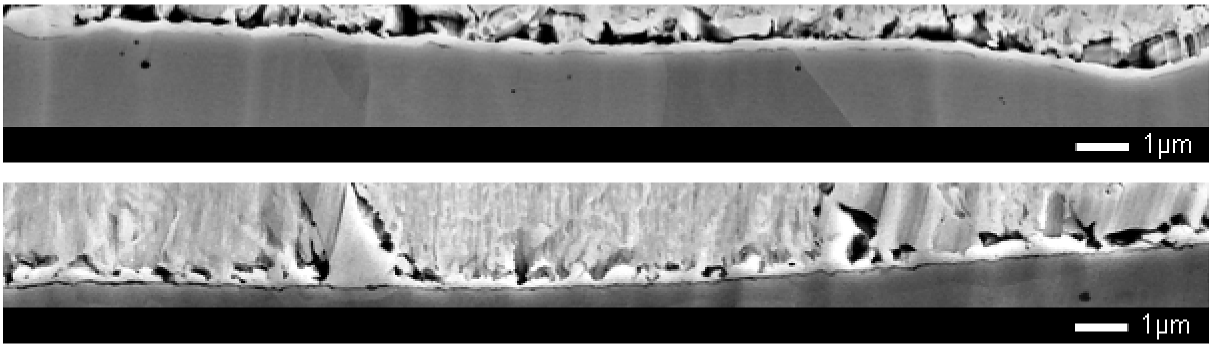

Figure 72: Cross section SEM micrographs of the inhibition layer performed on the CSP samples prepared from steels A (top) and B (bottom).

It can therefore be concluded from all the results presented here above that the steel surface grains orientation cannot explain the difference observed in the structure of the inhibition layer of steels A and B. The difference in the continuity of the $Fe_2Al_5Zn_x$ layer would be in principle not related to the steel surface state but to the different galvanizing conditions applied to coat both steels.

II.3.2. Final structure and phase composition of the inhibition layer

In order to simplify the analysis, the existence of epitaxial ζ rod crystals will be neglected because of their seldom presence within the inhibition layer, even at very low bath aluminium contents in the GA domain, compared to the presence of the δ and $Fe_2Al_5Zn_x$ phases. In addition, as it has been stated before, the evanescent ζ crystals must not be considered as they would not be formed in classical process conditions during galvannealed coatings production.

The previous considerations taken into account, it is important to highlight that although the formation of the inhibition layer formed in typical GA baths may pass through a metastable state with the nucleation of the $Fe_2Al_5Zn_x$ phase at the steel / liquid phase interface, the subsequent nucleation of the δ phase at the $Fe_2Al_5Zn_x$ / liquid phase interface allows the final whole microstructure to reach the thermodynamic equilibrium along all interfaces. This microstructure can be described by means of the concept of diffusion path in the Al-Fe-Zn ternary phase diagram at 450 - 460 ℃, as depicted in Figure 73.

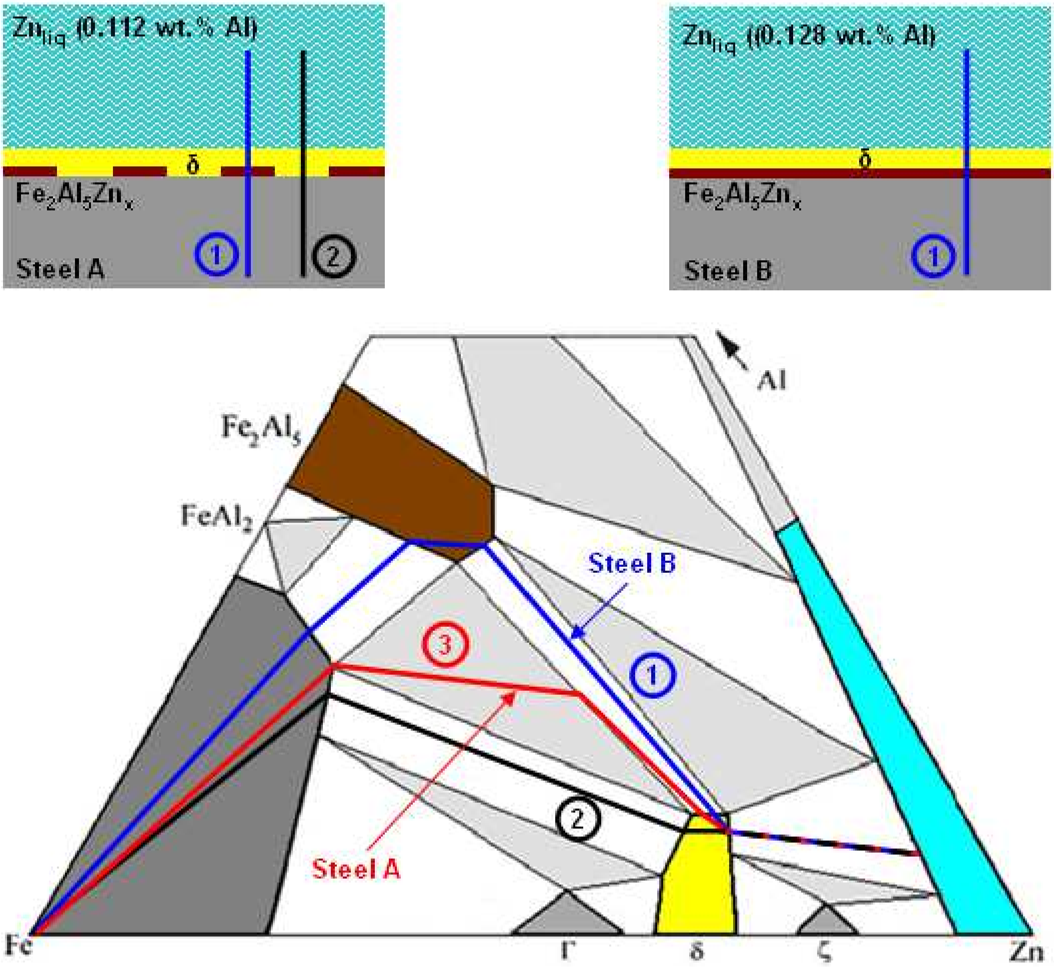

Figure 73: Schematic representation of diffusion paths on the Al-Fe-Zn ternary phase diagram at 450 - 460 ℃ describing the thermodynamic equili brium along all interfaces in the case of steels A (real diffusion paths 1 and 2, locally, and virtual diffusion path 3, globally) and B (real diffusion path 1) (bottom) and the corresponding microstructures (top).

The final microstructure of steel B consists of successive continuous ayers with planar interfaces: steel / $Fe_2Al_5Zn_x$ / δ / zinc overlay (top right-hand side of Figure 73). Assuming thermodynamic equilibrium along all interfaces, this microstructure can be represented by the real (along tie lines through binary domains) diffusion path 1 in Figure 73.

However, in the case of steel A, the $Fe_2Al_5Zn_x$ layer is discontinuous and the successive stratified layers can be locally either steel / $Fe_2Al_5Zn_x$ / δ / zinc or steel / δ / zinc (top left-hand side of Figure 73). Each of these local microstructures may be described by real diffusion paths 1 and 2 in Figure 73. The global diffusion path corresponding to steel A can be represented by the virtual diffusion path 3. Equilibrium along the steel surface is therefore a ternary equilibrium (steel, δ, $Fe_2Al_5Zn_x$).

In both cases, the nucleation and growth of the δ phase allows all the interfaces to reach thermodynamic equilibrium, temporarily stabilizing the inhibition layer.

II.4. Conclusions

The following main conclusions can be drawn from this chapter:

The inhibition layer formed in GA baths is mainly biphasic and composed of a very thin layer of $Fe_2Al_5Zn_x$ and a thicker layer of δ on top of it. Both observed microstructures (with continuous $Fe_2Al_5Zn_x$ for steel B and discontinuous $Fe_2Al_5Zn_x$ for steel A) allow thermodynamic equilibrium to be reached along all the interfaces and can be described by a diffusion path in the Al-Fe-Zn ternary phase diagram at 450 - 460 °C.

Proposed mechanism accounting for the formation of this inhibiting layer can be summarized in the following steps: wetting of the steel surface by the liquid zinc, iron dissolution from the steel surface into the liquid phase, iron supersaturation at the steel / liquid zinc interface, nucleation of metastable $Fe_2Al_5Zn_x$, due to preferential epitaxial relationships with the ferrite and better wetting than δ, and nucleation and growth of the δ phase, which allows all the interfaces of the final microstructure of the inhibition layer to reach thermodynamic equilibrium.

Metastable epitaxial ζ rod crystals have also been observed within the inhibition layer, although in lesser quantity compared to the $Fe_2Al_5Zn_x$ and δ phases. These ζ crystals would nucleate during immersion in the galvanizing bath on grains with the adequate crystallographic orientation of either the steel substrate or the thin $Fe_2Al_5Zn_x$ layer, which would have the ability to transfer the crystallography of the steel substrate.

The thin layer of $Fe_2Al_5Zn_x$ becomes discontinuous when decreasing the bath aluminium content. Assumption to explain this observation is that, as the bath aluminium content is decreased, the metastability of $Fe_2Al_5Zn_x$ becomes higher and its nucleation less probable. Similarly, when the bath aluminium content is decreased, the quantity of epitaxial ζ crystals increases as their metastability becomes lower and their nucleation more probable.

CHAPTER III: THE INHIBITION LAYER BREAKDOWN

It has been seen in section I.3.2 that the inhibitory action exerted by the so-called inhibition layer is only temporary. Although the interfaces are in thermodynamic equilibrium in the coating, diffusional phenomena will finally lead to the breakdown of this layer. The galvannealing heat treatment after the galvanizing bath will favour the iron and zinc inter-diffusion through this layer:

- The iron diffusion flux from the steel substrate towards the coating is expected to make the inhibition layer grow by consuming aluminium from the liquid phase. After wiping, if the aluminium depletion in the liquid is high enough, the inhibition layer / liquid zinc interface will be destabilized and aluminium-poor Fe-Zn compounds (ζ rod crystals) will nucleate.

- The zinc diffusion flux towards steel will induce zinc enrichment of the steel / inhibition layer interface. As the temperature remains too low to favour zinc diffusion within the steel grains, zinc atoms accumulate along the emerging lines of the steel grain boundaries. As a result, the increasing zinc concentration at these locations will finally lead to the local nucleation of Fe-Zn compounds. This nucleation induces local volume expansion that makes the inhibition layer break up. This phenomenon is commonly known as *outburst reaction* and the Fe-Zn phase nucleating at the steel grain boundaries predicted by the phase diagram is the Γ phase.

Two different reaction mechanisms can therefore exist in competition. However, as stated in section I.3.2, experiments performed on Ti IF steel grades show that the inhibition layer breakdown occurs in most typical process conditions through the outburst reaction controlled by zinc diffusion towards the steel grain boundaries. In other words, this reaction is very often the one with the fastest kinetics. The kinetics accounting for this reaction strongly depends on the steel substrate chemical composition and the bath aluminium content (section I.3.2.2).

Influence of the steel substrate chemical composition

As stated in section I.3.2.2.2.2, the presence in the steel of some chemical elements such as carbon, nitrogen, sulphur, phosphorous, titanium or niobium strongly influences the kinetics of the outburst reaction. On the one hand, carbon, nitrogen, sulphur and phosphorous tend to segregate towards the steel grain boundaries during continuous annealing (before galvanizing) and may act as a barrier against diffusion of zinc at these sites. On the other hand, titanium and niobium will trap the previous elements in the form of precipitates such as carbides and nitrides during continuous annealing, reducing their segregation and promoting the cleanliness of the steel grain boundaries. Therefore, while the presence of carbon, nitrogen, sulphur and phosphorous in the steel would a priori slow down the kinetics of the inhibition layer breakdown, the presence of titanium and niobium would accelerate it.

The definition of a parameter representative of the steel chemical reactivity with respect to the inhibition layer breakdown is not evident. In the case of Ti IF steel grades, this key parameter could be the weight fraction of excess solute titanium, $w_{Ti_{excess}}$, i.e., the weight fraction of titanium in solution in the ferrite structure. Very few authors have made a proposal for its calculation.

The most conventional equation to calculate the excess solute titanium is as follows:

$$w^*_{Ti_{excess}} = w_{Ti_{total}} - \frac{48}{12} w_C - \frac{48}{14} w_N - \frac{48}{32} w_S \qquad \text{(III.1)}$$

where $w_{Ti_{total}}$, w_C, w_N and w_S are the weight fractions of titanium, carbon, nitrogen and sulphur present in the steel. According to equation (III.1), the excess solute titanium is calculated as the amount of titanium remaining in solution when the total amounts of carbon, nitrogen and sulphur in the steel are stabilized as TiC, TiN and TiS respectively.

Toki *et al*. [76] reported that the precipitation of phosphorous as FeTiP should also be taken into account in the calculation of the excess solute titanium:

$$w^{**}_{Ti_{excess}} = w_{Ti_{total}} - \frac{48}{12} w_C - \frac{48}{14} w_N - \frac{48}{32} w_S - \frac{48}{31} w_P \qquad \text{(III.2)}$$

where w_P is the weight fraction of phosphorous present in the steel. As can be observed in equation (III.2), Toki *et al*. [76] also supposed that the total amounts of carbon, nitrogen sulphur and phosphorous are trapped by titanium during continuous annealing.

The above calculations found in the literature do not give precise estimations of the titanium content in solution in the steel (e.g., it could be negative for a given steel composition) but can be considered as a measure of the cleanliness of the steel grain boundaries and, therefore, of the reactivity of the steel with respect to the inhibition layer breakdown.

In the present study, a different calculation of the excess solute titanium, proposed internally by ArcelorMittal Global R&D, is also considered:

$$x_{Ti_{excess}} = \left(w_{Ti_{total}} - \frac{48}{12} w_C - \frac{48}{14} w_N - \frac{48}{32} w_S \right) \times \frac{31}{48 w_P} \qquad \text{(III.3)}$$

As shown in equation (III.3), this alternative calculation considers, as the previous ones do, that the total amounts of carbon, nitrogen and sulphur are trapped by titanium as TiC, TiN and TiS respectively, but supposes that phosphorous could be partially trapped in FeTiP precipitates. Indeed, this calculation represents the molar ratio between the solute titanium available after the supposed precipitation of the total amounts of carbon, nitrogen and sulphur and the phosphorous content in the steel. In other words, it represents the ability of titanium to trap phosphorous as FeTiP.

In addition, another parameter able to represent the steel chemical reactivity with respect to the inhibition layer breakdown has been proposed by ArcelorMittal Global R&D as well. Contrarily to the previous ones, it takes into account the silicon content in the steel. It has been named *Reactivity Index* and has been defined as follows:

$$Reactivity\ Index = \left(w_{Ti_{total}} - \frac{48}{12} w_C - \frac{48}{14} w_N - \frac{48}{32} w_S - \frac{48}{31} w_P \right) \times \frac{28}{48 w_{Si}} \qquad \text{(III.4)}$$

where w_{Si} is the weight fraction of silicon present in the steel.

As it can be seen, this last parameter represents the molar ratio between the solute titanium available after the supposed precipitation of the total amounts of carbon, nitrogen, sulphur and phosphorous (parameter $w^{**}_{Ti_{excess}}$, proposed by Toki *et al*. [76] and defined by equation (III.2)) and the silicon content in the steel.

Influence of the bath aluminium content

As advanced in section I.3.2.2.1.1 and demonstrated experimentally in the previous chapter, the bath aluminium content has a major effect on the structure and phase composition of the inhibition layer and, consequently, on the kinetics accounting for its breakdown.

However, it has been shown in section I.3.2.2.3 that, although experimental evidence and numerous qualitative results proving the effects reported above are available in the literature in the case of IF steel grades, very few kinetic data have been published. Moreover, these data are often quite inconsistent with each other.

This chapter synthesizes the results of a study with the objective to evaluate the effect of the steel chemical composition and the bath aluminium content on the kinetics of the inhibition layer breakdown in the case of Ti IF steel grades. As will be seen, these results provide additional precious information for a better understanding of the reaction mechanism for the inhibition layer breakdown, which will be tackled in detail as well. Modelling work is also carried out.

III.1. Experimental procedure

III.1.1. Materials

Four different commercial Ti IF full hard steel substrates, A, B, C and D, have been selected for this study. Their average chemical composition is shown in Table 22. The analysis was performed by means of Combustion and Infrared Detection for nitrogen (HORIBA EMGA-620W) and Spark-OES (SPECTROLAB M10) for the other elements in ArcelorMittal laboratories. It should be pointed out that steel C is actually the same full-hard steel substrate as steel B in chapter II (Table 9). The thicknesses of steels A, B, C and D are very similar and equal to 0.75, 0.70, 0.74 and 0.74 mm respectively.

Table 22: Average chemical composition (x 10^{-3} wt.%) of the commercial Ti IF steels studied.

Steel	C	Mn	P	S	N	Si	Cu	Ni	Cr	Sn	As	Nb	Mo	B	Ti	Al
A	3.0	100.2	12.4	14.1	3.4	9.3	25.5	17.4	21.8	5.7	2.7	0.1	2.6	0.5	57.4	44.6
B	2.1	89.9	13.6	15.2	3.9	4.0	24.8	13.9	22.3	3.0	1.8	-	2.2	-	83.6	29.1
C	2.0	110.0	9.1	9.0	2.1	4.0	17.0	14.3	18.2	5.7	-	0.1	1.8	0.0	67.3	49.1
D	2.2	99.9	6.9	12.5	3.4	4.6	36.6	20.3	27.9	3.9	2.0	0.1	1.9	-	84.1	55.8

As shown in Table 23, the chemical reactivity of these steels with respect to the inhibition layer breakdown was quantified by the parameters defined at the beginning of this chapter. The use of any of these parameters leads to the same steel reactivity classification: A < B < C < D, where < means *is less reactive than* (except for the reactivity of steels B and C when quantified by $w^{*}_{Ti_{excess}}$, which is the only parameter that does not take the steel phosphorous content into account). When the chemical reactivity parameter is less than 0, it means that there is not enough titanium in the steel to trap the total amounts of carbon, nitrogen, sulphur and phosphorous.

Table 23: Chemical reactivity parameters of the commercial Ti IF steels studied.

Steel	Chemical Reactivity Parameter			
	$w^{*}_{Ti_{excess}}$ (10^{-3} wt.%) (equation (III.1))	$w^{**}_{Ti_{excess}}$ (10^{-3} wt.%) (equation (III.2))	$x_{Ti_{excess}}$ (equation (III.3))	*Reactivity Index* (equation (III.4))
A	12.6	-6.6	0.7	-0.4
B	39.0	18.0	1.8	2.6
C	38.6	24.5	2.7	3.6
D	44.9	34.2	4.2	4.3

The experimental results obtained in the present study will be used to identify the most appropriate parameter to quantify the chemical reactivity of the steel with respect to the inhibition layer breakdown. In any case, steels A and D are expected to be the most different substrates in terms of reactivity behaviour: the inhibition layer breakdown would in principle be achieved noticeably earlier in the case of steel D when submitted to the same heat treatment.

III.1.2. Laboratory pilots and simulations

III.1.2.1. The Rhesca Hot Dip Galvanizing simulator

The commercial steel sheets received from the industrial lines were cut into samples with dimensions of 210 x 99 mm^2. These samples were cleaned with ethanol to remove residual oil from former manipulations. Samples were then submitted to an annealing heat treatment and galvanized at two different bath aluminium contents in a Rhesca Hot Dip Galvanizing simulator [15].

General description

An illustration of this simulator can be appreciated in the left-hand side of Figure 74. A detailed sketch of this pilot, where its different elements are clearly identified, is likewise shown in the right-hand side of Figure 74. This pilot comprises a zinc melting pot, an infrared furnace and a cooling section. The sample is introduced at the top of the pilot in front of the coolers. It is first lowered into the infrared furnace to be heated to the continuous annealing holding temperature and maintained at this temperature. It is then taken back to the cooling section to be cooled to the equalizing temperature and lowered again into the infrared furnace to be maintained at this temperature. Then the sample goes down to be immersed in the zinc pot, passes in front of the wipers to fix the coating thickness and is finally cooled in two different stages (first cooling to 200 ℃ just after wiping followed by final cooling to room temperature in the cooling section).

The annealing treatment is performed in an atmosphere of N_2 and 5 vol.% H_2 with -60 ℃ dew point.

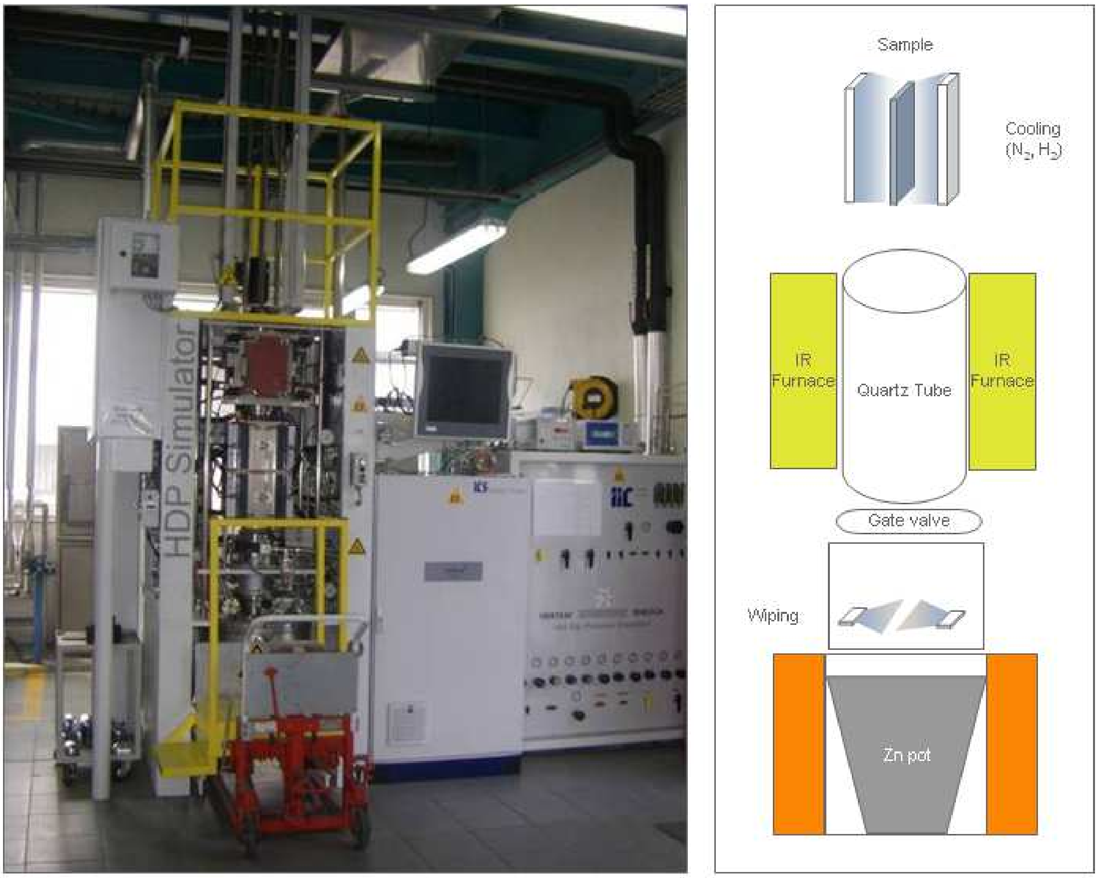

Figure 74: Illustration (left) and sketch (right) of the Rhesca Hot Dip Galvanizing simulator.

---

[15] The Rhesca / later Iwatani Surtec Hot Dip Process Simulator was purchased from Rhesca in 1989, and underwent major revamping by Iwatani Surtec in 2001, 2004 and 2011.

Thermal homogeneity of the Rhesca samples

It is crucial in this study to ensure the thermal homogeneity within the sample. Figure 75 depicts a schematic representation of a Rhesca sample. In order to check the thermal homogeneity, the temperature was measured by means of three type-K thermocouples spot-welded at different locations on the sample. The thermal homogeneity area is delimited by the red rectangle. The thermal homogeneity criterion is ± 5 ℃.

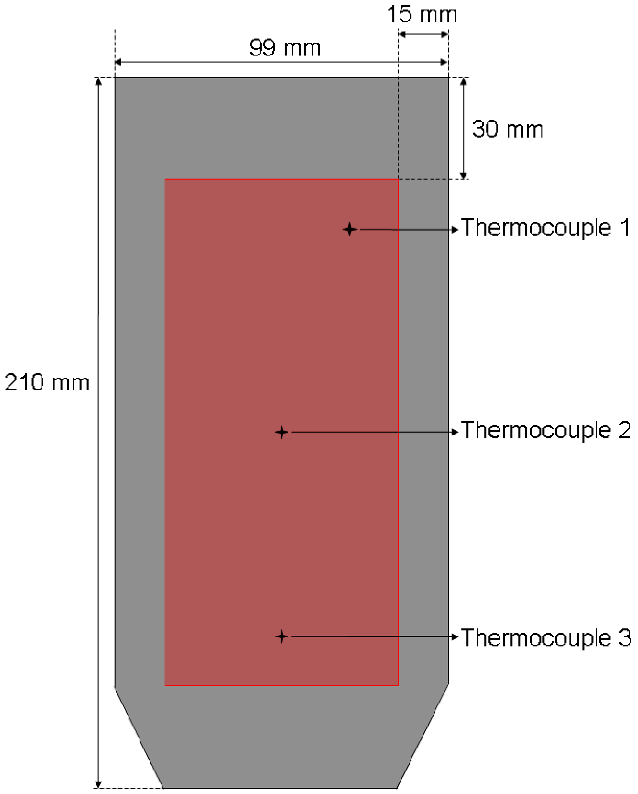

Figure 75: Schematic view of a Rhesca sample with its thermal homogeneity area in red.

Thermal cycles performed in the present study

All the samples were submitted to the same programmed Rhesca thermal cycle. The different setpoints of the thermal cycle were as follows:

- Heating to a soaking temperature of 800 ℃ at a heating rate of around 20 ℃/s;
- Soaking at 800 ℃ for 40 s;
- Cooling to an overaging temperature of 460 ℃ at a cooling rate of around 50 ℃/s;
- Overaging at 460 ℃ for 35 s;
- Immersion (15 mm coated length) in the zinc bath at 460 ℃ (immersion time of 0.7 s at the mid-length of the coated part of the sample);
- Wiping (150 L/min N_2[16]);
- Cooling to 200 ℃ just after wiping (150 L/min (N_2 + 5 vol.% H_2));
- Final cooling to room temperature in front of the coolers (1000 L/min N_2).

The temperature was measured by means of a type-K thermocouple placed in the thermal homogeneity area of the sample, more precisely in its right-hand upper side, as depicted by the

---

[16] All the flow rates correspond to temperature and pression conditions of 295.85 K and 100 kPa.

position of *thermocouple 1* in Figure 75. An example of a real thermal cycle together with the sample position within the Rhesca pilot is shown in Figure 76.

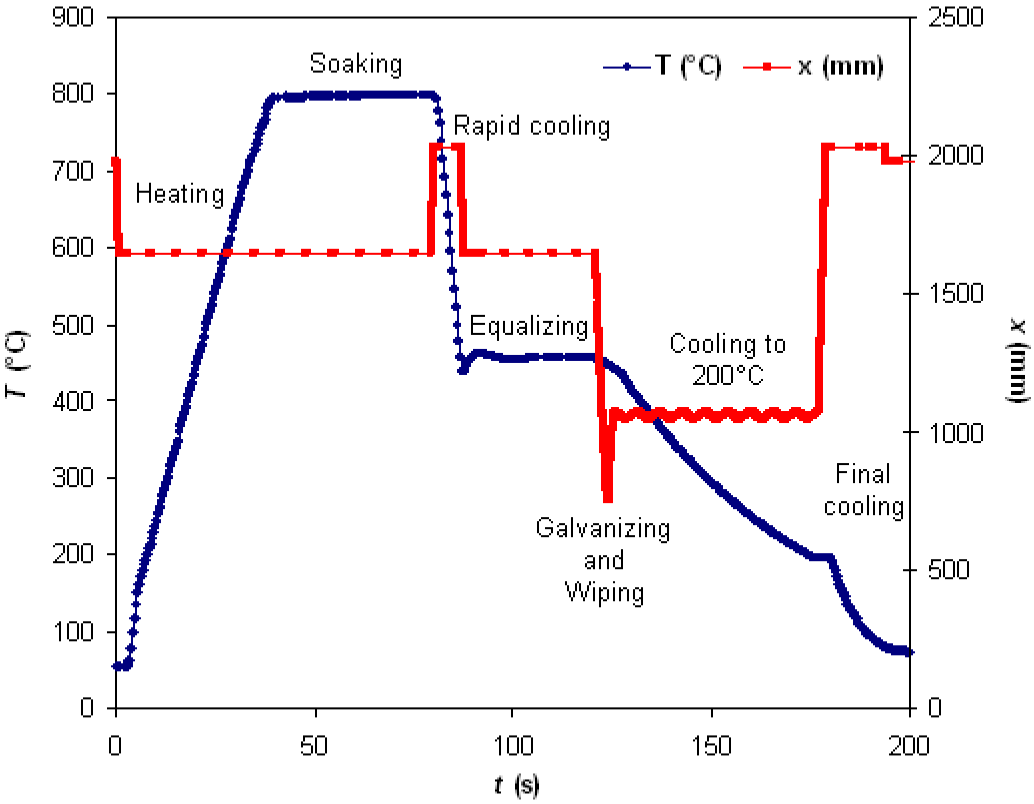

Figure 76: Example of a real thermal cycle performed on the Rhesca pilot simulator (blue) together with the sample position within the pilot with respect to ground level (red).

The cooling phase after hot-dip galvanizing in the Rhesca simulator is very important because the diffusion of zinc through the inhibition layer leading to its breakdown already takes place during immersion in the galvanizing bath and the cooling step and must be taken into account when determining the inhibition layer breakdown kinetics. The hot-dip galvanizing time is accurately controlled and special attention was therefore paid to the subsequent cooling phase. Figure 77 shows the temperature profiles obtained during the cooling step for four different samples of steel B. An almost instantaneous cooling of around 20 °C induced by the wiping operation, the slow cooling up to 200 °C and the fast cooling up to room temperature can be easily distinguished on these temperature profiles, found to be highly reproductible (± 2 °C) .

It should also be noticed that variations in the cooling after the exit of the zinc bath could be expected, depending on the sample thickness. However, as seen in section III.1.1, the thicknesses of the different steel substrates are very close to each other and no substantial variations in the cooling are observed (± 5 °C, Figure 78).

In addition, as it will be argued in section III.3.2.2.2, zinc diffusion towards the steel grain boundaries, responsible for the inhibition layer breakdown, can be neglected below 400 °C and coolings until reaching this temperature are in most cases nearly identical (± 1 °C).

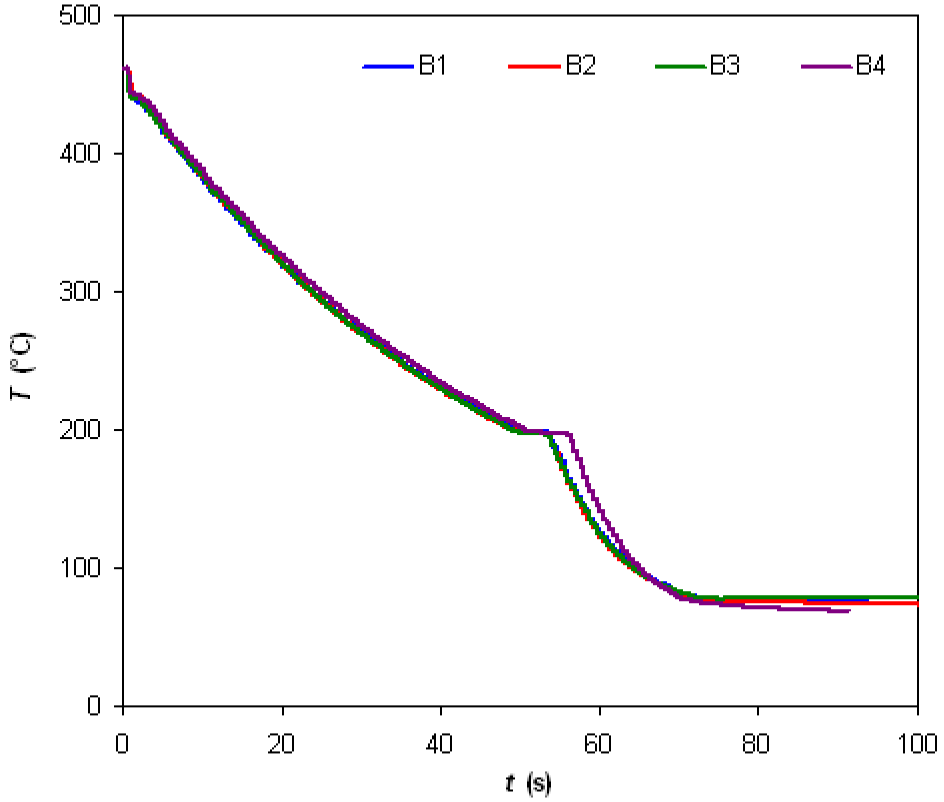

Figure 77: Reproductibility of the temperature profiles obtained (4 trials) during the cooling step performed on the Rhesca pilot simulator (steel B).

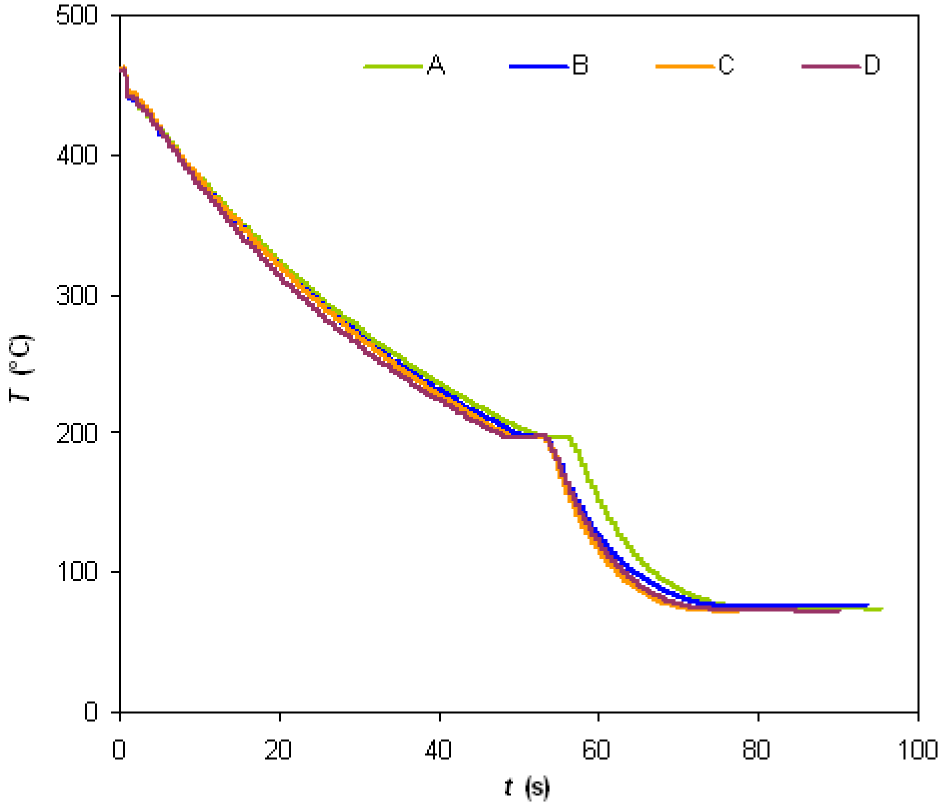

Figure 78: Cooling performed on the Rhesca pilot simulator for the different steels.

Control of the galvanizing bath composition and temperature

The composition of the zinc bath must also be extremely well controlled as it influences the nature of the inhibition layer and is therefore expected to have a substantial effect on the inhibition rupture kinetics. Two trials campaigns with different bath compositions were carried out. The targeted bath compositions were those of the steels samples studied in the previous chapter in order to obtain comparable inhibition layers. The first campaign was thus planned to be done in an iron-saturated zinc bath containing 0.128 wt.% Al and the second one in an iron-saturated zinc bath containing 0.112 wt.% Al.

In order to ensure that no significant variations of the bath composition took place, bath samples were regularly taken and analyzed by Inductively Coupled Plasma Mass Spectrometry (ICP-MS, SPECTROBLUE) throughout the trials. The ICP-MS analysis uncertainty was of ± 0.003 wt.% for aluminium and ± 0.001 wt.% for iron.

Figure 79 shows the evolution of the bath composition during the first Rhesca trials campaign (hot-dip galvanizing of 48 samples, 12 for each of the 4 Ti IF steel substrates during 5 days). Taking into account the analysis uncertainty, this composition can be assumed as steady on the targeted values during the whole trials campaign. The average bath composition throughout this campaign was of 0.127 ± 0.001 wt.% Al and 0.029 ± 0.001 wt.% Fe.

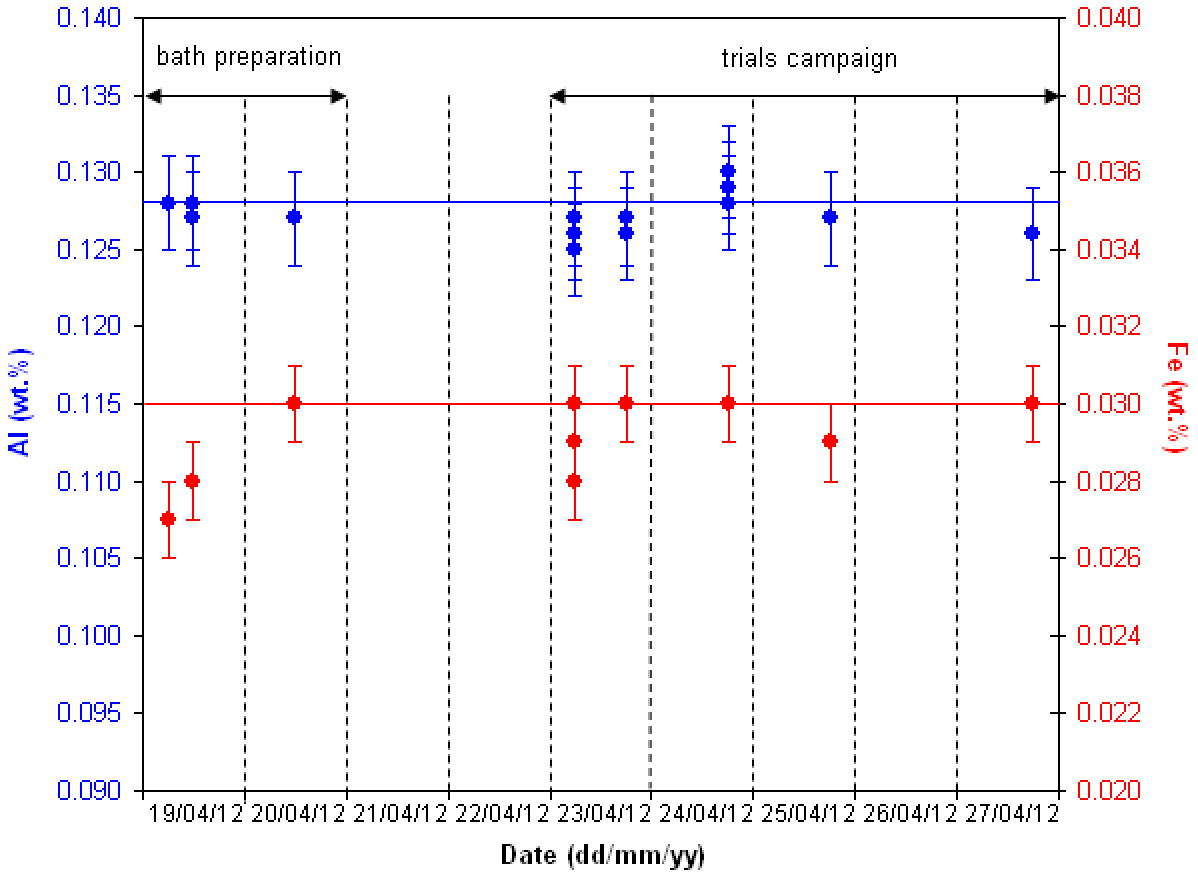

Figure 79: Evolution of the bath aluminium (blue) and iron (red) contents throughout the first Rhesca trials campaign (the error bars represent the ICP-MS analysis uncertainty around the measured values and the continuous lines the targeted bath composition).

Analogously, the evolution of the bath composition the during second Rhesca trials campaign (hot-dip galvanizing of 48 samples, 12 for each of the 4 Ti IF steel substrates during 5 days, as for the first campaign) is represented in Figure 80. As can be observed, this composition can be considered as steady although slightly lower but acceptably close to the targeted values. The average bath composition throughout this campaign was of 0.111 ± 0.003 wt.% Al and 0.027 ± 0.002 wt.% Fe. Therefore, the bath is not strictly saturated in iron but reasonabily close to the solubility limit (around 0.030 wt.% Fe at 460 °C, Table 1).

Only one analysis relatively far from the average bath aluminium content has been identified. However, it is very likely that some dross particles (in principle of an aluminium-rich δ phase) may have been integrated within the bath specimen uptaken for this analysis. Indeed, the aluminium content given by this analysis is higher than expected and both the preceding and subsequent analyses are in line with the targeted value of the galvanizing bath.

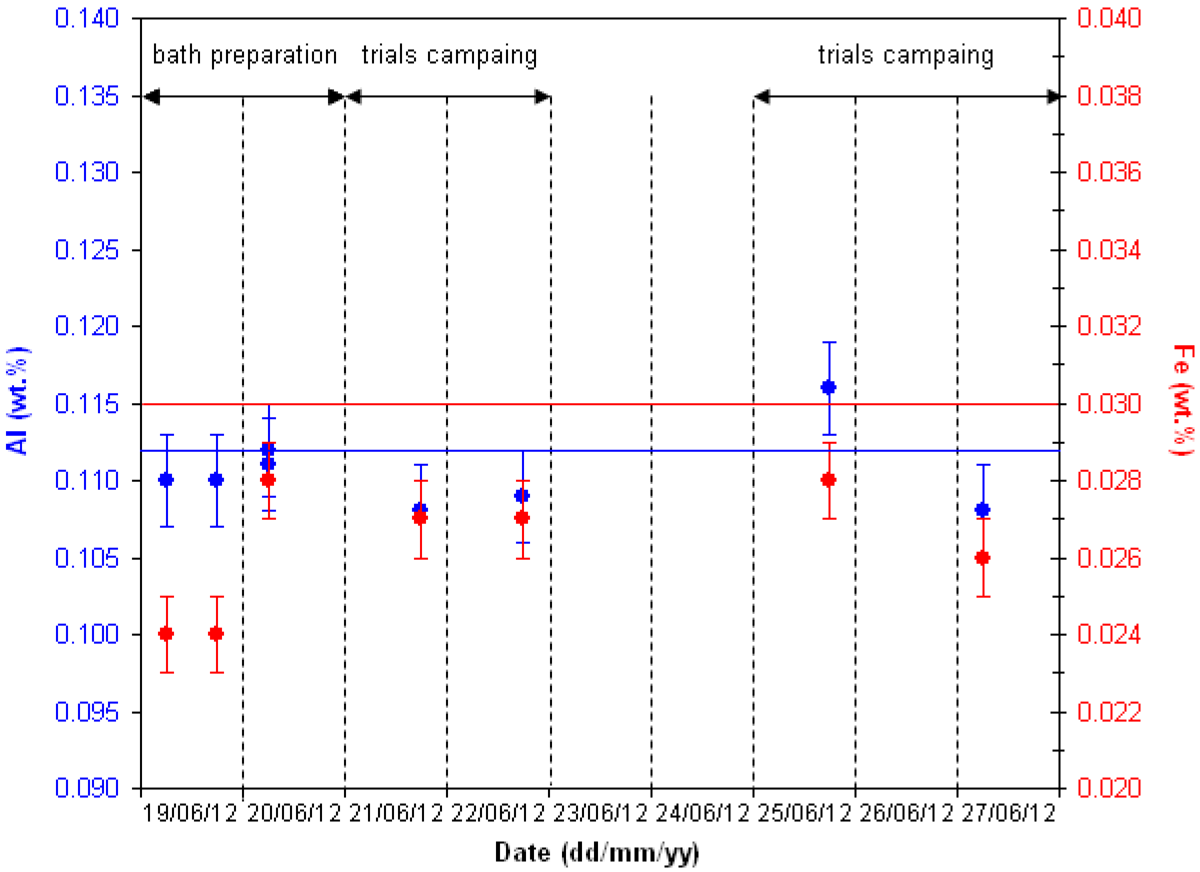

Figure 80: Evolution of the bath aluminium (blue) and iron (red) contents throughout the second Rhesca trials campaign (the error bars represent the ICP-MS analysis uncertainty around the measured values and the continuous lines the targeted bath composition).

The temperature of the zinc bath is likewise expected to influence the nature of the inhibition layer. This is the reason why it is controlled separately by a type-K thermocouple immersed in the melting pot, the targeted temperature being fixed to 460 °C. During the whole trials, the temperature of the zinc bath ranged between 458.9 and 461.6 °C, which is widely acceptable.

The results obtained through the follow-up of the zinc bath temperature and composition allow us to make the assumption that the inhibition layer is identical for all the samples coated during the same trials campaign. It is extremely important to meet this objective because it can therefore be assumed that any difference in the kinetics of the inhibition rupture can only be due to a difference in the chemical composition and/or in the grain size of the steel extreme surface. As will be seen in section III.2.3.1, the extreme surface grain size measurements have been carried out for the different substrates after galvanizing in order to determine whether this parameter can be neglected or not.

As a conclusion, the use of the Rhesca simulator offers some great advantages compared to the use of samples from industrially galvanized steel sheets. First of all, it makes possible to perform the same process (bath conditions and thermal cycle) on the desired steel substrates. Secondly, the thermal cycle is known accurately and is highly reproducible. And finally, the cooling of the sample can be performed with higher rates than typical industrial ones, which allows higher flexibility when performing any further heat treatment to provoke the inhibition layer breakdown.

III.1.2.2. The Gleeble 3500 simulator

The samples galvanized in the Rhesca simulator were then cut into samples with dimensions of 120 x 30 mm^2 in order to be submitted to isothermal heat treatments in the Gleeble 3500 pilot simulator. From each Rhesca sample, two Gleeble samples were obtained such that the centre of these samples corresponds to the mid-length of the coated part of the Rhesca sample and falls within its thermal homogeneity area. A schematic view of this sampling procedure is depicted in Figure 81.

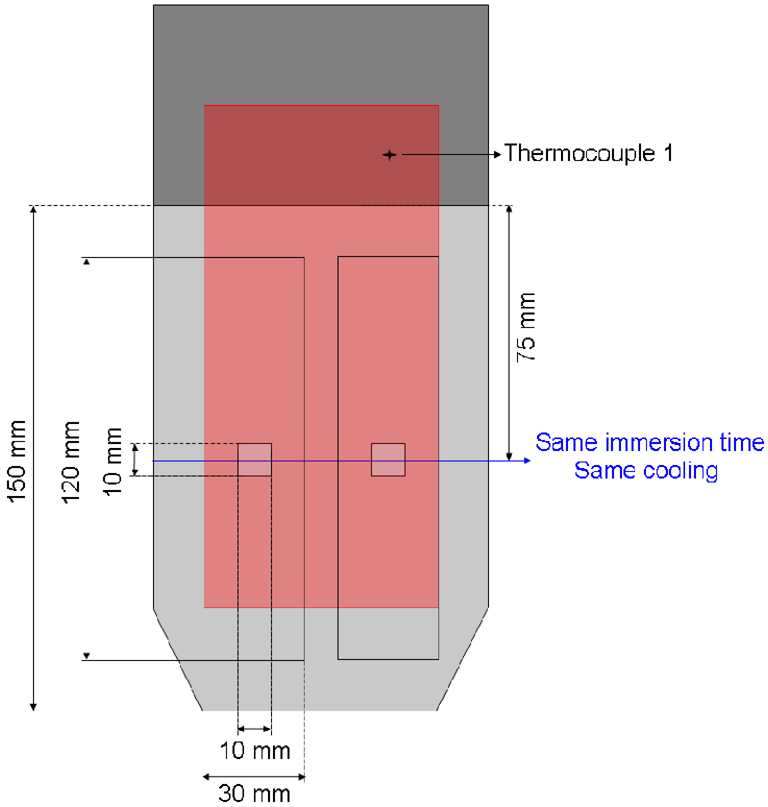

Figure 81: Schematic view of the position of the two Gleeble samples taken from each Rhesca sample (coated area in light grey, thermal homogeneity area in red).

An illustration of the Gleeble 3500 pilot simulator can be appreciated in Figure 82. This pilot is a polyvalent thermomechanical device, able to perform different mechanical tests (e.g., torsion, traction) with simultaneous heat treatments, and to provide water quench or gas flow for the sample cooling. For the present study, only the thermal properties of the Gleeble 3500 have been used. The great advantage of this pilot is to provide very high heating and cooling rates in order to perform controlled isothermal treatments.

Figure 82: Illustration of the Gleeble 3500 pilot simulator.

The configuration of the Gleeble 3500 enclosure is illustrated in Figure 83. The sample is fixed between four copper jaws and is heated by Joule effect to the targeted temperature for a targeted holding time. The sample temperature is measured by means of a type-K thermocouple, welded in the centre of the sample on the opposite face to the one studied. Rapid cooling of the sample is achieved by spraying this same face with ultracooled helium gas, as shown schematically in Figure 84.

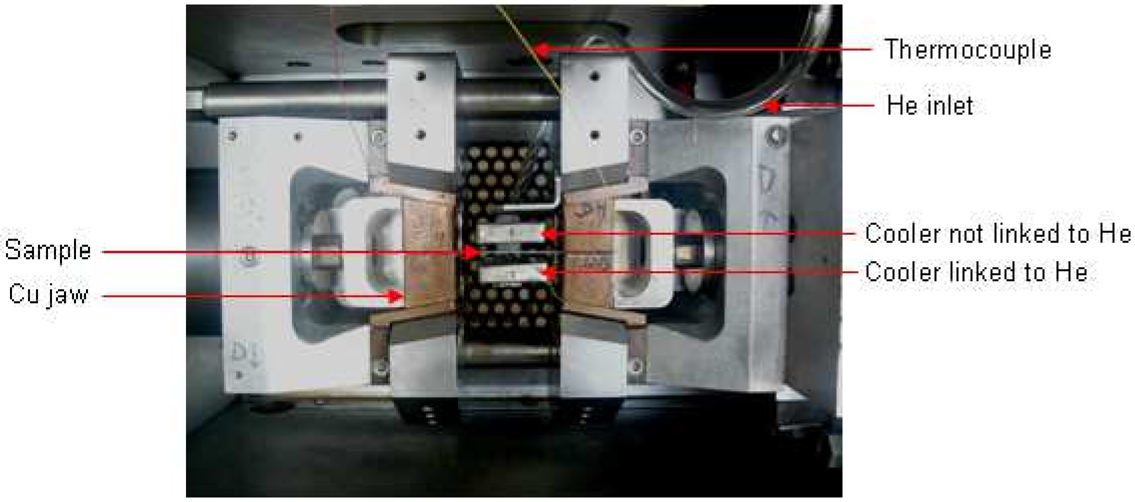

Figure 83: Configuration of the Gleeble 3500 enclosure.

The galvanized samples for Gleeble 3500 must be prepared in a particular way. Prior to the heat treatment in this pilot, the coating is removed from the edges of the sample (to prevent pollution of the copper jaws) but also from the opposite face to the one studied (in order to enhance the thermocouple welding). The coating is removed by chemical attack with a 33 vol.% aqueous solution of 37 wt.% HCl (Fisher Chemical) containing 2 g/L HMTA[17] (Fisher Scientific) to avoid the steel attack. The coating present on the part of the sample to be studied is protected from the chemical attack by covering it with an adhesive tape (Nichiban, No. 533). After this preparation, the samples were washed in tapping water, rinsed with ethanol and dried with pressured air. A schematic representation of a sample ready for the Gleeble treatments is depicted in Figure 84.

---

[17] Organic compound HexaMethyleneTetrAmine, $(CH_2)_6N_4$, used as corrosion inhibitor.

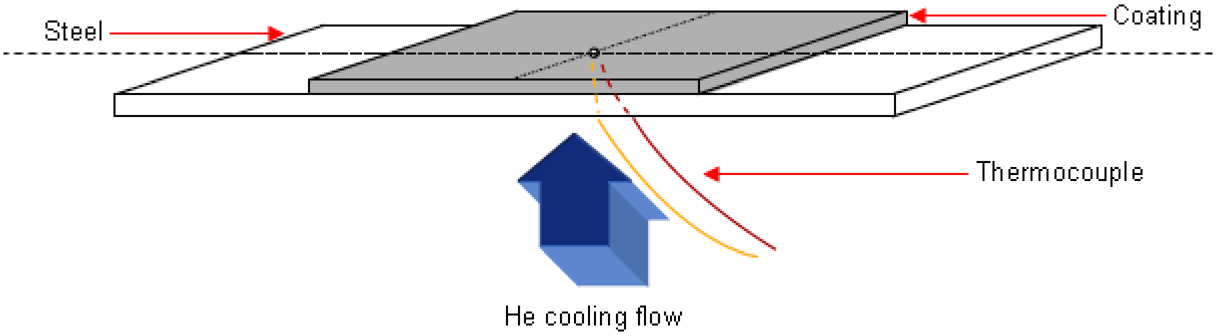

Figure 84: Schematic representation of a Gleeble 3500 sample.

The Gleeble isothermal treatments were performed on each steel substrate at holding temperatures of 430, 445 and 460 ℃ and for several times in order to determine accurately the time needed to achieve the inhibition rupture at each of these temperatures. In the case of steel C galvanized at 0.128 wt.% Al (first Rhesca trials campaign), supplementary holding temperatures of 425, 438 and 452 ℃ have been tested. As an exemple , the real Gleeble isothermal heat treatments performed on this galvanized steel corresponding to the extreme targeted holding times tested are shown in Figure 85. In addition, detailed data of all the Gleeble isothermal treatments performed on this material are summarized in Table 24.

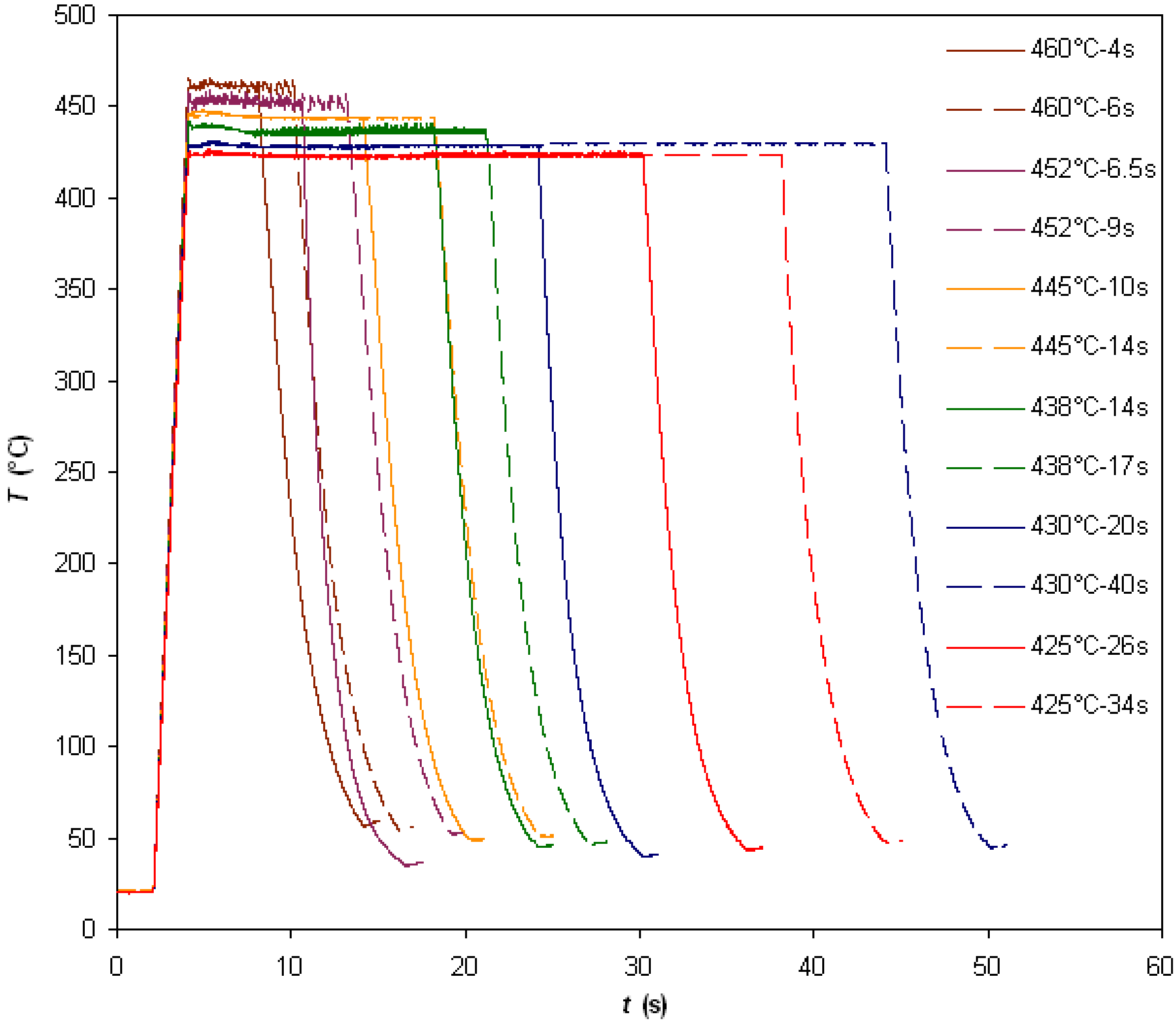

Figure 85: Example of real isothermal heat treatments performed on the Gleeble 3500 pilot simulator (steel C galvanized at 0.128 wt.% Al).

Table 24: Detailed data of all the isothermal heat treatments performed on the Gleeble 3500 pilot simulator in the case of steel C galvanized at 0.128 wt.% Al.

Target	$T_{hold,exp}$ (°C) [a]	$t_{hold,exp}$ (s) [b]	v_{heat} (°C/s) [c]	v_{cool} (°C/s) [d]	(t_{heat} + t_{cool}) / $t_{hold,exp}$ (%) [e]
425°C-26s	423.4 ± 0.9	26.0	132.5	132.9	1.3
425°C-29s	423.4 ± 0.9	29.0	151.7	239.3	1.0
425°C-34s	423.4 ± 0.8	34.0	131.7	231.4	0.9
430°C-20s	428.5 ± 0.6	20.0	146.6	170.1	1.8
430°C-23s	429.1 ± 0.7	23.0	158.2	233.4	1.3
430°C-25s	429.5 ± 0.7	25.0	155.9	221.7	1.3
430°C-30s	429.4 ± 0.7	30.1	161.9	298.0	1.0
430°C-40s	429.5 ± 0.6	40.1	167.6	248.6	0.7
438°C-14s	437.2 ± 1.8	14.1	217.9	98.9	4.2
438°C-17s	436.6 ± 1.6	17.0	137.8	118.7	3.4
445°C-10s	444.6 ± 1.2	10.0	178.7	115.5	6.3
445°C-12s	444.4 ± 0.8	12.0	150.2	155.2	4.8
445°C-14s	444.3 ± 0.7	14.0	182.1	101.9	4.8
452°C-6.5s	452.9 ± 1.6	6.6	212.0	352.8	6.3
452°C-7s	452.8 ± 1.3	7.0	168.3	227.7	7.5
452°C-8s	452.8 ± 1.4	8.1	204.0	288.3	5.8
452°C-9s	452.7 ± 2.3	9.0	222.7	104.0	8.7
460°C-4s	461.2 ± 0.7	4.1	201.1	171.9	16.0
460°C-5s	460.6 ± 0.8	5.0	177.1	167.9	13.9
460°C-5.5s	460.9 ± 0.9	5.6	191.3	118.8	14.8
460°C-6s	461.3 ± 1.8	6.1	211.7	172.2	11.0

[a] average experimental holding temperature and standard deviation; [b] experimental holding time; [c] heating rate from 400 °C to the holding temperature ; [d] cooling rate from the holding temperature to 400 °C; [e] ratio between the time spent during heating from 400 °C to the holding temperature and cooling from the holding temperature to 400 °C and the holding time.

As it can be appreciated in Table 24, the Gleeble 3500 simulator provides a great accuracy in the holding time. The values of the average holding temperature and standard deviation are also acceptable considering the accuracy of a type-K thermocouple (± 2 °C). Little deviations (less than or equal to 1 °C) of the average holding temperature with respect to the targeted holding temperature have been identified. As the determination of the average experimental holding temperature for each heat treatment represents a tedious task given the large number of heat treatments performed in this study and as its deviation from the target is reproducible in all cases, a constant holding temperature will be considered for each targeted holding temperature. These considered holding temperatures are shown in Table 25.

Table 25: Experimental holding temperature considered for each of the targeted holding temperatures.

$T_{hold,target}$ (°C)	$T_{hold,exp}$ (°C)
425	423.5
430	429
438	437
445	444.5
452	453
460	461

As already advanced, it is also important to highlight the very high heating and cooling rates that can be performed. The objective of the Gleeble simulator is to perform isothermal heat treatments and then to limit as far as possible the time needed to heat and to cool the samples. The ratio between the time spent during heating from 400 °C to the holding temperature and cooling from the holding temperature to 400 °C (as has been stated and will be justified later, zinc diffusion can be neglected below 400 °C) and the holding time is generally quite low (Table 24). Considering steady heating and cooling rates, this ratio increases when the holding temperature increases and the holding time decreases. The most limitant case in Table 24 corresponds to a targeted isothermal heat treatment of 460 °C and 4 s, for which the time spent during heating and cooling represents 16% of the holding time. Taking into account that the zinc diffusion kinetics during heating and cooling is slower than at the holding temperature, the previous value is still acceptable. In addition, it will be seen in section III.2.3 that the holding times at 460 °C performed in the framework of this study on steels A and B are not shorter than those presented in Table 24 for steel C. Only the Gleeble heat treatments performed on steel D galvanized at 0.112 wt.% Al (second Rhesca trials campaign) should be taken with some reserves as the holding times are very short.

Finally, it is important to clarify that the thermal homogeneity area on the Gleeble samples has been initially defined on the basis of a thermal homogeneity criterion of ± 5 °C which corresponds to a squared area of 10 x 10 mm^2 with the thermocouple placed in the centre of this area (Figure 81). It is obviously in this area of the sample that the characterizations have been done. However, the so-defined thermal homogeneity criterion becomes too large when performing isothermal treatments at holding times close to the time needed for the inhibition rupture at the targeted holding temperature. It has sometimes been observed in these cases that the inhibition rupture had been achieved in the centre of the thermal homogeneity area but not on the extreme zones of this area, at lower temperature. In these cases, priority is given to the characterization of the centered zone of the thermal homogeneity area, i.e., the zone corresponding to the thermocouple location.

III.1.3. Sample preparation and characterization techniques

The samples annealed in the Gleeble 3500 simulator have then been characterized in order to determine whether the inhibition layer breakdown has been achieved or not. The appearance of this phenomenon is identified through SEM (LEO DSM 982) observations of the sample surface after electrochemical dissolution at -800 mV/SCE by means of the experimental assembly and the electrolyte described in section II.1.2.1.1.1. With this potential, zinc and aluminium-free Fe-Zn phases are selectively removed while the whole inhibition layer (aluminium-saturated δ and $Fe_2Al_5Zn_x$) is kept at the surface of the sample because of its higher aluminium content. The inhibition layer breakdown has occurred when holes in the inhibition layer, created by outbursts formation at the steel grain boundaries, are observed.

The determination of the inhibition layer breakdown by surface SEM observations is illustrated below with an example corresponding to steel B galvanized at 0.128 wt.% Al in the Rhesca simulator and subsequently heated in the Gleeble 3500 device at 430 °C for 30 and 35 s.

Figure 86 shows the inhibition layer after the 30 s heat treatment. It can be seen that this layer is continuous over the whole sample surface, which indicates that the inhibition rupture has not occurred yet.

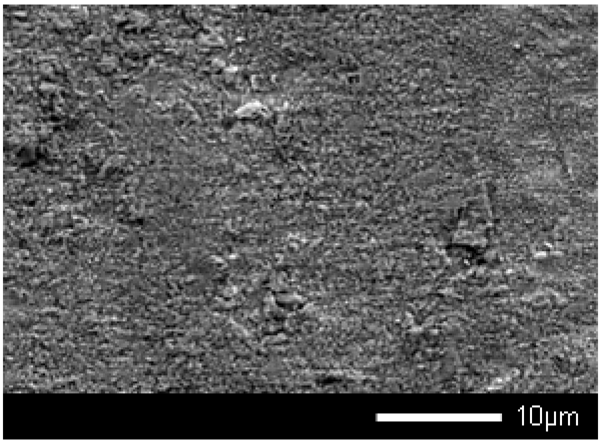

Figure 86: Surface SEM micrograph of an intact inhibition layer (steel B heated in the Gleeble 3500 pilot simulator at 430 °C for 30 s).

However, longer heat treatments at the same temperature will lead to the local breakdown of the inhibition layer by outburst formation at the steel grain boundaries. Figure 87 shows the inhibition layer after the 35 s heat treatment at 430 ℃. Holes are visible within this layer and the steel grain boundaries can be observed at their bottom. In addition, one can appreciate that this layer still covers quite effectively the interior of the ferrite grains (as will be seen in section III.2.3.1, the mean characteristic size of the extreme surface grains of steel B is around 10 µm, which corresponds very properly to the centered area of the micrograph depicted in Figure 87 where the inhibition layer remains intact).

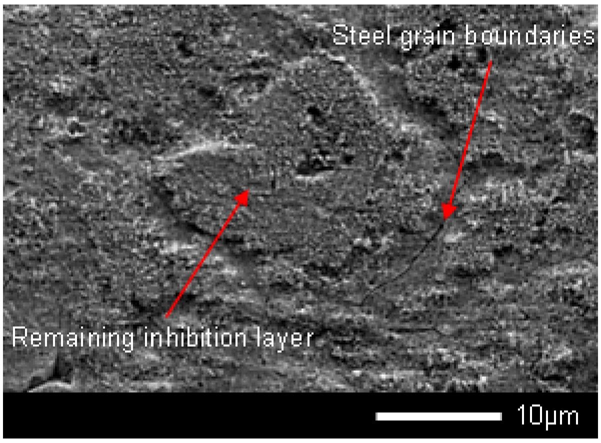

Figure 87: Surface SEM micrograph of a broken inhibition layer (steel B heated in the Gleeble pilot simulator at 430℃ for 35 s).

EDS analysis (Thermo Scientific) performed at the same location (Figure 87) confirms that the inhibition layer has been locally broken: the presence of either aluminium or zinc is not detected in the zones corresponding to the steel grain boundaries (Figure 88).

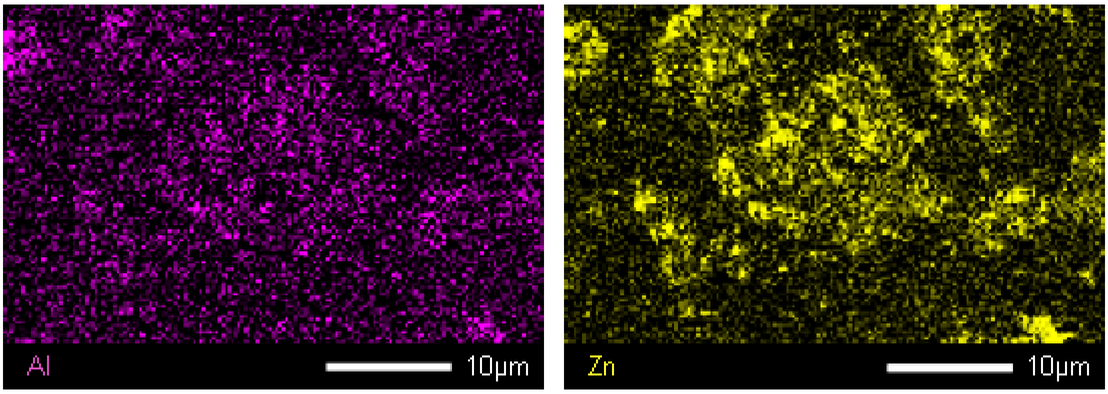

Figure 88: Aluminium (left) and zinc (right) EDS mapping corresponding to the micrograph shown in Figure 87.

It can therefore be considered that, in the case of a Gleeble isothermal heat treatment at 430 ℃ on steel B, the inhibition layer breakdown occurs at a holding time in the 30 - 35 s range.

In addition, some CSP cross section samples, prepared in the same way as described in section II.1.2.1.2.1, were characterized in SEM in order to check whether or not the inhibition layer of the samples galvanized in the Rhesca pilot simulator had a similar structure to that of the industrially galvanized samples of the previous chapter.

Finally, in order to study the mechanisms accounting for the inhibition layer breakdown in a more accurate way, mechanically polished cross section specimens have been prepared as described in section II.1.2.1.2.2 from well-chosen samples. For these samples, after the heat treatment performed by the Gleeble 3500 device, the inhibition layer breakdown has been achieved only in the thermal homogeneity area but not elsewhere (Figure 81, lower temperature compared to the centre of the sample). The mechanically polished specimens were taken at different positions along the longitudinal direction (more precisely, along the dotted line parallel to this direction, Figure 84). The so-obtained cross section samples were then characterized by EDS (Bruker AXS XFlash 4010 SDD) in a SEM (JEOL JSM-7001F).

III.1.4. Experimental protocol

Figure 89 depicts an exemple of the global thermal cycle undergone by each of the steel samples used for this study by means of the Rhesca and Gleeble 3500 procedures explained above.

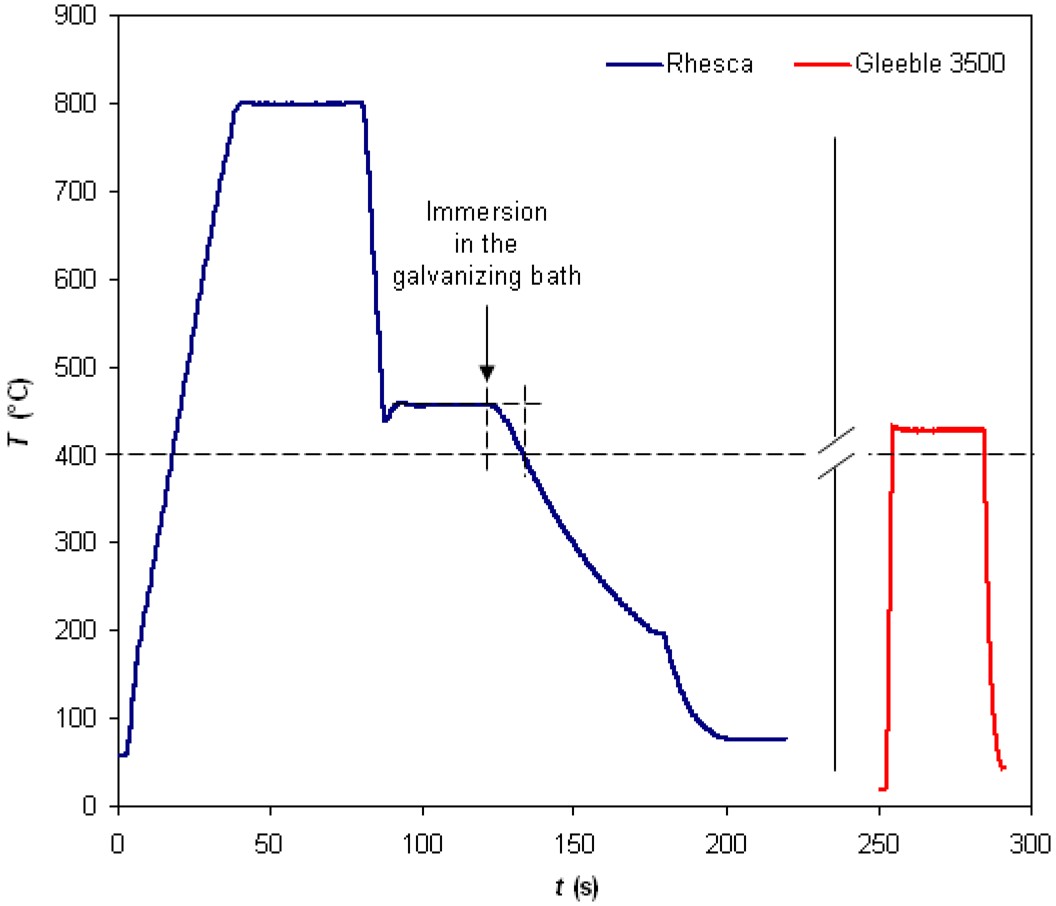

Figure 89: Exemple of the global thermal cycle undergone by the steel samples used for this study (steel B galvanized at 0.128 wt.% Al in the Rhesca simulator and subsequently heated in the Gleeble 3500 pilot simulator at 460℃ for 30s).

As stressed previously, all the steel samples have been submitted to the same targeted Rhesca thermal cycle (Figure 76) but to different holding temperatures and times in the Gleeble 3500 device. For each holding temperature $T_{hold,exp}$ in the Gleeble device, several samples were heated for different holding times and characterized in SEM in order to narrow down as much as possible the gap in holding time between the observation of an intact inhibition layer and the observation of a broken inhibition layer. The holding time necessary to achieve the inhibition layer breakdown $t_{hold,exp}$ has then been considered as the time in the middle of this gap and its uncertainty as the length of the gap.

Once the holding time to perform in the Gleeble 3500 pilot simulator necessary to achieve the inhibition layer rupture has been accurately determined for each holding temperature, a correction of this time has to be done. As stated earlier in this chapter, the diffusion of zinc towards the steel grain boundaries leading to the inhibition layer breakdown occurs not only during the heat treatment in the Gleeble 3500 device but also during the immersion in the galvanizing bath and the subsequent cooling down to 400℃ in the Rhesca simulator (thermal pat h delimited by the dotted lines in Figure 89). In order to characterize the inhibition layer breakdown kinetics correctly, the diffusion of zinc taking place during this thermal path must be considered to correct the holding time performed in the Gleeble 3500 pilot simulator. As seen before, all the Rhesca thermal cycles were extremely reproducible, which will make the correction task easier. Further details about this correction will be given in section III.3.2.2.2.

III.2. Experimental results

III.2.1. Characterization of the inhibition layer

As advanced above, the nature of the inhibition layer formed on the steel samples galvanized in the Rhesca pilot simulator has been first characterized in order to verify that it is comparable to that of the industrially galvanized samples of chapter II. For this purpouse, CSP cross section samples of steel A galvanized during the two Rhesca trials campaigns (galvanizing bath containing 0.128 and 0.112 wt.% Al) have been prepared and characterized in SEM (Figure 90).

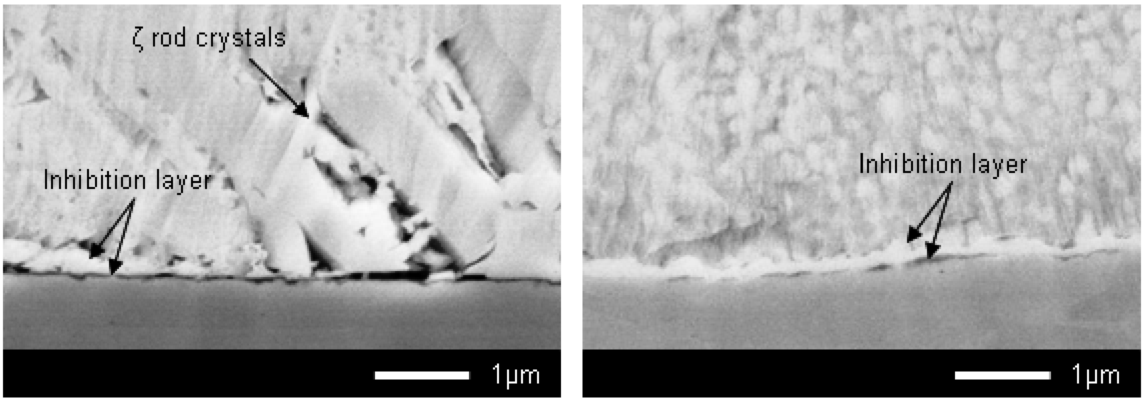

Figure 90: Cross section SEM micrographs of the inhibition layer performed on the CSP samples obtained for steel A galvanized during the first (0.128 wt.% Al, left) and second (0.112 wt.% Al, right) Rhesca trials campaigns.

As can be observed in the left-hand side micrograph of Figure 90, the structure of the inhibition layer formed on steel A when galvanizing during the first Rhesca trials campaign (0.128 wt.% Al) is perfectly comparable to the one investigated in the previous chapter for a commercial steel galvanized in a zinc bath with the same aluminium content (Figure 43). Indeed, the inhibition layer is in both cases composed of a very thin layer of $Fe_2Al_5Zn_x$ fairly continuous and a thicker layer of δ on its top.

The right-hand side micrograph of Figure 90 shows the inhibition layer of steel A galvanized during the second Rhesca trials campaign (0.112 wt.% Al). The structure of this layer is the same as that of the steel galvanized industrially in a zinc bath with the same aluminium content studied in the previous chapter (Figure 42). The main difference compared to the inhibition layer formed in a zinc bath containing 0.128 wt.% Al is that the $Fe_2Al_5Zn_x$ layer is now clearly discontinuous.

Nevertheless, it should be noted that the thickness of the inhibition layer, although similar, appears to be slightly smaller in the case of the samples galvanized in the Rhesca pilot simulator (around 200 and 150 nm for the first and second trials campaigns at 0.128 and 0.112 wt.% Al respectively), probably because the immersion time (0.7 s) was shorter than for the industrial samples (1.4 to 1.9 s).

In addition, it should be highlighted that no effect of the Ti IF steel chemical composition on the structure of the inhibition layer can be reported here nor can be found in the literature. In spite of their different chemical composition, the inhibition layer of the steel samples galvanized by means of the Rhesca pilot simulator can therefore be considered equivalent to the one investigated in the previous chapter for the commercial steels galvanized in the same conditions.

In the following, some results aiming to facilitate the precise understanding of the mechanisms accounting for the inhibition layer breakdown will be shown. The raw experimental results obtained on the kinetics of this reaction will then be presented and special attention will be paid to the effect of the steel chemical composition and the bath aluminium content.

III.2.2. Mechanisms accounting for the inhibition layer breakdown

As detailed in section I.3.2 and recalled at the beginning of this chapter, the inhibition layer breakdown occurs in most cases through the so-called *outburst reaction* at the steel grain boundaries. This reaction is controlled by zinc diffusion through the inhibition layer towards the steel grain boundaries so that its kinetics is expected to depend on the nature of this layer. In agreement with the phase diagram, this layer should be fully composed of the δ phase in the case of GA baths. Different authors in literature [27,30,33] have proposed a mechanism accounting for the inhibition layer growth and breakdown in total agreement with thermodynamics (sections I.3.1.1.3 and I.3.2.1.2.3). However, it has been seen in chapter II that the inhibition layer formed in GA baths is actually more complex than predicted by thermodynamics.

In order to try to clarify how the coating microstructure evolves from the inhibition situation showed in chapter II towards the inhibition layer breakdown situation, some cross section samples have been prepared, as explained in section III.1.3, from specimens taken at different locations along the longitudinal direction of one of the samples heated in the Gleeble 3500 device used to study the inhibition layer breakdown kinetics. Figure 91 shows a SEM micrograph and its EDS mapping for aluminium for each of the cross section samples extracted from a Gleeble sample of steel A galvanized in a zinc bath containing 0.128 wt.% Al in the Rhesca simulator and subsequently heated in the Gleeble 3500 device at 430 ℃ for 60 s. A gradient of temperature exists from top left-hand side micrograph (a) to the top right-hand side micrograph corresponding to the location at 430 ℃ (d). The precise temperature corresponding to each micrograph was not measured.

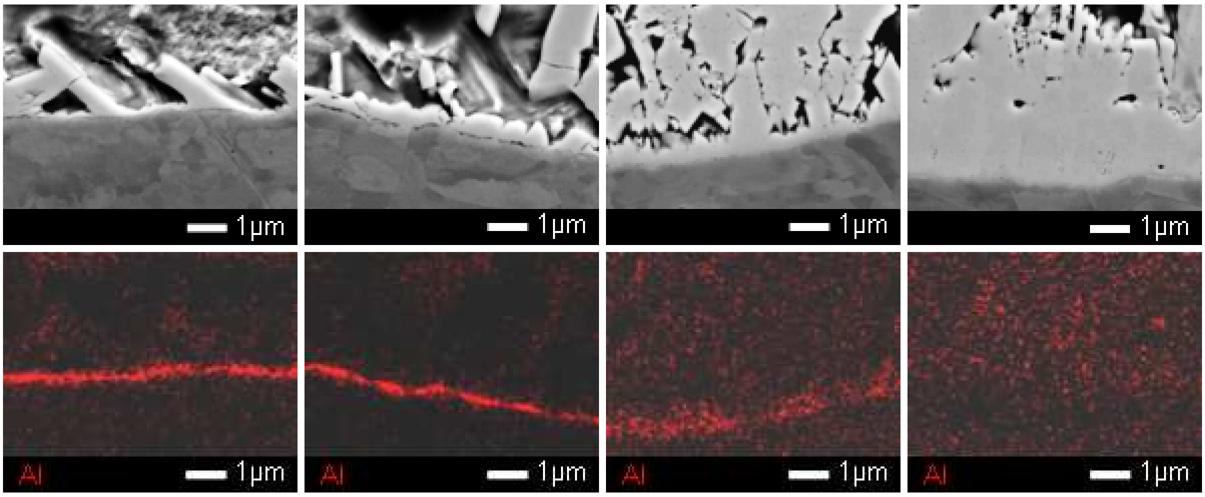

(a) (b) (c) (d)

Figure 91: Cross section SEM micrographs and corresponding EDS mappings for aluminium for each of the samples taken at different locations along the longitudinal direction of a Gleeble sample, from the outermost position (a) to the centre of the sample (d) (steel A galvanized at 0.128 wt.% Al in the Rhesca simulator and subsequently heated in the Gleeble 3500 device at 430 ℃ for 60 s).

The top left-hand side micrograph and associated EDS mapping (a) correspond to the outermost position, which has met the lowest temperature. In accordance with the results presented in chapter II, they represent an intact inhibition layer composed of a very thin continuous layer of $Fe_2Al_5Zn_x$ and a thicker layer of δ on its top. This microstructure will be considered as the initial or reference state. It can be assumed that, at this location of the Gleeble sample, the temperature is so low that no effect of diffusion phenomena can be observed.

The second micrograph from the left (b) corresponds to a location of the Gleeble sample closer to its centre than that of micrograph (a). The temperature is therefore slightly higher and the effect of the diffusion (of iron mainly) can already be observed by the growth of Fe-Zn intermetallic phases on top of $Fe_2Al_5Zn_x$ and δ (shown by the larger thickness of the interfacial layer). The temperature can be assumed to be below the melting point of zinc (419.5 ℃) because the EDS mapping for aluminium corresponding to micrograph (b) is very similar to the EDS mapping for aluminium corresponding to micrograph (a). If the temperature is supposed to be below the melting point of zinc, the nature of the Fe-Zn phase formed at this step could be ζ. Indeed, if zinc is in solid state, the aluminium supply at the δ / zinc interface is very limited and the diffusion flux of iron from the steel matrix cannot be consumed to make the δ phase grow. Aluminium-free Fe-Zn compounds, ζ crystals, instead nucleate and grow on the inhibition layer, consuming this flux of iron. This comment is only an assumption because the interface between the δ and ζ phases is not visible in the micrographs of Figure 91.

The third micrograph from the left (c) corresponds to a location even closer to the centre of the Gleeble sample than that of micrograph (b). The temperature at this location seems to be higher than the melting point of zinc (419.5 ℃). Aluminium can now diffuse faster to the δ / zinc interface, allowing the growth of the δ phase. In addition, the thin layer of $Fe_2Al_5Zn_x$ has completely disappeared on the SEM micrograph. The signal for aluminium associated to the inhibition layer is therefore thicker than that of the EDS mappings corresponding to micrographs (a) and (b) due to the growth of the δ layer but less intense due to the disappearance of the $Fe_2Al_5Zn_x$ layer. This observation represents a key result and will be recalled in section III.3.1 when a logical sequence of mechanisms accounting for the inhibition layer breakdown will be proposed. As in the case of micrographs (a) and (b), no presence of outbursts could have been observed. It is also to note that a large amount of intermetallic compounds is present on the top of the inhibition layer. These intermetallic compounds could correspond to evanescent ζ crystals formed during the rapid cooling performed in the Gleeble 3500 pilot simulator.

The top right-hand side micrograph (d) corresponds to the centre of the Gleeble sample, where the thermocouple has been welded and which has met the highest temperature within the sample (targeted holding temperature of 430 ℃, real average holding temperature of 429 ℃). It clearly shows an outburst.

Finally, it should be remarked that the results presented in Figure 91 show that the thin $Fe_2Al_5Zn_x$ layer may disappear before the outburst formation but do not demonstrate that an outburst cannot break the $Fe_2Al_5Zn_x$ layer (and the δ layer) off.

III.2.3. The inhibition layer breakdown kinetics

The experimental results obtained in the framework of the study on the inhibition layer breakdown kinetics are presented here below.

III.2.3.1. Steel grain size measurements

As shown in section I.3.2.2.2.1, the steel grain size influences the kinetics of the inhibition layer breakdown [24,25,70,76]. To be sure that this parameter can be neglected, size measurements of the steel extreme surface grain have been carried out after galvanizing in the Rhesca pilot. The uncoated part of the Rhesca samples prior to any Gleeble heat treatment was used (Figure 81). Measurements were performed according to the linear intercept procedure of the ISO 643 standard [93]. The results obtained for the *ASTM grain size number G* [94] (equation (I.12)) are presented in Table 26.

Table 26: ASTM grain size number *G* corresponding to the extreme surface of the Ti IF steels studied after heat treatment in the Rhesca pilot simulator.

Steel	*G*
A	10.6
B	9.9
C	10.3
D	9.9

Based on the above values and taking into account that the uncertainty in the determination of the ASTM grain size number is of ± 0.5, it can be assumed that all the substrates have equivalent ASTM grain size number, which corresponds to a grain size comprised between 9 and 11 µm. The effect of this parameter on the kinetics of the inhibition layer breakdown can therefore be neglected and any difference in kinetics could only be explained by the different chemical composition of the steels or by the different aluminium content of the galvanizing baths used in this study.

III.2.3.2. Effect of the steel chemical composition

The effect of the steel chemical composition on the kinetics of the inhibition layer breakdown has been mainly investigated from the results obtained during the first Rhesca trials campaign, for which the targeted bath aluminium content was of 0.128 wt.%. The raw experimental results for this campaign, obtained through the protocol described in section III.1.4, are presented in Figure 92, where the experimental holding time performed in the Gleeble 3500 device necessary for the inhibition rupture $t_{hold,exp}$ is plotted as a function of the holding temperature $T_{hold,exp}$ for the four steels studied.

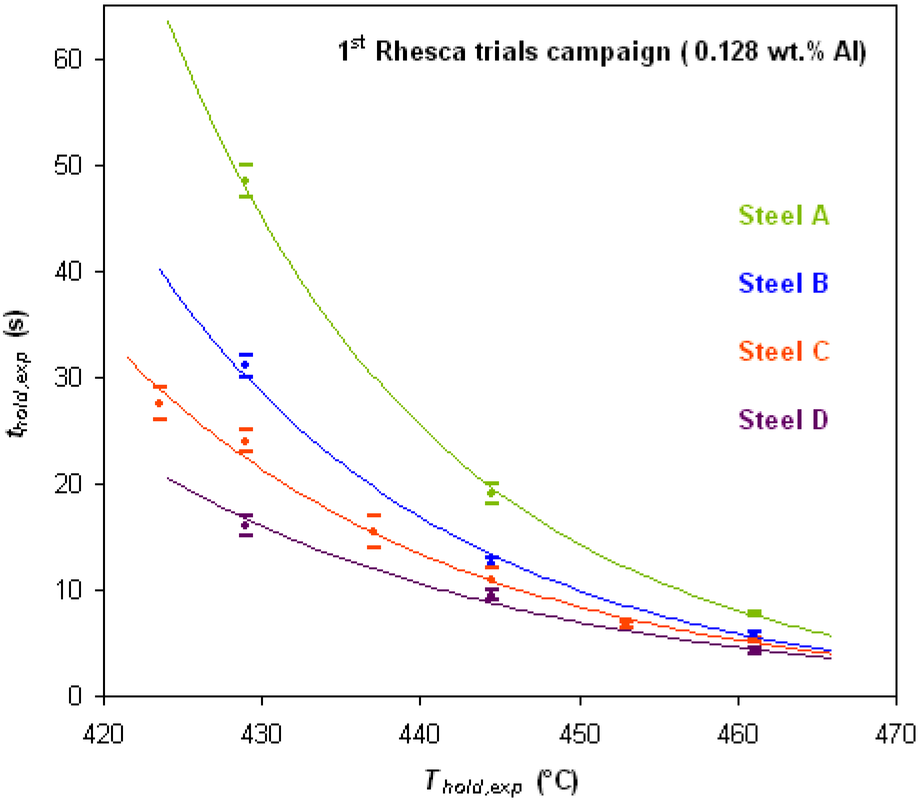

Figure 92: Experimental holding time needed for the inhibition layer breakdown against experimental holding temperature performed in the Gleeble 3500 pilot simulator (first Rhesca trials campaign).

Firstly, it should be highlighted that the temperature range to study the inhibition layer breakdown is very narrow. On the one hand, holding temperatures higher than 419.5 °C are needed to ensure that zinc is in liquid state. On the other hand, too high holding temperatures lead to experimental holding times for the inhibition rupture too short to be performed by the Gleeble 3500 device without a considerable uncertainty. These are the reasons why targeted holding temperatures of 430, 445 and 460 °C only have been performed on all the steel substrates. Holding temperatures of 425, 438 and 452 °C have been added in the case of steel C in order to confirm the tendency observed for all the steels in the range of temperatures studied.

As stated previously, the uncertainty in each point in Figure 92 represents the difference between the highest holding time for which the inhibition rupture has not occurred yet and the lowest time for which the inhibition rupture has been observed. The time for inhibition rupture has been chosen as the point in the middle of the interval defined by these two times. It is obvious that the smaller this interval is, the more accurate the determination of the time for inhibition rupture is, but a compromise between accuracy and number of trials has to be found.

At least in the range of temperatures tested, steel D is more reactive (the inhibition layer breakdown is achieved faster) than steel C and this latter is more reactive than steel B, steel A being the less reactive one.

III.2.3.3. Effect of the bath aluminium content

The effect of the bath aluminium content on the kinetics of the inhibition layer breakdown has been studied by comparison of the kinetic data obtained during the first and second Rhesca trials campaigns. The raw experimental results for the second campaign, for which the targeted bath aluminium content was of 0.112 wt.%, are available in Figure 93. As can be observed, only the extreme steel substrates in chemical reactivity, A and D, have been finally investigated, due to a lack of time. The raw experimental results obtained on these two steels galvanized during the first campaign (0.128 wt.%) are presented again in Figure 93 as well.

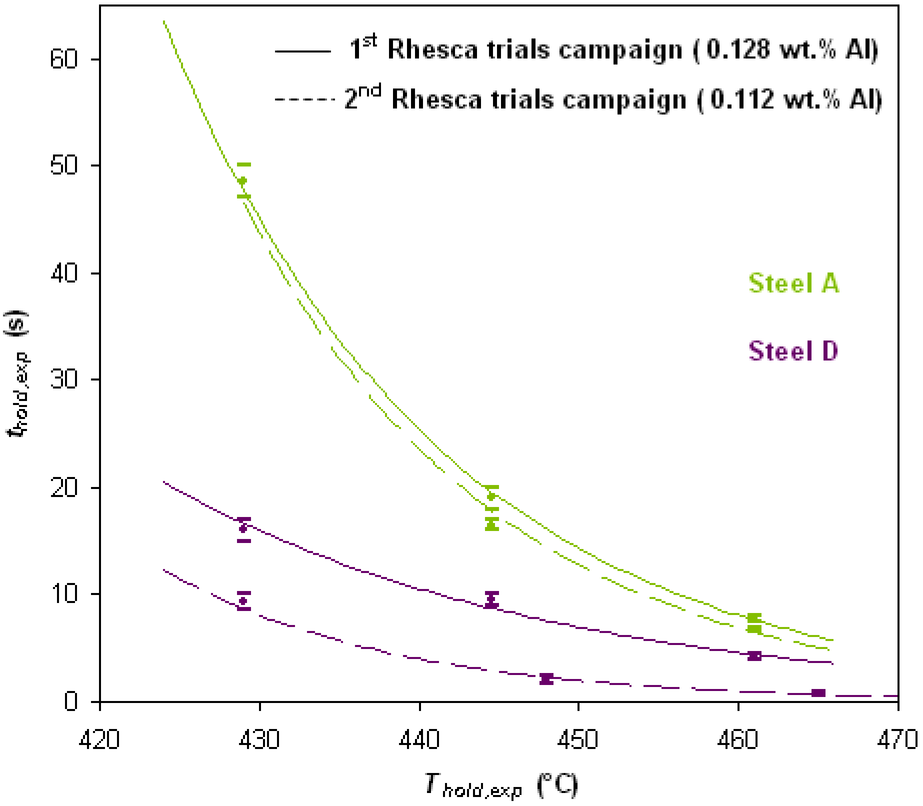

Figure 93: Experimental holding time needed for the inhibition layer breakdown against experimental holding temperature performed in the Gleeble 3500 pilot simulator (second Rhesca trials campaign).

As it can be seen, the experimental holding times necessary for the inhibition layer breakdown are shorter than for the first Rhesca trials campaign, especially in the case of steel D. While the holding time for rupture is slightly shorter in the case of steel A for the second Rhesca trials campaign, a great difference in this holding time is observed between the two campaigns in the case of steel D.

It is also to note that, even if the same targeted holding temperatures of 430, 445 and 460 °C have been applied for the Gleeble heat treatments on both steel substrates, the average experimental holding temperatures were found to be higher in the case of steel D when performing the targeted holding temperatures of 445 and 460 °C. A little overshoot in temperature usually took place at the beginning of the holding step of each heat treatment. In the case of the heat treatments performed on all the other steels investigated in this study, this overshoot had almost no influence on the average holding temperature as the holding times performed were very long. However, in the case of steel D galvanized during the second Rhesca trials campaign, the holding times performed in the Gleeble device for the targeted holding temperatures of 445 and 460 °C were very short and the overshoot in temperature cannot be neglected in these conditions. For this steel substrate, the corresponding average experimental holding temperatures were found to be 448 and 465 °C respectively.

Although the previous experimental holding times must still be corrected in order to take into account the diffusion of zinc during immersion in the galvanizing bath and cooling performed in the Rhesca simulator, it can be already advanced that the steel chemical composition and the bath aluminium content have an important effect on the kinetics of the inhibition layer breakdown. As shown in section III.1.2.1, no substantial differences were observed on the thermal profiles performed in the Rhesca simulator for the different steel substrates and it is very unlikely that the tendencies observed above can be inversed after correction. Moreover, as it will be seen later in section III.3.2.2, it is very important for the present study that all the samples corresponding to each couple steel-campaign have been submitted to an equivalent Rhesca thermal profile. All the Rhesca thermal profiles have therefore been checked, and samples with slightly different profile have been eliminated from the study.

To go further into a deep understanding of the inhibition layer breakdown kinetics, modelling of this phenomenon is absolutely necessary to quantify the diffusion flux of zinc through the inhibition layer towards the steel grain boundaries prior to the isothermal heat treatments carried out by means of the Gleeble 3500 device. Modelling of this phenomenon will then be proposed (section III.3.2.1) before correcting the experimental times in order to take into account this diffusion (section III.3.2.2).

III.3. Discussions

At first, a sequence of mechanisms accounting for the inhibition layer breakdown will be proposed (section III.3.1). Then the discussions about the inhibition layer breakdown kinetics will be tackled (section III.3.2).

III.3.1. Mechanisms accounting for the inhibition layer breakdown

As for the inhibition layer formation, the mechanisms accounting for the inhibition layer breakdown can be explained by means of the concept of diffusion paths in the Al-Fe-Zn ternary phase diagram at the holding temperature. The proposed mechanisms are based on the hypothesis extracted from the results presented in section III.2.2. In order to simplify the analysis, the explanations will be given in the case of a steel galvanized in a bath containing 0.128 wt.% Al, for which the $Fe_2Al_5Zn_x$ layer is expected to be fairly continuous. The presence of ζ rod crystals will be neglected as well.

The reference state of the inhibition layer is schematized in Figure 94a. As stated in chapter II, all interfaces (steel / $Fe_2Al_5Zn_x$, $Fe_2Al_5Zn_x$ / δ, δ / liquid zinc) are in thermodynamic equilibrium and the microstructure can be described by the real diffusion path 1 in Figure 95.

During the galvannealing heat treatment, the inhibition layer grows by iron diffusion towards the zinc, provided that this later is in liquid state (temperature higher than 419.5 °C). At the same time, zinc diffuses towards the steel matrix. The steel / $Fe_2Al_5Zn_x$ interface gets progressively enriched in zinc or, what is the same, impoverished in aluminium. At a given moment, this interface is no longer thermodynamically stable: the diffusion path crosses the ternary domain involving iron, $Fe_2Al_5Zn_x$ and δ. Further zinc enrichment rapidly leads to the consumption of $Fe_2Al_5Zn_x$ and the formation of δ. The microstructure of Figure 94b is therefore represented by the real diffusion path 2 in Figure 95. At this time, the $Fe_2Al_5Zn_x$ phase has completely disappeared and the steel / δ and δ / liquid zinc interfaces are planar and at thermodynamic equilibrium.

During all this time, the steel grain boundaries are short-circuit diffusion paths for zinc and become preferentially enriched in this element. When the zinc concentration at these locations is high enough, the steel / δ interface is locally destabilized: the diffusion path crosses the ternary domain involving iron, δ and Γ. The Γ phase therefore nucleates at the steel grain boundaries. Its volume expansion breaks the δ layer off locally and the Γ phase gets in direct contact with liquid zinc. This microstructure is depicted in Figure 94c and could be represented by path 3 in Figure 95, where the dotted line indicates that no equilibrium is possible between the Γ phase and liquid zinc. This non-equilibrium situation leads to the dissolution of the Γ phase surface and the nucleation of new Fe-Zn phases on its top. This microstructure, illustrated in Figure 91d, commonly known as *outburst*, has not been depicted here because the analysis in this document focuses only on the phenomena taking place until the inhibition layer breakdown occurs.

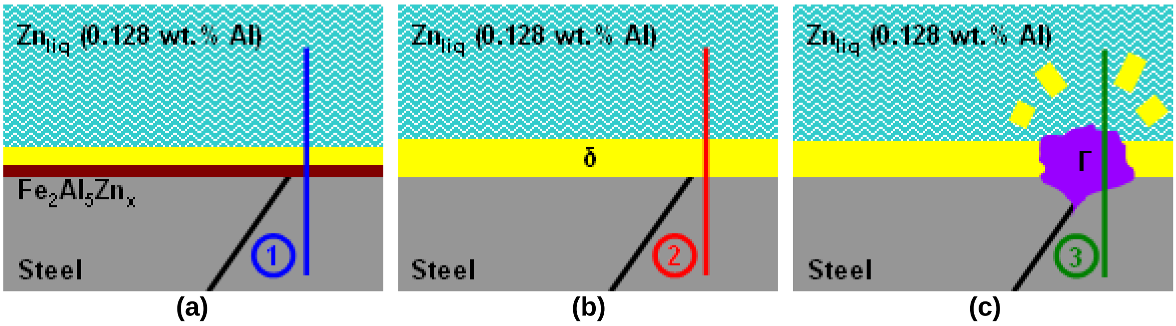

Figure 94: Schematic representation of the mechanisms accounting for the inhibition layer breakdown through outburst formation by zinc diffusion towards the steel grain boundaries (case of a steel galvanized in a bath containing 0.128 wt.% Al).

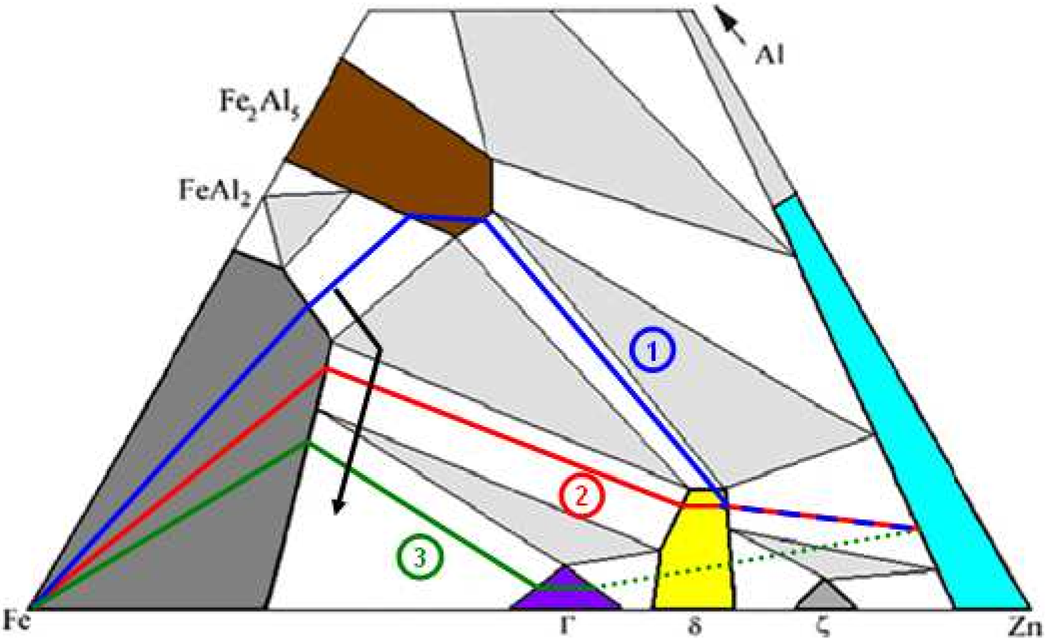

Figure 95: Schematic representation of diffusion paths on the Al-Fe-Zn ternary phase diagram at the holding temperature describing the mechanisms accounting for the inhibition layer breakdown through outburst formation by zinc diffusion towards the steel grain boundaries (case of a steel galvanized in a bath containing 0.128 wt.% Al).

It should be recalled that it has not been possible to obtain incontrovertible experimental evidence of the existence of all the phenomena described above and that some assumptions had to be made. As commented in section III.2.2, although the evolution of the $Fe_2Al_5Zn_x$ layer prior to the outburst formation has been observed (Figure 91c), no experimental proof can be provided to rule out the possibility that this phase can still be present on the steel grain boundaries when the inhibition layer is broken at this location. In addition, the fact that the Γ phase is the one nucleating at the steel grain boundaries and responsible for the inhibition layer breakdown has neither been demonstrated.

III.3.2.The inhibition layer breakdown kinetics

A simplified model aiming to predict the inhibition layer breakdown kinetics will be first proposed (section III.3.2.1). The constants of this model will be determined from the raw experimental kinetic results (section III.3.2.2). In order to determine these constants, the diffusion of zinc during immersion and cooling in the Rhesca pilot simulator needs to be taken into account to correct the experimental holding times performed in the Gleeble 3500 device necessary for the inhibition rupture. Once these times have been corrected and the constants of the model obtained, the effect of the steel chemical composition (section III.3.2.3) and the bath aluminium content (III.3.2.4) on the inhibition layer breakdown kinetics will be analysed in detail.

III.3.2.1. Modelling of the inhibition layer breakdown kinetics

A model aiming to describe the inhibition layer breakdown kinetics through outburst formation is presented here below. Due to the complexity of this reaction, some strong simplifications have to be made with respect to the mechanisms proposed in section III.3.1 in order to facilitate the modelling work. The following assumptions are considered:

- The iron diffusion is very slow compared to the zinc diffusion so that the thickness of the inhibition layer can be considered constant (the growth of the inhibition layer is assumed to be negligible even if, as shown in section III.2.2, this growth has been observed experimentally).

- There is no zinc concentration increase along the steel grains surface: the outburst reaction occurs along the emergence lines of steel grain boundaries, the rate of zinc diffusion from the middle of the steel grains towards the grain boundaries (i.e., diffusion parallel to the steel / inhibition layer interface) is assumed to be infinite. The considered zinc diffusion flux therefore depends only on one space variable in the *z* direction, perpendicular to the plane of the steel surface. This is also a strong assumption: if zinc is only accumulated locally at the steel grain boundaries, the destabilization of the steel / $Fe_2Al_5Zn_x$ interface leading to the subsequent disappearance of the $Fe_2Al_5Zn_x$ phase should only be observed at these locations. However, $Fe_2Al_5Zn_x$ disappears from the steel surface in a global manner and not only in the vicinity of the steel grain boundaries (section III.2.2). This hypothesis allows supposing that the zinc concentrations along all interfaces, assumed to be those at thermodynamic equilibrium (diffusion paths 1 and 3 in Figure 73), remain constant during the diffusion process.

Under the previous assumptions, the reaction mechanism really considered by the model should be described as shown in Figure 96.

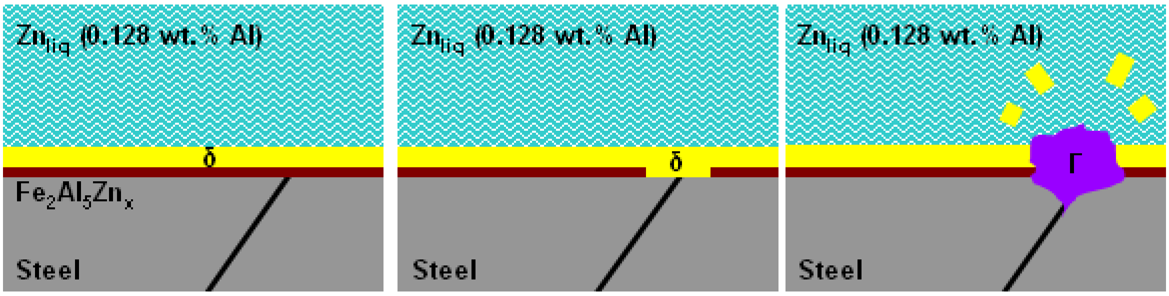

(a) (b) (c)

Figure 96: Schematic representation of the mechanisms accounting for the inhibition layer breakdown through outburst formation by zinc diffusion towards the steel grain boundaries according to the assumptions of the model (case of a steel galvanized in a bath containing 0.128 wt.% Al).

Based on these assumptions, a simplified diffusion model will be proposed from Fick's law in steady state. The zinc diffusion flux in the inhibition layer $\phi_{Zn}^{i.l.}$ (mol m^{-2} s^{-1}) can be expressed as follows in the direction from liquid zinc to ferrite (Figure 97):

$$\phi_{Zn}^{i.l.} = D_{Zn}^{\delta}\frac{c_{Zn}^{Zn(L)/\delta}(x_1+) - c_{Zn}^{\delta/Fe_2Al_5Zn_x}(x_2-)}{e_{\delta}} = D_{Zn}^{Fe_2Al_5Zn_x}\frac{c_{Zn}^{\delta/Fe_2Al_5Zn_x}(x_2+) - c_{Zn}^{Fe_2Al_5Zn_x/\,ferrite}(x_3-)}{e_{Fe_2Al_5Zn_x}} \tag{III.5}$$

where D_{Zn}^{δ} and $D_{Zn}^{Fe_2Al_5Zn_x}$ (m^2 s^{-1}) are the diffusion coefficients of zinc in δ and $Fe_2Al_5Zn_x$ and $c_{Zn}^{l_1/l_2}(x_k-)$ and $c_{Zn}^{l_1/l_2}(x_k+)$ (mol m^{-3}) the zinc concentrations at the two sides of the three l_1 / l_2 interfaces, namely liquid zinc / δ, δ / $Fe_2Al_5Zn_x$ and $Fe_2Al_5Zn_x$ / ferrite. These concentrations are those of the l_1 and l_2 phases at thermodynamic equilibrium. The expression proposed for this flux is open to criticism since, strictly speaking, it should be based on the activities in the compound and it should be used only for diffusion in a binary system [95]. In a given phase of a ternary system, the general equations for diffusion are function of four diffusion coefficients D_{ij}, defined as diffusion coefficient relating flux of component i (i.e., Zn or Fe) to chemical potential gradient of component j (i.e., Zn or Fe). Considering the uncertainties in the diffusion coefficients and based on our experimental results, a simplified model of diffusion (neglecting the cross diffusion coefficients D_{FeZn} and D_{ZnFe}) was used in order to obtain an estimation of the direct diffusion coefficients.

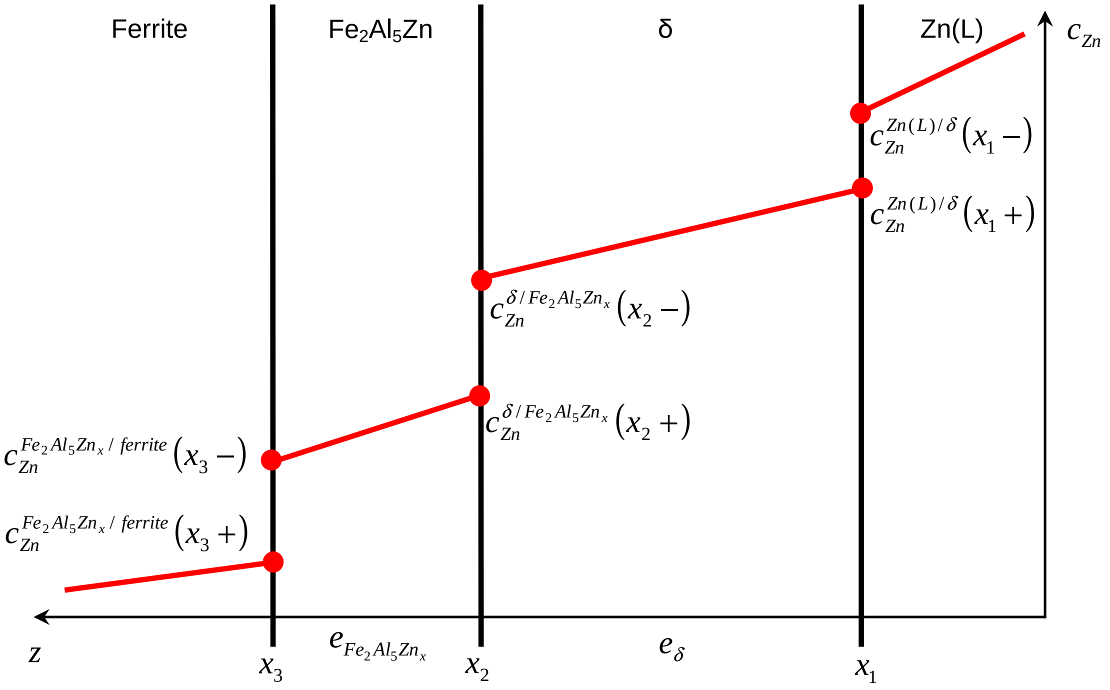

Figure 97: Schematic representation of the zinc concentration profiles in the two layers constituting the inhibition layer.

The diffusion coefficients involved in equation (III.5) are not precisely known. To our knowledge, the diffusion coefficient of zinc in δ has not been measured yet and there is only one measure for the diffusion coefficient of zinc in pure Fe_2Al_5 $D_{Zn}^{Fe_2Al_5}$ at 460 °C (= 5 x 10^{-15} m^2.s^{-1} [74]). The tie lines in the Al-Fe-Zn phase diagram are not known either. Finally, in order to be able to use the data obtained in this work, we decided to write the zinc diffusion flux in the inhibition layer as a function of temperature only with a global zinc concentration gradient in the inhibition layer, denoted $\nabla c_{Zn}^{i.l.}$ (mol m^{-4}):

$$\phi_{Zn}^{i.l.} = -D_{Zn}^{i.l.}\ \nabla c_{Zn}^{i.l.} = D_{Zn}^{i.l.}\ \left|\nabla c_{Zn}^{i.l.}\right| = D_0 \exp\left(\frac{-E_a}{RT}\right)\left|\nabla c_{Zn}^{i.l.}\right| \tag{III.6}$$

where $D_{Zn}^{i.l.}$ (m^2 s^{-1}) is the diffusion coefficient of zinc in the inhibition layer, whose variation with temperature T (K) has been expressed through an Arrhenius equation, D_0 (m^2 s^{-1}) being the pre-exponential factor, E_a (J mol^{-1}) the activation energy for diffusion and R (J mol^{-1} K^{-1}) the universal gas constant. As the zinc concentrations along all common interfaces of the inhibition layer and its thickness are assumed constant in the model, the zinc concentration gradient in the inhibition layer $\nabla c_{Zn}^{i.l.}$ is also constant.

With equation (III.6), the diffusion of zinc through the inhibition layer has been modelled globally. Instead of considering the diffusion of zinc through the $Fe_2Al_5Zn_x$ and δ phases separately, a global diffusion coefficient $D_{Zn}^{i.l.}$ taking into account the zinc diffusion in the entire layer has been defined. This new approach allows a very practical determination of the constants of this simplified model from the experimental results.

It is also to comment that for a given nature of the inhibition layer (structure, phase composition and thickness), D_0 and E_a are expected to be constant. In the present study, the nature of the inhibition layer is only dependent on the bath aluminium content, the bath temperature being fixed at around 460 °C for all the Rhesca trials.

The critical time at which the inhibition layer breakdown is achieved t_c (s) is such that a critical quantity of zinc Q_c (mol m^{-2}) diffuses through the inhibition layer at the steel grain boundaries. For a given steel substrate (chemical composition and grain size), this critical quantity is expected to be constant, independent of time and temperature:

$$Q_c = \int_{t_{growth}}^{t_c} \phi_{Zn}^{i.l.}\, dt = D_0 \left|\nabla c_{Zn}^{i.l.}\right| \int_{t_{growth}}^{t_c} \exp\left(\frac{-E_a}{RT}\right) dt \tag{III.7}$$

where t_{growth} (s) is the time necessary for the growth of a covering inhibition layer (around 0.2 s after the steel strip enters the galvanizing bath [32]).

As the thermal cycle undergone by the steel strip is an input data, it could then be possible to calculate the time needed to reach the inhibition layer breakdown according to the following law:

$$\int_{t_{growth}}^{t_c} \exp\left(\frac{-E_a}{RT}\right) dt = \frac{Q_c}{D_0 \left|\nabla c_{Zn}^{i.l.}\right|} \tag{III.8}$$

However, in order to estimate this time, the parameters E_a and $Q_c \Big/ \left(D_0 \left|\nabla c_{Zn}^{i.l.}\right|\right)$ need to be obtained experimentally.

Finally, as can be realised, strong simplifications have been applied to build this model, both in the reaction mechanisms and in the modelling work itself. The approach chosen therefore presents important scientific limitations but is the one allowing determining the parameters of the model without too much experimental workload. It will be evaluated below whether this level of modelling is enough to describe with acceptable accuracy the inhibition layer breakdown kinetics or not.

III.3.2.2. Experimental kinetic data processing

The raw kinetic results presented in section III.2.3 are used to determine the model parameters E_a and $Q_c \Big/ \left(D_0 \left| \nabla c_{Zn}^{i.l.} \right| \right)$.

III.3.2.2.1. Experimental determination of *E*$_a$

As stated above, the activation energy E_a corresponding to the diffusion coefficient of zinc in the inhibition layer $D_{Zn}^{i.l.}$ is expected to be unique for a given bath aluminium content. It can be determined directy from the isothermal heat treatments carried out in the Gleeble 3500 device provided that all the samples have met equivalent immersion and cooling thermal profiles during galvanizing in the Rhesca pilot simulator, what has been carefully checked. For an isothermal treatment at $T_{hold,\exp}$ lasting from 0 s to $t_{hold,\exp}$, the kinetic law given by equation (III.8) can be rewritten as follows:

$$\int_0^{t_{hold,\exp}} \exp\left(\frac{-E_a}{RT_{hold,\exp}} \right) dt = \exp\left(\frac{-E_a}{RT_{hold,\exp}} \right) \int_0^{t_{hold,\exp}} dt = \frac{Q_{hold,\exp}}{D_0 \left| \nabla c_{Zn}^{i.l.} \right|} \qquad \text{(III.9)}$$

where $Q_{hold,\exp}$ is the part of the critical quantity of zinc Q_c that diffuses through the inhibition layer to the steel grain boundaries during the isothermal treatment. Equation (III.9) leads to:

$$t_{hold,\exp} = \frac{Q_{hold,\exp}}{D_0 \left| \nabla c_{Zn}^{i.l.} \right|} \exp\left(\frac{E_a}{RT_{hold,\exp}} \right) \qquad \text{(III.10)}$$

And:

$$\ln t_{hold,\exp} = Ln\left(\frac{Q_{hold,\exp}}{D_0 \left| \nabla c_{Zn}^{i.l.} \right|} \right) + \frac{E_a}{RT_{hold,\exp}} \qquad \text{(III.11)}$$

The experiments performed on the Gleeble 3500 pilot will give directly the activation energy E_a when plotting $\ln t_{hold,\exp}$ against $1 \big/ T_{hold,\exp}$ (the slope of the straight line is equal to E_a / R).

The parameter $Q_c \Big/ \left(D_0 \left| \nabla c_{Zn}^{i.l.} \right| \right)$ cannot be determined yet for the reason that $Q_{hold,\exp}$ does not take into account the quantity of zinc which has already diffused in the Rhesca pilot simulator (during immersion in the zinc bath and cooling). The real time for the inhibition layer breakdown t_c is therefore underestimated when represented by $t_{hold,\exp}$. As a result, this latter needs to be corrected by taking into account the Rhesca thermal cycle. This correction is detailed in section III.3.2.2.2.

The results obtained for the experimental holding time necessary for the inhibition layer breakdown showed in Figure 92 for the first Rhesca trials campaign (0.128 wt.% Al) are represented in logarithmic scale against the reciprocal of experimental holding temperature in Figure 98.

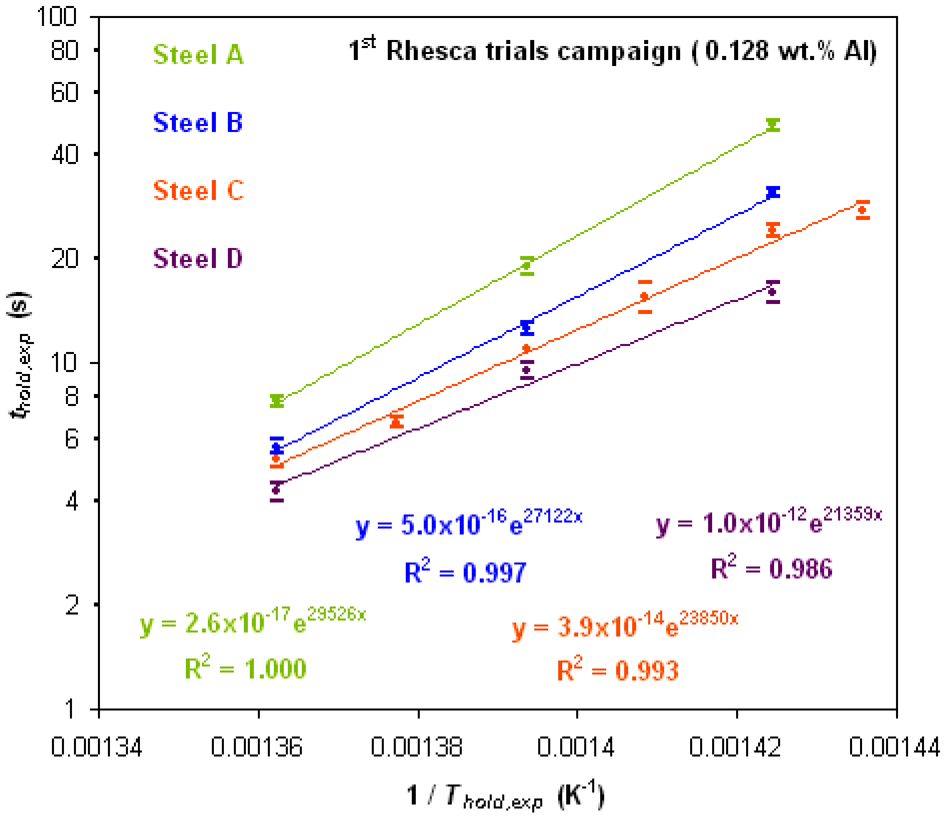

Figure 98: Experimental holding time needed for the inhibition layer breakdown (logarithmic scale) against the reciprocal of experimental holding temperature performed in the Gleeble 3500 pilot simulator (first Rhesca trials campaign).

The activation energy E_a can be directly obtained from the results shown in Figure 98 and its value is presented, for each steel, in Table 27.

Table 27: Values of the activation energy E_a for the Ti IF steels studied (first Rhesca trials campaign).

Steel	Slope=E_a/R (K)	E_a (J/mol)
A	29526	245500
B	27122	225500
C	23850	198300
D	21359	177600

It can be seen that the value of the activation energy varies from one steel substrate to another. In addition, it will be seen that this parameter seems to be correlated to the steel chemical composition. This unexpected behaviour will be discussed in section III.3.2.3.

Analogously, the experimental holding times needed for the inhibition layer breakdown showed in Figure 93 for the second Rhesca trials campaign (0.112 wt.% Al) are represented in logarithmic scale against the reciprocal of experimental holding temperature in Figure 99.

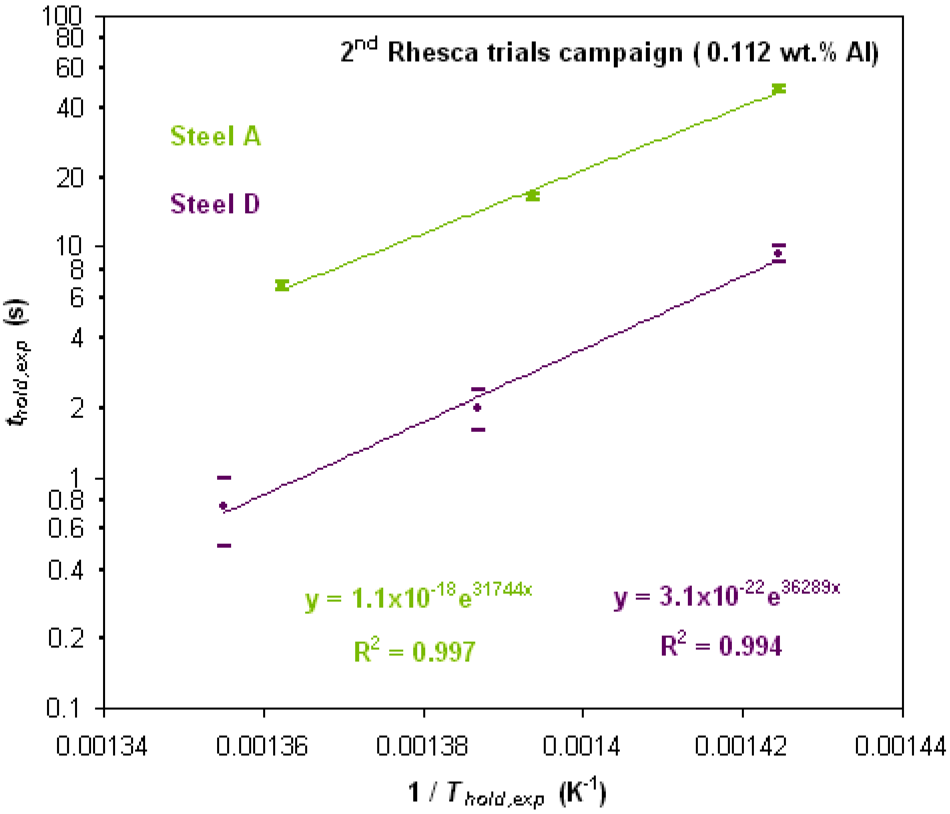

Figure 99: Experimental holding time needed for the inhibition layer breakdown (logarithmic scale) against the reciprocal of experimental holding temperature performed in the Gleeble 3500 pilot simulator (second Rhesca trials campaign).

The values of activation energy E_a obtained from the results shown in Figure 99 are presented, for steels A and D, in Table 28. As in the case of the first Rhesca campaign, the value of the activation energy varies from one steel substrate to another.

Table 28: Values of the activation energy E_a for steels A and D (second Rhesca trials campaign).

Steel	Slope=E_a/R (K)	E_a (J/mol)
A	31744	263900
D	36289	301700

As already commented, the experimental holding times necessary to achieve the inhibition layer breakdown at the different experimental holding temperatures have been determined through a trial and error method. Only these times are presented here. Nevertheless, all the Gleeble 3500 trials through which these times have been obtained are available in Appendix G.

III.3.2.2.2. Experimental determination of $Q_c / (D_0.|\nabla c_{Zn}^{i.l.}|)$

As told before, the determination of the parameter $Q_c / \left(D_0 \left|\nabla c_{Zn}^{i.l.}\right|\right)$ requires a previous estimation of the zinc quantity which has diffused in the Rhesca pilot in order to calculate the real time for inhibition layer breakdown t_c. The applied procedure is explained here below.

First of all, the following equation has been integrated along the Rhesca thermal cycle (immersion in the galvanizing bath and cooling) in order to calculate $Q_{Rhesca} \big/ \left(D_0 \cdot \left|\nabla c_{Zn}^{i.l.}\right|\right)$:

$$\int_{t_{growth}}^{t_{non\ isothermal}} \exp\left(\frac{-E_a}{R.T}\right).dt = \frac{Q_{Rhesca}}{D_0 \cdot \left|\nabla c_{Zn}^{i.l.}\right|} \tag{III.12}$$

where Q_{Rhesca} is the part of the critical quantity of zinc Q_c that diffuses through the inhibition layer to the steel grain boundaries during the Rhesca thermal cycle and $t_{non\ isothermal}$ is the duration of this thermal cycle from the immersion in the galvanizing bath to the end of the cooling.

The Rhesca thermal cycles were discretized (step of 0.4 s) for integration, which was performed by means of the trapezoidal method.

It has been noted that, in all cases, the value of this integration does not almost evolve below 400 °C (its evolution is estimated in most cases less than 4%, and in all cases less than 7%, of the integration value from 400 °C). This means that the zinc diffusion can be neglected below this temperature.

As already stated, the Rhesca thermal profiles of the samples considered in the present study for each couple steel-campaign are nearly identical above the temperature of 400 °C. This fact allows integrating equation (III.12) along the Rhesca thermal cycle of a unique sample for each couple steel-campaign to calculate $Q_{Rhesca} \big/ \left(D_0 \cdot \left|\nabla c_{Zn}^{i.l.}\right|\right)$ and to consider that this calculation is valid for all the other samples of the same couple. Nevertheless, the Rhesca thermal profiles of all the samples have been obviously checked in order to indentify any possible deviation from the reference sample.

The objective of our calculation is to estimate the critical quantity of zinc Q_c that diffuses through the inhibition layer to the steel grain boundaries during an isothermal treatment at $T_{hold,\exp}$. When the isothermal treatment begins, there is already a quantity of zinc Q_{Rhesca} present in the steel grain boundaries. Therefore, once $Q_{Rhesca} \big/ \left(D_0 \cdot \left|\nabla c_{Zn}^{i.l.}\right|\right)$ has been calculated, the equivalent time t_{Rhesca} necessary to make the same quantity of zinc Q_{Rhesca} diffuse during an isothermal heat treatment at a given experimental holding temperature $T_{hold,\exp}$ is calculated according to the following equation:

$$t_{Rhesca} = \frac{Q_{Rhesca}}{D_0 \left|\nabla c_{Zn}^{i.l.}\right|} \cdot \exp\left(\frac{E_a}{R T_{hold,\exp}}\right) \tag{III.13}$$

The real time (corrected time) necessary for the inhibition layer breakdown t_c during an isothermal heat treatment at the experimental holding temperature $T_{hold,\exp}$ is calculated as follows:

$$t_c = t_{hold,\exp} + t_{Rhesca} \tag{III.14}$$

It should be noticed that the time correction requires the previous determination of the activation energy E_a through the raw results obtained on Gleeble 3500 device (section III.3.2.2.1).

In order to put forward the weight of t_{Rhesca} and $t_{hold,\exp}$ compared to t_c, the ratio between t_{Rhesca} and t_c is available in Table 29 for each couple steel-campaign. As it can be seen, t_{Rhesca} is lower than $t_{hold,\exp}$, with the exception of steel D galvanized during the second Rhesca trials campaign (0.112 wt.% Al). The former ratio between t_{Rhesca} and t_c is, according to the modelling work done, independent of the value of $T_{hold,\exp}$, and is equal to the ratio between Q_{Rhesca} and Q_c, provided that D_0 and $\left|\nabla c_{Zn}^{i.l.}\right|$ remain constant.

Table 29: Ratio between t_{Rhesca} and t_c for each couple steel-campaign.

Steel	**t_{Rhesca} / t_c (%)**	
	1st campaign (0.128 wt.% Al)	**2nd campaign (0.112 wt.% Al)**
A	**~17**	**~21**
B	**~24**	**-**
C	**~30**	**-**
D	**~34**	**~64**

As seen before, the following equations can be written for a given holding temperature $T_{hold,\exp}$:

$$t_c = \frac{Q_c}{D_0 \left|\nabla c_{Zn}^{i.l.}\right|} \cdot \exp\left(\frac{E_a}{RT_{hold,\exp}}\right) \tag{III.15}$$

$$\ln t_c = \ln\left(\frac{Q_c}{D_0 \left|\nabla c_{Zn}^{i.l.}\right|}\right) + \frac{E_a}{RT_{hold,\exp}} \tag{III.16}$$

The value of the parameter $Q_c \big/ \left(D_0 \left|\nabla c_{Zn}^{i.l.}\right|\right)$ can then be obtained directly when plotting $\ln t_c$ against $1/T_{hold,\exp}$ (the y-intercept of the straight line obtained is equal to $\ln\left[Q_c \big/ \left(D_0 \cdot \left|\nabla c_{Zn}^{i.l.}\right|\right)\right]$). This parameter represents the real time necessary for the inhibition layer breakdown when an isothermal heat treatment at infinite temperature is performed.

The real time necessary for the inhibition rupture in the case of the first Rhesca trials campaign (0.128 wt.% Al) is plotted in logarithmic scale against the reciprocal of experimental holding temperature in Figure 100.

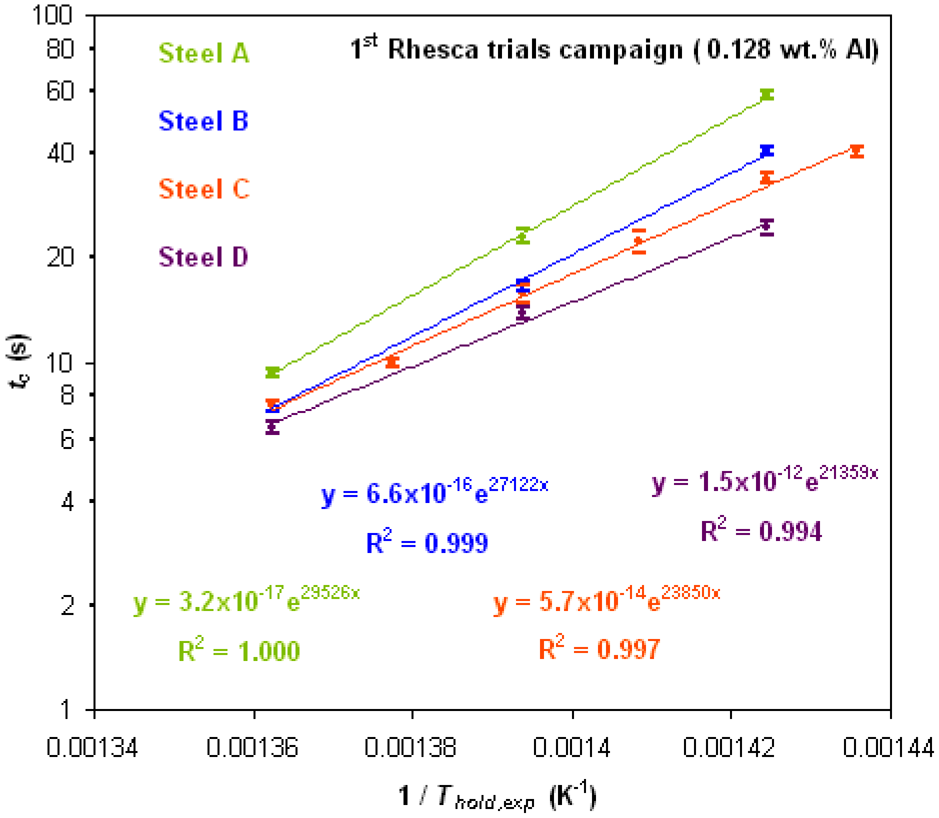

Figure 100: Real holding time needed for the inhibition layer breakdown (logarithmic scale) against the reciprocal of experimental holding temperature performed in the Gleeble 3500 pilot simulator (first Rhesca trials campaign).

The value of the parameter $Q_c/\left(D_0\left|\nabla c_{Zn}^{i.l.}\right|\right)$ is presented, for each steel substrate, in Table 30.

Table 30: Values of the parameter $Q_c/\left(D_0\left|\nabla c_{Zn}^{i.l.}\right|\right)$ for the Ti IF steels studied (first Rhesca trials campaign).

Steel	$Q_c/(D_0\|\nabla c_{Zn}^{i.l.}\|)$ (s)
A	3.2×10^{-17}
B	6.6×10^{-16}
C	5.7×10^{-14}
D	1.5×10^{-12}

As it happens with the activation energy, the value of the parameter $Q_c/\left(D_0\left|\nabla c_{Zn}^{i.l.}\right|\right)$ varies from one steel substrate to another and seems to be also correlated to the steel chemical composition. Assumptions aiming to explain these observations will be proposed in section III.3.2.3.

The results presented in Figure 100 could be compared with the kinetic data reported in the literature (Table 7 and Table 8). However, among these kinetic data only the results provided by Leprêtre [33] (Table 7) can be used for comparison because the other authors have done their experiments in much different conditions to the ones performed in this study and, in addition, they did not mention some important data on the steel chemical composition or the galvanizing and galvannealing conditions. Leprêtre [33] performed long immersion time experiments in a bath containing 0.13 wt.% Al at 460 ℃ (0.128 wt.% Al and same temperature in this work) and found that a steel with grain size of 20 µm (between 9 and 11 µm in this study) and parameter $w^{**}_{Ti_{excess}}$ equal to 6.8 (between -6.6 for steel A and 18.0 for steel B, Table 23) meets the inhibition rupture after 10 s of immersion. The times t_c obtained for steels A and B at 460 ℃ are 7.5 and 9 .5 s respectively. The time reported by Leprêtre [33] is therefore slightly longer than the previous times, but in the same order of magnitude. The fact that this author has found a longer time may be due to the higher grain size of the steel used for its experiments, which delays the inhibition layer breakdown (I.3.2.2.2.1).

In any case, the effect of the steel chemical composition on the inhibition layer breakdown kinetics reported in section I.3.2.2.2.2 can be appreciated in Figure 100: the steel with the highest amount of titanium and the lowest amounts of carbon, nitrogen, sulphur and phosphorous (steel D, Table 22) is the one which meets the inhibition rupture the earliest.

Analogously to Figure 100, the real time necessary for the inhibition layer breakdown in the case of the second Rhesca trials campaign (0.112 wt.% Al) is plotted in logarithmic scale against the reciprocal of experimental holding temperature in Figure 101.

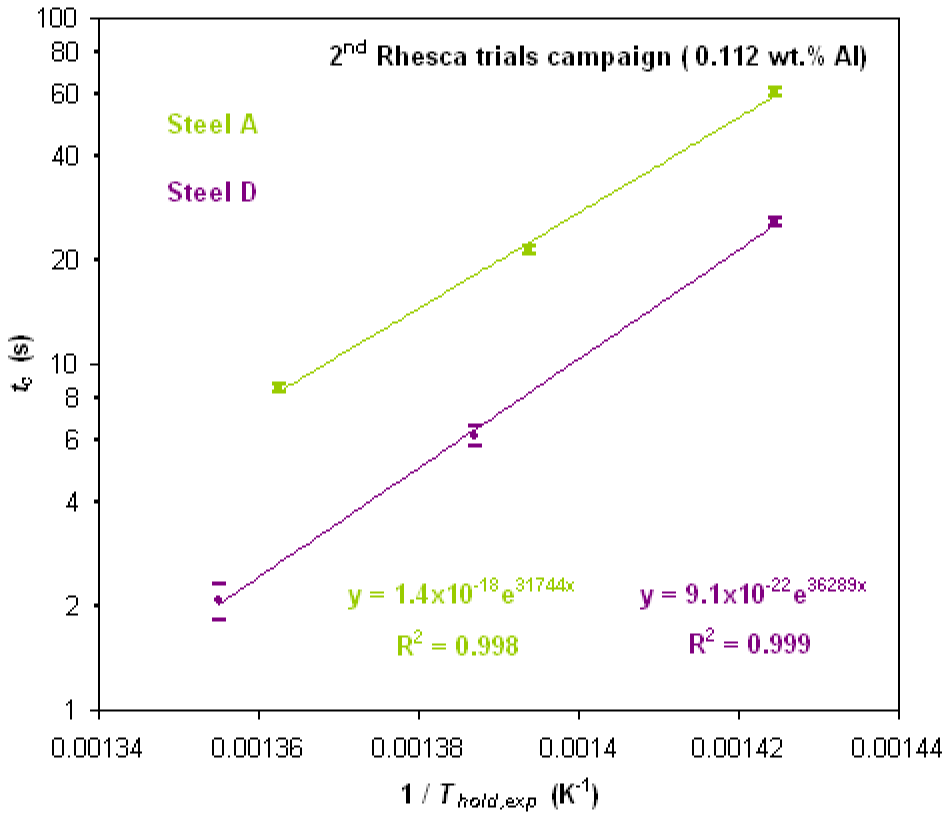

Figure 101: Real holding time needed for the inhibition layer breakdown (logarithmic scale) against the reciprocal of experimental holding temperature performed in the Gleeble 3500 pilot simulator (second Rhesca trials campaign).

The value of the parameter $Q_c \Big/ \left(D_0 \left|\nabla c_{Zn}^{i.l.}\right|\right)$ for steels A and D is presented in Table 31.

Table 31: Values of the parameter $Q_c \Big/ \left(D_0 \left|\nabla c_{Zn}^{i.l.}\right|\right)$ for steels A and D (second Rhesca trials campaign).

Steel	$Q_c/(D_0\|\nabla c_{Zn}^{i.l.}\|)$ (s)
A	1.4×10^{-18}
D	9.1×10^{-22}

III.3.2.3. Effect of the steel chemical composition

In this section, the arguments in order to choose the parameter which accounts the best for the steel chemical composition with regard to the inhibition layer breakdown kinetics will be first exposed. Experimental evidence of the influence of this parameter on E_a and $Q_c/\left(D_0\left|\nabla c_{Zn}^{i.l.}\right|\right)$ will then be reported and discussed in detail. Assumptions aiming to explain the effects observed will also be proposed. As advanced previously, this analysis will be made on the results obtained for the first Rhesca trials campaign (0.128 wt.% Al).

III.3.2.3.1. Selection of the most relevant chemical reactivity parameter

Four different chemical reactivity parameters describing the excess solute titanium were proposed at the beginning of chapter III. The value of each of these parameters was calculated in section III.1.1 for the four Ti IF steel substrates used for the present study (Table 23). These values are presented again in Table 32 together with the steel substrates chemical composition and the values of E_a and $Q_c/\left(D_0\left|\nabla c_{Zn}^{i.l.}\right|\right)$ obtained experimentally.

Table 32: Chemical composition, chemical reactivity parameters and E_a and $Q_c/\left(D_0\left|\nabla c_{Zn}^{i.l.}\right|\right)$ values for the different Ti IF steels studied (first Rhesca trials campaign) (a reference industrially galvanized steel is included).

Steel	A	B	C	D	reference
C (10^{-3} wt.%)	3.0	2.1	2.0	2.2	2.6
P (10^{-3} wt.%)	12.4	13.6	9.1	6.9	12.0
S (10^{-3} wt.%)	14.1	15.2	9.0	12.5	4.0
N (10^{-3} wt.%)	3.4	3.9	2.1	3.4	2.6
Si (10^{-3} wt.%)	9.3	4.0	4.0	4.6	13.0
Ti (10^{-3} wt.%)	57.4	83.6	67.3	84.1	58.0
$w^{*}_{Ti_{excess}}$ (10^{-3} wt.%) (equation III.1)	12.6	39.0	38.6	44.9	32.7
$w^{**}_{Ti_{excess}}$ (10^{-3} wt.%) (equation III.2)	-6.6	18.0	24.5	34.2	14.1
$x_{Ti_{excess}}$ (equation III.3)	0.7	1.8	2.7	4.2	1.8
Reactivity Index (equation III.4)	-0.4	2.6	3.6	4.3	0.6
E_a (J/mol)	245500	225500	198300	177600	225600
$Q_c/(D_0 \cdot \lvert \nabla c_{Zn}^{i.l.} \rvert)$ (s)	3.2×10^{-17}	6.6×10^{-16}	5.7×10^{-14}	1.5×10^{-12}	7.9×10^{-16}

As can be observed, a new steel substrate has been added in Table 32. This steel is a reference steel, galvanized in an industrial bath at 460 ℃ containing 0.128 wt.% Al (the same aluminium content as in the first Rhesca trials campaign). For this reference steel, the industrial galvannealing furnace was off-line. The samples obtained were then annealed by means of the Gleeble 3500 device in a previous study [96] in order to estimate the values of E_a and $Q_c/\left(D_0\left|\nabla c_{Zn}^{i.l.}\right|\right)$. As already explained in section III.3.2.2.1, E_a can be precisely determined from Gleeble 3500 experiments. On the contrary, the accurate determination of $Q_c/\left(D_0\left|\nabla c_{Zn}^{i.l.}\right|\right)$ requires a precise knowledge of the thermal cycle undergone by the steel substrate during immersion in the galvanizing bath and cooling to room temperature. In the case of industrially galvanized samples, the knowledge of this thermal cycle is submitted to a higher uncertainty compared to samples galvanized in the Rhesca pilot simulator. As a result, the value of $Q_c \Big/ \left(D_0 \left| \nabla c_{Zn}^{i.l.} \right| \right)$ estimated in the case of the reference steel should be taken with some reservations. But, in any case, this steel is extremely close to steel B in terms of reactivity behaviour, i.e., E_a and $Q_c \Big/ \left(D_0 \left| \nabla c_{Zn}^{i.l.} \right| \right)$ (this is the reason why both of them are presented in the same colour) and their comparison will contribute to identify the most pertinent chemical reactivity parameter.

As a complement to Table 32, Figure 102 depicts the difference in the values of E_a for the different steel substrates. The values of the chemical reactivity parameters $w_{Ti_{excess}}^{*}$, $w_{Ti_{excess}}^{**}$ and $x_{Ti_{excess}}$ as well as the phosphorous and silicon contents for each steel are also shown.

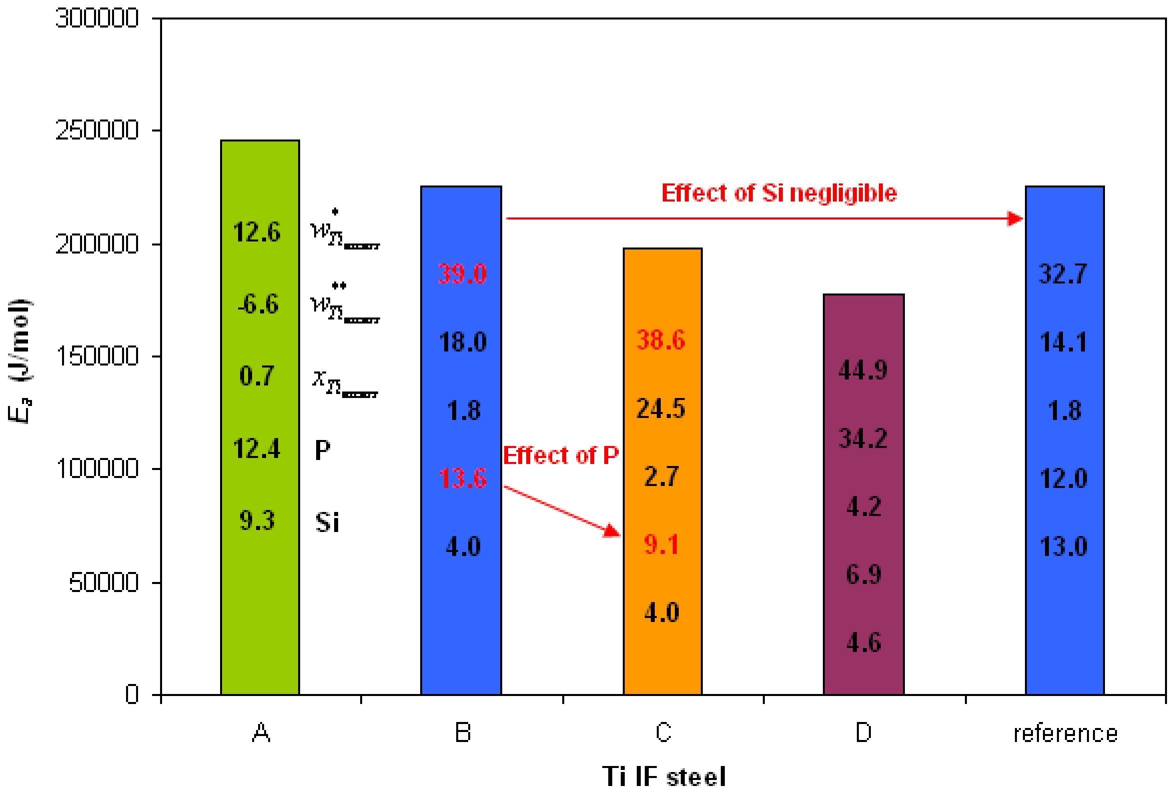

Figure 102: Comparison of E_a values for the different Ti IF steels studied (first Rhesca trials campaign) (a reference industrially galvanized steel is included).

A first sorting of the chemical reactivity parameters will be done on the basis of the data presented in Table 32 and Figure 102.

As can be appreciated in equation (III.1), the parameter $w_{Ti_{excess}}^{*}$ considers that solute titanium stabilize carbon, nitrogen and sulphur in the steel as TiC, TiN and TiS respectively. The parameter $w_{Ti_{excess}}^{*}$ is generally admitted in the literature for the precipitation phenomena in Ti IF steels. However, concerning the inhibition layer breakdown kinetics, the values of E_a and $Q_c \Big/ \left(D_0 \left| \nabla c_{Zn}^{i.l.} \right| \right)$ obtained for steels B and C are substantially different, even if the value of the parameter $w_{Ti_{excess}}^{*}$ is the same (Table 32 and Figure 102). In addition, for steels B and C, the silicon content is the same but the phosphorous content is different. The comparison of steels B and C allows concluding that the parameter $w^{*}_{Ti_{excess}}$ is not complete enough and that phosphorous precipitation should also be considered.

The parameters $w^{**}_{Ti_{excess}}$ and $x_{Ti_{excess}}$ (equations III.2) and (III.3) respectively) as well as the *Reactivity Index* (equation (III.4)) take all of them into account the phosphorous precipitation. In addition, the *Reactivity Index* considers a possible effect of silicon. The comparison between steel B and the reference steel leads to the conclusion that this effect can be neglected, at least for silicon contents in the steel up to 13 x 10^{-3} wt.%. Indeed, steel B and the reference steel present very close inhibition layer breakdown kinetics (very close values of E_a and $Q_c \Big/ \left(D_0 \left| \nabla c^{i.l.}_{Zn} \right| \right)$ as well as very similar values of $w^{*}_{Ti_{excess}}$ and phosphorous content. However they present very different values of the *Reactivity Index*, which is due to a substantial difference in the silicon content (4 x 10^{-3} wt.% for steel B compared to 13 x 10^{-3} wt.% for the reference steel). It can therefore be concluded that no effect of the silicon content on the inhibition layer breakdown kinetics is observed for the Ti IF steels used for this study. However, it would be interesting to check whether an effect of this element exists or not when present in the steel in higher amounts. Pending further results, the *Reactivity Index* will be rejected for the time being.

A final selection must be made between the parameters $w^{**}_{Ti_{excess}}$ and $x_{Ti_{excess}}$. The only difference between them is that they take into account the phosphorous precipitation in a different way. The parameter $w^{**}_{Ti_{excess}}$ considers that phosphorous fully precipitates as FeTiP provided that there is enough solute titanium in the steel while the parameter $x_{Ti_{excess}}$ considers that the precipitation of the whole amount of phosphorous is not assured even if the amount of solute titanium is stoechiometrically high enough to make the whole amounts of carbon, nitrogen, sulphur and phosphorous precipitate. The higher the value of $x_{Ti_{excess}}$ is, the higher the probability of phophorous precipitation is.

It has been seen in section III.3.2.2 that E_a and $Q_c \Big/ \left(D_0 \left| \nabla c^{i.l.}_{Zn} \right| \right)$ seem to be correlated to the steel chemical composition. As the good choice between $w^{**}_{Ti_{excess}}$ and $x_{Ti_{excess}}$ cannot be made from the elements of Table 32 and Figure 102, the criterion that will be taken to identify the most relevant parameter is its capacity to better correlate E_a and $Q_c \Big/ \left(D_0 \left| \nabla c^{i.l.}_{Zn} \right| \right)$.

Figure 103 depicts the evolution of E_a as a function of chemical reactivity parameters $w^{**}_{Ti_{excess}}$ (blue) and $x_{Ti_{excess}}$ (red). It can be seen that $x_{Ti_{excess}}$ provides a better representation than $w^{**}_{Ti_{excess}}$, on the basis of the correlation coefficient of the linear regression (closer to 1).

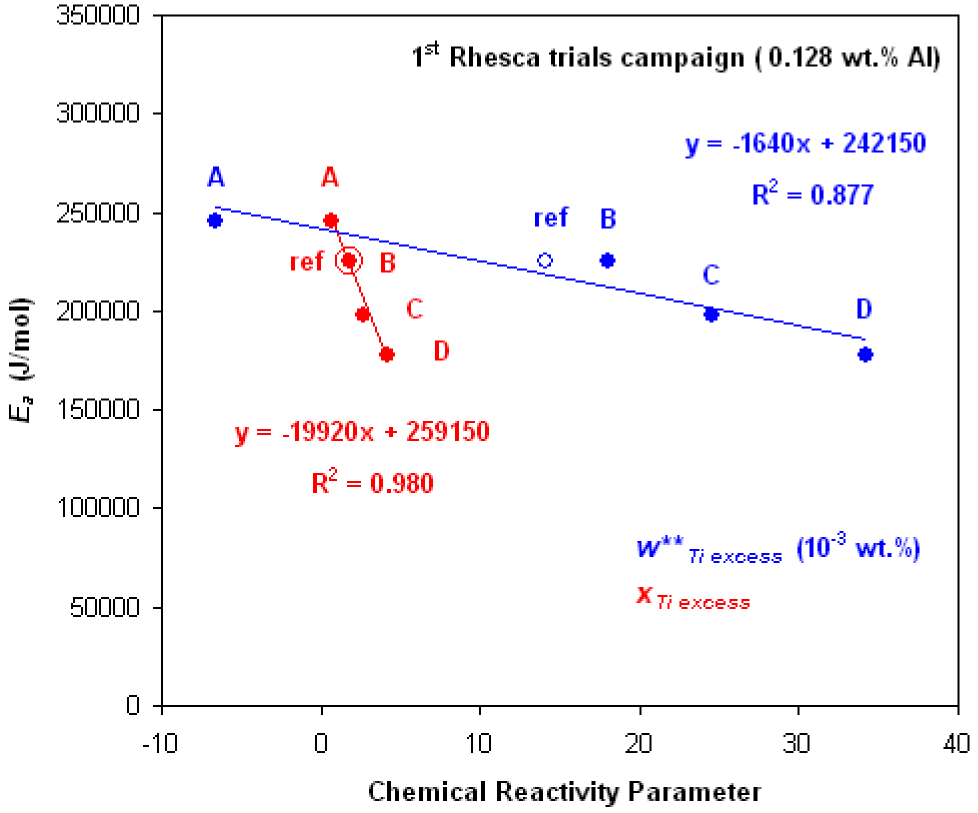

Figure 103: E_a against chemical reactivity parameters $w^{**}_{Ti_{excess}}$ (blue) and $x_{Ti_{excess}}$ (red) for the different Ti IF steels studied (first Rhesca trials campaign) (unfilled points correspond to the reference steel).

In the same way, Figure 104 represents the evolution of $Q_c / \left(D_0 \left| \nabla c^{i.l.}_{Zn} \right| \right)$ as a function of chemical reactivity parameters $w^{**}_{Ti_{excess}}$ (blue) and $x_{Ti_{excess}}$ (red). As happens with E_a, $x_{Ti_{excess}}$ provides a better representation than $w^{**}_{Ti_{excess}}$, on the basis of the correlation coefficient of the linear regression (closer to 1).

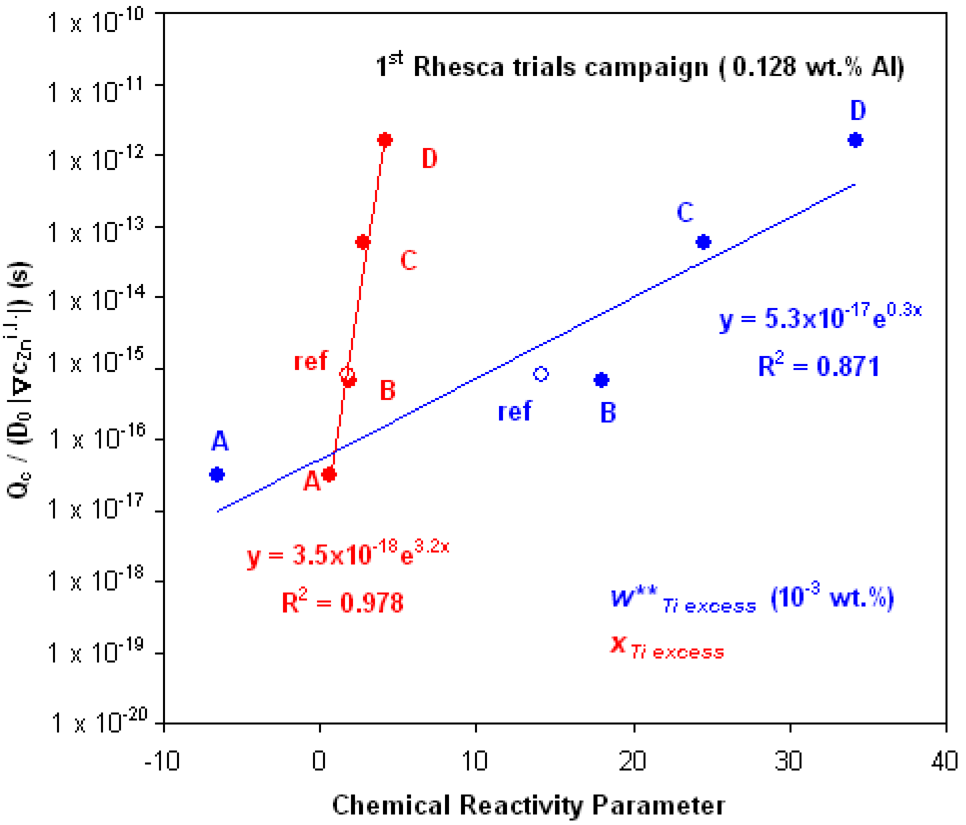

Figure 104: $Q_c / \left(D_0 \left|\nabla c_{Zn}^{i.l.}\right|\right)$ against chemical reactivity parameters $w_{Ti_{excess}}^{**}$ (blue) and $x_{Ti_{excess}}$ (red) for the different Ti IF steels studied (first Rhesca trials campaign) (unfilled points correspond to the reference steel).

In addition, crucial information can be obtained when comparing steel B with the reference steel. These steels present the same reactivity behaviour (same E_a and $Q_c / \left(D_0 \left|\nabla c_{Zn}^{i.l.}\right|\right)$). However, while the value of the parameter $x_{Ti_{excess}}$ for both substrates is the same (filled and unfilled points are superposed in Figure 103 and Figure 104), the parameter $w_{Ti_{excess}}^{**}$ for these steels adopts different values.

According to the previous observations, the parameter $x_{Ti_{excess}}$, which considers that FeTiP precipitation is not completely assured, will be selected as the most relevant chemical reactivity parameter. It is important to comment here that this is a quite arbitrary decision with the clear objective of determining an industrial indicator to evaluate the steel chemical composition with regard to the inhibition layer breakdown kinetics. For instance, there is no physical reason for E_a and $Q_c / \left(D_0 \left|\nabla c_{Zn}^{i.l.}\right|\right)$ to vary with the chemical reactivity parameter according to linear and exponential laws respectively. This selection is also strongly supported by the fact that the parameter $w_{Ti_{excess}}^{**}$ may eventually have negative values (case of steel A) and, from a physical point of view, a negative value of excess solute titanium makes no sense. On the contrary, the parameter $x_{Ti_{excess}}$ has a positive value in the whole range of chemical compositions of commercial Ti IF steel grades according to Mardyck databases (from 0 to 7).

III.3.2.3.2. Effect of the steel chemical composition on E_a and Q_c / (D_0.$|\nabla c_{Zn}^{i.l.}|$)

Now that parameter $x_{Ti_{excess}}$ has been choosen to describe the steel chemical composition, the effect of this parameter on E_a and $Q_c / \left(D_0 \left|\nabla c_{Zn}^{i.l.}\right|\right)$ will be analyzed in detail.

Figure 105 illustrates the effect of parameter $x_{Ti_{excess}}$ on E_a and $Q_c / \left(D_0 \left|\nabla c_{Zn}^{i.l.}\right|\right)$ (data from Figure 103 and Figure 104, respectively, recolted in a unique graph). These results are presented again in Table 33.

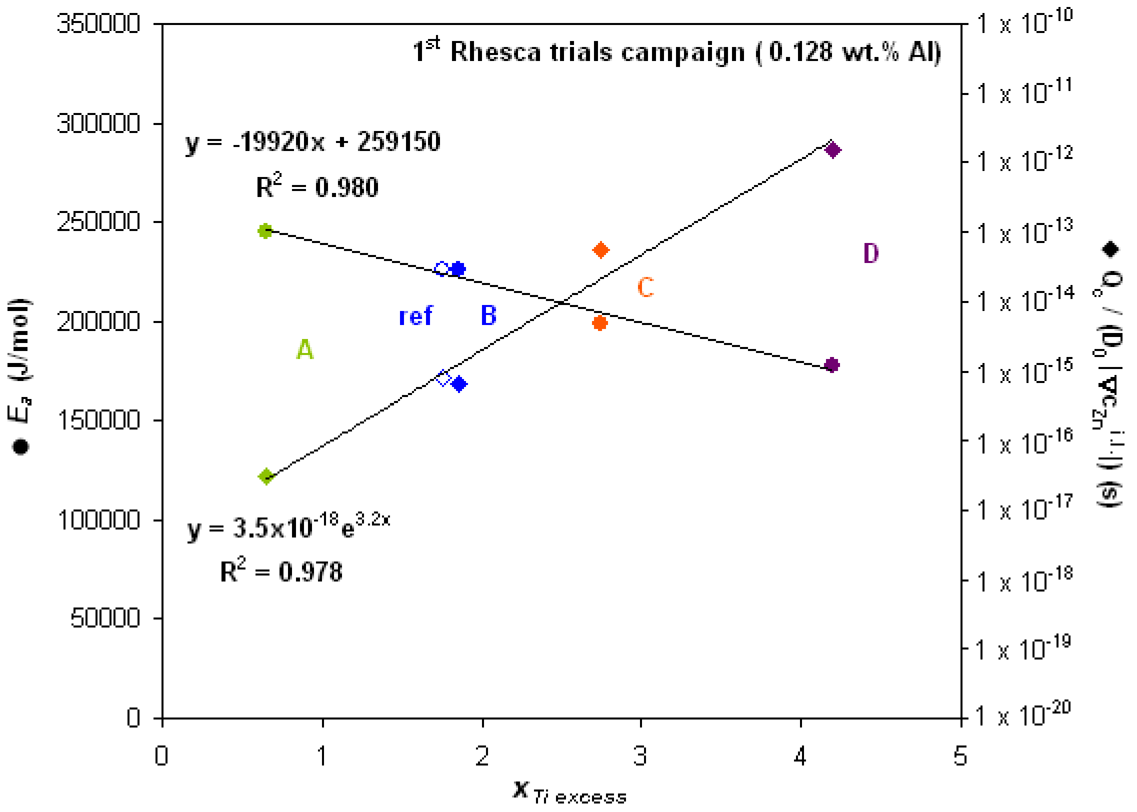

Figure 105: E_a **(circles) and** $Q_c / \left(D_0 \left|\nabla c_{Zn}^{i.l.}\right|\right)$ **(squares) against chemical reactivity parameter** $x_{Ti_{excess}}$ **for the different Ti IF steels studied (first Rhesca trials campaign) (unfilled points correspond to the reference steel).**

Table 33: Values of $x_{Ti_{excess}}$, E_a **and** $Q_c / \left(D_0 \left|\nabla c_{Zn}^{i.l.}\right|\right)$ **for the different Ti IF steels studied (first Rhesca trials campaign).**

Steel	$x_{Ti_{excess}}$ (equation III.3)	E_a (J/mol)	$Q_c/(D_0|\nabla c_{Zn}^{i.l.}|)$ (s)
A	0.7	245500	3.2×10^{-17}
B	1.8	225500	6.6×10^{-16}
C	2.7	198300	5.7×10^{-14}
D	4.2	177600	1.5×10^{-12}
reference	1.8	225600	7.9×10^{-16}

As can be seen, both E_a and $Q_c \Big/ \left(D_0 \left|\nabla c_{Zn}^{i.l.}\right|\right)$ are very well correlated to $x_{Ti_{excess}}$. The higher the $x_{Ti_{excess}}$ is, the lower the E_a is and the higher the value of parameter $Q_c \Big/ \left(D_0 \left|\nabla c_{Zn}^{i.l.}\right|\right)$ is.

III.3.2.3.3. General discussion

Pertinence of the hypothesis of the model proposed for the inhibition layer breakdown kinetics

The modelling of the inhibition layer breakdown kinetics assumes that the rate of zinc diffusion from the middle of the steel grains towards the grain boundaries (diffusion along the steel / inhibition layer interface) is infinite and that the structure of the inhibition layer only depends on the galvanizing and cooling conditions (section III.3.2.1). Under these assumptions, the experimentally obtained E_a and D_0 should only depend on the diffusion of zinc through the inhibition layer, with the same values for all the steel substrates galvanized in the same conditions (same bath temperature and composition in the first Rhesca trials campaign) as, up to now, there is no reason to think that the nature of the inhibition layer can be dependent on the Ti IF steel substrate. The difference in reactivity was then expected to be linked to a different value of the quantity of zinc present at the steel grain boundaries necessary for the inhibition layer breakdown Q_c. The expected graph for Figure 100 would therefore be characterized by parallel straight lines with the same slope, i.e., same E_a (equation (III.16)) and different y-intercept values (this difference expected to be associated with a different value of Q_c).

As shown in Figure 100, the slope of the straight lines linking $\ln t_c$ to the reciprocal of holding temperature is different for each steel substrate. This means that the value of E_a varies from one steel substrate to another and indicates that E_a takes into account not only the diffusion of zinc through the inhibition layer but also the diffusion of zinc at the steel / inhibition layer interface and at the steel grain boundaries. As commented in section III.3.2.1, the initial assumption that the diffusion of zinc along the steel / inhibition layer interface can be considered as infinite may be open to criticism. In addition, the fact that the value of E_a has been found to be correlated to $x_{Ti_{excess}}$ indicates that it is defined by the diffusion of zinc in the steel grain boundaries. The higher $x_{Ti_{excess}}$ is, the lower E_a is, i.e., the cleaner the steel grain boundaries are, the easier the diffusion of zinc in these locations is (with some reservations, as the evolution of the pre-exponential factor of the diffusion coefficient of zinc D_0 with $x_{Ti_{excess}}$ could not be evaluated in the present study). A higher diffusion rate in the grain boudaries (corresponding to lower E_a) would reduce the increase in the zinc activity along the steel / inhibition layer interface while a slower diffusion in the grain boundaries (higher E_a) would let it increase a bit more. The initial assumption that the zinc concentration gradient is kept constant is less true when E_a is high.

The parameter $Q_c \Big/ \left(D_0 \left|\nabla c_{Zn}^{i.l.}\right|\right)$ increases with increased $x_{Ti_{excess}}$ (Figure 105). It can be explained by supposing that the cleanliness of the steel grain boundaries could slow down the accumulation of zinc at these locations. If there is no substantial segregation of alloying elements at these sites, zinc atoms are less accumulated (they are more able to diffuse deeper into the grain boundaries). The zinc local concentration necessary for the nucleation of the Γ phase leading to the inhibition layer breakdown would require a higher quantity of zinc atoms Q_c. It should be noted that the pre-exponential factor of the diffusion coefficient of zinc D_0 is included in the parameter $Q_c \Big/ \left(D_0 \left|\nabla c_{Zn}^{i.l.}\right|\right)$. As told before, the evolution of this factor with $x_{Ti_{excess}}$ could not be obtained experimentally. However, it has been supposed above that the higher $x_{Ti_{excess}}$ is, the faster the diffusion of zinc at the steel grain boundaries is. Under this hypothesis, one could accept that D_0 increases when increasing $x_{Ti_{excess}}$, which would lower the value of the parameter $Q_c \Big/ \left(D_0 \left|\nabla c_{Zn}^{i.l.}\right|\right)$. It has been found that the higher $x_{Ti_{excess}}$ is, the higher parameter $Q_c \Big/ \left(D_0 \left|\nabla c_{Zn}^{i.l.}\right|\right)$ is. Although, stricly speaking, it cannot be guaranteed, it will be supposed that the increase in the parameter $Q_c \Big/ \left(D_0 \left|\nabla c_{Zn}^{i.l.}\right|\right)$ when increasing $x_{Ti_{excess}}$ is due to an increase of Q_c.

Finally, when $x_{Ti_{excess}}$ increases, the diffusion of zinc towards the steel grain boundaries becomes faster and the quantity of zinc diffusing to these locations necessary for the inhibition layer breakdown Q_c will be higher.

Effect of holding temperature on Q_c and t_c

If the slope of the straight lines linking $\ln t_c$ to the reciprocal of holding temperature is different for each steel substrate (Figure 100), it means that the straight lines will cross each other. When comparing two given steel substrates, the relative reactivity with regard to the inhibition rupture will be reversed from a given temperature. For instance, this relative reactivy between steels B and C is reversed at a holding temperature of about 460 °C (Figure 100). Higher holding temperatures (between 470 and 510 °C) would be needed in order to observe this behaviour in the case of all the other couples of steels. For such holding temperatures, times for inhibition rupture t_c would be extremely short and, as already commented, performing an accurate isothermal heat treatment by means of the Gleeble 3500 device is not possible. These are the reasons why clear evidence of the existence of this effect can not be proved at laboratory scale.

Steel C is characterized by a higher $x_{Ti_{excess}}$, a lower E_a and a higher $Q_c \Big/ \left(D_0 \left|\nabla c_{Zn}^{i.l.}\right|\right)$ than steel B. At temperatures lower than 460 °C, steel C is more reactive than steel B, i.e., the inhibition rupture is achieved earlier while, at temperatures higher than 460 °C, steel B becomes more reactive than steel C. As the activation energy obtained for steel C is lower than the one for steel B, the difference between the diffusion coefficient of zinc $D_{Zn}^{i.l.}$ in steel C and the one in steel B is positive and increases with temperature. This would mean that, at low temperatures, the flux of zinc atoms into the grain boudaries is so small in steel B that the outburst formation occurs first in steel C, more able to accumulate the critical amount of zinc in the required volume for the nucleation of Γ. At higher temperature, zinc diffusion is accelerated within the grain boundaries for both steels. For steel C, the faster diffusion (lower E_a) delays the accumulation of the critical amount of zinc in the required volume for nucleation of Γ, and steel B, exhibiting a slower zinc diffusion in its grain boudaries (larger E_a), is the first one able to accumulate this critical amount of zinc.

No evidence exists in the literature or in industrial practice that the inversion of inhibition layer breakdown kinetics described before can exist. The observations in Mardyck HDGA lines always show that the higher the value of $x_{Ti_{excess}}$ is, the more the Fe-Zn alloying reactions are favoured, this phenomenon being associated with an earlier inhibion layer breakdown. In the industrial process, the heat treatment is not isothermal and the inhibition layer breakdown generally occurs during the heating step in the induction furnace (Figure 7), due to the diffusion of zinc in the steel grain boundaries occurring during immersion in the galvanizing bath, wiping (which induces a non-negligible drop in temperature), natural cooling between the wipers and the inductor entry and induction heating. For two given steels, this switch in reactivity (i.e., the inhibition layer breakdown achieved earlier in the steel with the lowest $x_{Ti_{excess}}$) may be observed in industrial conditions only if the inhibition rupture occured for both steels at a temperature much higher than the switch temperature obtained with the isothermal heat treatments (460 °C for steels B and C and higher temperatures for all the other couples of steels studied in the present study, Figure 100). But, even then, this reversed behaviour cannot probably be observed in industrial conditions, taking into account typical line speeds and equipment dimensions.

Most of the quantity of zinc atoms necessary for the inhibition layer breakdown would have already diffused at the moment when this temperature has been reached.

Prediction of the effect of steel chemical composition on the inhibition layer breakdown kinetics

The model correlations between $x_{Ti_{excess}}$ and the parameters E_a and $Q_c/\left(D_0\left|\nabla c_{Zn}^{i.l.}\right|\right)$ presented in Figure 105 can be applied to predict the isothermal kinetics laws accounting for the inhibition layer breakdown in the whole range of parameter $x_{Ti_{excess}}$ for commercial Ti IF steel grades (from 0 to 7, in Mardyck databases):

$$\ln t_c = \ln\left(\frac{Q_c}{D_0\left|\nabla c_{Zn}^{i.l.}\right|}\right) + \frac{E_a}{RT_{hold,\exp}} \tag{III.17}$$

$$E_a = -19920\ x_{Ti_{excess}} + 259150 \tag{III.18}$$

$$\frac{Q_c}{D_0\left|\nabla c_{Zn}^{i.l.}\right|} = 3.5\cdot 10^{-18}\, e^{3.2 x_{Ti_{excess}}} \tag{III.19}$$

The results obtained are presented in Figure 106. The time t_c necessary for the inhibition rupture is predicted by the model as a function of holding temperature and $x_{Ti_{excess}}$.

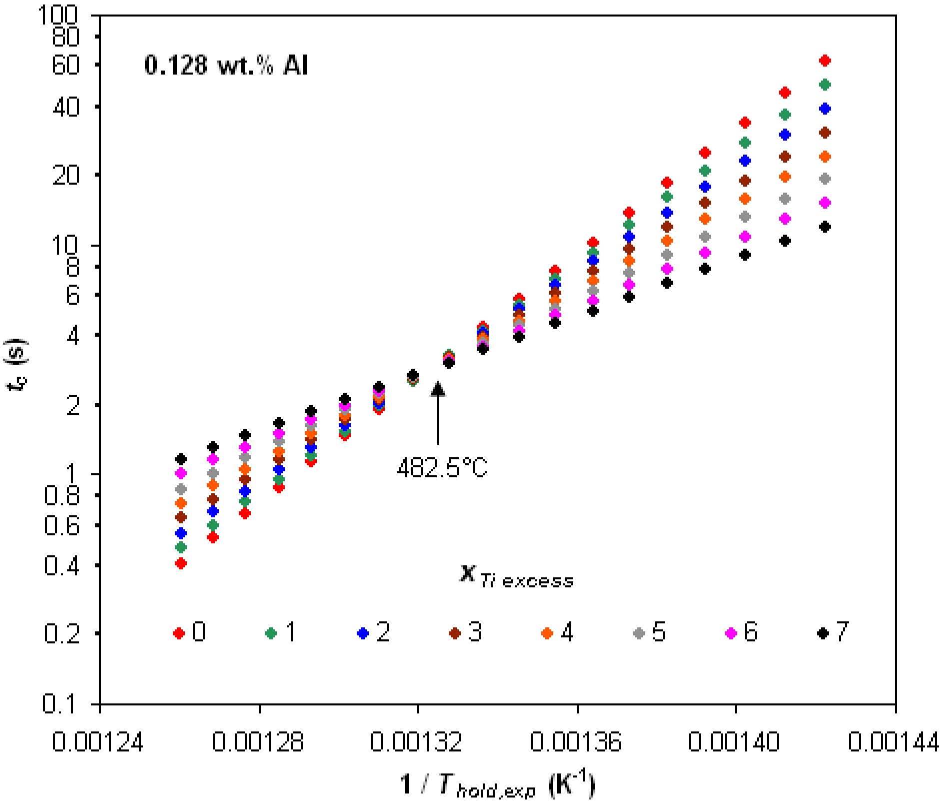

Figure 106: Holding time needed for the inhibition layer breakdown (logarithmic scale) against the reciprocal of holding temperature for a wide range of $x_{Ti_{excess}}$ values according to the model correlations shown in Figure 105 for a bath containing 0.128 wt.% Al.

At temperatures less than 482.5 °C, t_c is found to increase when $x_{Ti_{excess}}$ decreases, as reported in the literature. For this domain of temperature, the results provided by the model are quite in line with the kinetic laws of steels A to D (Figure 100) and the reference steel. These results were totally expected because the parameters of the model were estimated using these experimental results. But, at the same time, it is a reassuring result.

It can also be seen in Figure 106 that all the straight lines cross each other at the same point, corresponding to a temperature of 482.5 °C and a time of 2.9 s. This observation is inconsistent with the experimental results (in Figure 100 the different straight lines would cross each other at different points). As proven in Appendix H, this behaviour is the result of a mathematical artifact coming from the description of the parameters E_a and $Q_c / \left(D_0 \left| \nabla c_{Zn}^{i.l.} \right| \right)$ as linear and exponential functions of parameter $x_{Ti_{excess}}$ respectively.

Results of the model in the case of an industrial galvannealing treatment

In order to confirm that the results of the model are in agreement with industrial practice, calculations have been carried out for different galvannealing cycles. The process conditions performed in Mardyck Galma 1 line of ArcelorMittal were chosen in the case of Ti IF steel grades galvanized in an iron-saturated zinc bath containing 0.125 wt.% Al, i.e. with an aluminium content close to the one for which the model calculations are valid (0.128 wt.% Al). These cycles are depicted in Figure 107. The schematic representation of a typical HDGA tower depicted in Figure 7 may facilitate the understanding of the galvannealing cycles.

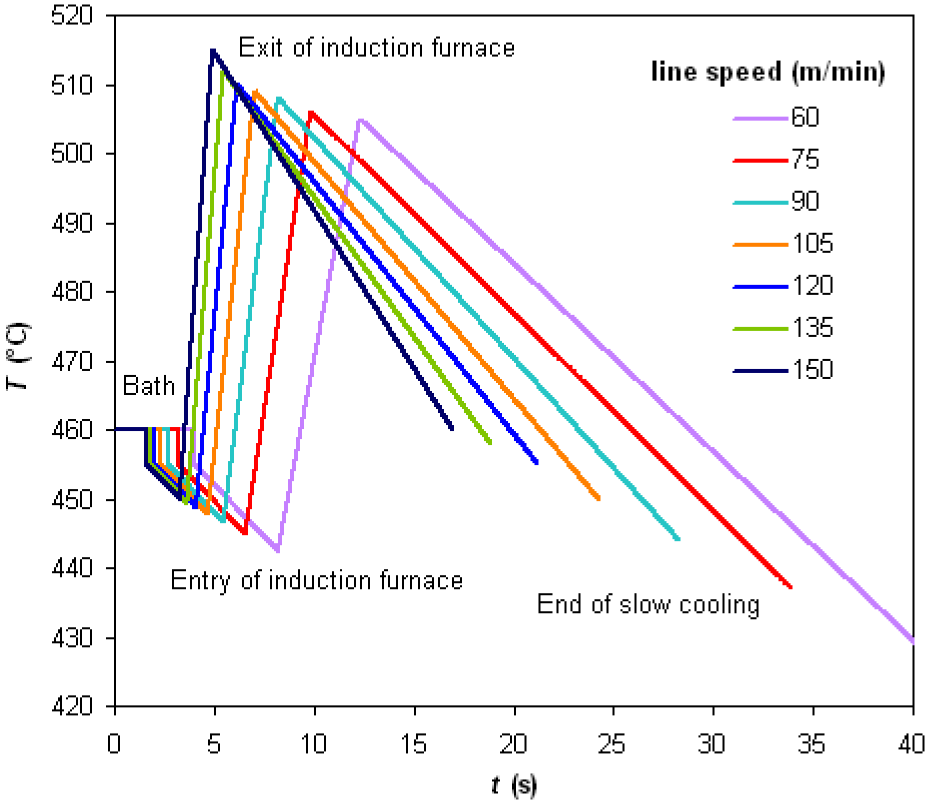

Figure 107: Industrial galvannealing cycles performed in Mardyck Galma 1 line of ArcelorMittal in the case of Ti IF steel grades galvanized in a bath containing 0.125 wt.% Al.

As can be seen in Figure 107, the galvannealing cycles have been represented only up to the end of the slow cooling, as the inhibition layer breakdwown always occurs before this point and generally during induction heating. It can be observed as well that the galvannealing cycles differ in the line speed (varying from 60 to 150 m/min) but also in the temperatures measured by the two pyrometers placed in the line at the end of the induction heating and slow cooling steps. In fact, the setting of these temperatures is associated with the line speed (the higher the line speed is, the higher these temperatures are). From here onwards, these galvannealing cycles will just be differentiated by the line speed. However it should be kept in mind that not negligible variations in temperature exist from one to another. It is also to comment here that the evolution of temperature between the bath exit and the induction furnace entry is unknown in the industrial line and had to be supposed. Concerning the drop in temperature generated by the wiping process, a constant instantaneous drop of 5 ℃ has been assumed for the model calculations. Concerning the natural cooling between the wipers and the induction furnace entry, a constant cooling rate of 3 ℃/s has been supposed.

Regarding the steel chemical composition, the same range of $x_{Ti_{excess}}$ as applied in Figure 106 (from 0 to 7) has been used as it covers the whole Ti IF steel grades production in Galma1 industrial line. The results, depicted and commented here below, show that the model is respectful with industrial observations.

Figure 108 represents the model predictions of the time for inhibition rupture when performing the galvannealing cycles depicted in Figure 107 on Ti IF steel grades with different values of $x_{Ti_{excess}}$.

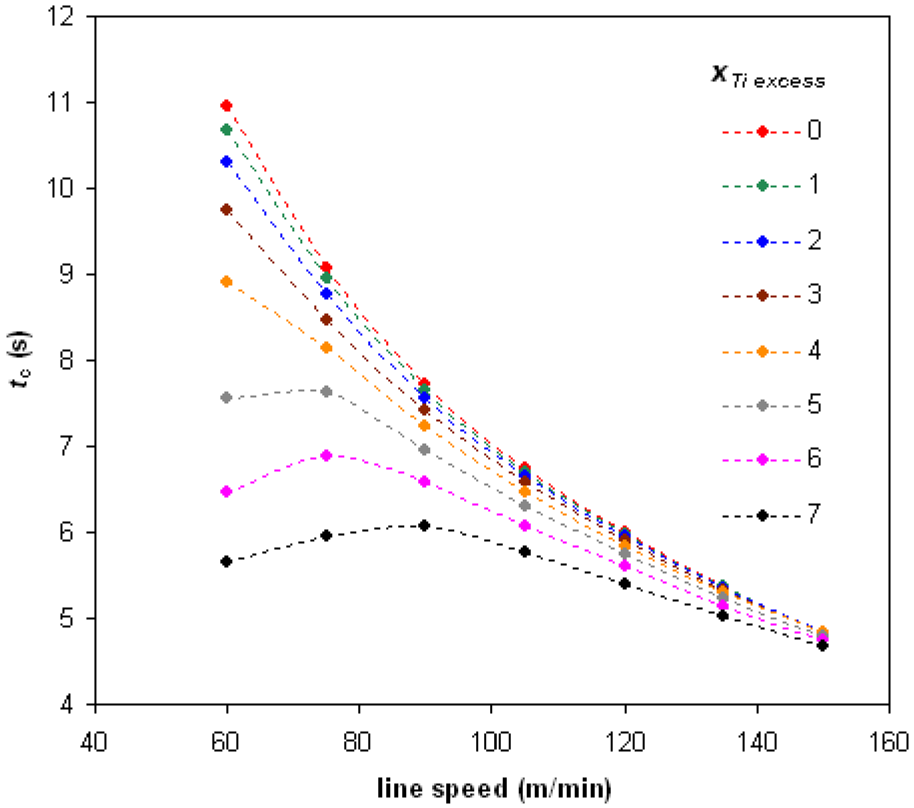

Figure 108: Model predictions of the effect of parameter $x_{Ti_{excess}}$ and the galvannealing cycle (Figure 107) on the time necessary for the inhibition layer breakdown in the case of a bath containing 0.128 wt.% Al.

As can be seen, the time necessary for the inhibition layer breakdown in the case of typical industrial galvannealing cycles is reduced when increasing the parameter $x_{Ti_{excess}}$. The model predictions also indicate that increasing the line speed reduces the difference in reactivity. These results are related to the switch in reactivity behaviour depicted in Figure 106. When the line speed is increased, the residence times are reduced and the heating rate in the induction furnace is increased. This makes the inhibition layer breakdown to be achieved at higher temperatures and, consequently, the reactivity behaviour at temperatures higher than 482.5 ℃, which counterbalances the one at low temperatures, will take more importance.

This behaviour can also be appreciated in Figure 109, where the temperature and time for inhibition rupture obtained for each of the steels ($x_{Ti_{excess}}$ ranging from 0 to 7) is represented on the seven galvannealing cycles. No legend for the parameter $x_{Ti_{excess}}$ is shown in this case because it has just been mentioned that for each of the present galvanneling cycles, the higher $x_{Ti_{excess}}$ is, the faster the inhibition rupture is achieved (Figure 108). As can be seen in Figure 109, the most important difference in relative reactivity corresponds to a line speed of 60 m/min, for which the quantity of zinc necessary for inhibition rupture fully diffuses, with the exception of the steel with $x_{Ti_{excess}}$ equal to 0, in the domain of low temperature (less than 482.5 ℃). This difference in reactivity is reduced when increasing the line speed because the diffusion of zinc in the domain of high temperatures becomes more and more important. For a line speed of 150 m/min, the zinc diffusion behaviour in the domain of high temperatures would have counteracted the one in the domain of low temperatures and, according to the model, all the steels would meet the inhibition layer breakdown at almost the same point of the galvannealing cycle. As a result, the effect of the parameter $x_{Ti_{excess}}$ on the inhibition layer breakdown kinetics would be expected to be reversed in such industrial galvannealing cycles at line speeds higher than 150 m/min. In the case of very low line speeds (60 and 75 m/min) those Ti IF steel grades with high value of parameter $x_{Ti_{excess}}$ may meet the inhibition rupture before entering the induction furnace.

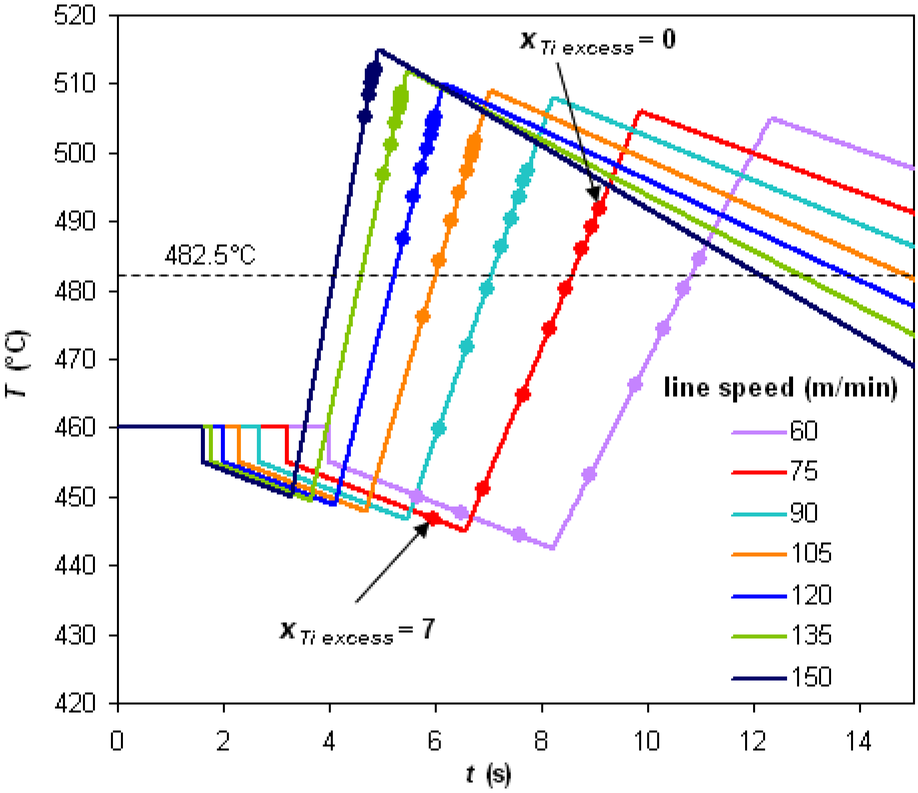

Figure 109: Model predictions of the effect of the parameter $x_{Ti_{excess}}$ and the galvannealing cycle (Figure 107) on the time necessary for the inhibition layer breakdown in the case of a bath containing 0.128 wt.% Al.

Finally, it should be highlighted that around 80 % of the Galma 1 line production is obtained at line speeds comprised between 120 and 135 m/min, and that this last line speed is the highest one performed in the current production of this industrial line (the speed line of 150 m/min is extremely rare and has just been performed in the framework of industrial trials). It can therefore be advanced that the results provided by the model are in line with the observation in industrial conditions that the higher the value of parameter $x_{Ti_{excess}}$ is, the more reactive the Ti IF steel grade is with respect to the inhibition layer breakdown. In addition, it is important to recall that in industrial lines the inhibition layer breakdown generally occurs during heating in the induction furnace. As it can be seen in Figure 109, this behaviour is also predicted by the model in most cases.

III.3.2.4. Effect of the bath aluminium content

As advanced in section III.2.3.3, the effect of the bath aluminium content on the inhibition layer breakdown kinetics has been evaluated through the comparison between the experimental results obtained for steels A and D galvanized in the first Rhesca trials campaign (0.128 wt.% Al) and those obtained for the same steels galvanized in the second Rhesca trials campaign (0.112 wt.% Al).

Figure 110 shows in a unique graph the results of inhibition layer breakdown kinetics for steels A and D galvanized in both Rhesca trials campaigns already presented in Figure 100 and Figure 101.

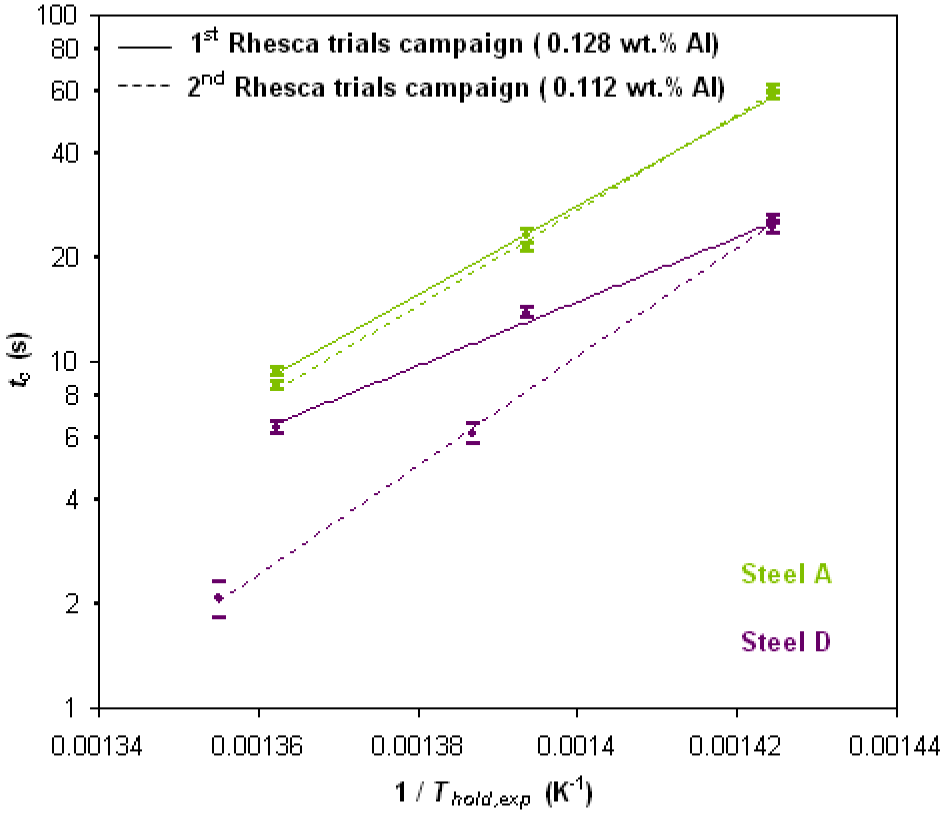

Figure 110: Real holding time needed for the inhibition layer breakdown (logarithmic scale) against the reciprocal of experimental holding temperature performed in the Gleeble 3500 pilot simulator (steels A and D galvanized in the first and second Rhesca trials campaigns).

As can be observed in Figure 110, while the reactivity of steel A with respect to the inhibition rupture remains almost the same when decresing the bath aluminium content from 0.128 to 0.112 wt.% (it is just very slightly faster when galvanizing at 0.112 wt.% Al), a great difference in the inhibition layer breakdown kinetics can be appreciated in the case of steel D. Indeed, in the range of temperature tested, steel D becomes globally much more reactive when decreasing the bath aluminium content from 0.128 to 0.112 wt.%. Only for the lowest experimental holding temperature tested (429℃), the reactivity of this steel remains unchanged when the bath aluminium content is lowered.

III.3.2.4.1. Effect of the bath aluminium content on E_a and Q_c / (D_0.|$\nabla c_{Zn}^{i.l.}$|)

Although it is not possible to report a clear effect of the bath aluminium content on the model parameters E_a and $Q_c \big/ \left(D_0 \left|\nabla c_{Zn}^{i.l.}\right|\right)$ as only two Rhesca campaigns with different bath aluminium contents could have been performed, it appears that decreasing the bath aluminium content would make E_a increase and $Q_c/\left(D_0\left|\nabla c_{Zn}^{i.l.}\right|\right)$ decrease. As commented above and can be observed in Figure 111 and Table 34, these differences are much less noticeable in the case of steel A as the kinetic laws obtained for both bath aluminium contents are very close to each other. In the case of steel D, the gap in parameters E_a and $Q_c/\left(D_0\left|\nabla c_{Zn}^{i.l.}\right|\right)$ between these two bath aluminium contents is very important.

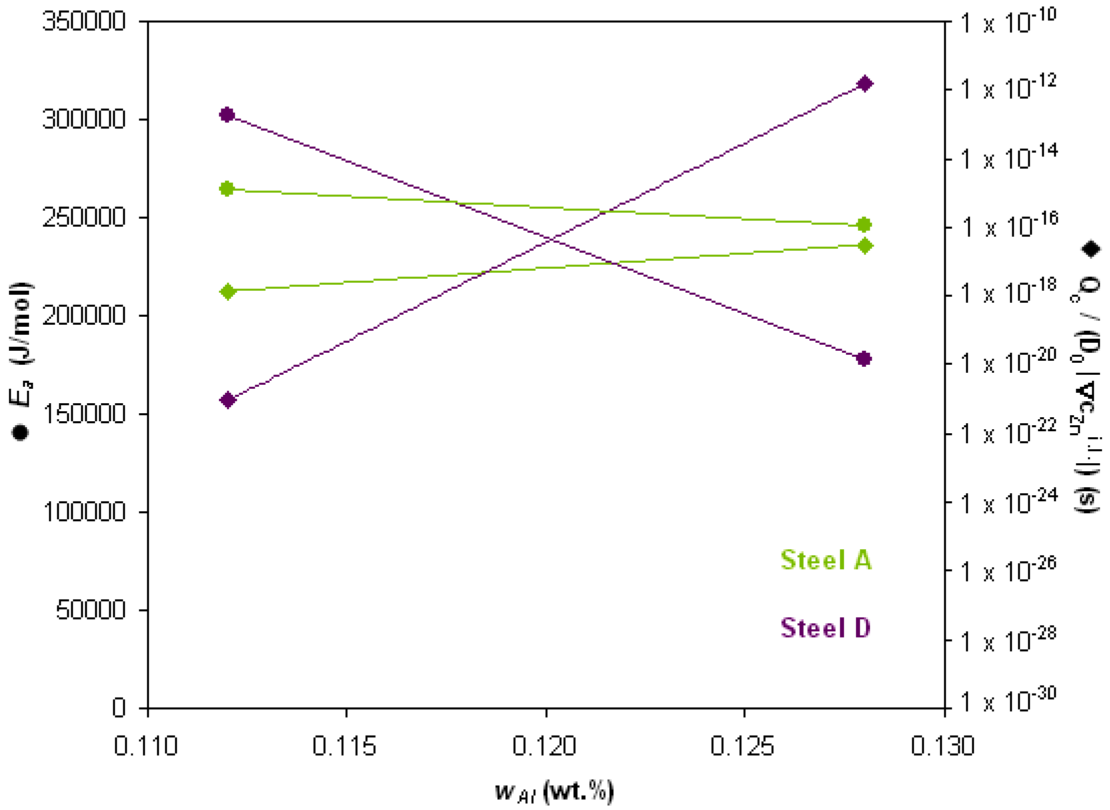

Figure 111: E_a (circles) and $Q_c/\left(D_0\left|\nabla c_{Zn}^{i.l.}\right|\right)$ (squares) against bath aluminium content for steels A and D.

Table 34: Values of E_a and $Q_c/\left(D_0\left|\nabla c_{Zn}^{i.l.}\right|\right)$ for steels A and D galvanized in the first and second Rhesca trials campaigns.

Steel	w_{Al} (wt.%)	E_a (J/mol)	$Q_c/(D_0\lvert\nabla c_{Zn}^{i.l.}\rvert)$ (s)
A	0.128	245500	3.2×10^{-17}
A	0.112	263900	1.4×10^{-18}
D	0.128	177600	1.5×10^{-12}
D	0.112	301700	9.1×10^{-22}

III.3.2.4.2. General discussion

Any difference observed in the inhibition layer breakdown kinetics when galvanizing the same steel substrate in baths with different aluminium content should be, in principle, related to a difference in the nature (structure, phase composition and thickness) of the inhibition layer only.

As shown in chapter II and verified for the samples galvanized in the Rhesca pilot simulator (section III.2.1), the main difference between the inhibition layers formed in iron-saturated zinc baths containing 0.128 and 0.112 wt.% Al is the surface coverage by the $Fe_2Al_5Zn_x$ phase layer. While this layer appeared to be fairly continuous for galvanizing in the bath containing 0.128 wt.% Al, it was clearly discontinuous for the same trial in the bath containing 0.112 wt.% Al.

In the case of steel A, no difference in the inhibition layer breakdown kinetics between the two Rhesca trials campaigns could have been observed in spite of the just reported difference in the inhibition layer structure (for both raw experimental data in Figure 93 and calculations of t_c in Figure 110). As depicted in Figure 112, the grain boundaries of this steel (the one with the lowest value of $x_{Ti_{excess}}$ among the steels studied) are polluted with alloying elements (red points), which hinder the diffusion of zinc in these locations. The zinc diffusion in the grain boundaries is the rate-determining step of the inhibition rupture, i.e., the lowest diffusion rate compared to the diffusion in the inhibition layer in both cases. The time t_c necessary for the inhibition rupture is therefore the same, whether the inhibition layer was continuous or not.

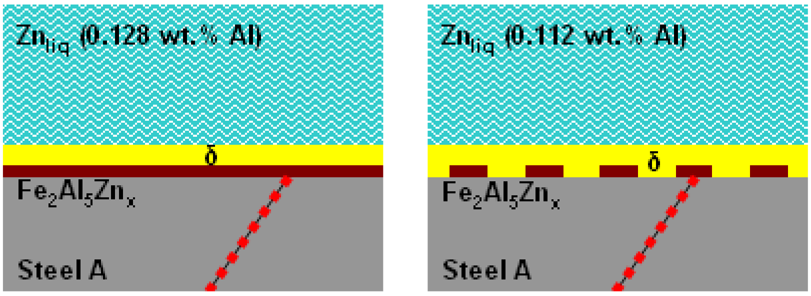

Figure 112: Microstructure through which zinc diffuses towards the steel grain boundaries for the inhibition layer breakdown in the case of steel A (low $x_{Ti_{excess}}$, polluted grain boundaries) and bath aluminium contents of 0.128 (fairly continuous $Fe_2Al_5Zn_x$ layer, left) and 0.112 wt.% (discontinuous $Fe_2Al_5Zn_x$ layer, right).

In the case of steel D (the one with the largest value of $x_{Ti_{excess}}$ among the steels studied), the grain boundaries are very clean (Figure 113) so that the diffusion of zinc in these locations is faster than in steel A. The zinc diffusion rate in the grain boundaries is now of the same order of magnitude as the zinc diffusion rate in the inhibition layer in both cases. The time t_c necessary for the inhibition rupture therefore depends on the structure of the inhibition layer. The main difference between the investigated inhibition layers is the discontinuity of the $Fe_2Al_5Zn_x$ layer in the case of the bath containing 0.112 wt.% Al. As explained earlier (section I.3.2.2.1.1), the diffusion of zinc is expected to be faster in the δ phase, as mainly composed of zinc, than in the $Fe_2Al_5Zn_x$ phase. This leads to times $t_{hold,\exp}$ (Figure 93) and t_c (Figure 110) lower in the case of the discontinuous $Fe_2Al_5Zn_x$ layer than in the case of a continuous $Fe_2Al_5Zn_x$ layer.

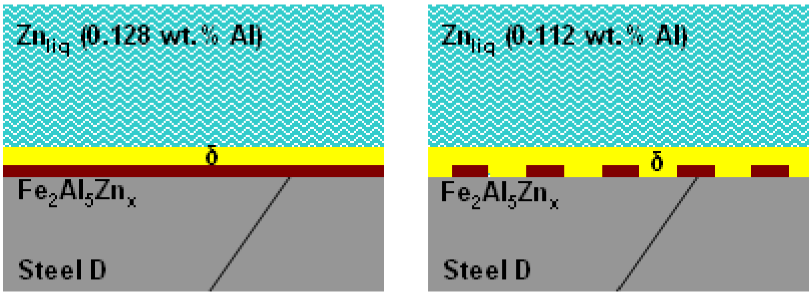

Figure 113: Microstructure through which zinc diffuses towards the steel grain boundaries for the inhibition layer breakdown in the case of steel D (high $x_{Ti_{excess}}$, clean grain boundaries) and bath aluminium contents of 0.128 (fairly continuous $Fe_2Al_5Zn_x$ layer, left) and 0.112 wt.% (discontinuous $Fe_2Al_5Zn_x$ layer, right).

Let's now consider the values of E_a and $Q_c \Big/ \left(D_0 \left|\nabla c_{Zn}^{i.l.}\right|\right)$ in Table 34. The comparison between steels A and D galvanized in a bath containing 0.128 wt.% Al has already been discussed in section III.3.2.3.3. The other results obtained are difficult to explain:

- When the bath aluminium content is decreased from 0.128 to 0.112 wt.% Al, E_a is increased, meaning that the global diffusion coefficient $D_{Zn}^{i.l.}$ is decreased (equation (III.6)), especially in the case of steel D. As the $Fe_2Al_5Zn_x$ layer is discontinuous, the opposite behaviour was expected.

- For the bath aluminium content equal to 0.112 wt.% Al, E_a is higher for steel D than for steel A, meaning that the global diffusion coefficient $D_{Zn}^{i.l.}$ is decreased (equation (III.6)), when the grain boundaries are cleaner (case of steel D). The opposite behaviour was also expected.

Three explanations of these unexpected results could be proposed:

- At first, the kinetic law corresponding to steel D galvanized in the bath containing 0.112 wt.%Al should be taken with some reservations. As advanced in section III.1.2.2, in this case, the experimental holding times needed for the inhibition rupture at the holding temperatures of 445 and 465 °C were very short, leading to some uncertainties in the determination of the kinetic law.

- Secondly, the global model proposed for industrial purpouses (equation (III.6)) is perhaps too simplified to account for the complex mechanisms involved in the inhibition layer breakdown. This one-dimensional model needs to describe two-dimensional mechanisms, such as the discontinuous $Fe_2Al_5Zn_x$ layer or the accumulation of zinc atoms in the steel grain boundaries. As shown in Figure 91, the gradient of zinc concentration used in equation (III.6) is probably not constant as the local zinc activity along the steel / inhibition layer interface likely increases (disappearance of the $Fe_2Al_5Zn_x$ layer) and the thickness of the inhibition layer evolves during the diffusional process. In addition, the fact that the phase composition of the inhibition layer evolves before outburst formation would imply that the global diffusion coefficient $D_{Zn}^{i.l.}$ is probably not constant during zinc diffusion either. The steady state condition is therefore questionable.

- Thirdly, the approach based on equation (III.6) consists in determining a single value of E_a for the complex mechanisms involved in the inhibition layer breakdown. Even if it seems to work well, especially in the study of the effect of the steel chemical composition on the kinetics of this reaction (section III.3.2.2), this approach is questionable in that the experimental range of temperatures investigated is narrow (from 425 to 460 °C) due to the zinc melting temperature equal to 420 °C and the high rate of the inhibition layer breakdown at temperatures higher than 460 °C.

Finally, the results obtained show that the inhibition layer breakdown kinetics would be always faster in a galvanizing bath at low aluminium content (0.112 wt.%) than at high aluminium content (0.128 wt.%). This behaviour is in line with the industrial experience, showing that decreasing the bath aluminium content enhances the kinetics for Fe-Zn alloying reactions.

III.4. Conclusions

The following conclusions can be drawn from this chapter:

The inhibition layer breakdown by outburst formation occurs through the diffusion of zinc in the steel grain boundaries and the nucleation of a Fe-Zn phase at these locations. A sequence of reaction mechanisms accounting for this inhibition rupture has been proposed (section III.2.2) and explained by means of the concept of diffusion paths in the Al-Fe-Zn ternary phase diagram at the galvannealing temperature (section III.3.1). The diffusion of zinc towards the steel enriches the inhibition layer / steel interface in this element. As a result of this enrichment, the disappearance of the $Fe_2Al_5Zn_x$ layer if present is expected to occur first, replaced by δ. Further enrichment of the steel grain boundaries in zinc leads to the nucleation of the Γ phase at these locations which breaks the inhibition layer off locally.

A simplified model has been developed in order to describe the inhibition layer breakdown kinetics (section III.3.2.1). The modelling work has been done in a global manner, without differentiating the various zinc diffusion steps involved (through the δ layer, through the $Fe_2Al_5Zn_x$ layer, at the interface with the steel and in the steel grain boundaries). Some strong assumptions were needed in order to facilitate as much as possible the experimental determination of the parameters of the model. Although some of these assumptions and the modelling work itself may be open to criticism, the model fits quite well to the experimental results and allows the understanding of some interesting effects.

The effect of the steel chemical composition on the inhibition layer breakdown kinetics has been investigated. Based on the results obtained, among all the chemical reactivity parameters initially proposed, the parameter $x_{Ti_{excess}}$ (equation (III.3)) has been found to describe the best the cleanliness of the steel grain boundaries and, consequently, the reactivity of the steel with respect to the inhibition layer breakdown (section III.3.2.3.1). This parameter represents the molar ratio between the solute titanium available after the supposed precipitation of the total amounts of carbon, nitrogen and sulphur and the phosphorous content in the steel and gives an idea of the ability of titanium to trap phosphorous as FeTiP. The experimental results obtained at temperatures from 425 to 460 ℃ have shown that the higher the parameter $x_{Ti_{excess}}$ is, the faster the inhibition layer breakdown occurs (section III.2.3.2).

Using the simplified model described earlier, it was found that two opposite phenomena are expected to influence the inhibition layer breakdown kinetics: the rate of zinc diffusion in the steel grain boundaries and the ability to accumulate zinc atoms there (section III.3.2.3.3). Two different behaviours are predicted by the model depending on the temperature (Figure 106). At low temperatures, the steel with the highest value of $x_{Ti_{excess}}$, corresponding to clean grain boundaries, will be the most reactive steel with respect to the inhibition rupture, because it is characterized by the highest diffusion coefficient in the steel grain boundaries, leading to the accumulation of zinc atoms there the fastest. On the contrary, at high temperatures, the same steel with clean grain boundaries will meet the inhibition rupture the latest. Indeed, in this steel, the critical amount of zinc atoms necessary for the nucleation of the Γ phase is now accumulated the slowest in a required volume due to a too high zinc diffusion coefficient in the steel grain boundaries. In comparison, in the steel with polluted grain boundaries, the critical amount of zinc atoms necessary for the nucleation of the Γ phase is accumulated faster in a required volume, due to the presence of impurities in the grain boundaries and a larger zinc diffusion coefficient compared to low temperature. In typical industrial galvannealing cycles, the inhibition layer breakdown generally occurs in the domain of low temperatures and, consequently, the steel with the highest value of $x_{Ti_{excess}}$ will be the most reactive one.

The effect of the bath aluminium content on the inhibition layer breakdown kinetics has also been studied (section III.3.2.4). For the two aluminium contents investigated, the only difference was the structure of the inhibition layer composed of $Fe_2Al_5Zn_x$ and δ in both cases: the $Fe_2Al_5Zn_x$ layer is discontinuous for the bath with 0.112 wt.% Al and continuous for the bath with 0.128 wt.% Al (section III.2.1). It has been found that, in the typical range of temperatures of industrial galvannealing heat treatments, a decrease in the bath aluminium content increases the inhibition layer breakdown kinetics. The magnitude of such increase in kinetics depends on the steel chemical composition (Figure 93 and Figure 110). In the case of a steel with a low value of $x_{Ti_{excess}}$, i.e., with polluted grain boundaries, the zinc diffusion in the grain boundaries is the rate-determining step of the inhibition rupture, i.e., the lowest diffusion rate compared to the diffusion in the inhibition layer. The time t_c necessary for the inhibition rupture is therefore almost the same, whether the inhibition layer was continuous or not. In a steel with a high value of $x_{Ti_{excess}}$, i.e., with clean grain boudaries, the zinc diffusion rate in the grain boundaries is of the same order of magnitude as the zinc diffusion rate in the inhibition layer, whether continuous or discontinuous. The time t_c necessary for the inhibition rupture therefore strongly depends on the structure of the inhibition layer.

CHAPTER IV: GENERAL CONCLUSIONS AND PERSPECTIVES

The production of galvannealed coatings requires an accurate control of the process conditions performed in industrial lines. Indeed, the final microstructure of this kind of coatings is composed of a sequence of different stratified Fe-Zn phases and its in-use properties highly depend on the distribution of these phases within the coating. The development of a galvannealed coating passes through complex reaction mechanisms involving different reactions in series: the inhibition layer formation, the inhibition layer breakdown, the consumption of the liquid zinc through the formation of Fe-Zn phases and the further enrichment of the solid coating in iron. Contrarily to typical galvanized coatings production, the steel strip is heated, after immersion in the zinc bath and wiping, into an induction furnace in order to transform, through the previous reactions, the liquid zinc coating into a solid Fe-Zn coating. In order to improve the quality of galvannealed coatings while minimizing production costs, the mechanisms and kinetics of these reactions should be well known as they play a key role on the microstructure of the final coating.

The present work focused in the study of the two first reactions: the inhibition layer formation and its breakdown. These reactions have been investigated in the case of Ti IF steel grades.

The inhibition layer formation

The nature of the inhibition layer will obviously depend on the galvanizing conditions. In industrial galvanizing lines, the bath is usually iron-saturated at a temperature of around 460 °C and its aluminium content is expected to play a key role on the nature of the inhibition layer. The zinc-rich corner of the Al-Fe-Zn ternary phase diagram proposed by Tang [12] at different temperatures, generally accepted by the galvanizers, can be used to determine the composition of the inhibition layer if it were in thermodynamic equilibrium with the galvanizing bath (section I.3.1.1.1): this phase diagram suggests that the galvanizing temperature has almost no effect on the nature of this layer and that the galvanizing bath aluminium content is the parameter determining the nature of the intermetallic compound(s) constituting the inhibition layer. Considering an iron-saturated zinc bath at 460 °C, the inhibition layer should be fully composed either of the $Fe_2Al_5Zn_x$ phase, in the case of typical GI production (bath aluminium contents at around 0.2 wt.%), or of the δ ($FeZn_7$) phase, in the case of typical GA production (bath aluminium contents ranging between 0.1 and 0.135 wt.%). For bath aluminium contents lower than 0.1 wt.%, the stable compound would be the ζ ($FeZn_{13}$) phase. Nevertheless, so low bath aluminium contents are rarely performed in industrial galvanizing lines, due to an uncontrolled growth of Fe-Zn phases in these conditions.

In agreement with the phase diagram proposed by Tang [12], most of the researchers in the literature have reported that the inhibition layer formed in typical GI baths is composed of the $Fe_2Al_5Zn_x$ phase only. However, in the case of typical GA baths, the nature of the inhibition layer is still a subject of controversy today. It remains not clear whether the inhibition layer in such baths is composed of metastable $Fe_2Al_5Zn_x$, stable δ or both (section I.3.1.1.3 and I.3.1.1.4). In addition, some authors have also observed the presence of metastable epitaxial ζ crystals together with the inhibition layer, especially in the case of GA baths with low aluminium contents (section I.3.1.3.3.3).

The nature of the inhibition layer formed in GA baths has been investigated in detail in the present work. The results obtained for the two steel samples studied (steel A, galvanized in a zinc bath containing 0.112 wt.% Al, and steel B, galvanized in a zinc bath containing 0.128 wt.% Al) clearly show that this layer is composed of a very thin layer of $Fe_2Al_5Zn_x$ (around 20-30 nm) and a much thicker layer of δ on top of it (around 200 nm) (section II.2). A substantial difference in the continuity of the $Fe_2Al_5Zn_x$ layer has been observed between both samples: while this layer has been found to be fairly continuous in the case of steel B, it was clearly discontinuous in the case of steel A. Nevertheless, both observed final microstructures allow thermodynamic equilibrium to be reached along all the interfaces and can be described by a diffusion path in the Al-Fe-Zn ternary phase diagram at 460 °C (section II.3.2).

A logical reaction mechanism accounting for the formation of the inhibition layer observed in the framework of this study can be proposed on the basis of the general mechanism found in the literature. It can be summarized in the following steps: wetting of the steel surface by the liquid zinc, iron dissolution into the liquid phase, the iron supersaturation at the steel / liquid zinc interface, nucleation of metastable $Fe_2Al_5Zn_x$, favoured by preferential epitaxial relationships with the ferrite, and nucleation and growth of the δ phase, which allows all the interfaces of the final microstructure of the inhibition layer to reach thermodynamic equilibrium (section II.3.1.1). The nucleation of metastable $Fe_2Al_5Zn_x$, instead of stable δ can be justified by the nucleation of this intermetallic compound in epitaxy with ferrite. Different researchers have reported preferential epitaxial relationships between $Fe_2Al_5Zn_x$ and ferrite. In this study, an epitaxial relationship between $Fe_2Al_5Zn_x$ and ferrite, which was never reported before, has also been found (section II.2.3.1).

In addition, metastable epitaxial ζ rod crystals have also been observed within the inhibition layer, in much lesser quantity compared to the presence of the $Fe_2Al_5Zn_x$ and δ phases (section II.3.1.1). These ζ crystals would nucleate during immersion in the galvanizing bath on grains with the adequate crystallographic orientation of either the steel substrate or the thin epitaxial $Fe_2Al_5Zn_x$ layer. Different epitaxial relationships between ζ and ferrite are available in the literature. This topic could not be investigated in this study. Electron diffraction in TEM at the ferrite / ζ rod crystals interface would have been very interesting and is kept in perspective as a possible future work.

The inhibition layer breakdown

The inhibition layer breakdown represents a key step in the galvannealing process of Ti IF steel grades as, contrarily to the other following reactions involved in the development of a galvannealed coating, its kinetics varies strongly with the steel chemical composition and grain size (section I.3.2.2.2). In addition, the kinetics accounting for this reaction depends also on the nature of the inhibition layer, which, as stated earlier, mainly depends on the bath aluminium content. It is therefore very suitable to understand the mechanisms accounting for this reaction and to evaluate the effect of the previous parameters on the inhibition layer breakdown kinetics.

As far as the mechanisms accounting for the inhibition layer breakdown are concerned, the literature review carried out in the framework of the present work leads to the conclusion that the inhibition layer breakdown occurs in most cases through an outburst formation reaction at the steel grain boundaries due to the diffusion of zinc through the layer itself and the subsequent nucleation of a Fe-Zn phase (section I.3.2.1.2). This phase would be the Γ phase according the Al-Fe-Zn phase diagram (section I.3.2.1.2.3).

In galvanizing line practice, as the steel strip enters the induction furnace, the rise in temperature activates the interdiffusion of iron and zinc through the inhibition layer. The diffusion of iron towards liquid zinc will make the inhibition layer grow. This growth may be limited by the aluminium supply from the liquid phase after wiping. Zinc diffuses simultaneously towards the steel grain boundaries and is responsible for the inhibition rupture through the mechanism evoked here above.

In the present work, an additional stage was highlighted in the mechanism accounting for the inhibition rupture (section III.2.2). It begins with the disappearance of the $Fe_2Al_5Zn_x$ layer at the inhibition layer / steel interface as a result of the enrichment of this interface in zinc. The outburst formation then occurs with the local nucleation of the Γ phase at the steel grain boundaries, breaking the inhibition layer (composed at this precise instant of the δ phase only) off, when the zinc concentration at these locations has become high enough. This reaction mechanism, controlled by the diffusion of zinc towards the steel grain boundaries, can be described by means of the concept of diffusion paths in the Al-Fe-Zn ternary phase diagram at the galvannealing temperature (section III.3.1).

It should be pointed out here that no experimental evidence could be provided in this work proving that the nature of the first Fe-Zn phase nucleating during the outburst formation is the Γ phase. This is only an assumption based on thermodynamic considerations: the stable intermetallic compound nucleating at the δ phase / steel interface as a result of the enrichment of this interface in zinc should be the Γ phase. This assumption, stated earlier by different authors in the literature (section I.3.2.1.2.3), has never been confirmed experimentally. Hence, it would be very interesting to obtain irrefutable proof of this assumption. In this sense, electron diffraction in TEM on a FIB thin foil containing the root of an outburst is kept in mind as a future work. The microstructure to be kept in the FIB foil should be the one corresponding to a just nucleated Γ phase at the emergence of a steel grain boundary before the inhibition layer breakdown. It is not evident at all whether this microstructure can be easily obtained or not as the time between the nucleation of this phase and the local rupture of the inhibition layer is expected to be extremely short.

Concerning the kinetics of the inhibition layer breakdown, it is obviously enhanced by higher temperatures (section I.3.2.2.1.2). In addition, the literature review advanced that it is also influenced by other parameters. Different authors reported that this kinetics is favoured by lower bath aluminium contents (section I.3.2.2.1.1). The effect of the Ti IF steel substrate has also been stated by different researchers. On the one hand, some studies indicate that the smaller the steel surface grain size is, the more the kinetics accounting for this reaction is favoured (section I.3.2.2.2.1). On the other hand, a strong effect of the steel substrate chemical composition on the inhibition layer breakdown kinetics has also been evoked: while elements such as carbon, nitrogen, sulphur and phosphorous in the steel pollute the steel grain boundaries, delaying the inhibition layer breakdown, others as titanium and niobium, promote the cleanliness of the steel grain boundaries, accelerating the inhibition layer breakdown (section I.3.2.2.2.2).

Nevertheless, although different studies available in the literature show the effects reported above in a qualitative way, very few kinetic data quantifying them have been published. In addition, these data are often inconsistent with each other (section I.3.2.2.3). The kinetics accounting for the inhibition layer breakdown has then been investigated in detail in this study with the aim of evaluating the effect of the steel chemical composition and the bath aluminium content, not only in a qualitative but also in a quantitative way. These two parameters were chosen first and foremost as their variability in industrial galvannealing lines is important. The effect of the steel grain size has not been investigated because, for the process conditions typically performed during the continuous annealing prior to galvanizing, very little variability exists in the grain sizes of Ti IF steel grades.

In addition, a diffusion-based model aiming to predict the inhibition layer breakdown kinetics has been developed (section III.3.2.1). Although different diffusion steps are involved in this reaction (diffusion of zinc through the δ layer, through the $Fe_2Al_5Zn_x$ layer, along the interface with the steel and at the steel grain boundaries), this model remains quite simple and describe the inhibition layer breakdown reaction with a single global zinc diffusion coefficient taking into account the different steps of zinc diffusion. The decision to proceed in this way lies in the compromise between the accuracy of the model for industrial applications and the experimental workload needed to determine the parameters of the model. In spite of the simplifications done, the model represents the experimental results successfully and facilitates the understanding of the effects of the Ti IF steel grade chemical composition on the inhibition layer breakdown kinetics.

At first, the kinetic results obtained in the framework of this study lead to the conclusion that the effect of the Ti IF steel chemical composition on the inhibition layer breakdown kinetics would be ruled by the competition between two opposite phenomena (section III.3.2.3.3): the rate of zinc diffusion in the steel grain boundaries and the ability of the steel to accumulate the zinc atoms at these locations. As commented above, the steel chemical composition is representative of the cleanliness of its grain boundaries. The cleaner the steel grain boundaries are, the faster the rate of zinc diffusion in the steel grain boundaries at a given temperature is but the more difficult the accumulation of zinc at these locations becomes as no alloying elements prevents the diffusion of zinc atoms deeper in the grain boundaries. The results obtained show that an effect of temperature on the competition between these two phenomena can also be assumed. At low temperatures, the inhibition layer breakdown kinetics mainly depends on the rate of zinc diffusion in the steel grain boundaries. In this case, a steel with clean grain boundaries will be more reactive than other with polluted grain boundaries. However, at high temperatures, the kinetics accounting for this reaction mainly depends on the ability of the steel to accumulate zinc at the steel grain boundaries. In this case, the steel with the polluted grain boundaries will be more reactive. However, in spite of this different behaviour depending on the temperature regime, the predictions of the kinetic model when used for typical industrial galvannealing cycles are in line with the industrial observations that the steel with the cleanest grain boundaries is the most reactive one. Indeed, most of the zinc quantity needed to be accumulated in the steel grain boundaries for the inhibition layer breakdown has diffused at these locations in the domain of low temperatures.

Regarding the effect of the bath aluminium content on the inhibition layer breakdown kinetics (section III.3.2.4), it should be noted that it is associated with the nature of the inhibition layer and, more precisely in the case of GA baths, to the surface coverage by the thin $Fe_2Al_5Zn_x$ layer: for the two bath aluminium contents investigated, the only difference was the structure of the inhibition layer composed of $Fe_2Al_5Zn_x$ and δ in both cases: the $Fe_2Al_5Zn_x$ layer is discontinuous for the bath with

0.112 wt.% Al and continuous for the bath with 0.128 wt.% Al (section III.2.1). According to the results obtained, a decrease in the bath aluminium content increases the inhibition layer breakdown kinetics. The magnitude of such increase in kinetics strongly depends on the Ti IF steel grade chemical composition, i.e., on the cleanliness of its grain boundaries. Thus, in the case of a steel with polluted grain boundaries, the zinc diffusion in the grain boundaries is the rate-determining step of the inhibition rupture, i.e., lower diffusion rate compared to the diffusion in the inhibition layer. The time t_c necessary for the inhibition rupture is therefore almost the same, whether the $Fe_2Al_5Zn_x$ layer was continuous or not. In contrast, in the case of a steel with clean grain boundaries, the zinc diffusion rate in the grain boundaries is of the same order of magnitude as the zinc diffusion rate in the inhibition layer whether continuous or discontinuous. The time t_c necessary for the inhibition rupture therefore strongly depends on the structure of the inhibition layer.

Finally, it should be pointed out that only two different bath aluminium contents could have been tested in the framework of the present study. Although the results obtained in this study show how this parameter influences the inhibition layer breakdown kinetics, additional trials with other aluminium contents should be performed in order to obtain a precise quantification of this effect. In this sense, the determination of the minimum bath aluminium content needed to ensure the continuity of the $Fe_2Al_5Zn_x$ layer would be a key result. For bath aluminium contents in the GA domain higher than this value, no significant decrease of the inhibition layer breakdown kinetics is expected to be observed even for those Ti IF steels with very clean grain boundaries.

REFERENCES

1 D. Quantin, “Les aciers revêtus”, Chapter 49 in “Le livre de l’acier”, (Edited by G. Béranger, G. Henry and G. Sanz), Technique et Documentation - Lavoisier, pp. 1059 - 1091, 1994.

2 M. François, D. Deparis, “Les revêtements”, Chapter 61 in “Le livre de l’acier”, (Edited by G. Béranger, G. Henry and G. Sanz), Technique et Documentation - Lavoisier, pp. 1357 - 1388, 1994.

3 D. Quantin, “Les traitements de surface par immersion en bain métallique fondu – la galvanisation à chaud”, Techniques de l’Ingénieur, Traité de Métallurgie, M 1534, pp. 1 - 28.

4 E. Buscarlet, “Galvanisation et aluminiage en continu”, Techniques de l’Ingénieur, Traité de Matériaux Métalliques, M 1536, pp. 1 - 15, Doc. M 1536, pp. 1 – 2.

5 ArcelorMittal’s Fact Book 2012 (http://annualreview2012.arcelormittal.com/fact-book).

6 M. Urednicek, J. S. Kirkaldy, “Investigation of the phase constitution of iron-zinc-aluminium at 450℃”, Z. Metallkd.,Vol. 64, No. 6, pp. 419 - 427, 1973.

7 Z. W. Chen, R. M. Sharp, J. T. Gregory, “Fe-Al-Zn ternary phase diagram at 450℃ ”, Mater. Sci. Technol., Vol. 6, No. 12, pp. 1173 - 1176, 1990.

8 J.-C. Tissier, “Équilibres stables et métastables dans le système Fe-Zn-Al en relation avec les processus de galvanisation à 450℃”, PhD Thesis, Université des Sciences et Techniques de Lille Flandres - Artois, 1991.

9 S. Bélisle, V. Lezon, M. Gagné, “The Solubility of Iron in Continuous Hot Dip Galvanizing Baths”, Journal of Phase Equilibria, Vol. 12, No. 3, pp. 259 - 265, 1991.

10 N. Y. Tang, “Refined 450℃ isotherm of Zn-Fe-Al phase diagram”, Materials Science and Technology, Vol. 11, pp. 870 - 873, September 1995.

11 N. Y. Tang, X. Su, “On the ternary phase in the zinc-rich corner of the Zn-Fe-Al system at temperatures below 450℃”, Metall. Mater. Trans. A, Vol. 33A, No. 5 , pp. 1559 - 1561, 2002.

12 N. Y. Tang, “Determination of liquid-phase boundaries in Zn-Fe-Mx systems”, Journal of Phase Equilibria, Vol. 21, No. 1, pp. 70 - 77, 2000.

13 M. Dauzat, F. Stouvenot, T. Moreau, “Zinc-rich corner of the Fe-Zn-Al revised phase diagram”, Proceedings of the 2nd International Conference on Zinc and Zinc Alloy Coated Steel Sheet (Galvatech’92), Amsterdam, pp. 449 - 454, September 1992.

14 J. R. McDermid, M. H. Kaye, W. T. Thompson, “Fe solubility in the Zn-rich corner of the Zn-Al-Fe system for use in continuous galvanizing and galvannealing”, Metall. Mater. Trans. B, Vol. 38B, No. 2, pp. 215 - 230, 2007.

15 M. Dauzat, F. Stouvenot, “Étude du diagramme d’équilibre Fe - Zn - Al dans le coin riche en zinc”, report IRSID SCR RI 90/315, September 1990.

16 H. Yamaguchi, Y. Hisamatsu, “Reaction of dross formation in continuous galvanizing”, Tetsu – to - Hagane, -Vol. 60, No. 1, pp. 96 - 103, 1974.

17 A. Aubry, “Nature et mécanisme de formation des mattes : synthèse bibliographique et premiers résultats expérimentaux”, report IRSID SCA 88/185, September 1988.

18 R. J. Barnhurst, S. Bélisle, M. Gagné, “Intermetallic particle formation in continuous galvanizing baths”, 4th International Conference on Zinc Coated Steel Sheet, Paris, June 1994.

19 Z. Zermout, M. Cecotti, "Détermination de la composition du liquide en équilibre avec les mattes de fond et les mattes de surface à 450°C et 480°C", highlight IRSID, June 1998.

20 C. Gatellier, P. Riboud, "Cinétique de décantation des mattes (Fe, Zn)$_2$Al$_5$ dans les cuves de galvanisation de Montataire", report IRSID PCM 88/N 223, November 1988.

21 I. Linarès, P. Abed, D. Cucheval, "Cartographie du bain de Galvallia de SOLLAC Florange", note IRSID SCR N 94/135, September 1994.

22 O. Kubaschewski, "Iron-binary phase diagrams", Springer - Verlag, Berlin, pp. 172 - 175, 1982.

23 M. Guttmann, "Diffusive phase transformations in hot-dip galvanizing", Materials Science Forum, Vols. 155 - 156, pp. 527 - 548, 1994.

24 C. E. Jordan, A. R. Marder, "Effect of substrate grain size on iron-zinc reaction kinetics during hot-dip galvanizing", Metallurgical and Materials Transactions A, Vol. 28A, pp. 2683 - 2694, December 1997.

25 Y. Hisamatsu, "Science and technology of zinc and zinc alloy coated steel sheet", Proceedings of the 1st International Conference on Zinc and Zinc Alloy Coated Steel Sheet (Galvatech'89), Tokyo, pp. 3 - 12, September 1989.

26 M. Saito, Y. Uchida, T. Kittaka, Y. Hirose, Y. Hisamatsu, "Formation behaviour of alloy layer in initial stages of galvanizing", Tetsu - to - Hagane, Vol. 77, No 7, pp. 947 - 954, 1991.

27 Y. Leprêtre, J.-M. Mataigne, M. Guttmann, J. Philibert, "Reactive interdiffusion in the Fe-Al-Zn system: Reaction mechanisms during hot-dip galvanizing", Zinc-Based Steel Coating Systems: Production and Performance (Edited by F.E. Goodwin), The Minerals, Metals & Materials Society, pp. 95 – 106, 1998.

28 E. T. McDevitt, M. Meshii, "Electron microscopy study of the microstructural evolution in the early stages of galvannealing", Zinc-Based Steel Coating Systems: Production and Performance (Edited by F.E. Goodwin), The Minerals, Metals & Materials Society, pp. 127 – 136, 1998.

29 J.-S. Kim, J. H. Chung, "Alloying behaviour of hot-dip galvannealed sheet steels containing silicon", Zinc-Based Steel Coating Systems: Production and Performance (Edited by F.E. Goodwin), The Minerals, Metals & Materials Society, pp. 157 – 164, 1998.

30 J.-M. Mataigne, "Key mechanisms in galvanization of steel sheets", La Revue de Métallurgie Paris, Vol. 106, No. 1, pp. 27 – 33, January 2009.

31 M. Guttmann, Y. Leprêtre, A. Aubry, M. J. Roch, T. Moreau, P. Drillet, J.-M. Mataigne, H. Baudin, "Mechanisms of the galvanizing reaction. Influence of Ti and P contents in steel and of its surface microstructure after annealing", Proceedings of the 3rd International Conference on Zinc and Zinc Alloy Coated Steel Sheet (Galvatech'95), Chicago, pp. 295 – 307, September 1995.

32 M.-L. Giorgi, "Étude des cinétiques des réactions de galvanisation", PhD Thesis, Ecole Centrale Paris, 2000.

33 Y. Leprêtre, "Étude des mécanismes réactionnels de la galvanisation", PhD Thesis, Université Paris XI Orsay, 1996.

34 J. Faderl, W. Maschek, J. Strutzenberger, "Spangle size and aluminium pick up for hot dip zinc coatings", Proceedings of the 3rd International Conference on Zinc and Zinc Alloy Coated Steel Sheet (Galvatech'95), Chicago, pp. 675 – 685, September 1995.

35 A. R. Borzillo, W. C. Hahn, “Growth of the inhibiting aluminium rich alloy layer on mild steel during galvanizing in zinc that contains aluminium”, Trans. A.S.M., Vol. 62, pp. 729, 1969.

36 J. Faderl, M. Pimminger, L. Schönberger, “Influence of steel grade and surface topography on the galvannealing reaction”, Proceedings of the 2nd International Conference on Zinc and Zinc Alloy Coated Steel Sheet (Galvatech’92), Amsterdam, pp. 194 – 198, September 1992.

37 N. Y. Tang, G. R. Adam, “Studies on the inhibition of alloy formation in hot-dip galvanized coatings”, The physical metallurgy of zinc coated steel (Edited by A. R. Marder), The Minerals, Metals and Materials Society, pp. 41 - 54, 1993.

38 E. Baril, G. L’Espérance, “Studies of the morphology of the Al-rich interfacial layer formed during the hot dip galvanizing of steel sheet”, Metallurgical and Materials Transactions A, Vol. 30A, pp. 681 - 695, March 1999.

39 R. Kiusalaas, G. Engberg, H. Klang, E. Schedin, L. Shön, “Control of texture and formation of intermetallic phases in continuously hot-dip galvanized coatings”, Proceedings of the 1st International Conference on Zinc and Zinc Alloy Coated Steel Sheet (Galvatech’89), Tokyo, pp. 485 - 492, September 1989.

40 P. Drillet, “Mise au point d’une méthode de réalisation de lames minces pour l’étude en microscopie électronique en transmission de la zone interfaciale acier/revêtement : application à la galvanisation”, minute IRSID N MS 92/436, July 1991.

41 M. Bobadilla, P. Drillet, D. Loison, “Métallurgie de la solidification des revêtements galvanisés”, report IRSID RI 98/058, November 1998.

42 A. Reignier, D. Bouleau, P. Drillet, “Détermination de la nature de la phase interfaciale formée sur des tôles galvanisées au Rhesca du CED en fonction du pourcentage en Al du bain de zinc”, minute IRSID MPM N 99/2259, July 1999.

43 K.-K. Wang, L. Chang, D. Gan, H.-P. Wang, “Heteroepitaxial growth of Fe_2Al_5 inhibition layer in hot-dip galvanizing of an interstitial-free steel”, Thin Solid Films, Vol. 518, No. 8, pp. 1935 – 1942, 2010.

44 E. McDevitt, Y. Morimoto, M. Meshii, “Characterisation of the Fe-Al interfacial layer in a commercial hot-dip galvanized coating”, ISIJ International, Vol. 37, No. 8, pp. 776 - 782, 1997.

45 L. Chen, R. Fourmentin, J. R. McDermid, “Morphology and kinetics of interfacial layer formation during continuous hot-dip galvanizing and galvannealing”, Metallurgical and Materials Transactions A, Vol. 39A, pp. 2128 - 2142, September 2008.

46 M. Úředníček, J. S. Kirkaldy, “Mechanism of iron attack inhibition arising from additions of aluminium to liquid Zn(Fe) during galvanizing at 450℃”, Zeitschrift für Metallkunde, Vol. 64, H. 12, pp. 899 - 910, 1973.

47 H. Yamaguchi, Y. Hisamatsu, “Reaction mechanism of the sheet galvanizing”, Transactions ISIJ, Vol. 19, pp. 649 – 658, 1979.

48 A. Nishimoto, J. Inagaki, K. Nakaoka, “Effects of surface microstructure and chemical compositions of steels on formation of Fe-Zn compounds during continuous galvanizing”, Transactions ISIJ, Vol. 26, pp. 807 – 813, 1986.

49 H. Nitto, T. Yamazaki, N. Morita, K. Yabe, S. Bandoo, “Effect of Aluminium in Zinc on Alloying of Zinc Coating of Galvanized Steels”, Tetsu – to – Hagane, Vol. 70, No. 14, pp. 1719 – 1726, 1984.

50 G. J. Harvey, P. D. Mercer, “Aluminium rich alloy layers formed during the hot dip galvanizing of low carbon steel”, Metallurgical Transactions, Vol. 4, pp. 619 - 621, 1973.

51 A. R. P. Ghuman, J. I. Goldstein, "Reaction mechanisms for the coatings formed during the hot dipping of iron in 0 to 10 Pct Al-Zn baths at 450-700℃", Met. Trans., Vol. 2A, pp. 2903, 1971.

52 A. I. Vitkin, G. A. Kokorin, A. G. Grishko, P. A. Tyukanov, "Effect of aluminium in zinc baths on the formation of the diffusion coating in hot dip galvanizing of steel", Metalloved., Termich., Obrab., Metall., Vol. 4, pp. 60, 1973.

53 M. Sugiyama, M. Okada, Y. Takada, "Characterization of crater microstructure on galvannealed steels by focused ion beam fabrication with extraction technique of micro-scaled samples", J. Japan Inst. Metals, Vol. 65, No. 5, pp. 397 - 403, 2001.

54 S. Dionne, G. Botton, M. Charest, F. Goodwin, "A study of interrupted galvannealing of Interstitials Free steels with different substrate compositions", Proceedings International Symposium on Materials in the Automotive Industry, Toronto, pp. 351 - 365, 2001.

55 M. Isobe, "Initial alloying behaviour in galvannealing process", CAMP - ISIJ, Vol. 5, pp. 1629 - 1633, 1992.

56 A. R. Marder, "The metallurgy of zinc-coated steel", Progress in Materials Science, Vol. 45, No. 3, pp. 191 – 271, 2000.

57 C. Wagner, "Types of reactions in the oxidation of alloys", Z. Electrochem., Vol. 63, pp. 772, 1959.

58 M.-L. Giorgi, J. Diawara, S. Chen, A. Koltsov, J.-M. Mataigne, "Influence of Annealing Treatment on Wetting of Steels by Zinc Alloys", Journal of Materials Science, Vol. 47, No. 24, pp. 8483 - 8495, 2012.

59 L. Zhang, T. R. Bensinger, "Hot Dip Galvannealing of Interstitial Free Steel Strengthened by Manganese", Proceedings of the 3rd International Conference on Zinc and Zinc Alloy Coated Steel Sheet (Galvatech'95), Chicago, pp. 115 – 120, September 1995.

60 J.-M. Mataigne, M. Lamberigts, V. Leroy, "Selective oxidation of cold-rolled steel during recrystallization annealing", Developments in the Annealing of Sheet Steels (Edited by R. Pradhan and I. Gupta), The Minerals, Metals and Materials Society, pp. 511-528, 1992.

61 J. Staudte, M. Mataigne, D. Loison, F. Del Frate, "Galvanizability of high Mn grade versus mixed Mn-Al and Mn-Si grades", Proceedings of the 8th International Conference on Zinc and Zinc Alloy Coated Steel Sheet (Galvatech'11), Genova, pp. 53 – 60, June 2011.

62 Y. H. Liu, N.-Y. Tang, "Computer Modeling of Aluminum Uptake and Iron Dissolution in Galvanizing and Galvannealing", Proceedings of the 6rd International Conference on Zinc and Zinc Alloy Coated Steel Sheet (Galvatech'04), Chicago, pp. 1155-1164, April 2004.

63 G. K. Mandal, R. Balasubramaniam, S. P. Mehrotra, "Theoretical Investigation of the Interfacial Reactions during Hot Dip Galvanizing of Steel", Metall. and Mater. Trans. A, Vol 40A, No. 3, pp. 637 - 645, 2009.

64 I. Linarès, "Modélisation du réacteur de galvanisation en continu", PhD Thesis, Ecole Centrale Paris, 1993.

65 N. Y. Tang, "Modeling Al enrichment in galvanized coatings", Metallurgical and Materials Transactions A, Vol. 26A, pp. 1699 - 1704, July 1995.

66 P. Toussaint, L. Segers, R. Winand, M. Dubois, "Mathematical modelling of Al take-up during the interfacial inhibiting layer formation in continuous galvanizing", ISIJ International, Vol. 38, No. 9, pp. 985 - 991, 1998.

67 J. B. Clark, "Conventions for plotting diffusion paths in multiphase ternary diffusion couples on the isothermal section of a ternary phase diagram", Trans. Met. Soc. AIME, Vol. 227, No. 5, pp. 1250- 1251, 1963.

68 T. Nakamori, “Effects of crystal orientation of base steel on growth of Fe-Zn intermetallics on extra low carbon Ti-added steel during galvanizing and galvannealing”, CAMP – ISIJ, Vol. 5, pp. 1637 – 1640, 1992.

69 Y. Adachi, T. Nakamori, K. Kamei, “Crystallographic Study of Hot Dip Galvanized Steel”, J. Japan Inst. Metals, Vol. 56, No. 11, pp. 1235- 1241, 1992.

70 C. E. Jordan, A. R. Marder, “Inhibition layer breakdown and outburst Fe-Zn alloy formation during galvanizing”, Zinc-Based Steel Coating Systems: Production and Performance (Edited by F. E. Goodwin), The Minerals, Metals & Materials Society, pp. 115 – 126, 1998.

71 P. Bahnweg, T. Moreau, “Élaboration de couche de diffusion Fe_2Al_5”, report IRSID SCA N 92/296, December 1992.

72 L. N. Larikov, V. M. Fal'chenko, D. F. Polishchuk, V. R. Ryabov, A. V. Lozovskaya, “Opredeleniye parametrov diffuzii v intermetallidnykh fazakh, obrazuyushchikhsya pri svarke”, Avtomat.Svarka, No. 5, pp. 68 - 69, 1968.

73 L. D. Lucas, “Données physico-chimiques des principaux métaux et métalloïdes - Densité”, Techniques de l’ingénieur, Traité des matériaux métalliques MI, M65, pp. 1 - 14, 1996.

74 P. Bahnweg, T. Moreau, “Mécanismes de réaction acier - métal liquide dans le cadre de la galvanisation - Approche méthodologique”, report IRSID RI 93/322, July 1993.

75 D. Horstmann, “Reactions between iron and molten zinc - Part 2: “The course of reactions between iron and molten zinc containing aluminium”, published by Zinc Development Association, London, pp. 20 - 32, 1978.

76 T. Toki, K. Oshima, T. Nakamori, Y. Saito, T. Tsuda, Y. Hobo, “Effect of P content in ultra-low carbon Ti stabilized steel on the rate of Fe-Zn alloy formation through ferrite grain boundary diffusion during hot-dip galvanizing”, The Physical Metallurgy of Zinc Coated Steel (Edited by A.R. Marder), The Minerals, Metals & Materials Society, pp. 169 - 180, 1993.

77 S. Gomi, C. Kato, T. Fujimura, K. Mochizuki, “In-situ high temperature X-ray diffraction study on phase changes during galvannealing”, Zinc-Based Steel Coating Systems: Production and Performance (Edited by F.E. Goodwin), The Minerals, Metals & Materials Society, pp. 147 - 156, 1998.

78 M. Abe, S. Kanbara, “Influence of Ti Content in Steel and Al content in Zn bath on Fe-Zn Reactivity in Galvanizing”, Tetsu - to - Hagane, Vol. 69, S1061, 1983.

79 G. Claus, J. Dilewijns, B.C. De Cooman, U. Meers, “Determination of the process window for optimal galvannealing of Ti-IF steel”, Proceedings of the 3rd International Conference on Zinc and Zinc Alloy Coated Steel Sheet (Galvatech’95), Chicago, pp. 107 - 113, September 1995.

80 F. A. Vallim Fonseca, V. T. Lopes Buono, J.G. de Sousa, R.A. Carneiro, “Aço ultra baixo carbono ao titânio – avaliação do revestimento Galvannealed obtido por simulação em Gleeble”, Contribuição técnica ao 44° Seminario de Laminação – Processos e Produtos Laminados e Revestidos, Campos do Jordão - SP, Brazil, October 2007.

81 C. E. Jordan, A. R. Marder, “Alloy layer growth during hot-dip galvanizing at 450°C”, Proceedings of the 3rd International Conference on Zinc and Zinc Alloy Coated Steel Sheet (Galvatech’95), Chicago, pp. 319 - 325, September 1995.

82 M. Lamberigts, V. Leroy, M. Beguin, M. Dubois, A. Van der Heiden, G. Verhoeven, “Kinetics of Fe-Zn reactions during galvannealing”, Proceedings of the 2nd International Conference on Zinc and Zinc Alloy Coated Steel Sheet (Galvatech’92), Amsterdam, pp. 199 - 203, September 1992.

83 M. Mahe, A. Storhaye, “Essai de dissolution selective d’une tôle galvanisée”, report IRSID SCA 91/122, April 1991.

84 R. de Kermadek, “Etude du système Zn-$FeZn_7$-Fe_2Al_5 à la limite de solubilité du fer à 450°C”, report IRSID SCR 96/229, November 1996.

85 M. Martin, “Dissolution électrochimique de revêtements métalliques”, internship report ArcelorMittal, 2009.

86 R. Mishra, “Quantification of Galvannealed Coating Phases Using the Galvanostatic Technique”, Metall. and Mater. Trans. A, Vol. 39A, No. 10, pp. 2275 – 2277, 2008.

87 U. Burkhardt, Y. Grin, M. Ellner, K. Peters, “Structure Refinement of the Iron-Aluminium Phase with the Approximate Composition Fe_2Al_5”, Acta Crystallographica, Vol. B50, pp. 313 - 316, 1994.

88 Z.W. Chen, R.M. Sharp, J.T. Gregory, “Lattice parameters and interplanar spacings of Fe_2Al_5 and Fe_2Al_5-Zn_x”, Materials Forum, Vol. 14, No. 2, pp. 130 – 136, 1990.

89 M. A. Delesse, “Procédé mécanique pour déterminer la composition des roches”, Cr. Hebd. Seanc. Acad. Sci. Paris, Vol. 25, pp. 544 – 545, 1847.

90 A. K. Rosiwal, “Ueber geometrische Gesteinsanalysen. Ein einfacher Weg zur ziffermässigen Feststellung des Quantitätsverhältinesses der Mineralbestandtheile gemengter Gesteine”, Verhandlungen der K. K. Geolog. Reichsanstalt Wien, Vol. 5, No. 6, pp. 143 - 174, 1898.

91 M.-L. Giorgi, J.-B. Guillot, R. Nicolle, “Theoretical model of the interfacial reactions between solid iron and liquid zinc-aluminium alloy”, Journal of Materials Science, Vol. 40, No. 9 - 10, pp. 2263 - 2268, 2005.

92 H. Réglé, “Mechanisms of Microstructure and Texture Evolution during Recrystallisation of Ferritic Steels Sheets”, Recrystallization and Grain Growth, Proceedings of the 1st Joint International Conference (Edited by G. Gottstein and D. A. Molodov), Springer-Verlag, Vol. 1, No. 2, pp. 707 – 718, August 2001.

93 ISO 643 Standard.

94 ASTM E112 Standard Test Methods for Determining Average Grain Size.

95 J. S. Kirkaldy, D. J. Young, “The multicomponent Fick equations and their solutions”, in: “Diffusion on the Condensed State”, The Institute of Metals, London, pp. 150–171, 1987.

96 C. Karl, “Optimization of the alloying stage of galvannealing process”, internship report ArcelorMittal, 2009.

APPENDICES

Appendix A: The inhibition layer formation in GI baths

A.1. Nature of the inhibition layer

Most of the investigations on the nature of the inhibition layer focused on GI bath compositions, more precisely on bath aluminium contents around 0.20 wt.%. For such galvanizing baths, it is generally admitted that the main component of the inhibition layer is the $Fe_2Al_5Zn_x$ phase [23-43], in agreement with the phase diagram.

Nevertheless, a small group of researchers has suggested the presence of other compounds within the inhibition layer which forms in GI baths. Table 35 summarizes the studies carried out by these authors.

Table 35: Summary of studies which reported the presence of other compounds that $Fe_2Al_5Zn_x$ within the inhibition layer in GI baths.

Authors [Ref.]	Analysis techniques	wt.% Al	Nature of the inhibition layer
Harvey and Mercer [50]	XRD, TEM, EPMA	0.18 0.15	$Fe_2Al_5Zn_x$ $Fe_2Al_5Zn_x$ or Fe-Al-Zn ternary compound
Ghuman and Goldstein [51]	XRD	0.25	Fe-Al-Zn ternary compound
Nitto *et al*. [49]			Fe_2Al_4Zn ternary compound
McDevitt *et al*. [44]	SEM, TEM, XRD	0.20	$Fe_2Al_5Zn_x$ and $FeAl_3Zn_x$
Chen *et al*. [45]	EBSD	0.20	$Fe_2Al_5Zn_x$ and transient $FeAl_3Zn_x$
Úředníček and Kirkaldy [46]	Low angle XRD	0.15-1.10	$Fe_2Al_5Zn_x$ and transient $FeAl_3Zn_x$, $FeAl_2Zn_x$
Nishimoto *et al*. [48]	Electron Back-Scattering Mössbauer spectroscopy	0.16	δ over an Fe-Al layer

Some of the previous authors have reported the presence of Al-Fe-Zn ternary compounds within the inhibition layer which forms in GI baths [49-51].

Thus, Harvey and Mercer [50] investigated the interfacial layer formation on industrial samples using a combination of XRD, TEM and Electron Probe Micro-Analysis (EPMA). They observed a continuous inhibition layer composed of $Fe_2Al_5Zn_x$ in a zinc bath containing 0.18 wt.% Al. In a zinc bath containing 0.15 wt.% Al, an aluminium-rich inhibition layer composed of either $Fe_2Al_5Zn_x$ or an Al-Fe-Zn ternary compound was observed.

According to Ghuman and Goldstein [51], after galvanizing in a zinc bath containing 0.25 wt.% Al at 450 ℃, $Fe_2Al_5Zn_x$ was not detected by XRD whereas two Fe-Al-Zn ternary compounds would have been observed: a “primary” one, which would be replaced locally by a “secondary” one.

As well as the previous author, Nitto *et al*. [49] have mentioned a purely ternary intermetallic compound (Fe_2Al_4Zn) as the main constituent of the inhibition layer.

However, the high solubility of zinc in Fe_2Al_5 (up to 20 wt.%, Figure 10) can explain, as advanced by Guttmann [23], that these ternary inhibiting compounds, which are inexistent in the Fe-Al-Zn equilibrium phase diagrams, are nothing else than zinc-containing Fe_2Al_5 ($Fe_2Al_5Zn_x$).

In addition, other authors [44-47] have reported the presence of other Fe-Al intermetallic compounds in coexistence with the $Fe_2Al_5Zn_x$ phase for aluminium contents corresponding to GI baths.

McDevitt *et al*. [44] have analysed by SEM, TEM and XRD the inhibition layer which forms in a zinc bath containing 0.20 wt.% Al at 470 ℃. They f ound this layer to be composed of $Fe_2Al_5Zn_x$ and metastable $FeAl_3Zn_x$.

By their side, Chen *et al*. [45] have also found via EBSD phase determination a transient $FeAl_3Zn_x$ phase in the inhibition layer in coexistence with $Fe_2Al_5Zn_x$ in the earlier stages of immersion in galvanizing baths containing 0.20 wt.% Al at temperatures varying from 450 to 480 ℃.

Úředníček and Kirkaldy [46] investigated the nature of the inhibition layer formed on pure iron by metallography and low angle XRD. They tested different immersion times (10 s, 1, 3, 10 and 30 min) and aluminium contents (0.15, 0.22, 0.32 and 1.10 wt.% Al) in galvanizing baths at 450 ℃. In all cases, they found the inhibition layer to be composed by a transient $FeAl_3Zn_x$ phase and $Fe_2Al_5Zn_x$. According to the authors, these latter two phases form the bulk of the inhibition layer but may occasionally be accompanied by particles of the $FeAl_2Zn_x$ phase. We have no elements to criticize these results but it should be appropriate to revise in detail the experimental procedure and the obtained diffraction lines of this work, especially for the $FeAl_3Zn_x$ and the $FeAl_2Zn_x$ phases.

Finally, Yamaguchi and Hisamatsu [47] submitted the assumption that, for bath aluminium contents between 0.15 and 0.30 wt.%, $FeAl_3Zn_x$ forms on the steel substrate in coexistence with $Fe_2Al_5Zn_x$ in the earlier stages of immersion, but rapidly transforms into $Fe_2Al_5Zn_x$.

However, the domain of existence of the $FeAl_3Zn_x$ phase in equilibrium with the liquid zinc is far away from the typical aluminium contents used in industrial galvanizing baths. The minimum aluminium content in the zinc bath allowing its thermodynamic equilibrium with $FeAl_3Zn_x$ is 1.3 wt.% Al [10]. Therefore, the presence of metastable $FeAl_3Zn_x$ seems quite doubtful in the inhibition layer which forms in GI baths. The lack of accuracy of the analysis techniques used by some of these authors, as EBSD [45], could be responsible of this strange presence of $FeAl_3Zn_x$. Even less probable appears the presence of the $FeAl_2Zn_x$ phase suggested by Úředníček and Kirkaldy [46].

On the other hand, Nishimoto *et al*. [48] observed a “fine granular” structure over a Fe-Al layer as constituents of the inhibition layer formed in a zinc bath containing 0.16 wt.%Al at 470 ℃. They confirmed by Electron Back-Scattering Mössbauer spectroscopy that this “fine granular” structure is mainly composed of the δ phase. Yamaguchi and Hisamatsu [47] have also proposed such an inhibition layer in the case of bath aluminium contents between 0.09 and 0.15 wt.%.

These last two studies should be highlighted as the only ones which suggest the presence of the δ phase in the inhibition layer for a so high aluminium content in the galvanizing bath (0.15 wt.% or higher).

A.2. Experimental data on the inhibition layer growth kinetics

A.2.1. Effect of the bath aluminium content

Giorgi [32] developed a model describing the nucleation and growth of the inhibition layer which forms in GI baths. In order to fit some parameters and validate her model, she made a compilation of experimental growth data obtained by other researchers and published in the literature. These experimental data are quite in agreement with each other, as can be appreciated in Figure 114. The author made the approach that the aluminium uptake by the inhibition layer and its thickness are proportional. This approach would be inconsistent with the contributions made by other authors that the structure (degree of compaction) of the inhibition layer varies through its thickness [31,45] or, as will be seen later, with the bath aluminium content [34]. As can be seen in Figure 114, the aluminium uptake by the inhibition layer increases with an increase of the bath aluminium content in the case of zinc baths with 0.15, 0.16 and 0.20 wt.% Al. However, there is a point, corresponding to a bath with 0.3 wt.% Al, which is out of this tendency. Indeed, for a 6 s immersion time, the aluminium uptake by the inhibition layer is considerably lower in a bath containing 0.30 wt.% Al than in a bath containing 0.20 wt.% Al. This unexpected behaviour has been explained by Faderl *et al*. [34].

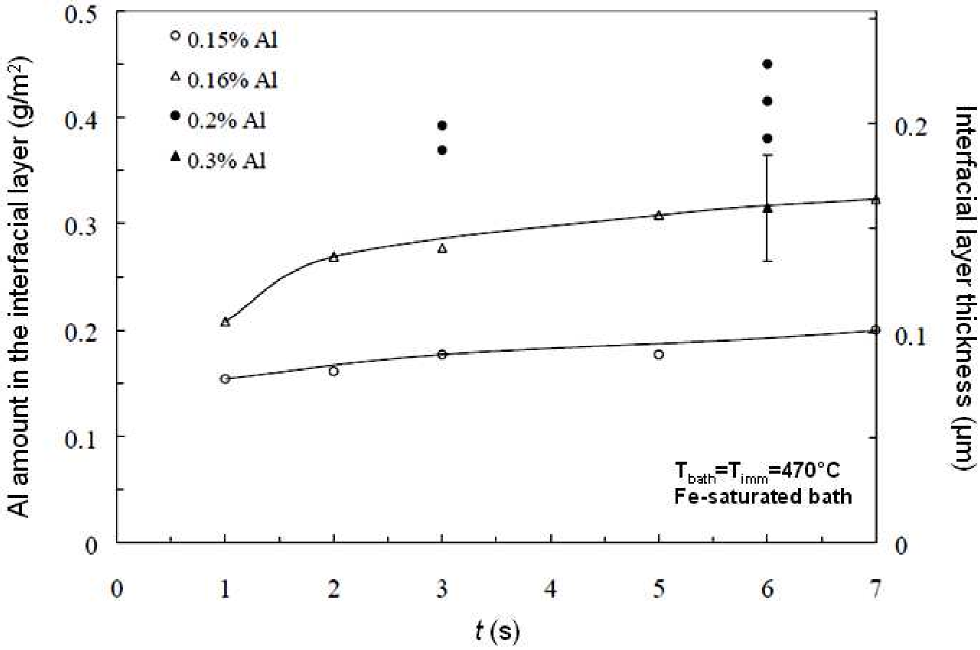

Figure 114: Effect of the bath aluminium content on the inhibition layer growth kinetics (compilation of experimental data carried out by Giorgi [32]).

Faderl *et al*. [34] studied as well the effect of the bath aluminium content on the inhibition layer growth kinetics. Their research was carried out on GI baths at 470 ℃ but with higher aluminium contents than in the previous cases. Figure 115 illustrates the unexpected effect reported above. An increase in the bath aluminium content from 0.2 to 0.4 wt.% leads to a significant decrease of the aluminium uptake by the inhibition layer. This behaviour drove the authors to propose the following mechanism for this domain of bath aluminium content. Due to the better supply of aluminium, as a result of a higher aluminium content in the zinc bath, an accelerated formation of a dense interfacial layer acting as a strong diffusion barrier occurs. As a consequence of the reduced diffusion time, a thinner $Fe_2Al_5Zn_x$ inhibition layer is formed.

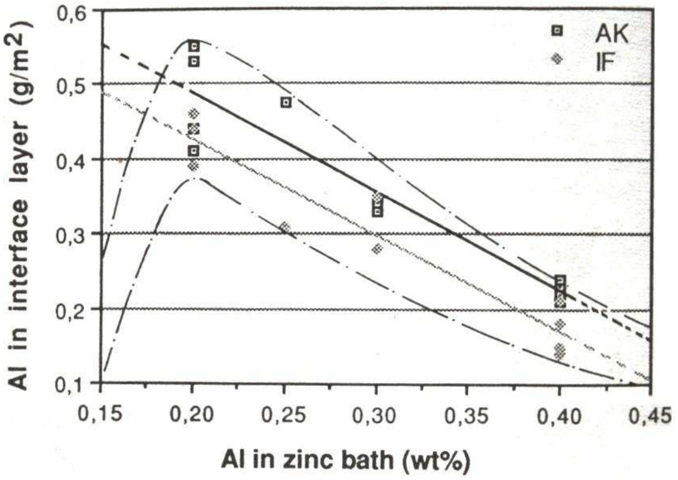

Figure 115: Effect of the bath aluminium content on the inhibition layer growth kinetics (Faderl *et al*. [34]).

On the contrary, in zinc baths with lower aluminium contents (less than 0.2 wt.%), the aluminium supply from the zinc bath is limited and after the nucleation step there is not remaining aluminium enough to make the inhibition layer grow.

According to the authors, a turning point can be fixed at 0.20 wt.% Al. For bath aluminium contents lower than or equal to 0.20 wt.%, the aluminium supply from the zinc bath is limited and, consequently, an increase of the bath aluminium content will result in a higher growth rate of the inhibition layer. This is the reason why the development of the inhibition layer increases with increased bath aluminium content. For higher bath aluminium contents, the aluminium supply becomes high enough to lead to the nucleation of a dense inhibition layer. In this case, further growth of the inhibition layer is limited by solid state diffusion of iron through this layer. This is the reason why the development of the inhibition layer decreases with increased bath aluminium content.

A.2.2. Effect of the bath temperature

The effect of the bath temperature on the inhibition layer growth kinetics has been studied by Chen *et al*. [45] and Giorgi [32].

During the development of her model, Giorgi [32] also collected published experimental growth data at different bath temperatures. These data are shown in Figure 116, in the case of zinc baths containing 0.19 to 0.20 wt.% Al.

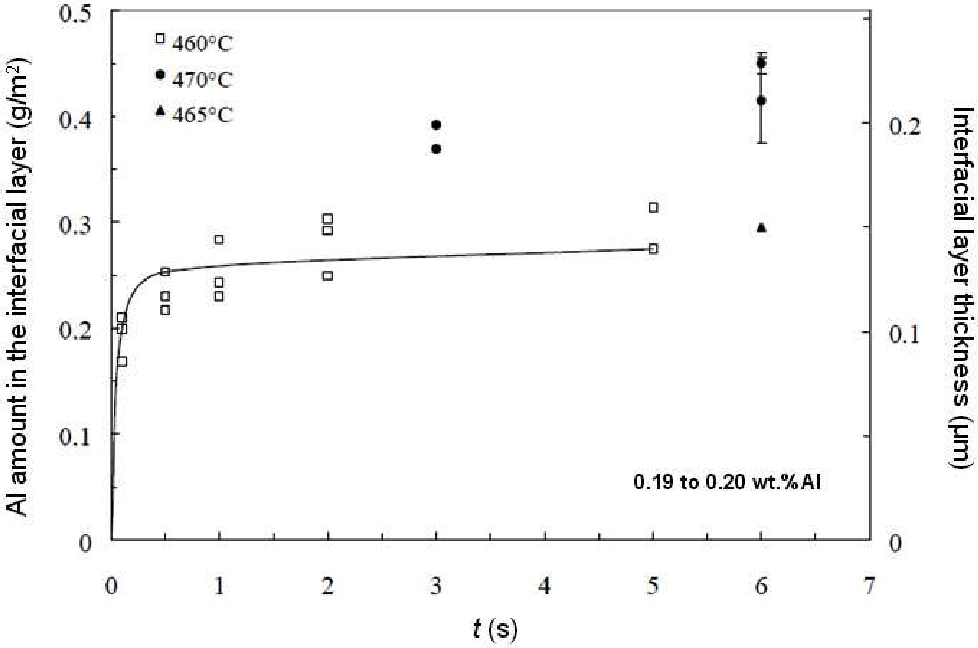

Figure 116: Effect of the bath temperature on the inhibition layer growth kinetics (compilation of experimental data carried out by Giorgi [32]).

As could be expected due to the fact that diffusion is activated by temperature, the aluminium uptake by the inhibition layer increases with an increase of the bath temperature.

Chen *et al*. [45] had also proposed a kinetic model (section A.3) which specifically describes the growth of the inhibition layer in 0.20 wt.% Al containing zinc baths as a function of the reaction time and the bath temperature. Calculations of their model compared to their own experimental growth data are shown in Figure 117 and indicate, in agreement with Giorgi [32], that the inhibition layer develops more rapidly when the bath temperature is increased.

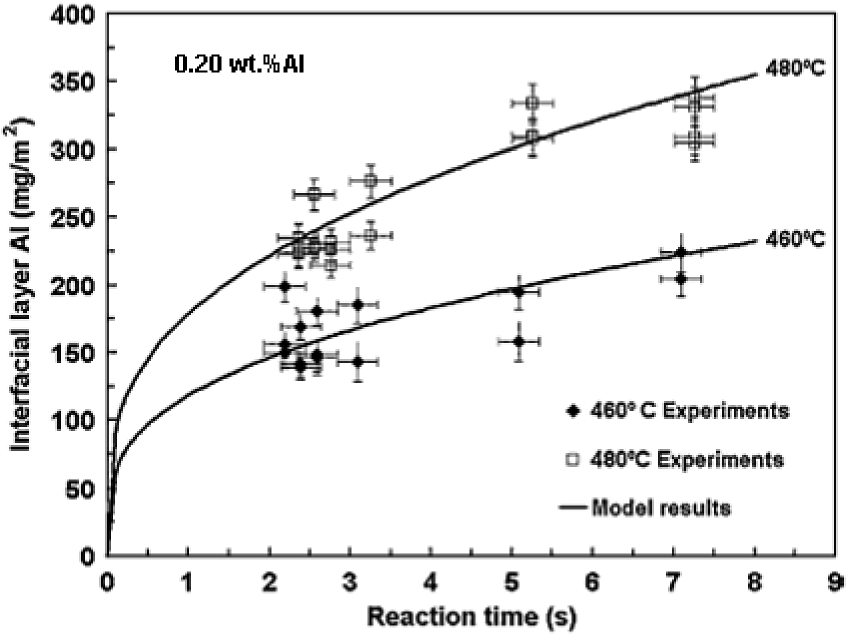

Figure 117: Effect of the bath temperature on the inhibition layer growth kinetics (Chen *et al*. [45]).

A.2.3. Effect of the immersion time

In addition, it can be seen, as expected, that the longer the immersion time is, the higher the aluminium uptake by the inhibition layer is (Figure 114, Figure 116 and Figure 117).

To sum up, the growth of the inhibition layer is favoured by higher bath temperatures [32,45], longer immersion times [32,45] and higher bath aluminium contents [32,34], provided that this last parameter does not exceed a threshold value, fixed at 0.20 wt.% [34].

A.3. Mechanisms of formation of the inhibition layer

It has been seen in section I.3.1.3 that, regardless the nature of the intermetallic compound formed, the mechanisms of formation of the inhibition layer could be generalized and summarized in the following steps: wetting of the steel suface by liquid zinc, iron dissolution from the steel surface into the liquid and nucleation and growth of the inhibition layer. In this section, focus is only given to the mechanisms of nucleation and growth of the intermetallic compound which forms in the case of GI baths. A review of the models proposed in the literature for this type of baths is also presented.

Thermodynamic considerations

Although very few authors have reported the presence of metastable phases in the inhibition layer which forms in GI baths (the proposed mechanisms accounting for the formation of these phases will be seen later), the nucleation and growth of the $Fe_2Al_5Zn_x$ phase in thermodynamic equilibrium with both the steel and the liquid zinc is widely accepted in such baths (section I.3.1.1.2).

Leprêtre *et al*. [27,33] used the idea of diffusion paths in the Al-Fe-Zn ternary phase diagram proposed by Úředníček and Kirkaldy [46] as a powerful tool to detail the mechanisms of formation of the inhibition layer.

As the obtained microstructure consists of a layer with planar interfaces at thermodynamic equilibrium, the inhibition by $Fe_2Al_5Zn_x$ in GI baths can be represented by a real diffusion path (path 4 in Figure 118). Consequently, the system does not require the nucleation of any other intermetallic compound. Even if the $Fe_2Al_5Zn_x$ phase acts as a strong barrier against zinc and iron diffusion, the interdiffusion process can then go ahead with the growth of the $Fe_2Al_5Zn_x$ layer, which corresponds to the inhibiting period during the first times of galvanization. This mechanism is also supported by Guttmann [23], Mataigne [30] and Giorgi [32].

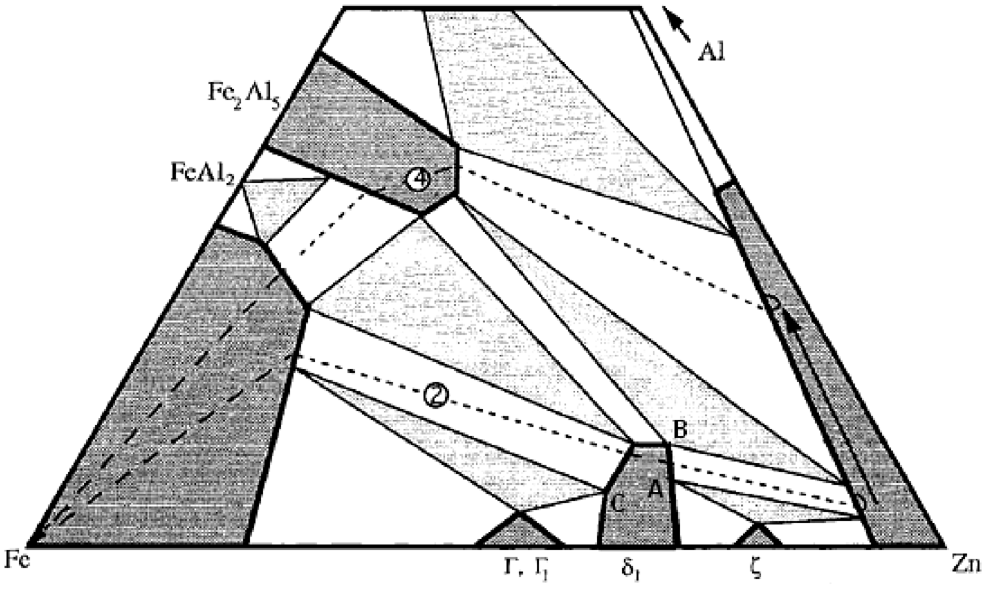

Figure 118: Schematic representation of the isothermal Al-Fe-Zn phase diagram at 450 °C illustrating the diffusion path corresponding to the Fe-Zn inhibition in GI baths (path 4) (Leprêtre [33]).

Final structure

Concerning its final structure, some researchers [31,45] have pointed out that this $Fe_2Al_5Zn_x$ inhibition layer is characterized by a two-layer structure: a compact thin layer in contact with the steel substrate (lower layer) and a coarser non-compact upper layer. This difference in coarsening can be explained by the difference in iron and aluminium supply, necessary for the growth of the inhibition layer. This two-layer structure is shown in Figure 119.

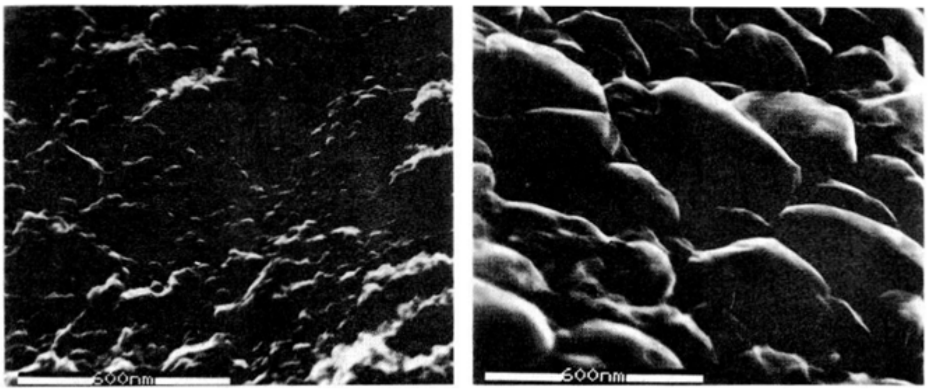

Lower layer **Upper layer**

Figure 119: Structure of the $Fe_2Al_5Zn_x$ inhibition layer formed in GI baths (Guttmann *et al*. [31]).

Modelling of the nucleation and growth of the inhibition layer

In 1993, Linarès [64] proposed the first overall model for the galvanizing process, involving the resolution of the equations of iron and aluminium diffusion in the zinc bath. The results depend on time and on a space variable in the direction perpendicular to the plane of the steel sheet. The boundary conditions at the steel / zinc bath interface involve the iron dissolution according to zero order kinetics (dominant term) and the growth of $Fe_2Al_5Zn_x$ at the interface. In this model, growth is assumed to be limited by the diffusion of iron through the $Fe_2Al_5Zn_x$ layer in course of formation. However, this model does not account for the nucleation of $Fe_2Al_5Zn_x$.

Subsequently, Tang [65] considered the nucleation and growth of the $Fe_2Al_5Zn_x$ layer. The nucleation rate employed by the author depends in particular on the mole fraction of aluminium at the steel / liquid zinc interface and on the number of iron atoms per unit area on the steel surface, which was considered to be equal to the number of nucleation sites. Growth was assumed to be controlled by the diffusion of aluminium in the zinc bath.

Later, Toussaint *et al*. [66] proposed two modifications to the model developed by Tang [65]:

- The nucleation rate takes into account the surface roughness of the steel and the average number of iron atoms involved in the formation of an embryo.

- Growth is controlled by the diffusion of iron through the just nucleated $Fe_2Al_5Zn_x$. This assumption, considered also by Linarès [64], seems more probable than that of Tang [65].

Giorgi [32] improved and completed the kinetic laws for the reactions at the steel / liquid zinc interface in order to identify the rate controlling step in the growth of the interface layer at short times. She developed a model based on the assumption that growth starts once nucleation is over. She also supposed the formation of a monolayer intermetallic compound. For the nucleation phenomenon, she introduced a classical law where the Gibbs free energy of formation of a nucleus of critical size is a function of the iron supersaturation at the solid / liquid interface. The author introduced as well a first order law for the iron consumption flux ($mol.m^{-2}.s^{-1}$) by the growth phenomenon in order to take into account the deviation from saturation:

$$J_{Fe}^{cons} = k_{growth}\left(c_{Fe}^{\text{int}\,2} - c_{Fe}^{sat}\right) \tag{A.1}$$

where k_{growth} ($m.s^{-1}$) is the interface alloy growth rate constant, $c_{Fe}^{\text{int}\,2}$ ($mol.m^{-3}$) is the iron concentration at the interface alloy / liquid zinc interface and c_{Fe}^{sat} ($mol.m^{-3}$) the iron concentration in the liquid zinc in equilibrium with the interface alloy.

The kinetic model from Giorgi [32] is based on the resolution of the equations of iron and aluminium diffusion in the zinc bath. The boundary conditions at the interface between the steel and the molten zinc involve iron dissolution, nucleation and growth of $Fe_2Al_5Zn_x$ and iron diffusion in the $Fe_2Al_5Zn_x$ formed. The solid state diffusion of aluminium within the interfacial layer is neglected. A schematic representation of the considered phenomena is shown in Figure 120.

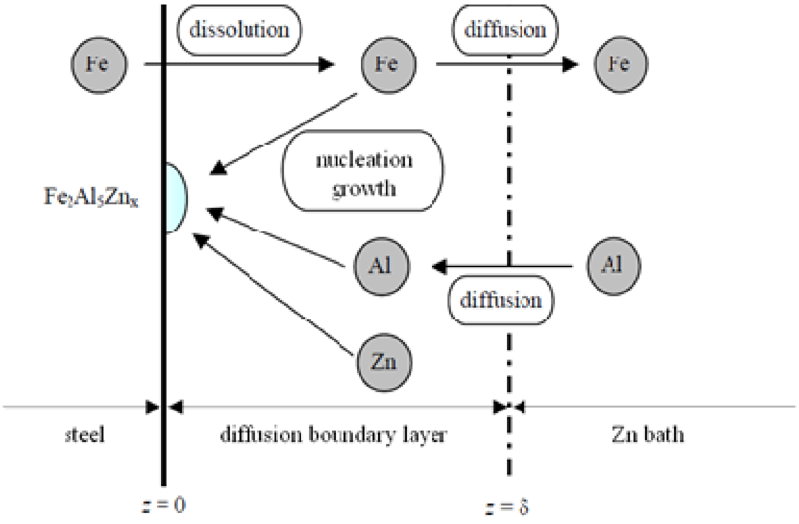

Figure 120: Schematic representation of the reactions in the galvanizing bath (Giorgi [32]).

Figure 121 shows the crystal growth kinetics prediction of the model [32] in the case of a zinc bath containing 0.20 wt.% Al at 450 ℃. $d_{crystal}$ is the edge length of the crystals assumed to be in the form of cubes. As it can be seen, the iron dissolution takes place during an incubation period of less than 0.1 s. At this moment, the iron supersaturation of the liquid zinc at the interface is such that the nucleation phenomenon starts. Small nuclei of the intermetallic compound begin to appear at the steel surface and grow laterally until forming a continuous layer after 0.2 s. At this point in time, the crystal size has reached 50 nm.

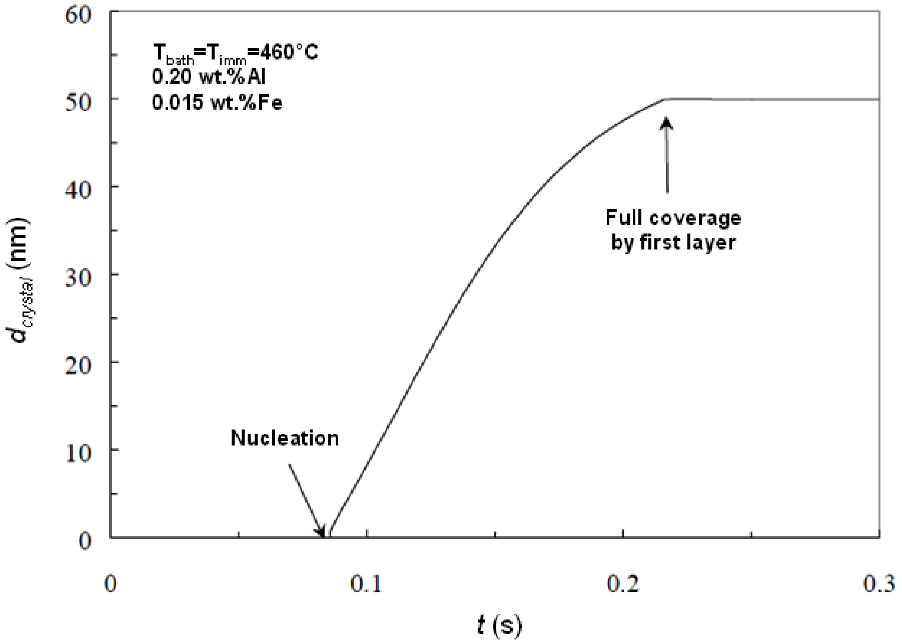

Figure 121: Kinetics of crystal growth against immersion time (Giorgi [32]).

Figure 122 illustrates the kinetics of aluminium pick-up by the inhibition layer against the immersion time. The initial rapid increase corresponds to the nucleation and lateral growth represented in Figure 121. Then, the growth kinetics slows down as controlled by solid state diffusion of iron through the just formed continuous layer.

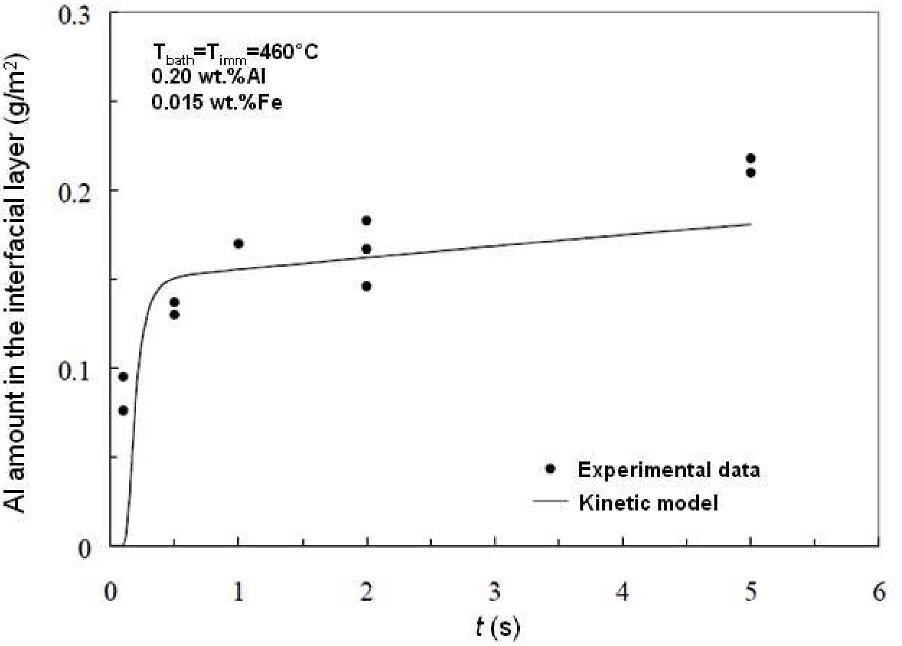

Figure 122: Kinetics of aluminium pick-up against immersion time (Giorgi [32]).

More recently, Liu and Tang [62] reviewed the model developed by Tang [65] in order to make it valid also for GA baths, but the main assumptions of the new version of the model remain unchanged.

By their side, Chen *et al*. [45] proposed a model aiming to describe the inhibition layer growth kinetics in the case of a zinc bath containing 0.20 wt.% Al as a function of the reaction time and the bath temperature. However, unlike the model developed by Giorgi [32], the authors do not take into account the early stages of formation of the interfacial layer, i.e., the incubation period, during which iron dissolution takes place, and the nucleation stage. The authors reported that the inhibition layer microstructure coarsening has significant effect on the effective diffusion coefficient of iron through the layer itself, calculated as the weighted sum of lattice and grain boundary diffusion, and on the growth rate of this layer, which was found to be non-parabolic. So, the model developed by Chen *et al*. [45] calculates instantaneous variations of the interfacial layer grain size (considered by the authors to be proportional to time) and accounts for instantaneous variations in the value of the effective diffusion coefficient and the non-parabolic growth rate. Aluminium uptake calculations of their model compared to experimental data are shown in Figure 117.

Finally, Mandal *et al*. [63] also proposed a model accounting for the reactions taking place at the steel / liquid zinc interface during immersion in the galvanizing bath. This model considers the dissolution of iron, the nucleation of the $Fe_2Al_5Zn_x$ inhibiting layer and its growth, assumed to be controlled by solid state diffusion of iron towards the liquid.

Particular mechanisms involving phases different from $Fe_2Al_5Zn_x$

As shown in section A.1, some authors found intermetallic compound(s) different from $Fe_2Al_5Zn_x$ at the steel / liquid zinc interface in the case of GI baths. Even if the interface alloy is most likely composed of $Fe_2Al_5Zn_x$ only, the mechanisms of formation of the other intermetallic compounds proposed in the literature are described here below.

McDevitt and Meshii [28] studied the inhibition layer which forms in a zinc bath containing 0.14 wt.% Al at very short dipping times. They found this layer to be primarily composed of $Fe_2Al_5Zn_x$. However, they observed, just in the case of P-added steel grades, that the inhibition layer went through a transition from “a Fe-Al solid solution or ordered phase” to the $Fe_2Al_5Zn_x$ phase. No other author reported such an observation.

As advanced in section A.1, a group of researchers [44-47] affirmed to have observed the $FeAl_3Zn_x$ phase in coexistence with $Fe_2Al_5Zn_x$ within the inhibition layer which forms in GI baths. The mechanisms of formation of this layer remain controversial:

- McDevitt *et al*. [44] confirmed by TEM that metastable $FeAl_3Zn_x$ forms first on the steel surface. Then $Fe_2Al_5Zn_x$ nucleates at the steel / $FeAl_3Zn_x$ interface with preferential orientations with regard to the steel surface and grows by consuming $FeAl_3Zn_x$.

- Chen *et al*. [45] pointed out, in agreement with the previous authors, that the first phase nucleating on the steel surface is $FeAl_3Zn_x$, forming a finely crystalline, compact layer. In opposition to McDevitt *et al*. [44], they reported that the $FeAl_3Zn_x$ layer transforms into $Fe_2Al_5Zn_x$ from the liquid to the steel by a diffusive reaction mechanism given by:

$$FeAl_3 + 2\,Al(bath) + Fe(substrate) + X\,Zn(bath) \rightarrow Fe_2Al_5Zn_X \qquad \text{(A.2)}$$

Simultaneously to this transformation, the $Fe_2Al_5Zn_x$ crystals already formed continue their development and form a non compact, coarser $Fe_2Al_5Zn_x$ upper layer. Finally, the metastable $FeAl_3Zn_x$ phase disappears and the two-layer structure of the inhibition layer is completely composed of $Fe_2Al_5Zn_x$. According to the authors, both $FeAl_3Zn_x$ and $Fe_2Al_5Zn_x$ phases showed preferred crystallographic orientations with respect to the steel. A schematic representation of their mechanism is shown in Figure 123.

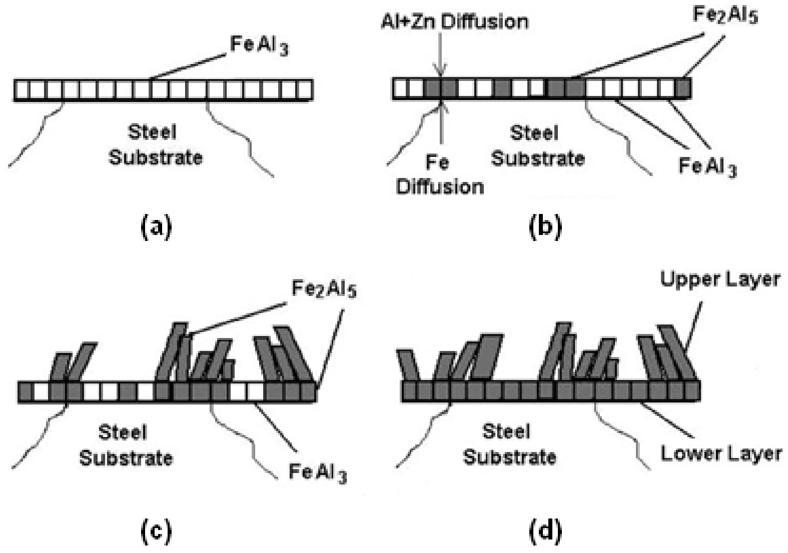

Figure 123: Mechanism of formation of the inhibition layer suggested by Chen *et al*. [45].

Úředníček and Kirkaldy [46] were pioneers in the use of diffusion paths in the Al-Fe-Zn ternary phase diagram in order to propose a detailed description of the reaction mechanisms in galvanizing and galvannealing. Concerning the inhibition layer, they found experimentally that the phase initially formed on the steel surface is $Fe_2Al_5Zn_x$, followed immediately by the nucleation of $FeAl_3Zn_x$. This stage is represented by diffusion path Fe-IJKD'C'' in Figure 124.

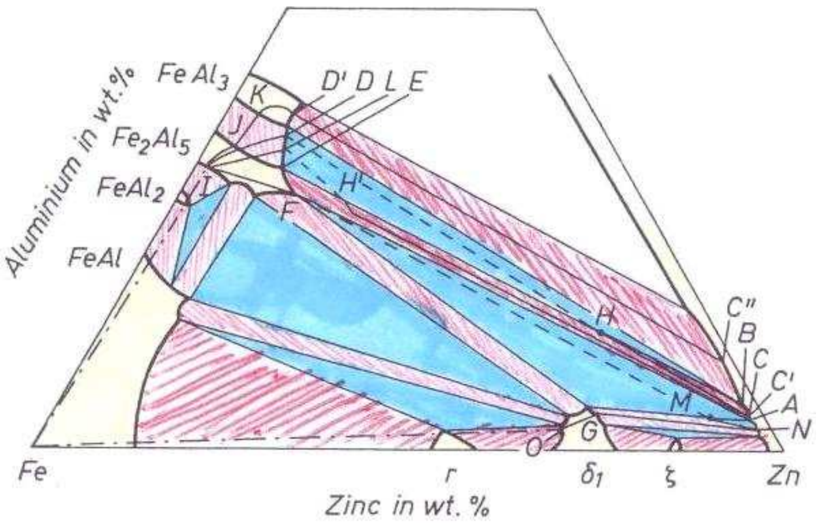

Figure 124: Schematic representation of the isothermal Al-Fe-Zn phase diagram at 450 °C illustrating diffusion paths proposed by Úředníček and Kirkaldy [46].

The authors [46] indicated that the aluminium concentration gradient in the liquid zinc can be dispersed to allow the initial activity of this component, minor in the bulk liquid, to be maintained at a high level at the solid / liquid interface, thus favouring the stability of aluminium-rich Fe-Al compounds. So, according to the authors, it could be reasonably assumed that even if the aluminium content in the bulk liquid corresponds to GI baths, where $Fe_2Al_5Zn_x$ should be thermodynamically stable, the aluminium content in the liquid zinc at the interface with steel can be high enough to allow the nucleation of $FeAl_3Zn_x$. But the question now is why $Fe_2Al_5Zn_x$ nucleates first on the steel surface. Assumptions on epitaxial relationship between the steel and $Fe_2Al_5Zn_x$ (Guttmann [23]) lowering its nucleation barrier can be made to try to explain this behaviour. Once the $Fe_2Al_5Zn_x$ phase is formed, $FeAl_3Zn_x$ nucleates at the interface with liquid zinc. Therefore, it could be presumed that the crystallographic properties of the steel surface, which are thought to favour the epitaxial nucleation of $Fe_2Al_5Zn_x$, are not transferred to the next layer.

According to Úředníček and Kirkaldy [46], it is very likely that the interface compositions evolve by aluminium depletion to those defined by virtual diffusion path Fe-IDHC. Instabilities are to be expected next to the liquid since this path crosses both two and three-phase domains. This path implies a local equilibrium surface involving three phases, $Fe_2Al_5Zn_x$, $FeAl_3Zn_x$ and liquid zinc, in contact with a two-phase domain $Fe_2Al_5Zn_x$-liquid zinc. The microstructure corresponding to this path exhibits a nearly planar interface between $FeAl_3Zn_x$ and liquid zinc along with a very limited number of protruding small crystals of $Fe_2Al_5Zn_x$.

In locations where instability has become critical, the zinc-saturated $FeAl_3Zn_x$ has been penetrated by columns of the zinc-containing $Fe_2Al_5Zn_x$ phase, which grow into the liquid zinc. The aluminium required for the growth of this phase can be supplied by the zinc bath and by the dissolution of the $FeAl_3Zn_x$ phase. The first of these processes will result in a decrease in the amount of liquid zinc residing between the columns of $Fe_2Al_5Zn_x$. Thus, the point H will be displaced toward H'. At the same time, the aluminium concentration in the liquid zinc in the vicinity of the $Fe_2Al_5Zn_x$ growing tips will decrease towards point C'. The second of these processes will result in a decrease in the amount of $FeAl_3Zn_x$ and the subsequently displacement of the point D towards L. At this stage, the microstructure is therefore represented by virtual diffusion path Fe-ILH'C'.

If the aluminium content in the zinc bath is not maintained, further growth of the $Fe_2Al_5Zn_x$ phase would continue until complete consumption of the $FeAl_3Zn_x$ phase. Correspondingly, the diffusion profile would swing towards diffusion path Fe-IFA. At this moment, further columnar growth of the $Fe_2Al_5Zn_x$ phase would receive its aluminium supply from the zinc bath only.

Yamaguchi and Hisamatsu [47] were greatly interested in the work carried out by Úředníček and Kirkaldy [46] and, based on their methodology, proposed a set of diffusion paths whose evolution enables the description of all the successive morphologies observed during galvanization for different aluminium contents in the zinc bath. The diffusion paths proposed by the authors as well as their corresponding microstructures are shown in Figure 125.

As far as concerned in this section, the authors consider that the inhibition layer evolves with reaction time towards its final structure as the result of a local aluminium depletion in the bath consecutive to its nucleation, as reported by Úředníček and Kirkaldy [46].

However, contrary to Úředníček and Kirkaldy [46], Yamaguchi and Hisamatsu [47] found the inhibition layer to be different depending on the aluminium content in GI baths. For GI baths with an aluminium content between 0.15 and 0.30 wt.%, the authors reported the same mechanisms, present phases and final structure as Úředníček and Kirkaldy [46]. For GI baths with an aluminium content lower than 0.15 wt.%, they reported the initial nucleation of $Fe_2Al_5Zn_x$ on the steel surface and the subsequent drop of aluminium at the solid / liquid interface, likely due to the formation of this aluminium-rich interfacial layer. As a result, the aluminium content at the interface cannot be maintained and, consequently, the δ phase nucleates over the $Fe_2Al_5Zn_x$ phase.

Nishimoto *et al.* [48] also reported this last mechanism for the inhibition layer which forms in a zinc bath containing 0.16 wt.% Al. The authors identified “fine granular” crystals, mainly composed of the δ phase, on the Fe-Al interfacial layer and attributed their nucleation to an aluminium depletion in the liquid zinc as well.

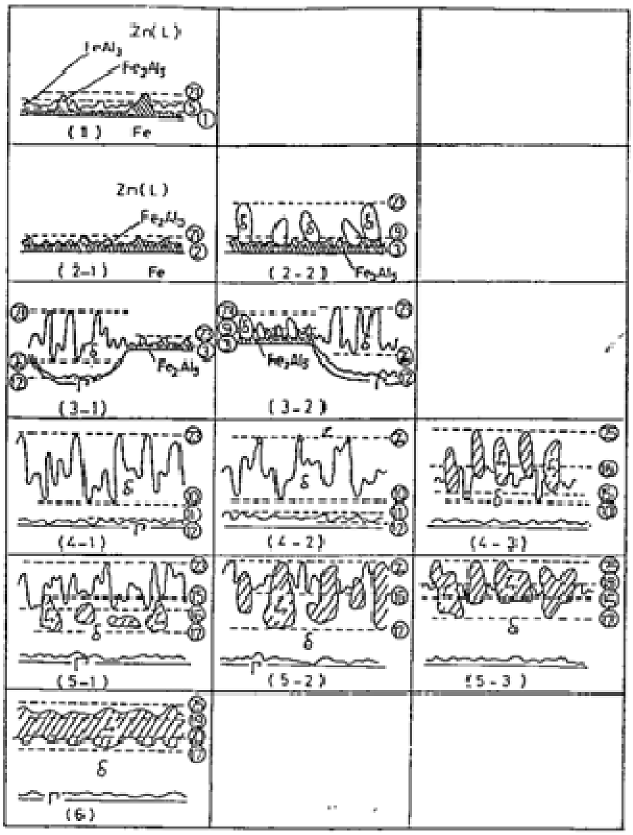

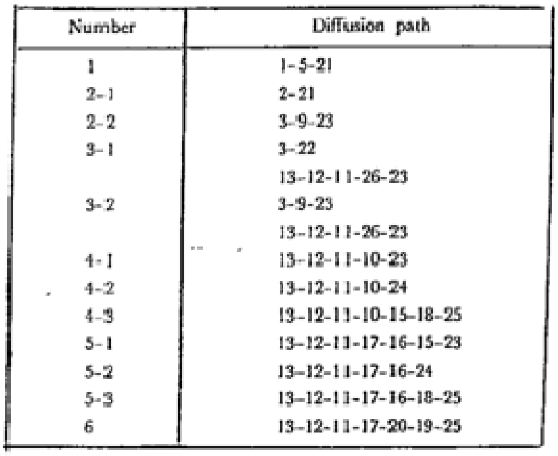

Number	Diffusion path
1	1-5-21
2-1	2-21
2-2	3-9-23
3-1	3-22 13-12-11-26-23
3-2	3-9-23 13-12-11-26-23
4-1	13-12-11-10-23
4-2	13-12-11-10-24
4-3	13-12-11-10-15-18-25
5-1	13-12-11-17-16-15-23
5-2	13-12-11-17-16-24
5-3	13-12-11-17-16-18-25
6	13-12-11-17-20-19-25

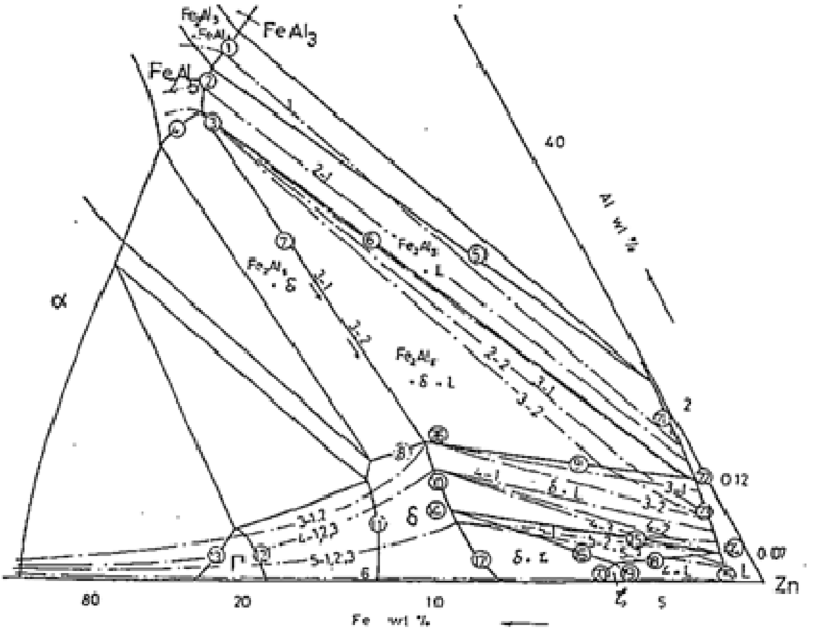

Figure 125: Set of diffusion paths proposed by Yamaguchi and Hisamatsu [47] and their corresponding observed microstructures.

Appendix B: The inhibition layer breakdown in GI baths

As seen in Appendix A (section A.3), Leprêtre *et al*. [27,33] used the concept of diffusion paths in the Al-Fe-Zn ternary phase diagram to explain the mechanism of formation of the inhibition layer in GI baths. These authors have also used this tool to explain their experimental results concerning the inhibition layer breakdown through outburst formation.

According to the phase diagram (Figure 11), the inhibition layer in GI baths is composed of $Fe_2Al_5Zn_x$ phase and the different interfaces (steel / $Fe_2Al_5Zn_x$ / liquid zinc) can be described by diffusion path 4 in Figure 126. The diffusion of zinc through the $Fe_2Al_5Zn_x$ inhibition layer leads to a local enrichment in zinc of the steel / $Fe_2Al_5Zn_x$ interface, at the steel grain boundaries. The representation of this enrichment consists in a displacement towards higher zinc contents (see arrow from point A) of the tie-line corresponding to the equilibrium satisfied at this interface. The zinc concentration at the steel grain boundaries increases progressively and, after a while, it finally reaches the critical content corresponding to the three-phase equilibrium domain involving the δ phase. The diffusion path is then no longer real but virtual (path V4 in Figure 126) and represents the local nucleation of the δ phase at the steel / $Fe_2Al_5Zn_x$ interface, which is consistent with the mechanism proposed by Hisamatsu [25] in the case of a zinc bath containing 0.16 wt.% Al (Figure 26). This process could go ahead until path 5 (superposed layers of Γ, δ and $Fe_2Al_5Zn_x$). However, the authors indicated that the microstructure corresponding to this path is not observable as the volume expansion associated with the local nucleation of δ leads to the immediate detachment of the $Fe_2Al_5Zn_x$ layer and subsequent formation of outbursts, which corresponds to path V6 in Figure 126. A perfect illustration of the microstructure corresponding to this path is given in Figure 127.

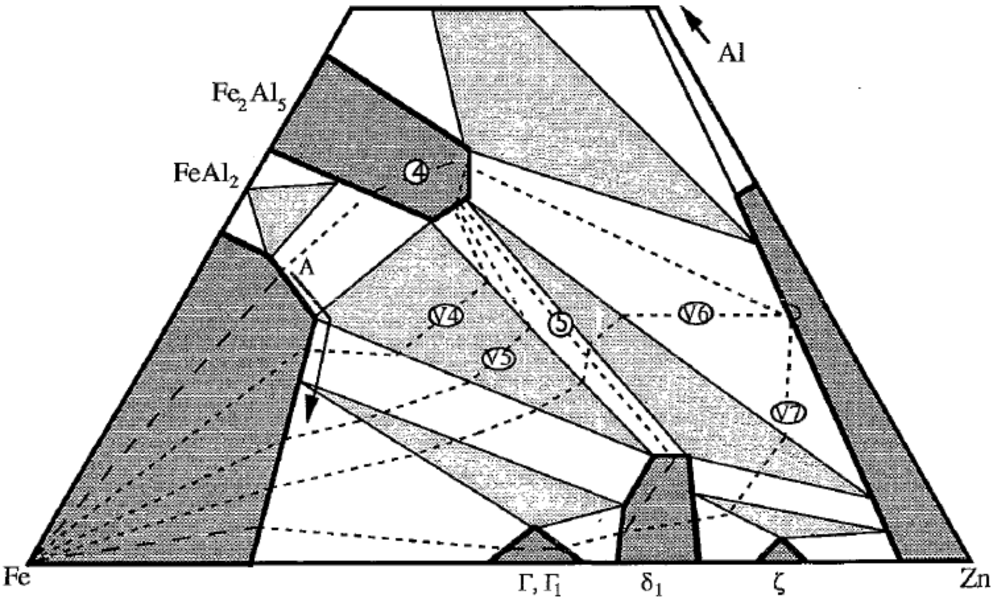

Figure 126: Schematic representation of the isothermal Al-Fe-Zn phase diagram at 450 °C illustrating diffusion paths representing the evolution of the microstructure of coatings in GI baths (Leprêtre [33]).

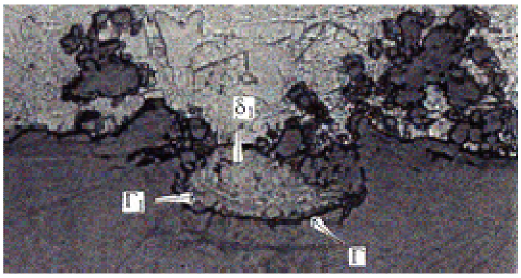

Figure 127: Detailed cross section of an outburst formed in a GI bath (Leprêtre *et al*. [27]).

Jordan and Marder [24] studied the breakdown of the inhibition layer in the case of a zinc bath containing 0.20 wt.% Al. They reported a two-phase layer outburst structure which perfectly corresponds to that of Figure 127. In addition, they indicated that the δ phase forms first at the steel grain boundaries, followed by the nucleation of the Γ phase at the steel / δ interface, which is in total agreement with the mechanism proposed by Leprêtre *et al*. [27,33].

Appendix C: The Fe-Zn alloying reactions

In the following paragraphs, the development of the galvannealed coating from the precise instant when the inhibition layer is broken up by the outburst formation until the final coating microstructure is achieved will be described.

First of all, the mechanisms through which this development occurs will be approached. In this framework, the representation of diffusion paths on the Al-Fe-Zn ternary phase diagram will be used again to explain some of these suggested mechanisms.

Secondly, the kinetics of the Fe-Zn alloying reactions will be discussed through the presentation of different models proposed in the literature. As it will be seen, two different types of models have been identified: kinetic models describing the evolution of iron content in the coating and other models describing the evolution of the phase distribution within the coating.

C.1. Proposed mechanisms for the Fe-Zn alloying reactions

During the development of the galvannealed coating, two stages are clearly differentiated: the growth of Fe-Zn phases until total consumption of the liquid zinc overlay and the subsequent iron enrichment of the solid coating.

C.1.1. Consumption of the liquid phase. Growth of Fe-Zn phases

C.1.1.1. Experiments

It is well known that once the outbursts form, they develop by consuming the liquid zinc, both laterally, joining the adjacent outbursts, and in thickness. However, few authors have proposed logical reaction mechanisms considering this observation.

By their side, Gomi *et al*. [77] performed in-situ time XRD measurements in order to understand the galvannealing phenomena. After determining the diffraction peaks of the ζ, δ and Γ phases, measurements were conducted to study the effect of the aluminium in the coating, the galvannealing temperature and silicon and manganese additions into the base steel on the development of Fe-Zn phases during galvannealing. The authors tested two different aluminium contents in the coating (0.12 and 0.17 g Al/m^2 for 35 g Zn/m^2 in both cases), two different steel substrates (ultra-low carbon steel and 0.2 wt.% Si-1.0 wt.% Mn ultra-low carbon steel) and three different galvannealing temperatures (440, 470 and 500 ℃). However, the authors did not clearly specify in their paper the aluminium content of the zinc bath, so it remains unknown whether it belongs to the GI or GA domain. Nevertheless, interesting conclusions can be drawn from their work.

The XRD measurements obtained by Gomi *et al*. [77] allowed them to propose, for each case, a logical sequence for the galvannealing reaction, as depicted in Figure 128. As it can be seen, once the outbursts formed, they grew laterally until joining all together in all cases. Furthermore, while the ζ phase grew within the outbursts in the case of the 440 (cases c and e) and 470 ℃ (cases a and b) galvannealing temperatures, no presence of this phase was observed in the case of the 500 ℃ (case d) galvannealing temperature.

In addition, the results obtained by the present authors indicated that the ζ phase formed first, followed by the δ phase and finally by the Γ phase. As it has been already reported, the phase nucleating at the steel grain boundaries responsible for the inhibition layer breakdown is the δ phase, in the case of GI baths (Appendix B), or the Γ phase, in the case of GA baths (section I.3.2.1.2.3). According to the authors, it is quite likely that, due to the X-ray penetration factor, other Fe-Zn phase nucleates before the ζ phase but it would be at this point too little to be detected.

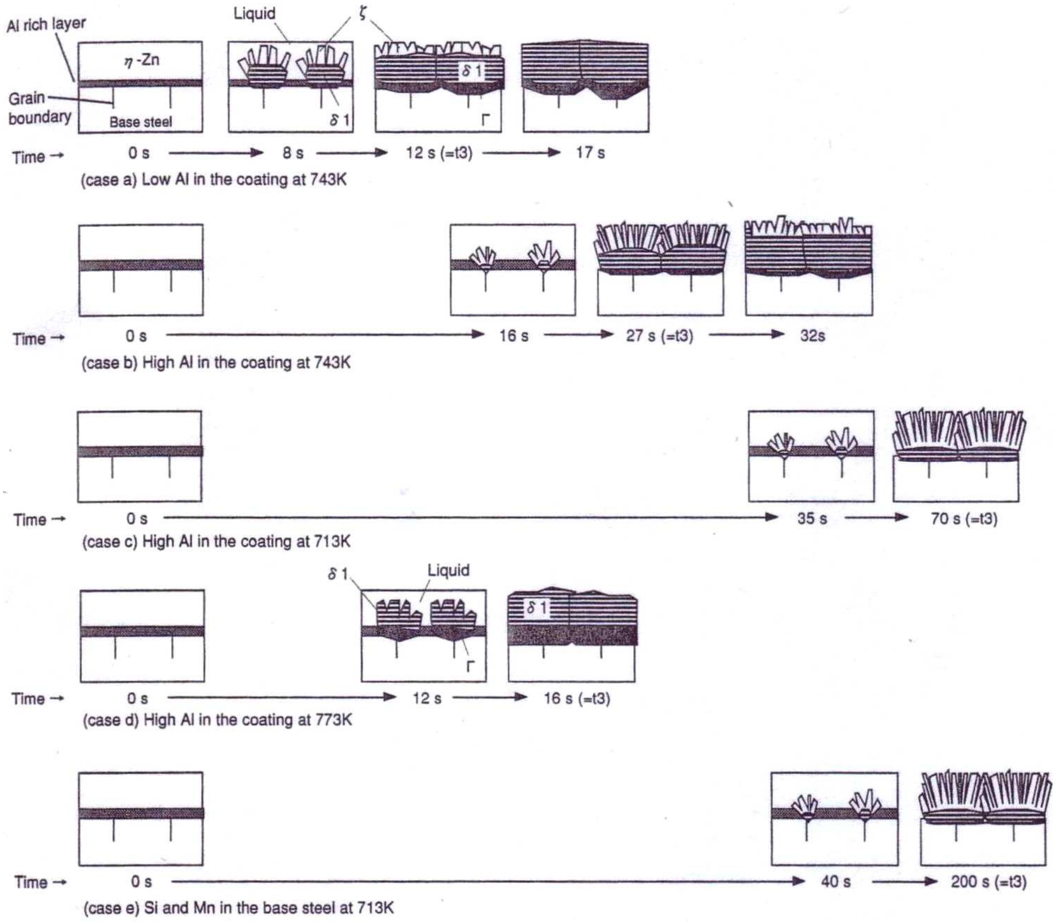

Figure 128: Schematic cross-sectional presentation of the Fe-Zn growth behaviour during galvannealing proposed by Gomi *et al*. [77].

In addition, results from Gomi *et al*. [77] showed that all the Fe-Zn compounds continue to grow until total consumption of the liquid zinc.

In relation with the total consumption of the liquid phase, Mataigne [30] submitted that, as after wiping, limited amount of liquid zinc is available, it may happen that zinc is fully consumed before all the outbursts join together. As a result, small holes in the coating can subsist at grain interior which makes the coating surface roughness increase. According to the author, this is particularly true for reactive steel grades with strong inhibition. Mataigne [30] reported as well that holes in the coating can also be the result of the epitaxial nucleation of ζ crystals on the steel substrate, as can be observed in Figure 129.

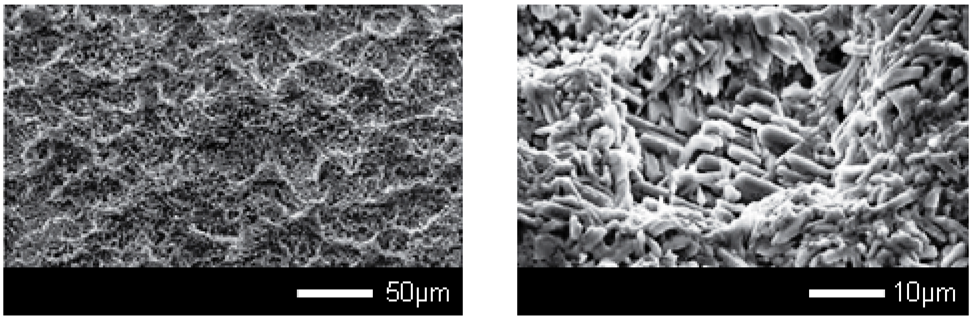

Figure 129: Surface micrographs of a GA coating showing holes with epitaxial ζ crystals at their bottom (Mataigne [30]).

During the Fe-Zn alloying reactions, outbursts do not propagate along those areas where epitaxial ζ crystals are present. As a result, local available liquid zinc is consumed along surrounding areas, where outbursts are growing. Zones with depressed coating weight (holes) are clearly noticeable in the left-hand side micrograph in Figure 129 and the higher magnification of the right-hand side micrograph confirms the presence of unchanged epitaxial ζ crystals at the bottom of the holes. This experimental evidence would definitely rule out the fact that these epitaxial ζ crystals disappear for longer reaction times, as Leprêtre [33] had suggested.

C.1.1.2. Proposed mechanisms

The proposed mechanisms accounting for the growth of Fe-Zn phases until the liquid zinc is fully consumed will be discussed for both GI and GA baths.

Growth of Fe-Zn phases until total consumption of the liquid zinc in GI baths

According to Úředníček and Kirkaldy [46], once the three-phase equilibrium is established between $Fe_2Al_5Zn_x$, δ and liquid zinc, the system will tend to minimize its Gibbs free energy through the following reaction:

$$Zn_{liq} + Fe_2Al_5(Zn) \rightarrow \delta \tag{C.1}$$

This stage is characterized by a very rapid lateral growth of the δ phase, encouraging the peeling of the $Fe_2Al_5Zn_x$ layer, which is ultimately dissolved during upward growth of the δ phase. At the locations where the δ phase is first formed, the nucleation of Γ phase at the steel / δ phase interface follows within a short time (in order to reach the thermodynamic equilibrium at the steel / coating interface, path FeOGN in Figure 124, Appendix A). The authors consider that aluminium depletion at the interface with the liquid zinc allows the thermodynamic equilibrium with the δ phase and, consequently, a diffusion controlled development of the coating. Thus, solid state interdiffusion of iron and zinc induces the displacement of the interfaces until total consumption of the liquid phase. The diffusion of iron from the steel substrate towards the liquid zinc induces the growth of the Γ phase at the expense of the δ phase and the growth of δ phase at the expense of the liquid zinc. On the other hand, the diffusion of zinc from the liquid towards the steel would induce the growth of the δ phase to the detriment of the Γ phase and, possibly, the growth of the Γ phase to the detriment of the steel substrate.

McDevitt and Meshii [28] investigated the Fe-Zn alloying reactions by performing galvannealing treatments at 500 °C and different times on samples galvanized in a zinc bath containing 0.14 wt.% Al at 460 °C. As commented in the previous chapter, the authors have reported that the inhibition layer began to disappear during reheating, probably due to a dissolution process. Concurrently with this phenomenon, the nucleation and growth of the δ phase was observed. However, this growth was not characteristic of an outburst structure. In addition, simultaneously to the growth of the δ phase, the nucleation of the Γ phase at the interface with the steel substrate was also noticed. With continued annealing treatment, both δ and Γ phases grew until total consumption of the liquid zinc. The present authors are quite in agreement with the mechanisms proposed by Úředníček and Kirkaldy [46] for the development of the coating until total consumption of the liquid zinc.

Leprêtre *et al*. [27,33] have also proposed a mechanism based on diffusion paths accounting for the evolution of the coating microstructure after the inhibition layer breakdown. The authors indicated that the δ phase (with the eventual presence of the Γ phase, as supposed in Figure 127) which induces the inhibition layer breakdown in the case of GI baths cannot reach the thermodynamic equilibrium with the liquid phase. Indeed, this phase can only be in equilibrium with a liquid zinc with lower aluminium content and higher iron content. As a result of this non-equilibrium situation, Leprêtre [33] submitted that the contact of the δ phase with the zinc bath, once the inhibition layer is broken up, causes its dissolution. It has been already seen that, at this point, the presence of outbursts is still localized and the microstructure of the coating can be represented by path V6 in Figure 126. As the reaction goes further, outbursts propagate towards the grain interior and the latest inhibited zones disappear. At this point, further development of the coating occurs in a stratified way, as described by path V7 in Figure 126. Nevertheless, the interface with the liquid phase will be non-planar as the dissolution process proceeds, being the $Fe_2Al_5Zn_x$, δ and liquid zinc phases expected to coexist until total consumption of the liquid phase. The system evolves therefore into a stratified structure similar to that observed in the pure zinc baths, with the difference that, the thermodynamic equilibrium with the liquid phase being modified by the presence of aluminium, the final diffusion path is not real but virtual and the structure of the coating in the vicinity with the liquid zinc will be also modified in order to satisfy the different thermodynamic equilibria.

Thus, while Úředníček and Kirkaldy [46] seem to indicate that the development of the coating, from the moment when the inhibition layer has been completely peeled off to the moment when liquid zinc has been fully consumed, is diffusion controlled, Leprêtre *et al*. [27,33] support that it occurs through a dissolution process.

Finally, as depicted in Figure 25, Nishimoto *et al*. [48] have proposed that once the just nucleated δ phase penetrates through the inhibition layer at the steel grain boundaries (stage b), it will then transform into ζ phase at the cooling stage of the strip through the peritectic reaction:

$$Zn_{liq} + \delta \rightarrow \zeta \qquad \text{(C.2)}$$

The ζ phase will rapidly grow in thickness over the steel grain boundaries. The authors indicated that since the reaction rate at grain interior is lower than at the steel grain boundaries, a transition of alloy phases from Fe-Al compounds to Fe-Zn compounds is considered to take place at a later stage of reaction in these locations (stage c). The formation of outburst structures does not occur at the centre of surface grain interior, and only sidewise growth of the ζ phase, consuming the liquid available, is observed at the latest stage (stage d). However, the reaction described by equation (C.2) is not expected to occur only in the cooling stage of the strip, as the authors indicated, but at every moment (heating or cooling) provided that the temperature remains below the peritectic reaction temperature involving the ζ phase (see Figure 16 and comments below in section I.2). In addition, as will be seen below, this reaction of dissolution of the δ phase in the liquid zinc gives as products not only a ζ phase but also a δ phase with different composition. On the other hand, according to Nishimoto *et al*. [48], the Γ phase does not nucleate while liquid zinc is available, contrary to that reported by the previous authors [27,28,33,46].

Growth of Fe-Zn phases until total consumption of the liquid zinc in GA baths

Úředníček and Kirkaldy [46] have reported no substantial difference between the Fe-Zn alloying reaction mechanisms in GI and GA baths.

However, as advanced in section I.3.2.1.2.3, a group of authors [27,30,33] has reported that the Γ phase breaks the inhibition layer off in the case of GA baths. This phase can reach the thermodynamic equilibrium with the steel but not with the liquid zinc. In order to keep the liquid phase at equilibrium, the system requires at least the nucleation of the δ phase (paths V2, V2bis, 3, V3 and V3bis in Figure 28).

According to Mataigne [30], as the Γ phase cannot reach thermodynamic equilibrium with liquid zinc, it gets dissolved and a very intense flux of iron into the liquid is then established. This sudden increase in the iron concentration is consumed by the formation of aluminium-free Fe-Zn compounds in the liquid zinc side. At this stage, two different regimes for outburst development can be differentiated depending on the galvannealing temperature and on the peritectic reaction temperature (according to the author, this temperature would vary with the liquid phase aluminium content).

If the galvannealing temperature is higher than the peritectic reaction temperature, the coating evolves under a solid state diffusion regime. The increase in the iron concentration at the Γ phase / liquid zinc interface due to the dissolution of the Γ phase leads to the nucleation of the δ phase. At this moment, thermodynamic equilibrium is reached along all the interfaces. This implies that further development of the coating is controlled by solid state interdiffusion of iron and zinc. The diffusion path representing this diffusion regime is depicted in detail in Figure 130. Similar diffusion paths corresponding to diffusion regime are observable in Figure 28. While the virtual diffusion path V2 describes the microstructure where the outburst development is not very advanced and a portion of the steel surface is still occupied by the δ phase inhibition layer, the diffusion path 3 represents a microstructure where outbursts have already joined the adjacent outbursts at grain interior and, consequently, the steel / Γ phase and Γ phase / δ phase interfaces have become planar. But, in both cases, the outburst growth occurs through a diffusion regime and is characterized by planar interfaces between the δ phase within the outbursts and the liquid zinc.

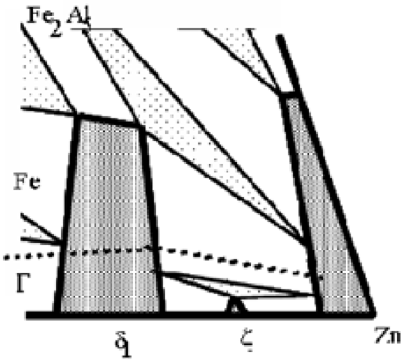

Figure 130: Zinc-rich corner of schematic Al-Fe-Zn phase diagram illustrating the diffusion path representing the outburst / liquid interface in the case of diffusion regime (Mataigne [30]).

On the contrary, if the galvannealing temperature is lower than the peritectic reaction temperature, the coating development evolves under a dissolution regime. As in the previous case, the increase in the iron concentration at the Γ phase / liquid zinc interface due to the dissolution of the Γ phase should lead to the nucleation of the δ phase. However, unlike the previous case, the thermodynamic equilibrium along the δ phase / liquid zinc interface cannot be reached. As indicated by Leprêtre [33], the aluminium content of the δ phase in equilibrium with the Γ phase is too low to allow its thermodynamic equilibrium with the liquid zinc and the ζ phase must also appear. As a result, the δ phase gets dissolved in the liquid, leading to the simultaneous nucleation of a δ phase with higher aluminium content and the ζ phase. The exact composition of each of these phases should in principle be given by the vertices of the triangle corresponding to the three-phase domain in question (δ, ζ and liquid zinc). The diffusion path representing this dissolution regime can be appreciated in detail in Figure 131. However, alternative mechanisms to the one from Leprêtre [33] are envisageable to describe the evolution of the coating towards the microstructure described by path in Figure 131. One can suppose that it is the liquid phase which reaches the thermodynamic equilibrium first and, consequently, that the nucleation of the δ and ζ phases occur without any other dissolution process that the one of the Γ phase.

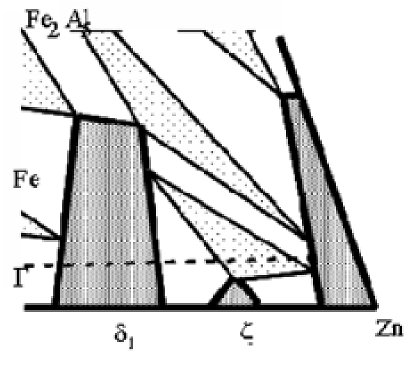

Figure 131: Zinc-rich corner of schematic Al-Fe-Zn phase diagram illustrating the diffusion path representing the outburst / liquid interface in the case of dissolution regime (Mataigne [30]).

Similar diffusion paths corresponding to dissolution regime are also observable in Figure 28. While the virtual diffusion path V2bis describes the microstructure where outburst formation has just occurred and a portion of the steel surface is still occupied by the δ phase inhibition layer, the diffusion path V3 represents a microstructure where outbursts have already met each other at grain interior. But, in both cases, the outbursts growth occurs through a dissolution regime and is characterized by non-planar solid / liquid interfaces. Leprêtre [33] even suggested the possibility of considering a microstructure consisting in a complete ζ phase layer with a planar δ / ζ interface, but at the interface with the liquid, crystals of the δ phase should necessarily be present, as represented by path V3bis in Figure 28. However, the author reported the impossibility to observe such a continuous ζ phase layer.

As can be seen, a dissolution process occurs due to a non-equilibrium situation and gives rise to non-planar interfaces. Consequently, it is always represented by a virtual diffusion path.

It is to highlight that in both diffusion and dissolution regimes, the δ phase nucleating within the outbursts has a lower average aluminium content and higher average iron content than the δ phase which constitutes the inhibition layer. This is easily noticeable by comparing path 2 (corresponding to the inhibition situation) with paths V2, V2bis, 3 and V3 in Figure 28.

On the other hand, in relation with the shift from dissolution regime to diffusion regime, Guttmann [23] has stressed that it takes actually place at a temperature slightly lower than the peritectic reaction temperature and hence that the diffusion reaction occurs in metastable conditions within a narrow range of temperature. So, in order to be rigorous with this contribution, it will be henceforth used “threshold temperature”, and not anymore “peritectic reaction temperature”, to refer to the temperature at which the switch of regime takes place.

Contributions made by Mataigne [30] and Guttmann [23] would be consistent with the results of the experiments performed by Gomi *et al*. [77] that have described in section C.1.1.1. For the 440 and 470 °C galvannealing temperatures, lower than the threshold temperature, the outburst development occurs under a dissolution regime which requires the nucleation of the ζ phase. However, for the 500 °C galvannealing temperature, no dissolution of the δ phase is required and outbursts grow under a solid state diffusion regime.

C.1.2. Iron enrichment of the solid coating. Fe-Zn phase distribution

For both GI and GA baths, once the liquid zinc has been fully consumed, the diffusion path describing the microstructure of the coating is not expected to move anymore and just the displacement of the interfaces, induced by reactive solid state diffusion of iron, is expected to occur.

As will be seen later, Lamberigts *et al*. [82] developed a model accounting for the evolution of Fe-Zn phase distribution within the coating. The authors explained the evolution of all the interfaces on the basis of the iron flux through each of the moving interfaces. Thus, once the liquid zinc is fully consumed, a part of the total iron diffusion flux through the steel / Γ phase interface is consumed by the growth of the Γ phase leading to the displacement of the Γ / δ interface perpendicular to the sense of diffusion and the rest will constitute the iron diffusion flux through this latter interface itself. Finally, this flux is totally consumed by the growth of the δ phase leading to the displacement of the δ / ζ interface.

Thus, the Γ phase will grow to the detriment of the δ phase and the δ phase will grow to the detriment of the ζ phase provided this latter phase had nucleated within the liquid phase during outburst development, fact which occurs when the dissolution regime governs. In the case that ζ rod crystals grow on top of the outbursts (Figure 132 left), further iron enrichment of the coating will induce the transformation of these crystals into δ rod crystals different in morphology (Figure 132 middle) from the δ crystals nucleating within the outbursts (Figure 132 right). This morphological difference has been submitted by Mataigne [30] and is illustrated in Figure 132.

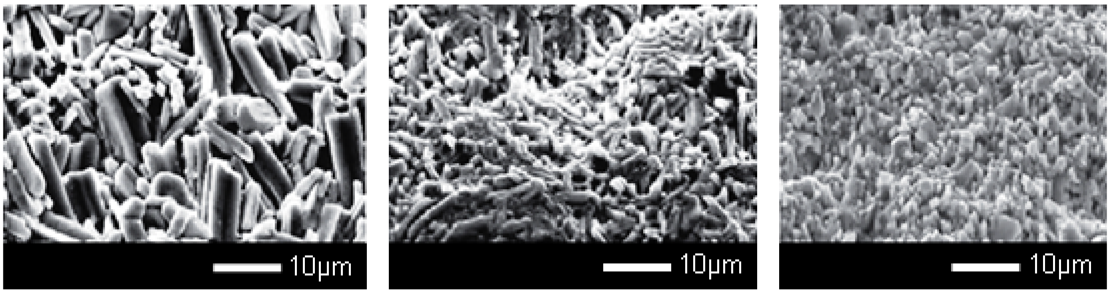

Figure 132: Micrographs showing ζ rod crystals on the left, δ rod crystals on the middle (δ has nucleated within ζ) and isotropic δ crystals on the right (δ has nucleated within the liquid zinc) (Mataigne [30]).

As can be appreciated in Figure 132, while the δ phase nucleated within the ζ phase appears as rod crystals, morphologically similar to ζ crystals, but with lesser sharp edges, the δ crystals nucleating on top of outbursts appear as isotropic small crystals.

Once the ζ phase has completely disappeared, if it existed, further iron enrichment of the coating through solid state diffusion will just make the Γ phase grow at the expense of the δ phase. This behaviour is easily noticeable in Figure 133, which represents the evolution of the δ phase as a function of the iron content in the coating obtained by Vallim Fonseca *et al*. [80] in the case of a Ti IF steel galvanized in a zinc bath containing 0.12 wt.% Al at 470 ℃ and subjected to galvannealing treatments at 470, 520 and 570 ℃ and different tim es. At the beginning, the δ phase grows as the coating gets enriched in iron. However, this tendency is reversed at an iron content in the coating close to 12 wt.%. This is very likely due to the full consumption of the ζ phase. Further iron enrichment of the coating leads to the consumption of the δ phase to the benefit of the Γ phase.

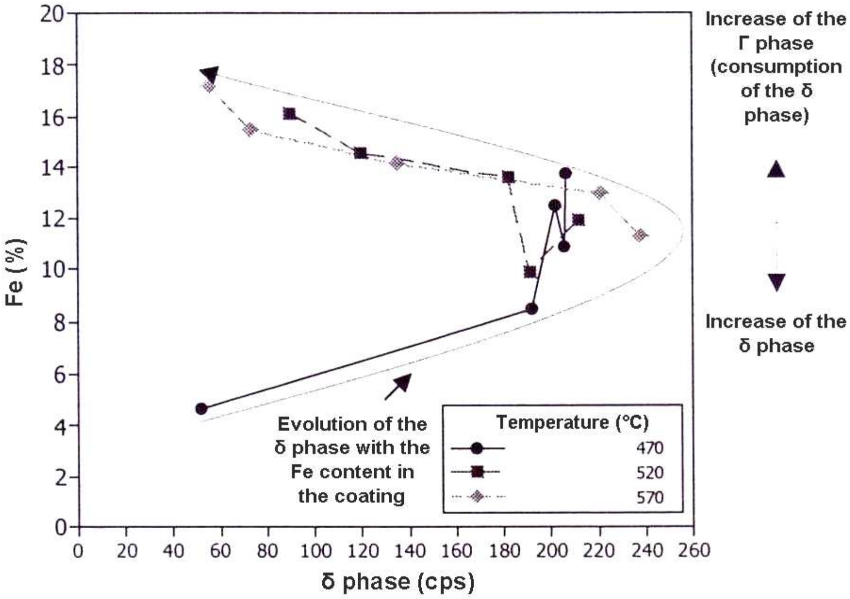

Figure 133: Evolution of the presence of δ phase (counts per second) as a function of the iron content in the coating (Vallim Fonseca *et al*. [80]).

The just explained evolution of interfaces can be appreciated in the schematic representation of the Fe-Zn growth behaviour proposed by Gomi *et al*. [77] (Figure 128). This evolution is also clearly observable in Figure 134, which shows the micrographs obtained by Vallim Fonseca *et al*. [80] for the different galvannealing treatments tested in the framework of the work described above.

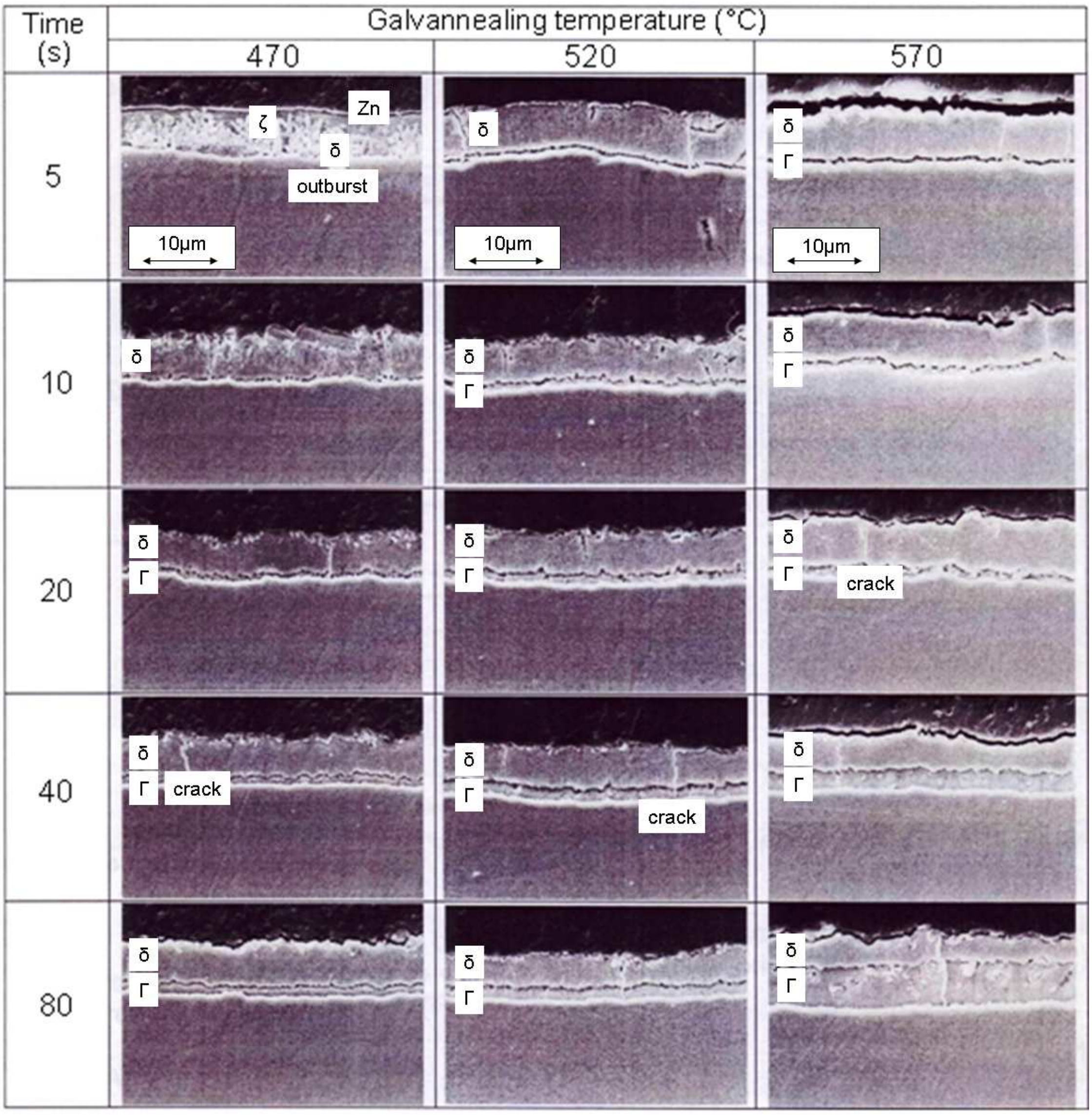

Figure 134: Micrographs showing the evolution of the coating microstructure with time for galvannealing treatments at 470, 520 and 570 ℃ (Vallim Fonseca *et al*. [80]).

As can be seen in Figure 134, for the 470 ℃ galvannealing temperature, after a 5 s-treatment, the liquid zinc has not been consumed yet and outbursts are still under development. The ζ phase is clearly differentiable on top of outbursts as the temperature is low enough to allow the dissolution regime to occur. After a 10 s-treatment, the liquid zinc has been totally consumed. It is not clear in the corresponding micrograph whether the ζ phase has also been fully consumed or residual ζ crystals remain at the extreme surface of the coating. For longer galvannealing times, just the δ and Γ phases exist and the displacement of their common interface towards the free surface of the coating is noticeable. For the 520 and 570 ℃ galvannealing treatments, no remaining liquid zinc is observed even for the 5 s-treatment. In addition, no presence of the ζ phase can be appreciated. Looking at the corresponding micrographs, it is difficult to discern whether the ζ phase has already been consumed or it has never existed. However, due to the high galvannealing temperatures, it is almost sure that liquid zinc consumption has occurred through the diffusion regime and the ζ phase has never existed within the outbursts. For increased galvannealing times, the Γ phase grows to the detriment of the δ phase. For the 80 s-treatment at 570 ℃, more than half the coating is already composed of the Γ phase.

C.2. The Fe-Zn alloying reactions kinetics. Proposed models

C.2.1. General considerations on the kinetic laws

C.2.1.1. Consumption of the liquid phase

Case of GI baths

Concerning the consumption of the liquid phase in the case of GI baths, the kinetics behaviour is not clear as the regime through which it occurs remain quite doubtful. As already commented, Leprêtre [33] reported that liquid zinc gets completely consumed through a dissolution regime, independently of the galvannealing temperature, as indicated by paths V6 and V7 in Figure 126. The kinetics of this stage should therefore be considered linear with time. However, according to Úředníček and Kirkaldy [46], this stage would be diffusion controlled, thus characterized by parabolic kinetics.

Case of GA baths

Regarding to the consumption of the liquid phase in the case of GA baths, the kinetics of this stage will depend on the regime through which it occurs. As advanced by Mataigne [30], when the liquid zinc is consumed through a dissolution process, the kinetics can be considered proportional to time (linear), as governed by atoms exchanges along interfaces. However, when the consumption of the liquid phase proceeds by solid state diffusion, the kinetics becomes proportional to the square root of time (parabolic), so slows down compared to dissolution kinetics. This difference in kinetics is easily noticeable in Figure 135, which illustrates the iron content in the coating as a function of the galvannealing temperature in the case of Ti IF and Nb-Ti IF steel samples galvanized in zinc baths containing 0.135 (black points) and 0.125 wt.% Al (red points) respectively. The galvannealing time is the same for all samples.

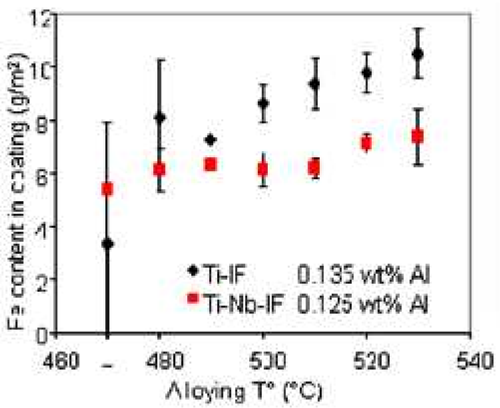

Figure 135: Iron content in the coating against galvannealing temperature (Mataigne [30]).

Taking a look at the values of iron content in the coating presented in Figure 135 and considering typical zinc coating weights around 40-60 g/m^2, one can conclude that in most cases, the stage of consumption of the liquid phase has already taken place and further iron enrichment of the coating has occurred.

As can be observed in Figure 135, in the domain of low galvannealing temperatures, where the dissolution regime governs, the reaction rate is favoured by the increased temperature. However, when the galvannealing temperature reaches the threshold temperature, kinetics is suddenly slowed down because controlled by diffusion. Once in the diffusion regime domain, further increase of the temperature favours as well the reaction rate. So, in the temperature domain of both dissolution and diffusion regimes, the reaction rate is favoured by the increased temperature. However, for the same increment of temperature, kinetics is expected to be more enhanced in the case of the dissolution regime.

From the results presented in Figure 135, Mataigne [30] extracted that this kinetic shift occurs at a different galvannealing temperature for each of the two presented cases. Indeed, the author suggested that the zinc bath aluminium content has an influence on the threshold temperature. According to him, while for the zinc bath containing 0.135 wt.% Al the threshold temperature is around 490 ℃, in the case of the zinc bath containing 0.125 wt.% Al this temperature seems to be somewhere around 500 ℃. However, while this observation is quite clear in the case of the zinc bath containing 0.135 wt.% Al, it is not so clear in the case of the one containing 0.125 wt.% Al. One can suppose that all the red points in Figure 135 belong to the diffusion regime. Under this assumption, the threshold temperature would be in this case lower than supposed by Mataigne [30]. In order to remove all doubt about a possible effect of the bath aluminium content on the threshold temperature, it would be interesting to complete the Figure 135 with new points at lower temperatures and additional bath aluminium contents. In any case, it should be reminded here that, according to the Fe-Zn binary phase diagram from Kubaschewski [22] (Figure 16), the peritectic reaction temperature involving the ζ phase is 530 ℃ and different galvannealing experiments, as the one from Gomi *et al*. [77], have shown that the ζ phase is already unstable at lower temperatures. Guttmann [23] had assumed that the diffusion regime for liquid zinc consumption occurs in metastability in a narrow range of temperature below the peritectic reaction temperature. It is likely that the previous author has based on the peritectic reaction temperature involving the ζ phase in the Fe-Zn binary system to report this metastability and has not taken into account a possible effect of the aluminium content when considering the Al-Fe-Zn ternary system.

It is also to highlight in Figure 135 that, for a given galvannealing temperature, the iron content in the coating is generally lower in the case of the Ti-Nb IF steel substrate galvanized in the zinc bath containing 0.125 wt.% Al. This is not in principle related to a difference in the liquid zinc consumption kinetics but to a difference in the inhibition layer breakdown kinetics. It has been seen in section I.3.2.2.2.2 that Ti IF steels are more reactive, with respect to the inhibition rupture, than Ti-Nb IF steels. On the other hand, as commented in section I.3.2.2.1.1, the higher the zinc bath aluminium content is, the slower the inhibition layer breakdown kinetics is. It can be therefore concluded that, at least in the present case, the effect of the steel chemical composition overtakes the effect of the bath aluminium content.

In any case, this shift in the kinetic behaviour can have an important impact in industry. In industrial HDGA lines, the reaction time is fixed by the line speed and the galvannealing tower dimensions. Very little variations of the alloying temperature can be responsible of under-alloyed or over-alloyed products. Thus, a precise control of the alloying temperature is highly needed in order to prevent modifications in the degree of alloying in the coating.

C.2.1.2. Iron enrichment of the solid coating

As stated above for both GI and GA baths, once the liquid zinc has been fully consumed, further development of the coating occurs through solid state diffusion of iron. This stage is so characterized by parabolic kinetics.

C.2.1.3. Recapitulation

To sum up, the Fe-Zn alloying kinetics are globally favoured by temperature, but a backward leap can eventually be observed at a given temperature in the case of GA baths (Figure 135), corresponding to the switch of regime governing the consumption of the liquid zinc.

In spite of this difference in kinetics depending on the reaction through which the coating develops, most of the few models found in the literature have been developed in a global manner, without differentiating the possible regimes discussed above.

As already advanced, two different types of kinetic models have been identified. Both of them will be discussed here below. First, kinetic models describing the evolution of the iron content in the coating will be presented, followed by the models which describe the evolution of the Fe-Zn phase distribution within the coating.

C.2.2. Evolution of the iron content in the coating

Claus *et al*. [79] and Vallim Fonseca *et al*. [80] have each of them developed a kinetic model aiming to describe the evolution of the iron content within the coating.

By their side, Claus *et al*. [79] performed thirty different galvannealing treatments on Ti IF steel samples, galvanized in a zinc bath containing 0.18 wt.% Al (GI bath) by combining six different galvannealing temperatures (430, 450, 470, 490, 510 and 530 ℃) and five different times (5, 10, 15, 20 and 30 s). After determining the iron content in the coating for each sample, these measurements were fitted to mathematical equations using multiple regression analysis. The basic equation chosen by the authors for the fit was an Arrhenius-type equation for kinetic processes with activation control:

$$Z = A\,t^{n} \exp\left(-B/T\right) \tag{C.3}$$

where Z (wt.%) is a quantitative parameter, A, B and n the regression parameters, T (K) the galvannealing temperature and t (s) the galvannealing time.

As can be seen in equation (C.4), the iron content in the coating is directly related to the galvannealing temperature and time by the Arrhenius equation. After regression, the authors found the following relation between the galvannealing parameters and the iron weight fraction w_{Fe} in the coating:

$$w_{Fe}\ (wt.\%) = 5790\,.\,t^{0.28}\,.\exp\left(-6015/T\right) \tag{C.4}$$

Equation (C.4) is illustrated, together with the experimental results, in Figure 136. The exponent of this equation is equal to 0.28 and this value is close to half the value for a diffusion controlled process for which n is equal to 0.5. According to the authors, this fact shows that galvannealing is rather a diffusion reaction process. However, as has been stated before, the present authors have modelled in a global manner a process which passes through different phenomena: solid state diffusion of zinc until the inhibition layer breakdown (time for inhibition rupture can be assumed as a delaying time with regard to the evolution of the iron content in the coating), the consumption of the liquid zinc and further iron enrichment of the coating through solid state diffusion (considering the values of iron content in the coating depicted in Figure 136 and taking into account that the zinc coating weight for all the galvanized samples varied between 45 and 50 g/m^2, it can be accepted that this stage has already started in most of the cases). It would be more suitable to model each of these stages separately instead of determining just a set of regression parameters A, B and n, which, strictly speaking, lacks of physical sense.

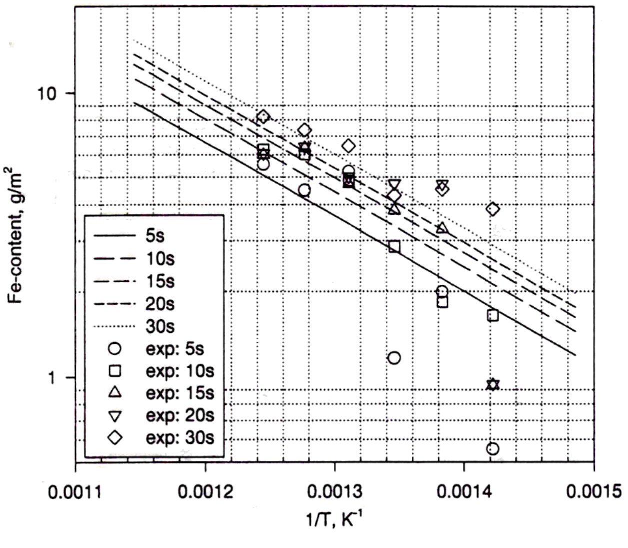

Figure 136: Iron content in the galvannealed coating for a Ti IF steel according to an Arrhenius-type equation, as a function of galvannealing time and temperature (Claus *et al*. [79]).

Vallim Fonseca *et al*. [80] also performed different isothermal galvannealing cycles in a pilot simulator in order to study the effect of time and temperature on the Fe-Zn alloying kinetics. Different temperatures (470, 520 and 570 °C) and times (5, 10 , 20, 40 and 80 s) were tested by the authors on Ti IF steel samples, galvanized in a zinc bath containing 0.12 wt.% Al at 470 °C (GA bath). The authors measured the iron content in the coating for each galvannealing treatment and modelled the evolution of this parameter by using two different mathematical equations: the same Arrhenius-type equation as used by Claus *et al*. [79] (equation (C.3)) and the Rios equation.

This latter equation, typical of irreversible first-order kinetics, can be written as follows:

$$W = W_0 + (W_S - W_0)(1 - \exp(-k\,t)) \tag{C.5}$$

where W (wt.%) is the instantaneous iron content in the coating, W_0 (wt.%) the initial iron content in the coating, W_S (wt.%) the iron content in the coating at saturation, t (s) the galvannealing time and k (s^{-1}) the kinetic constant, which is a function of temperature. As in the Arrhenius equation, the iron content in the coating described by the Rios equation is related to temperature and time.

Experimental results obtained by the authors, compared to both of the above equations with fitted parameters, are shown in Figure 137. As can be seen, the iron enrichment rate increased rapidly at the beginning of the galvannealing treatments, after which this rate began to decrease.

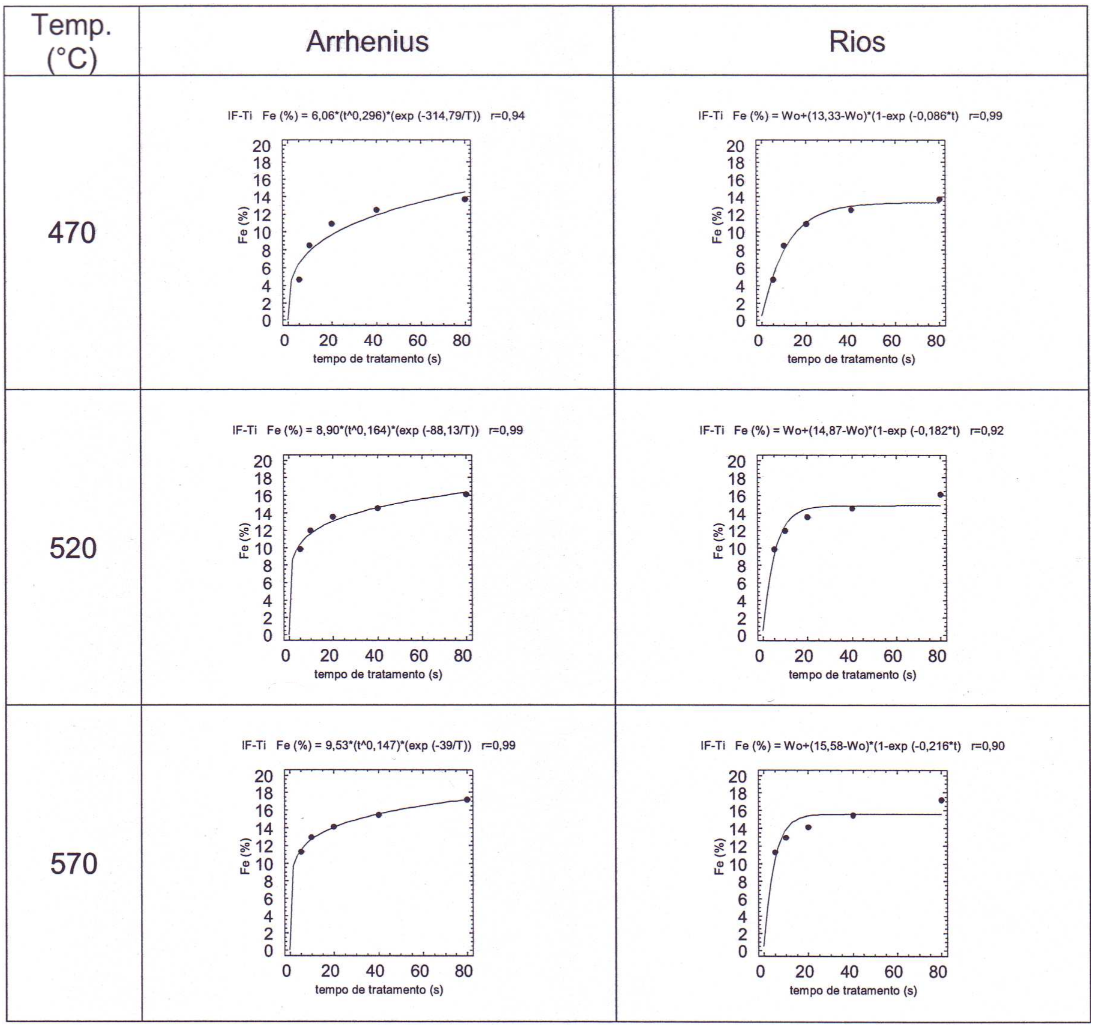

Figure 137: Galvannealing kinetics for a Ti IF steel according to an Arrhenius type equation (left) and Rios equation (right) (Vallim Fonseca *et al*. [80]).

According to Figure 137, the Arrhenius equation represents very well the experimental results for the 520 and 570 ℃ galvannealing temperatures. Experimental results for the 470 ℃ galvannealing temperature are better represented by the Rios equation.

As Claus *et al*. [79] have done, the present authors have modelled the galvannealing process globally, as if just one phenomenon occurred. Thus, for each temperature, they proposed a unique set of parameters for the whole process, which is not physically consistent. In addition, for both equations, the values of these global parameters change with each of the three tested temperatures. While in the case of the Rios equation, the fitted parameters W_S and k are expected to vary with temperature, no reason exists to think that the parameters in the Arrhenius equation vary with temperature. Parameters A and B in this equation are included in the kinetic constant, whose variation with temperature is already taken into account (see equation (C.3)). Parameter n is neither expected to vary with temperature. Therefore, in the case of the Arrhenius equation, it would have been better to use for the fit the experimental results all together, independently of temperature, as Claus *et al*. [79] have done. On the other hand, the fact that the authors have obtained a different set of Arrhenius parameters for each of the galvannealing temperatures would confirm that the galvannealing process passes through different phenomena and that the relative weight of each phenomenon on the global kinetics of the process varies with temperature and time.

C.2.3. Evolution of the Fe-Zn phase distribution in the coating

Jordan and Marder [81] and Lamberigts *et al*. [82] have both developed kinetic models aiming to describe the evolution of the Fe-Zn phase distribution within the coating.

Jordan and Marder [81] performed hot-dip galvanizing laboratory trials on IF steel samples in a zinc bath containing 0.20 wt.% Al at 450 ℃ (GI bath) for different immersion times (5, 30, 60, 120 and 300 s). Based on cross section micrographs, as the one shown in Figure 138, the authors determined the evolution with time of the thickness of each of the Fe-Zn phases.

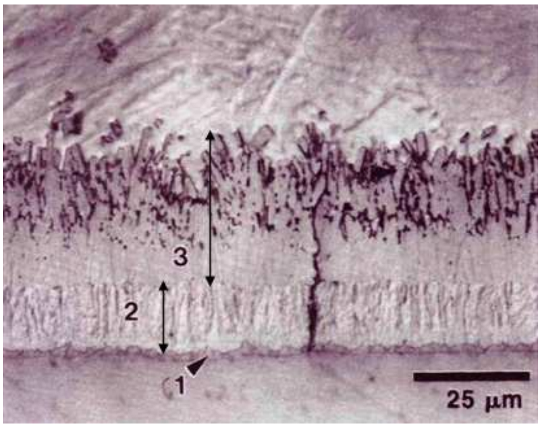

Figure 138: Cross section micrograph showing Fe-Zn phases formed during hot-dip galvanizing: Γ phase (1), δ phase (2) and ζ phase (3) layers with the zinc overlay (Jordan and Marder [81]).

The experimental results obtained were then fitted to the following simple power law equation:

$$Y = k\, t^{n} \tag{C.6}$$

where Y (µm) is the thickness of the phase layer under analysis, t (s) the reaction time and n a time constant for individual Γ, δ and ζ phase layers which constitute the total alloy layer.

The growth data for the Γ, δ and ζ phase layers, precisely measured on the micrographs depicted in Figure 139, are represented in Figure 140, together with the results of the linear regression analysis performed on these data.

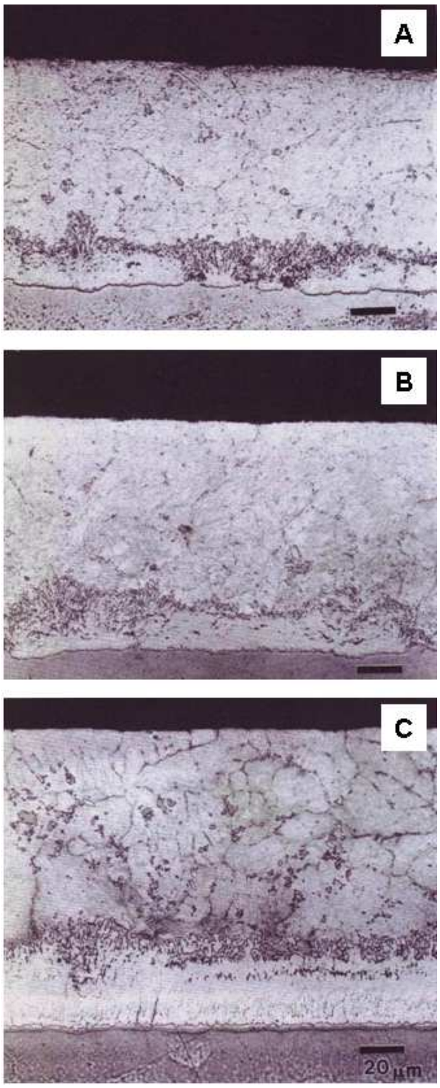

Figure 139: Cross section micrographs representing the Fe-Zn alloy layer development during hot-dip galvanizing in a zinc bath containing 0.20 wt.% Al at 450 °C for different immersion times: 60 (A), 120 (B) and 300 s (C) (Jordan and Marder [81]).

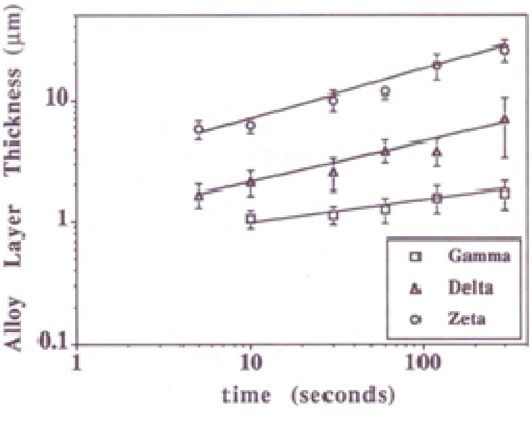

Figure 140: Evolution of individual layer thickness with time during hot-dip galvanizing in a zinc bath containing 0.20 wt.% Al at 450 °C (Jordan and Marder [81]).

The time constant values (n) determined by the authors for the layers of Γ, δ and ζ phase were found to be 0.16, 0.32 and 0.39, respectively. These values are lower than the time constant value of 0.5, typical of a growth controlled by solid state diffusion.

However, as stated for the previous models, different phenomena are taken into account in these time constants. Thus, at least both the inhibition layer breakdown, considered as a delaying phenomenon with regard to Fe-Zn phase development, and the continued consumption of the liquid zinc are included in these global parameters. In addition, as no wiping was used, liquid zinc remained unlimited and it is very likely that, subsequently to the dissolution process, further Fe-Zn growth may have occurred through solid state diffusion of iron from the steel substrate towards the liquid zinc. The above parameters would also include this phenomenon. The joint consideration of all these phenomena gives rise to the above values of time constants.

Lamberigts *et al*. [82] developed a model accounting for the evolution of all common interfaces of the Fe-Zn compounds, in the basis of the normal flux of iron through each of the moving interfaces. This model was developed from the results obtained with galvanizing laboratory trials on Ti-Nb IF steel samples in a zinc bath containing 0.13 wt.% Al (GA bath) and subsequent galvannealing treatments. The progress of the Fe-Zn alloying reactions was monitored in-situ by Hot X-Ray Diffraction (HXRD) when galvanized specimens were reheated to the galvannealing temperature by Joule effect inside the diffractometer. Diffraction spectra were recorded every 5 s. According to the authors, over the galvannealing temperature range considered in these trials (400-650 ℃), the isochronous curves of the Fe-Zn phase distribution showed:

a. the progressive disappearance of the ζ phase,
b. the fast growth of the δ phase to its maximum volume fraction at around 500 ℃, and its subsequent decrease, once step c begins.
c. the rapid growth of the Γ phase, initiated from the ζ phase disappearance temperature (530 ℃).

The authors considered that the Fe-Zn alloying reactions can be fully explained by the reactive diffusion of iron from the steel substrate into the coating. The created phases are supposed to grow into the liquid zinc at distinct rates as perfectly stratified Γ, δ and ζ layers in an orderly way. They supposed as well that the transformation proceeds exclusively by interface chemical exchanges, with no limiting effect from solid state diffusion of iron inside the various phases. Their model aims to account for the experimentally observed alloying behaviours, based on two successive steps: the concurrent stratified growth of the Γ, δ and ζ phases (a) and the consumption of the ζ phase to the benefit of the δ phase once the liquid zinc has disappeared (b). In addition, for those treatments carried out at high galvannealing temperatures, solid state diffusion of iron may further proceed, once the δ phase has reached the free surface, leading to dramatic growth of the Γ phase (c). However, as commented for the previous models, this model does not take into account other phenomena which experimentally occur. Particularly in this case, the inhibition layer breakdown and the outburst development until the coating acquires a stratified structure are not considered.

As closure of this section, it can be summarized that the precise reaction mechanisms accounting for the Fe-Zn alloying reactions, especially in regard to the consumption of the liquid phase, still remain quite unknown. Further investigation for a better understanding of the involved phenomena is highly required. In addition, it would be more interesting to model the kinetics of each of these phenomena separately, and not globally as done in the models presented above, in order to obtain characteristic parameters with a strict physical sense which can be perfectly extrapolated to other galvannealing conditions.

Appendix D: Representation of microstructures by means of the concept of diffusion paths in the ternary phase diagram

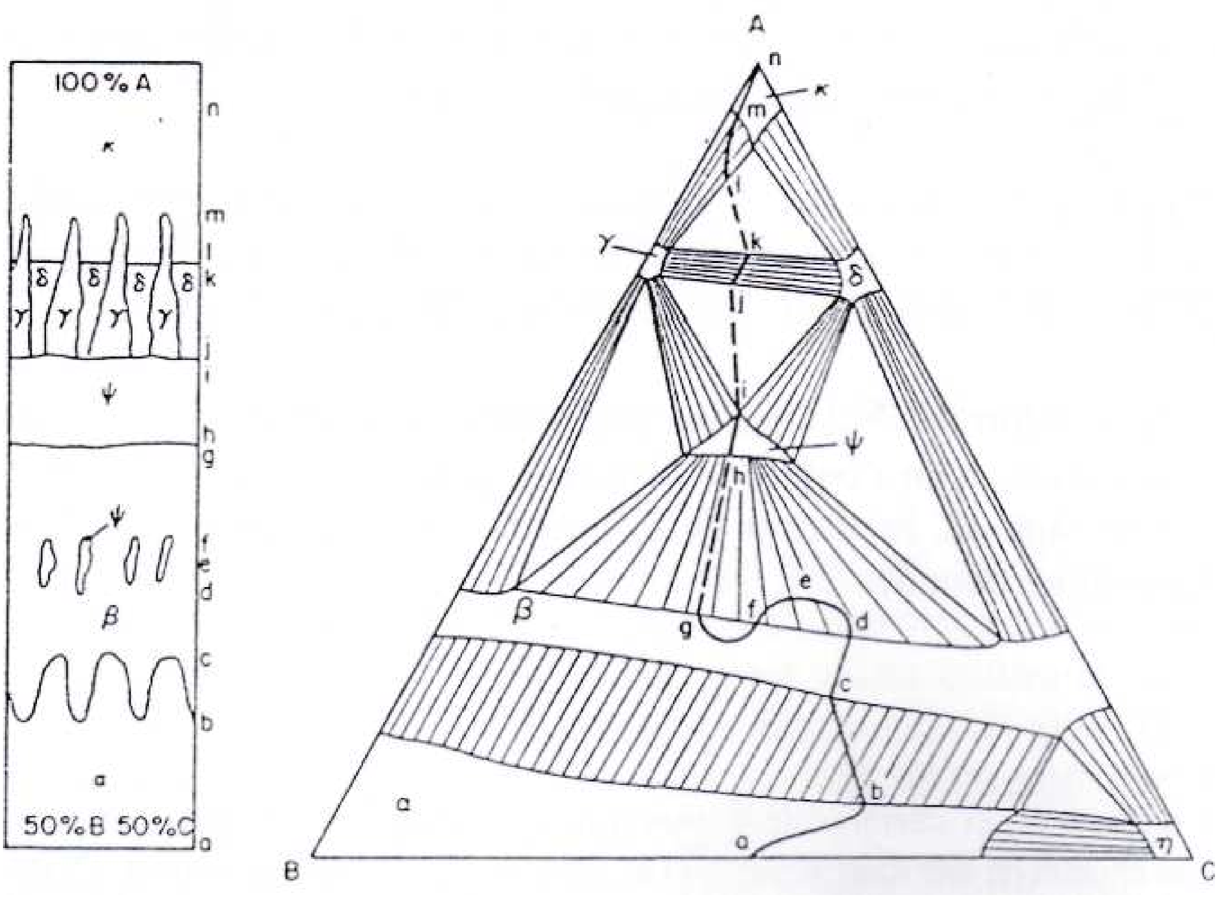

Figure 141: Schematic ternary phase diagram illustrating the representation of different kinds of microstructures by means of diffusion paths (Clark [67]).

Appendix E: FIB device operation for the preparation of thin foils

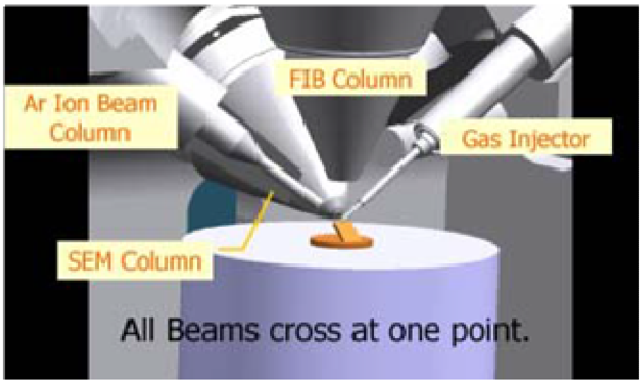

Figure 142: Schematic representation of the FIB device.

As can be seen in Figure 142, the system is composed of a SEM column, a gas injection column for carbon or platinum deposition, the so-called FIB column for gallium ion beam milling and an argon ion beam column for the final thinning and cleaning of the sample. It is also equipped with an EDS detector for chemical analysis. The preparation of the thin foils is detailed here below in Figure 143.

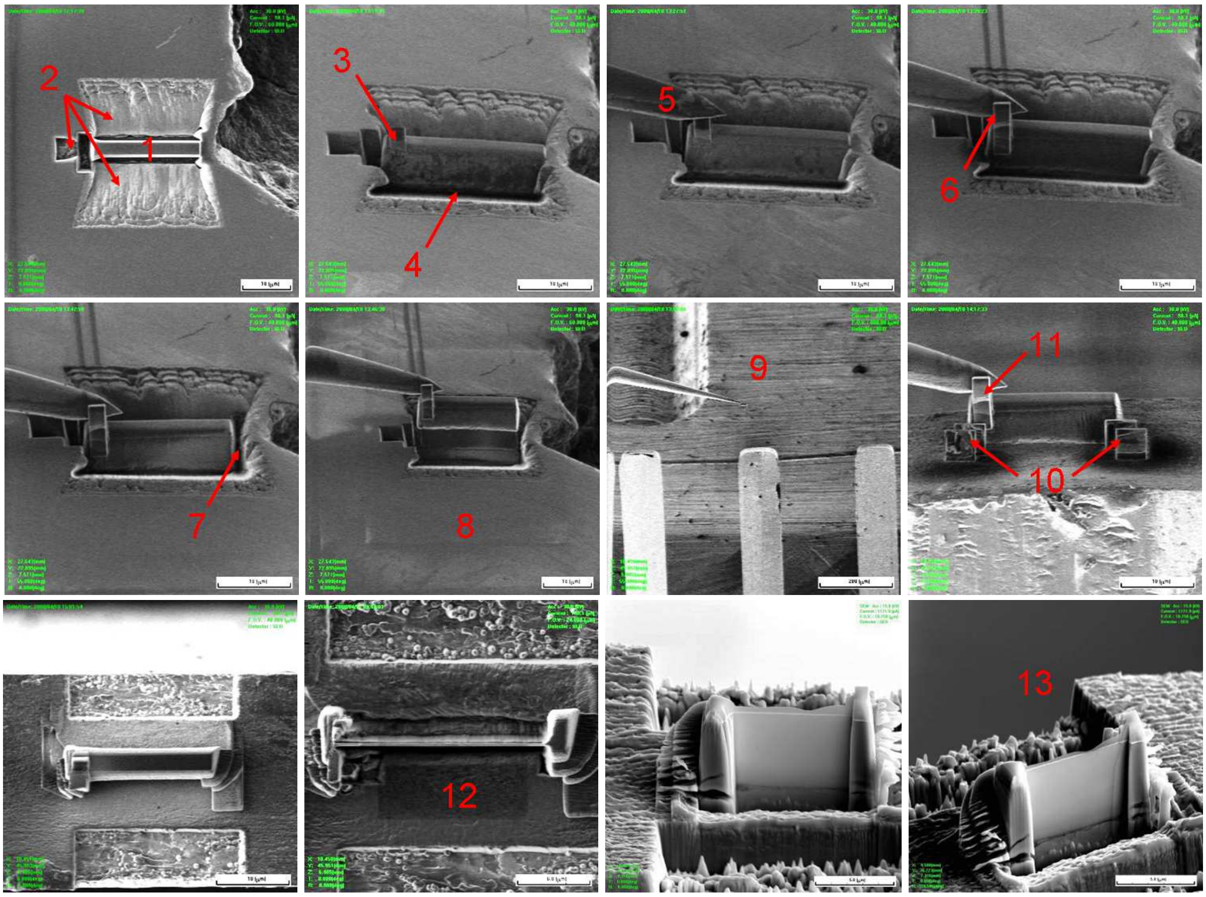

Figure 143: Different steps during the preparation of FIB thin foils.
1, deposition of carbon or platinum on the defined location; 2, milling with gallium ion beam; 3, deposition of a carbon chimney; 4, bottom cut; 5, needle approach; 6, carbon-welding of the needle to the sample; 7, side cut; 8, sample pick-up; 9, deposition of the sample on a comb-shaped copper grid; 10, carbon-welding of the sample to the copper grid; 11, separation of the sample from the needle; 12, thinning of the sample with gallium ion beam, 13, final thinning and cleaning of the sample with argon ion beam.

Appendix F: Additionnal experiments performed to improve the surface state of the $Fe_2Al_5Zn_x$ layer

As shown in section II.2.3.3.3, the surface characterization of the $Fe_2Al_5Zn_x$ layer was performed on samples electrochemically dissolved at -680 mV/SCE. Additional experiments have been carried out in order to improve the surface quality of this layer: electrochemical dissolutions at -630 mV/SCE and immersion into fuming HNO_3.

The first option did not lead to better results. As it can be seen in Figure 144, the surface state of $Fe_2Al_5Zn_x$ after electrochemical dissolutions at -630 mV/SCE is not substantially different from those corresponding to -680 mV/SCE (Figure 59).

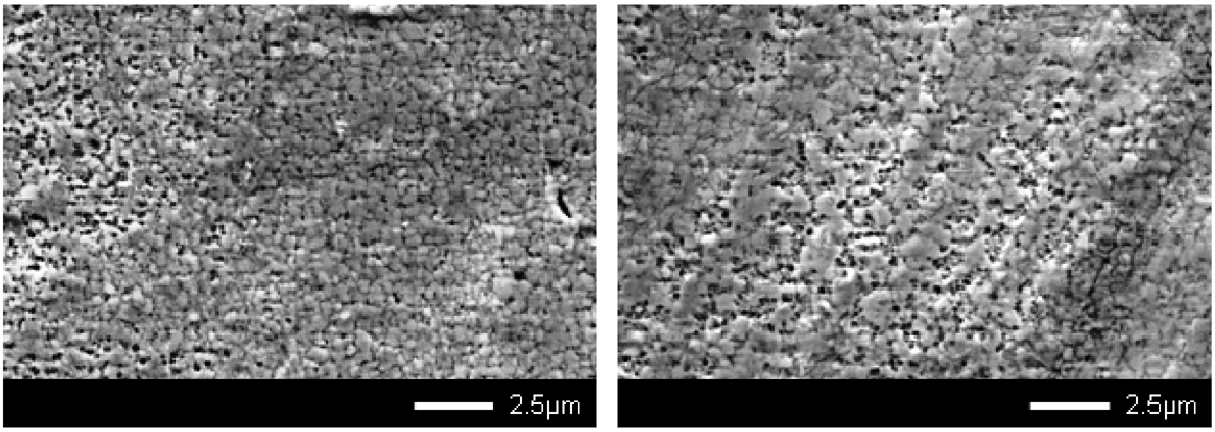

Figure 144: Surface SEM micrographs of the inhibition layer of steels A (left) and B (right) after electrochemical dissolution at -630 mV/SCE.

As for the second option, samples of steels A and B were immersed into fuming HNO_3 (100% purity, MERCK) for 15 min. This treatment is supposed to allow the removal of zinc and Fe-Zn phases while conserving the $Fe_2Al_5Zn_x$ phase at the steel surface. As an example, the result of this treatment on a reference GI steel is shown in the right-hand side micrograph of Figure 145. This micrograph can be compared to the left-hand side micrograph of Figure 145, corresponding to the sample surface state after eclectrochemical dissolution at -680 mV/SCE. As it can be observed, the zinc coating has been fully removed by means of the two types of sample preparation (in the reference GI steel no δ layer is expected to grow on the $Fe_2Al_5Zn_x$ layer) and well defined crystals of the $Fe_2Al_5Zn_x$ intermetallic layer are present at the sample surface in both cases. It is also to note that some oxidation of the sample surface has occurred in both cases, especially when using fuming HNO_3.

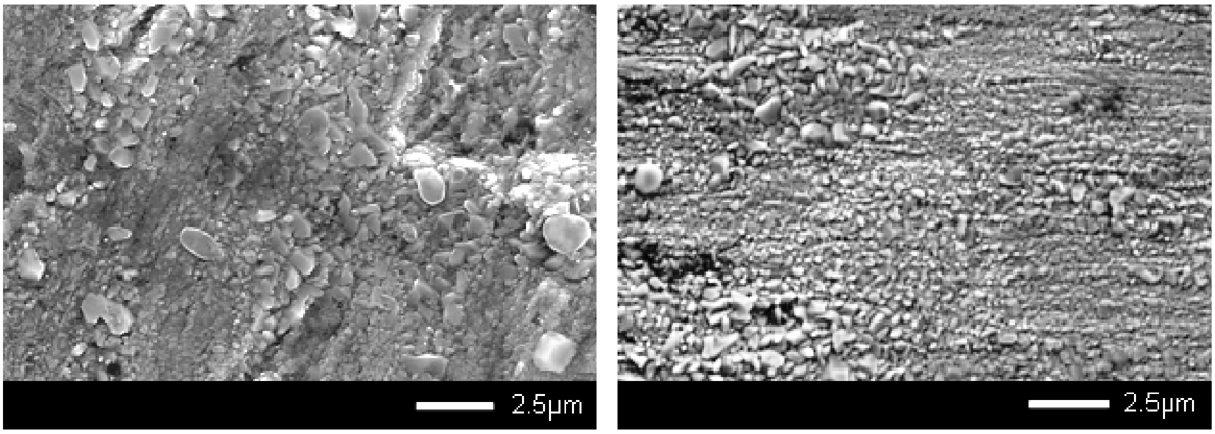

Figure 145: Surface SEM micrographs of the $Fe_2Al_5Zn_x$ phase layer of the inhibition layer of a reference GI steel after electrochemical dissolution at -680 mV/SCE (left) and after immersion in fuming HNO_3 for 15 min (right).

The same 15 min-treatment in fuming HNO_3 was then performed on steels A and B. As can be observed in Figure 146, the surface state of the samples after acid attack is not substantially different from those after electrochemical dissolution at -680 (Figure 59) and -630 mV/SCE (Figure 144).

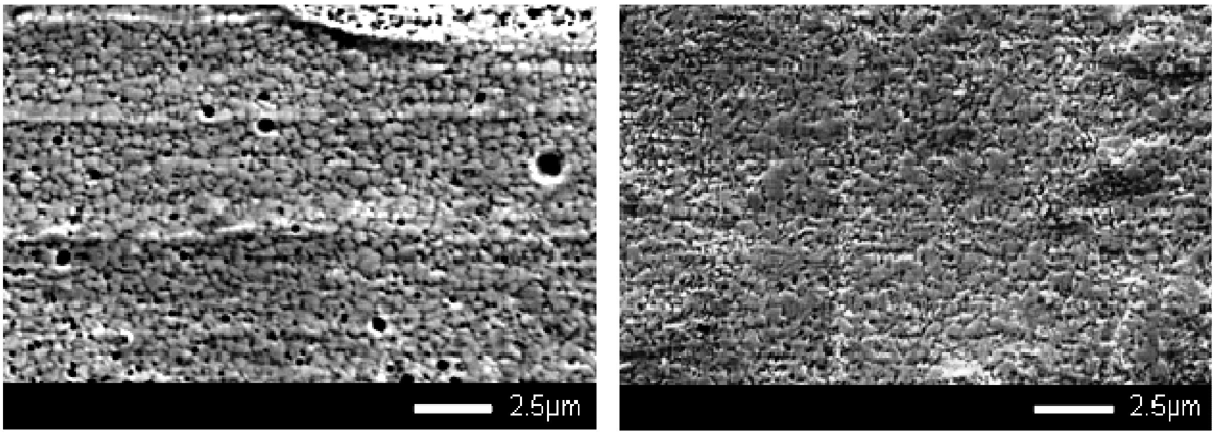

Figure 146: Surface SEM micrographs of the inhibition layer of steels A (left) and B (right) after immersion in fuming HNO_3 for 15 min.

Appendix G: Results of all the Gleeble 3500 trials through which the inhibition layer breakdown kinetics has been determined

The results obtained in the case of the steel substrates galvanized during the first Rhesca trials campaign (0.128 wt.% Al) are presented here below in Figure 147.

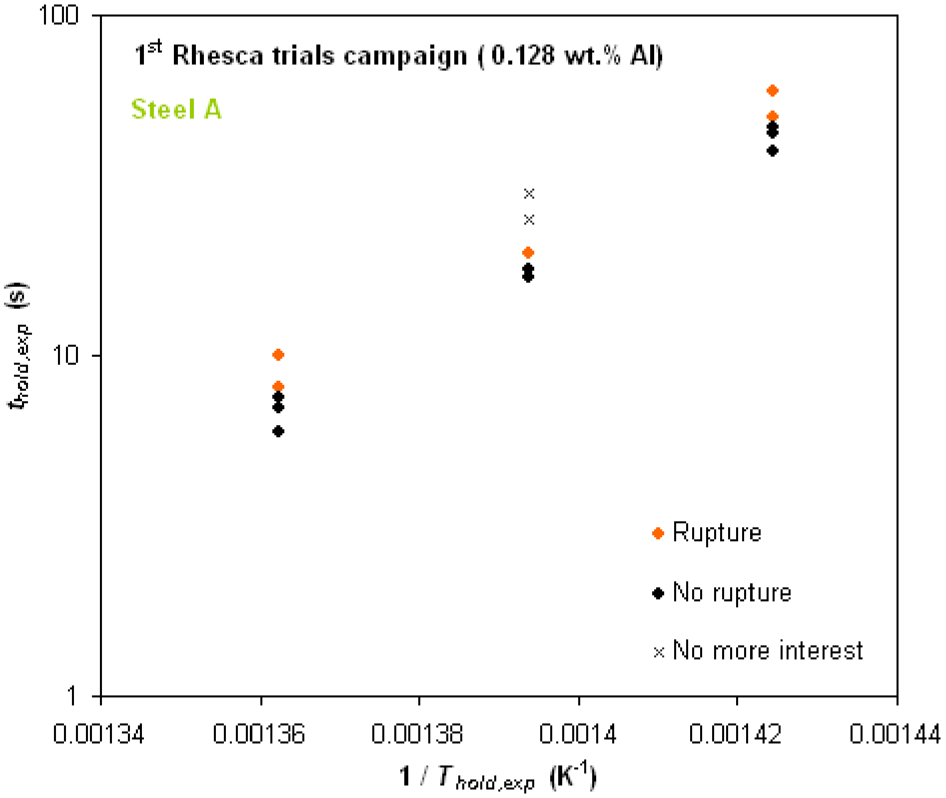

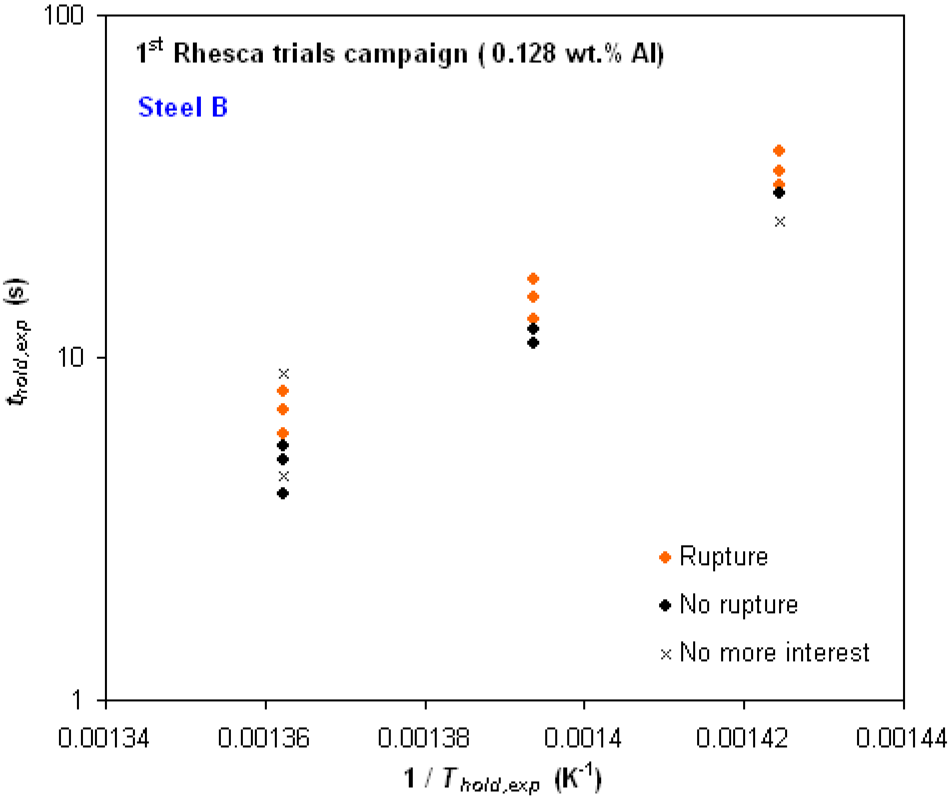

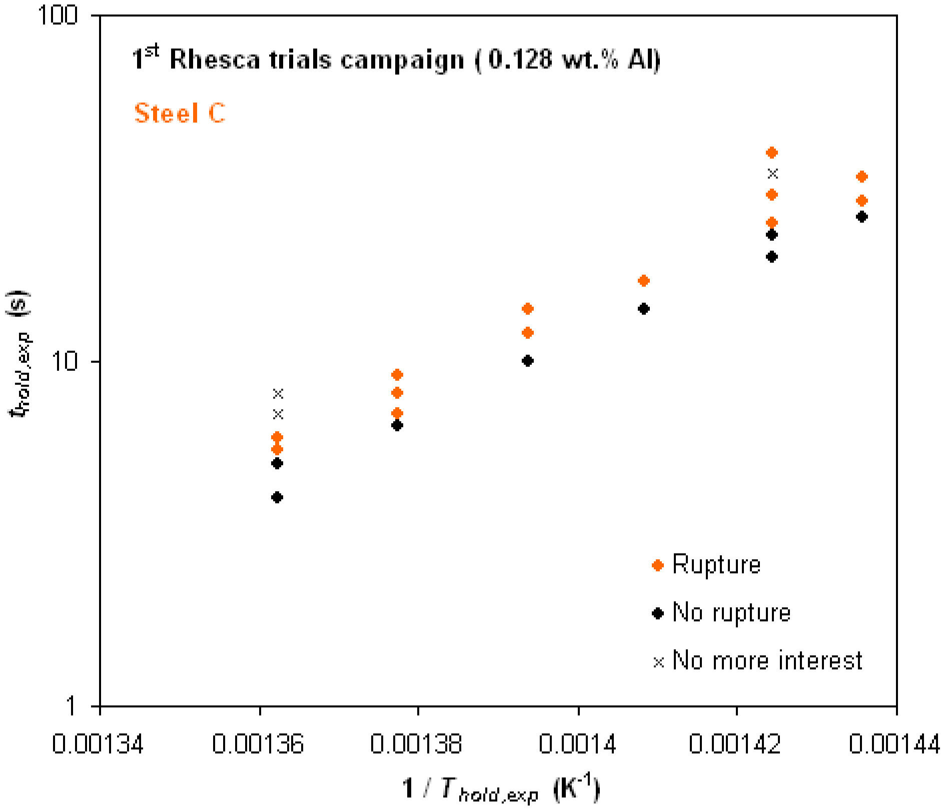

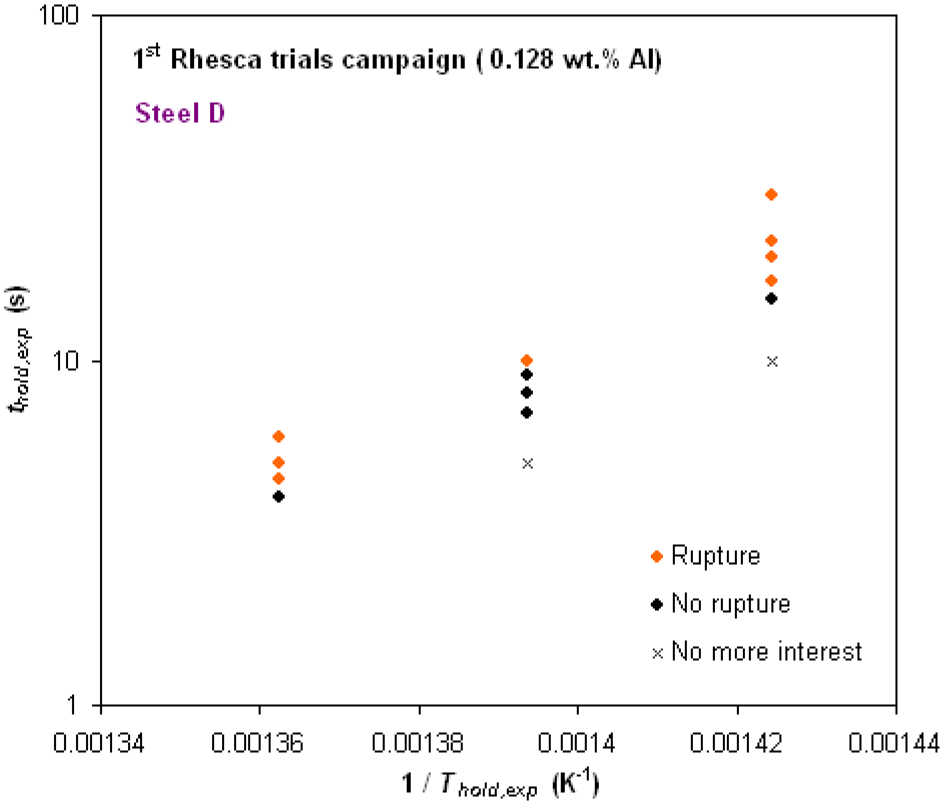

Figure 147: Experimental holding times (logarithmic scale) against inverse experimental holding temperature performed in the Gleeble 3500 pilot simulator to determine the inhibition layer breakdown kinetics (steels A to D, first Rhesca trials campaign).

Analogously, the results obtained in the case of the steels A and D galvanized during the second Rhesca trials campaign (0.112 wt.% Al) are available below in Figure 148.

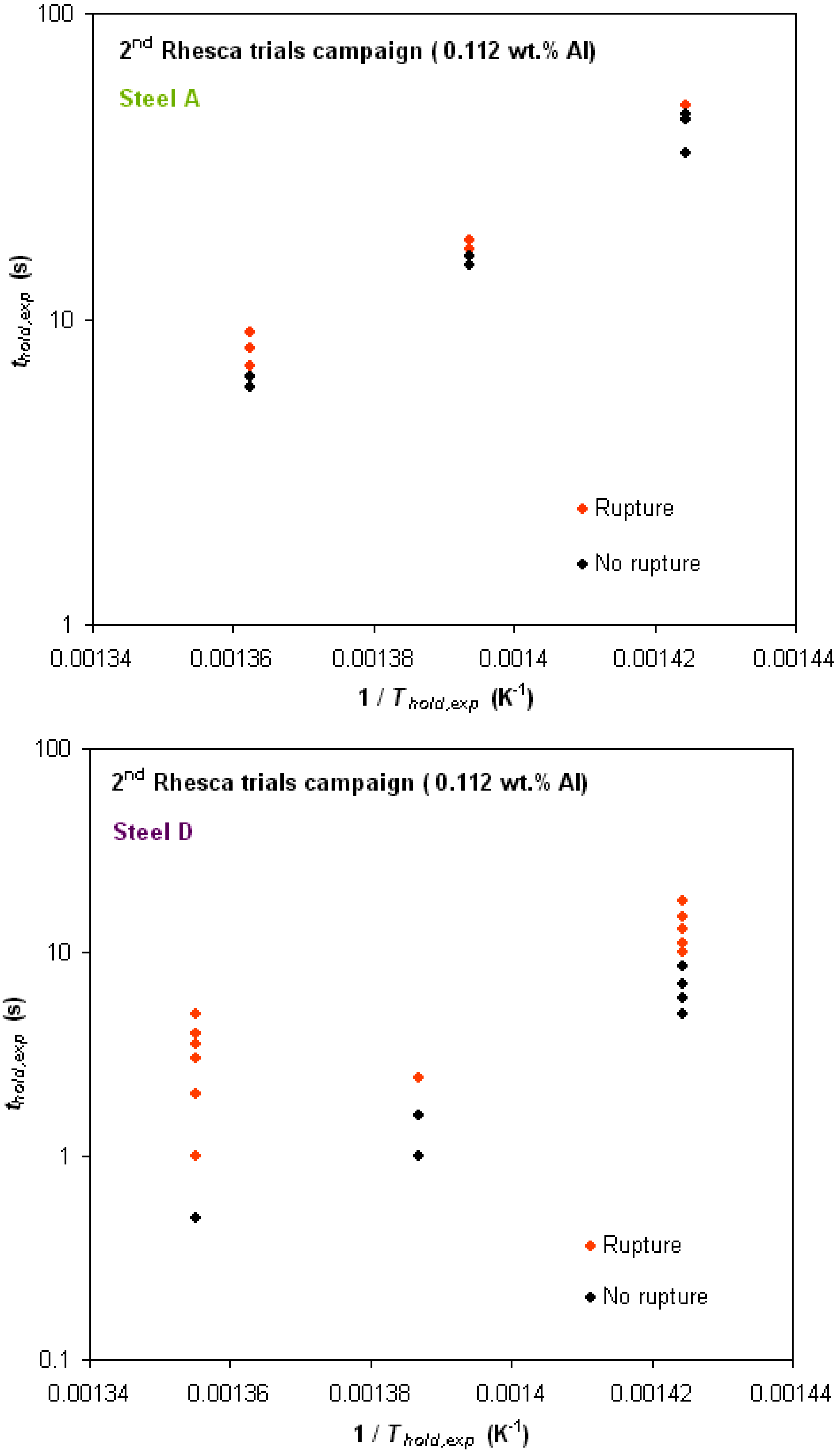

Figure 148: Experimental holding times (logarithmic scale) against inverse experimental holding temperature performed in the Gleeble 3500 pilot simulator to determine the inhibition layer breakdown kinetics (steels A and D, second Rhesca trials campaign).

Appendix H: Mathematical proof that the switch in relative reactivity with respect to the inhibition layer breakdown between two different Ti IF steels galvanized in the same conditions predicted by the model occurs at the same temperature independly of their chemical composition (Figure 106)

It has been seen in section III.3.2.2.2 that the kinetic law accounting for the inhibition layer breakdown can be written, in the case of isothermal heat treatments, as follows:

$$Ln\, t_c = Ln\left(\frac{Q_c}{D_0 \left|\nabla c_{Zn}^{i.l.}\right|}\right) + \frac{E_a}{RT_{hold}} \tag{H.1}$$

or:

$$y = a + bx \tag{H.2}$$

with:

$$y = Ln\, t_c\,;\; a = Ln\left(\frac{Q_c}{D_0 \cdot \left|\nabla c_{Zn}^{i.l.}\right|}\right);\; b = \frac{E_a}{R}\;;\; x = \frac{1}{T_{hold}} \tag{H.3}$$

If now the intersection of two given lines representing two given steel substrates with different chemical composition galvanized in the same conditions is considered (line and line'):

$$y = y'\,;\; a + bx = a' + b'x \tag{H.4}$$

$$x = \frac{a' - a}{b - b'} \tag{H.5}$$

According to the results depicted in Figure 105, the following linear equations can be written:

$$Ln\left(\frac{Q_c}{D_0 \cdot \left|\nabla c_{Zn}^{i.l.}\right|}\right) = a = a_1 x_{Ti_{excess}} + a_2 \tag{H.6}$$

$$E_a = bR = b_1 x_{Ti_{excess}} + b_2 \tag{H.7}$$

So that:

$$x = \frac{a' - a}{b - b'} = \frac{\left(a_1 x_{Ti_{excess}}' + a_2\right) - \left(a_1 x_{Ti_{excess}} + a_2\right)}{\frac{1}{R}\left[\left(b_1 x_{Ti_{excess}} + b_2\right) - \left(b_1 x_{Ti_{excess}}' + b_2\right)\right]} = \frac{a_1\left(x_{Ti_{excess}}' - x_{Ti_{excess}}\right)}{\frac{b_1}{R}\left(x_{Ti_{excess}} - x_{Ti_{excess}}'\right)} = -\frac{a_1 R}{b_1} \tag{H.8}$$

and:

$$y = a + bx = a_1 x_{Ti_{excess}} + a_2 + \frac{1}{R}\left(b_1 x_{Ti_{excess}} + b_2\right)\left(-\frac{a_1 R}{b_1}\right) = a_2 - \frac{a_1 b_2 R}{b_1} \tag{H.9}$$

According to equations H.8 and H.9 and taking into account that a_1, a_2, b_1 and b_2 are constants of the model with fixed value whatever the steel chemical composition, the intersection point (x, y) is always the same. Intersection time and temperature constant values can be directly obtained by substituting the values of constants a_1, a_2, b_1 and b_2 in equations H.8 and H.9:

$$x = -\frac{a_1 R}{b_1} = \frac{1}{T_{hold}} \rightarrow T_{hold} = 482.5\,°C \tag{H.10}$$

$$y = a_2 - \frac{a_1 b_2 R}{b_1} = Ln\, t_c \rightarrow t_c = 2.9\ s \tag{H.11}$$

ABSTRACTS

Mechanisms and kinetics of the galvannealing reactions on Ti IF steels

Hot-Dip GalvAnnealed (HDGA) coatings are produced by the immersion of the steel strip into an iron-saturated liquid zinc bath at around 460 °C containing small amounts of aluminium (from 0.1 to 0.135 wt.%, normally) and its subsequent heating (up to temperatures around 500-530 °C for about 10 s, typically) in order to trigger the alloying reactions between iron and zinc. The final microstructure of this kind of coatings is composed of a sequence of stratified Fe-Zn phase layers and its in-use properties are directly related to the phase distribution within the coating. The process parameters to be performed in industrial lines must therefore be optimized in order to obtain a successful coating microstructure with the minimum costs. The development of such a coating passes through different and complex reactions: the inhibition layer formation, the inhibition layer breakdown, the liquid zinc consumption and the iron enrichment of the solid coating. The kinetics accounting for these reactions must be studied and modelled separately in order to accurately control the evolution of the coating along the heat treatment performed in the industrial line. In the present work, the two first reactions were investigated in the case of Ti IF steel grades.

The kinetics of the inhibition layer formation is extremely fast and has therefore not been investigated in detail. Concerning this reaction, the focus was given to the nature of this inhibition layer and to the mechanisms accounting for its formation. It has been found that the inhibition layer formed in typical baths for galvannealed coatings production is composed of a very thin layer of the $Fe_2Al_5Zn_x$ phase (20-30 nm) on the steel surface and a thicker layer of the δ ($FeZn_7$) phase (around 200 nm) on its top. As the steel strip enters the zinc bath, iron dissolution from the former into the latter leads to an iron supersaturation at the solid / liquid interface. As a result, a very thin layer of metastable $Fe_2Al_5Zn_x$ nucleates on the steel surface favoured by preferential epitaxial relationships with ferrite. Subsequently, δ nucleates on the $Fe_2Al_5Zn_x$ layer allowing the final microstructure of the inhibition layer to become thermodynamically stable. The effect of the bath aluminium content on the nature of this inhibiting structure has also been studied. As the bath aluminium content is lowered, the $Fe_2Al_5Zn_x$ layer becomes discontinuous: the lower the bath aluminium content is, the higher the metastability of $Fe_2Al_5Zn_x$ is and the less probable its nucleation on the steel surface is.

The inhibition state is only transient and continued heat treatment will lead to the inhibition layer breakdown and the development of the further Fe-Zn alloying reactions. The present work has allowed proposing a particular mechanism accounting for the rupture of the observed inhibition layer. This reaction mechanism, controlled by the diffusion of zinc towards the steel grain boundaries, can be explained using the Al-Fe-Zn ternary phase diagram and summarized in two steps: the disappearance of the $Fe_2Al_5Zn_x$ layer at the inhibition layer / steel interface as a result of the enrichment of this interface in zinc, and the local nucleation of the Γ (Fe_3Zn_{10}) phase at the steel grain boundaries, breaking the inhibition layer off, when the zinc concentration at these locations becomes high enough.

The kinetics accounting for this reaction strongly depends on the Ti IF steel chemical composition, representative of the cleanliness of its grain boundaries, and on the nature of the inhibition layer, which is in turn closely related to the bath aluminium content. The effects of these two parameters on this kinetics have been investigated in this work. On the one hand, it has been found that the effect of the steel chemical composition on the inhibition layer breakdown kinetics would be ruled by the competition between two opposite phenomena: the rate of zinc diffusion at the steel grain boundaries and the ability of the steel to accumulate the zinc atoms at these locations. The cleaner the steel grain boundaries are, the faster the rate of zinc diffusion in these sites is but the most difficult the accumulation of zinc at these locations becomes as no alloying elements hamper the diffusion of zinc atoms. An effect of temperature on this competition could also be assumed. At low temperatures, the inhibition layer breakdown kinetics is controlled by the rate of zinc diffusion in the steel grain boundaries while at high temperatures it is controlled by the ability of the steel to accumulate zinc at the steel grain boundaries. However, in typical industrial cycles, most of the zinc quantity needed for the inhibition layer breakdown diffuses in the domain of low temperatures, so that the steel with the cleanest grain boundaries is the most reactive one. On the other hand, decreasing the bath aluminium content favours the discontinuity of $Fe_2Al_5Zn_x$, which accelerates the inhibition layer breakdown as zinc is expected to diffuse faster through δ (mainly composed of zinc) than through $Fe_2Al_5Zn_x$.

Keywords: Al-Fe-Zn ternary system; interfacial reactions; galvannealing; inhibition layer; inhibition breakdown; intermetallic compounds;

Mécanismes et cinétiques des réactions de galvannealing dans des aciers IF Ti

Les revêtements galvanisés alliés sont produits par immersion à chaud d'une bande d'acier dans un bain de zinc fondu à environ 460 °C, saturé en fer et contenant de faibles quantités d'aluminium (de 0,1 à 0,135% poids), suivie d'un traitement thermique (jusqu'à des températures voisines de 500-530 °C pendant environ 10 s) afin de déclencher les réactions d'alliation entre le fer et le zinc. La microstructure finale de ce type de revêtement est composée d'une succession de couches stratifiées de phases Fe-Zn et ses propriétés d'usage sont directement liées à la distribution de ces phases dans le revêtement. Les paramètres process à appliquer sur ligne industrielle doivent donc être optimisés pour obtenir la microstructure de revêtement souhaitée avec des coûts minimaux. Le développement d'un tel revêtement passe par différentes réactions complexes : la formation de la couche d'inhibition, la rupture de cette couche, la consommation du zinc liquide et l'enrichissement en fer du revêtement solide. Les cinétiques de ces réactions doivent être étudiées et modélisées séparément afin de contrôler avec précision l'évolution du revêtement au cours du cycle thermique. Dans ce travail, les deux premières réactions ont été étudiées dans le cas des aciers IF Ti.

La cinétique de formation de la couche d'inhibition est extrêmement rapide et n'a par conséquent pas été étudiée. L'attention a été portée sur la nature de cette couche et sur les mécanismes responsables de sa formation. Il a été démontré que la couche d'inhibition formée dans des bains classiques pour la production de ces revêtements est composée d'une première couche très mince de $Fe_2Al_5Zn_x$ (20-30 nm) sur la surface de l'acier et d'une seconde couche plus épaisse de δ ($FeZn_7$) (environ 200 nm) au-dessus. Lorsque l'acier est immergé dans le bain de zinc, la dissolution du premier dans le second conduit à une sursaturation en fer à l'interface solide / liquide. Une très fine couche de $Fe_2Al_5Zn_x$ métastable germe alors sur la surface de l'acier favorisée par des relations préférentielles d'épitaxie avec la ferrite. Par la suite, une couche de δ germe sur la couche de $Fe_2Al_5Zn_x$ ce qui permet à la microstructure finale de devenir thermodynamiquement stable. L'effet de la teneur en aluminium du bain sur la nature de la couche d'inhibition a également été étudié. Quand la teneur en aluminium du bain diminue, la couche de $Fe_2Al_5Zn_x$ devient discontinue car cette phase devient plus métastable et sa germination sur la surface de l'acier moins probable.

Cette étape d'inhibition n'est que transitoire et un traitement thermique prolongé conduira à la rupture de la couche d'inhibition et au développement des réactions Fe-Zn. Ce travail a permis de proposer un mécanisme de rupture compatible avec la nature biphasée de la couche d'inhibition. Ce mécanisme réactionnel, contrôlé par la diffusion du zinc dans les joints de grains de l'acier, peut être expliqué à l'aide du diagramme de phase ternaire Al-Fe-Zn et résumé en deux étapes : la disparition de la couche de $Fe_2Al_5Zn_x$ à l'interface couche d'inhibition / acier résultant de l'enrichissement de cette interface en zinc, et la germination de la phase Γ (Fe_3Zn_{10}) aux joints de grains de l'acier lorsque la concentration en zinc y devient suffisante. C'est cette germination qui va provoquer localement la rupture de la couche d'inhibition.

La cinétique de cette réaction dépend fortement de la composition chimique de l'acier IF Ti, qui va conditionner la propreté de ses joints de grains, et de la nature de la couche d'inhibition, qui est quant à elle étroitement liée à la teneur en aluminium du bain. Les effets de ces deux paramètres sur cette cinétique ont été étudiés dans ce travail. D'une part, il apparaît que l'effet de la composition chimique de l'acier sur la cinétique de rupture d'inhibition est contrôlé par la compétition entre deux phénomènes opposés : la vitesse de diffusion du zinc dans les joints de grains de l'acier et la capacité de l'acier à y accumuler les atomes de zinc. Plus les joints de grains de l'acier sont propres, plus la vitesse de diffusion du zinc dans ces sites est élevée mais plus l'accumulation de zinc y devient difficile car aucun élément d'alliage n'empêche la diffusion des atomes de zinc. Un effet de la température sur cette compétition a également été proposé. A basse température, la cinétique de rupture de la couche d'inhibition est contrôlée par la vitesse de diffusion du zinc dans les joints de grains de l'acier tandis qu'à haute température elle est contrôlée par la capacité de l'acier à accumuler du zinc aux joints de grains. Cependant, pour des cycles industriels classiques, la plupart de la quantité de zinc nécessaire pour la rupture d'inhibition diffuse dans le domaine de basses températures, de sorte que l'acier avec des joints de grains propres est le plus réactif. D'autre part, la diminution de la teneur en aluminium du bain favorise la discontinuité de la couche de $Fe_2Al_5Zn_x$, ce qui accélère la rupture de la couche d'inhibition car le zinc est supposé diffuser plus rapidement dans δ (constitué essentiellement de zinc) que dans $Fe_2Al_5Zn_x$.

Mots-clés: système ternaire Al-Fe-Zn; réactions interfaciales; galvannealing; couche d'inhibition; rupture d'inhibition; composés intermétalliques;